CORA Cork Open Research Archive
Cartlann Taighde Oscailte Chorcaí

Title	Development of miniaturized antennas and adaptive tuning solutions for body sensor network applications
Authors	Buckley, John
Publication date	2016
Original Citation	Buckley, J. 2016. Development of miniaturized antennas and adaptive tuning solutions for body sensor network applications. PhD Thesis, University College Cork.
Type of publication	Doctoral thesis
Rights	© 2016, John Buckley. - http://creativecommons.org/licenses/by-nc-nd/3.0/
Download date	2026-11-07 00:28:51
Item downloaded from	https://hdl.handle.net/10468/2817



UCC
University College Cork, Ireland
Coláiste na hOllscoile Corcaigh

Development of Miniaturized Antennas and Adaptive Tuning Solutions for Body Sensor Network Applications

John Buckley

BEng, MEngSc



NATIONAL UNIVERSITY OF IRELAND, CORK

Thesis submitted for the degree of Doctor of Philosophy

May 2016

Supervisor: [1]Dr. Kevin G. McCarthy

Supervisor: [2]Brendan O' Flynn

Head of School: [1]Professor Nabeel A. Riza

[1] School of Engineering, Electrical and Electronic Engineering, University College Cork

[2] Tyndall National Institute, University College Cork

Abstract

Wireless Sensor Networks (WSNs) are currently having a revolutionary impact in rapidly emerging wearable applications such as health and fitness monitoring amongst many others. These types of Body Sensor Network (BSN) applications require highly integrated wireless sensor devices for use in a wearable configuration, to monitor various physiological parameters of the user. These new requirements are currently posing significant design challenges from an antenna perspective.

This work addresses several design challenges relating to antenna design for these types of applications. In this thesis, a review of current antenna solutions for WSN applications is first presented, investigating both commercial and academic solutions. Key design challenges are then identified relating to antenna size and performance. A detailed investigation of the effects of the human body on antenna impedance characteristics is then presented. A first-generation antenna tuning system is then developed. This system enables the antenna impedance to be tuned adaptively in the presence of the human body. Three new antenna designs are also presented. A compact, low-cost 433 MHz antenna design is first reported and the effects of the human body on the impedance of the antenna are investigated. A tunable version of this antenna is then developed, using a higher performance, second-generation tuner that is integrated within the antenna element itself, enabling autonomous tuning in the presence of the human body. Finally, a compact sized, dual-band antenna is reported that covers both the 433 MHz and 2.45 GHz bands to provide improved quality of service (QoS) in WSN applications.

To date, state-of-the-art WSN devices are relatively simple in design with limited antenna options available, especially for the lower UHF bands. In addition, current devices have no capability to deal with changing antenna environments such as in wearable BSN applications. This thesis presents several contributions that advance the state-of-the-art in this area, relating to the design of miniaturized WSN antennas and the development of antenna tuning solutions for BSN applications.

Acknowledgements

The work described in the following pages is based on outputs from a number of funded programs, which I have been fortunate to work on over the past years. I would like to acknowledge the support of Enterprise Ireland for funding project (PC_2008_324) “An energy saving reconfigurable antenna matching system". I would also like to acknowledge Science Foundation Ireland (SFI) for co-funding this work under the European Regional Development Fund under GRANT Number 07/CE/I1147 (CLARITY) as well as the SFI-funded National Access Program (NAP). The support of the European Community is also greatly acknowledged under the Framework 7 SMAC (SMArt systems Co-design) Project (Reference: 288827).

I would especially like to thank my supervisors Dr. Kevin McCarthy and Brendan O'Flynn. Without Kevin's expert advice, enthusiasm, patience and encouragement, this thesis would not have been possible. Kevin's insight, attention to detail and love of teaching is something that I greatly admire and I hope that this thesis does some justice to his commitment to me. Without Brendan's constant support and encouragement, I would have given up a long time ago and this thesis would not have been possible. Brendan has always been a pillar of support during my time at Tyndall and this is something I deeply appreciate and respect.

I would also like to thank Professor Cian O' Mathuna for his support and encouragement during this work and Cian has always been a source of inspiration since my early days at Tyndall.

I would like to thank the Tyndall National Institute and the School of Engineering, Electrical and Electronic Engineering, University College Cork for their support in carrying out the work described in this thesis.

I would also like to pay a special thanks to Helen Buckley in the Graduate Studies Office and Niamh O' Sullivan in the School of Engineering who have both been so helpful to me throughout this work.

I would especially like to acknowledge the support of all the members of the Wireless Sensor Networks Group and Microsystems Centre in Tyndall, both past and present with a special thanks to Domenico Gaetano, Loizos Loizou, Javier Torres Sanchez, Philip Angove, John Doyle, Peter Haigh, Marco Belcastro, Alan Mathewson, Michael Grufferty, Ted O' Shea, John Barry, John Rae, Donal O' Sullivan and many more. I would also like to acknowledge all members of other departments in Tyndall for their help including the IT, HR and Finance departments.

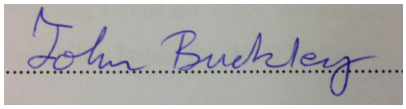
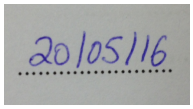
I would also like to pay a special thanks to Professor Max Amann of the Dublin Institute of technology, Professor Philippe Le Thuc of the Université of Nice, France and Dr. Colin Murphy of University College Cork for their expertise, time and effort in examining this thesis.

I would like to pay a special thanks to Bob Savage and Les Gosnell of EMC who have always been a source of inspiration and provided me with many opportunities in my early career for which I am deeply indebted.

Finally, I would like to thank Maeve, my mother Catherine and my sisters Noreen and Anita for their support and encouragement over the years. Without their inspiration and support, this work would not have been possible.

Declaration

Declaration: I hereby declare that this thesis is entirely my own work and has not been submitted for another degree, either at The National University of Ireland, Cork or elsewhere.

Signed:  Date: 

Dedication

To my wonderful mother Catherine

and to the memory of my beloved father John T. Buckley

Table of Contents

List of Figures ix

Chapter 1. Introduction 1

Chapter 2. Background 7

2.1 Antenna Parameters 7
2.2 Impedance Matching 19
2.3 Design and Measurement Methodology 27
2.4 Conclusions 31

Chapter 3. Literature review 32

3.1 Wireless Sensor Networks (WSN) 33
3.2 Antenna Size Issues For WSN Devices 40
3.3 Antenna Detuning Issues for WSN Devices 47
3.4 Wireless Reliability Issues for WSN Devices 50
3.5 Conclusions 52

Chapter 4. First-Generation Adaptive Antenna Tuning System 53

4.1 Background 53
4.2 Example of Antenna Detuning for a Wrist-Mounted Antenna 54
4.3 Antenna Tuner System Design 71
4.4 Prototype and Measured Results 75
4.5 Design of Tuner Module 77
4.6 Tuning Algorithm 86
4.7 Conclusions 92

Chapter 5. 433 MHz Antenna Design and Characterization 93

5.1 Background 93
5.2 Antenna Design 94
5.3 Antenna Prototype and Measured Results 103
5.4 Human Body Effects on Antenna Performance 109
5.5 Human-Body Antenna Impedance Measurements 112
5.6 Antenna Transmission Line Model 115
5.7 Conclusions 120

Chapter 6. Second-Generation Antenna-Integrated Tuner Design 122

6.1 Background 122
6.2 Reconfigurable Matching Network Design 123
6.3 Antenna Tuner Implementation 128
6.4 Prototype Measurement and Verification 133
6.5 Conclusions 141

Chapter 7. Dual-Band Antenna Design 143

7.1 Background 143
7.2 Review of the original 433 MHz antenna design 144
7.3 Antenna Design 145
7.4 Antenna Simulation 148
7.5 Measured Results 156
7.6 Conclusions 163

Chapter 8. Conclusions and Future Work 164

8.1 Summary 164
8.2 Contributions to state-of-the-art 165
8.3 Future Work 165

Bibliography 168

List of Figures

Figure 1-1 Thesis outline 6
Figure 2-1 Transmitting source connected to an antenna 8
Figure 2-2 Transmitting source connected to a transmission line and antenna 9
Figure 2-3 Spherical co-ordinate system 10
Figure 2-4 Transmission line terminated in a load impedance Z_L 12
Figure 2-5 Two-port Scattering parameter definition 14
Figure 2-6 Two-port network with arbitrary source and load impedances 17
Figure 2-7 (a) Electrically small antenna definition, (b) Calculated Q_A versus *ka* [36] ... 18
Figure 2-8 Series to parallel equivalent circuit 20
Figure 2-9 *L*-matching network using the *Q*-Based method 21
Figure 2-10 Transformation of series to parallel equivalent circuit 22
Figure 2-11 (a) *Π*-type matching network, (b) Resulting impedance transformation 23
Figure 2-12 Impedance matching example, (a) Circuit, (b) Smith chart 25
Figure 2-13 HFSS model setup (a) Waveport, (b) Airbox boundary conditions 28
Figure 2-14 Dipole fed antenna (a) Balanced, (b) Unbalanced 29
Figure 2-15 (a) Sleeve balun, (b) Dual-Band sleeve balun and ferrite beads 30
Figure 3-1 Block diagram of typical WSN node 34
Figure 3-2 Example of a BSN tennis application [63, 65] 35
Figure 3-3 433 MHz wireless sensor to monitor concrete curing [75] 36
Figure 3-4 Example of body sensor network for health applications 37
Figure 3-5 Platforms (a) Mica [83], (b) Mica Dot [84], (c) Wasp [85], (d) Tyndall [23] 38
Figure 3-6 Tyndall mote size specifications [23] 39
Figure 3-7 Commercial antenna size versus 25 mm mote platform 40
Figure 3-8 Commercial antenna examples (a) 1/4-Wave Whip [90], (b) Helical [92], ... 41
Figure 3-9 Tyndall mote layer physical size requirements 43
Figure 3-10 Antenna physical size requirements 43

Figure 3-11 433 MHz meandered IFA antenna [95] 44
Figure 3-12 Spiral shaped meander-line 433 MHz antenna [43] 45
Figure 3-13 Double loop 433/ 868 MHz antenna [96] 45
Figure 3-14 Slotted PIFA for bio-implantable applications [97] 46
Figure 3-15 CDMA antenna tuner [117], (a) Block diagram, (b) Double stub tuner 49
Figure 3-16 Cellular antenna tuner, (a) Block diagram, (b) Tuner module [120] 50
Figure 4-1 (a) 433 MHz AUT, (b) AUT on human wrist 56
Figure 4-2 Phantom measurement setup 57
Figure 4-3 Measured antenna characteristics for human and phantom test cases: 57
Figure 4-4 Comparing measured AUT S_{11} characteristics on human and phantom 58
Figure 4-5 (a) 433 MHz AUT, (b) AUT placed on phantom arm 59
Figure 4-6 AUT to phantom distance d using foam insulating material 59
Figure 4-7 Measured antenna S_{11} and mismatch loss for varying distance d 60
Figure 4-8 Measured S_{11} (magnitude and phase) versus distance d at f_0 61
Figure 4-9 Π-type matching circuit connected to VNA 62
Figure 4-10 (a) Manual tuner, (b) Offset board 62
Figure 4-11 Photograph of test setup (a) Unmatched, (b) Matched 63
Figure 4-12 Measured antenna S_{11} in matched and unmatched cases 64
Figure 4-13 433 MHz WSN mote 65
Figure 4-14 Test cases (a) Free-Space, (b) No match, (c) Manual tuner, (d) Test setup 67
Figure 4-15 Measured P_{RX} and I_{SUPPLY} for the three configurations of T_X antenna 68
Figure 4-16 Measured Tx mote current consumption versus transmit power 70
Figure 4-17 Block diagram of antenna tuner system 72
Figure 4-18 Test setup for RF power detector characterization 74
Figure 4-19 Measured power detector response 74
Figure 4-20 Photograph of antenna tuner system 75
Figure 4-21 Simplified tuner schematic and details of tunable capacitor implementation 78
Figure 4-22 RF switch (a) Functional view, (b) ON-parasitics, (c) OFF-parasitics 79

Figure 4-23 Test fixture to measure RF switch parasitics 80
Figure 4-24 Measured S_{11} of RF switch in ON and OFF states 81
Figure 4-25 Simulation model for the 4-bit tunable capacitor C_S 82
Figure 4-26 Simulated capacitance C_S versus control word 83
Figure 4-27 Prototype tuner, (a) Schematic, (b) Prototype 84
Figure 4-28 Comparing measured and simulated 4-bit capacitance C_S 86
Figure 4-29 Flow chart of the antenna tuning algorithm 87
Figure 4-30 Screenshot of the antenna tuner GUI 89
Figure 4-31 Oscilloscope measurement of V_{REF} signal during tuning 90
Figure 4-32 Measured S_{11} and G_T of the tuner module 91
Figure 5-1 Outline of 433 MHz Antenna Topology 94
Figure 5-2 Effects of spiral element length L_{AB} on antenna resonant frequency 95
Figure 5-3 Effects of spiral and patch element on resonant frequency 96
Figure 5-4 Effects of inductive length parameter L_L 97
Figure 5-5 Effects of varying inductive width parameter W_L 98
Figure 5-6 Effects of varying stub length L_S 99
Figure 5-7 Effects of soldermask on antenna resonant frequency 100
Figure 5-8 Simulated antenna surface current distribution at 433 MHz 100
Figure 5-9 Prototype 433 MHz antenna (a) Top side, (b) Bottom side, (c) Test setup .. 103
Figure 5-10 Measured and simulated antenna S_{11} 104
Figure 5-11 Simulated 433 MHz 3D Gain, (a) Normalized, (b) Un-normalized 105
Figure 5-12 Normalized measured and simulated radiation patterns at 433 MHz 106
Figure 5-13 (a) Photograph of AUT, (b) Heterogeneous phantom arm model [42] 109
Figure 5-14 (a) Photograph of test setup, (b) Measured and simulated S_{11} at f_0 111
Figure 5-15 Overview of measurement setup for on-body AUT characterization 112
Figure 5-16 Summary of AUT measurements (a) Upper body, (b) Lower body, ... 114
Figure 5-17 Simplified schematic of the 433 MHz antenna 115
Figure 5-18 Equivalent circuit of the 433 MHz antenna 116

Figure 5-19 Equivalent circuit model versus measured data 118
Figure 5-20 Human body loading effects added to antenna equivalent circuit 119
Figure 5-21 On-body equivalent circuit versus measured data 120
Figure 6-1 Summary of this chapter 123
Figure 6-2 Total measured impedance variation and *ML* with no tuning 124
Figure 6-3 Simplified circuit for the *Π* -type matching network 125
Figure 6-4 Equivalent circuit of PE64102 DTC capacitance [167] 126
Figure 6-5 (a) *ML* no matching, (b) G_T with matching 127
Figure 6-6 Block diagram and photograph of tuner module 128
Figure 6-7 RF power detector characterization (a) Test setup, (b) Measured results 130
Figure 6-8 Total measured on-body antenna impedance variation 131
Figure 6-9 Simulated optimal states for C_1 and C_2 vs $|\Gamma_L|$ for $0° \le \Theta_L \le 90°$ 132
Figure 6-10 (a) Tuner module test setup, (b) S_{22}* at 433 MHz 134
Figure 6-11 Measured and simulated values of ΔG_T at 433 MHz 135
Figure 6-12 Photograph of final tunable antenna 136
Figure 6-13 (a) Measured AUT $S_{11,}$ (b) Narrow and wideband balun designs 137
Figure 6-14 Measured AUT S_{11} response using narrow and wideband balun 138
Figure 6-15 Measured antenna S_{11} for the tunable antenna 139
Figure 6-16 Comparing measured S_{11} of AUT and tunable antenna 139
Figure 6-17 Oscilloscope measurement of V_{FWD} signal during tuning 140
Figure 7-1 Simulated surface currents of 433 MHz antenna [153] 144
Figure 7-2 (a) Configuration of proposed antenna, (b) Photograph (top and bottom) 145
Figure 7-3 Simulated antenna S_{11} with and without the parasitic element 148
Figure 7-4 Simulated antenna S_{11} with and without the parasitic element 149
Figure 7-5 Simulated surface current distributions (a) 433 MHz, (b) 2.45 GHz 150
Figure 7-6 Simulated surface current distribution (a) 433 MHz, (b) 2.45 GHz 151
Figure 7-7 Simulated antenna S_{11} for varying L_6 (a) Low-band, (b) High-band 152
Figure 7-8 Simulated antenna S_{11} for varying L_3 (a) Low-band, (b) High-band 153

Figure 7-9 Simulated antenna S_{11} for varying L_S (a) Low-band, (b) High-band 154
Figure 7-10 Photograph of prototype antenna 156
Figure 7-11 Comparing measured and simulated antenna S_{11} at 433 MHz 157
Figure 7-12 Comparing measured and simulated antenna S_{11} at 2.45 GHz 157
Figure 7-13 Simulated 3D gain at 433 MHz, (a) Normalized, (b) Un-normalized 158
Figure 7-14 Simulated 3D Gain at 2.45 GHz, (a) Normalized, (b) Un-normalized 159
Figure 7-15 Measured and simulated radiation patterns 161
Figure 7-16 Radiation pattern measurement setup (a) *x-z* plane, (b) *x-y* plane 162

List of Tables

Table 3-1 Summary of mote platform size and frequency performance 40
Table 3-2 Specification summary of commercial-type 433 MHz antennas 42
Table 3-3 Specification summary of several 433 MHz antennas in the literature 47
Table 4-1 S_{11} accuracy measurements for the antenna tuner system 76
Table 4-2 Summary of PE4210 RF switch parasitics 81
Table 4-3 Simulated capacitance values for CS_0 to CS_3 82
Table 4-4 Prototype tuner component values 85
Table 4-5 DC current consumption for individual tuner system blocks 91
Table 5-1 Optimized antenna design parameters 102
Table 5-2 Summary of antenna Gain and Efficiency parameters at 433 MHz 106
Table 5-3 Comparing proposed antenna performance to commercial solutions 107
Table 5-4 Comparing proposed antenna performance to the literature 108
Table 5-5 Numerical model dielectric characteristics specified at 433 MHz 110
Table 5-6 Final optimized equivalent circuit model parameters 117
Table 6-1 DTC equivalent model parameters [167] 126
Table 6-2 Performance comparison between first and second-generation tuners 142
Table 7-1 Final design parameters for the antenna 147
Table 7-2 Antenna design parameters included for optimization 155
Table 7-3 Antenna Gain and Radiation Efficiency at 433 MHz and 2.45 GHz 162

GLOSSARY OF TERMS

ADC	Analog to Digital Converter
ADS	Analog Design System (Keysight)
AUT	Antenna under Test
BALUN	Balanced-to-unbalanced
BER	Bit Error Rate
CMOS	Complementary Metal Oxide Semiconductor
DAC	Digital to Analog Converter
DTC	Digitally Tunable Capacitor
FEM	Finite Element Method
FOM	Figure of Merit
FR-4	Flame Retardant Type-4 (Glass epoxy PCB substrate material)
HFSS	High Frequency Structure Simulator (Ansys)
IFA	Inverted F Antenna
IoT	Internet of Things
ISM	Industrial Scientific and Medical
JTAG	Joint Test Action Group (JTAG)
LTCC	Low Temperature Co-Fired Ceramic
LUT	Lookup Table
MEMS	Micro-ElectroMechanical Systems
MICS	Medical Implant Communication Service
PA	Power Amplifier
PCB	Printed Circuit Board
PIN	P-Intrinsic-N
RF	Radio Frequency

GLOSSARY OF TERMS

RFID	Radio Frequency Identification
RISC	Reduced Instruction Set Computer
RL	Return Loss
Rx	Radio Receiver
Tx	Radio Transmitter
SMA	Sub-Miniature Version A
SMD	Surface Mount Device
SNR	Signal to Noise Ratio
SOI	Silicon on Insulator
SOS	Silicon on Sapphire
SPDT	Single Pole Double Throw
SRD	Short Range Device
VNA	Vector Network Analyzer
VSWR	Voltage Standing Wave Ratio
WBAN	Wireless Body Area Network
WSN	Wireless Sensor Network
XCVR	Radio Transceiver

LIST OF SYMBOLS and their SI Units

(Φ, θ)	Spherical co-ordinates (°)
BW_{-3dB}	-3 dB Bandwidth (Hz)
C	Capacitance (F)
c_0	Speed of light in vacuum (299,792,458 ms^{-1})
D	Antenna Directivity (dBi)
ε_R	Effective dielectric permittivity
ε_{RAD}	Antenna radiation efficiency
F	Frequency (Hz)
f_0	Resonant Frequency (Hz)
f_C	Centre frequency (Hz)
G	Antenna Gain (dBi)
G_R	Antenna Realized Gain (dBi)
G_T	Transducer Power Gain (dB)
L	Inductance (H)
ML	Mismatch Loss (dB)
Q	Quality Factor
RL	Return Loss (dB)
S_{mn}	Two-port scattering Parameters
$tan\delta$	Dielectric material loss tangent
x, y, z	Cartesian co-ordinates (m)
Z_A	Antenna input impedance (Ω)
Γ_{IN}	Input Reflection Coefficient
Γ_L	Load Reflection Coefficient
Γ_{OUT}	Output Reflection Coefficient
Γ_S	Source Reflection Coefficient

R_R	Antenna radiation resistance (Ω)
λ_0	Free-space wavelength (m)

Chapter 1. Introduction

Wireless sensor networks (WSNs) are a collection of sensor devices commonly referred to as *nodes* or *motes* with each node containing a small computer processor and a radio that enables information to be transferred wirelessly between nodes. Wireless sensor networks, with their distributed processing capabilities, are being employed in a rapidly growing range of application areas where monitoring and interaction with the physical world is essential. For example, wireless sensor networks are having a revolutionary effect on how physiological parameters are sensed for health care applications using small, wearable wireless sensor devices for patient tracking [1] as well as smart wearables for the visually impaired [2]. The key reasons for their adoption relates to their ease of use and deployment as well as their cost effectiveness when compared with traditional wired networks. The combination of wearable computing and wireless communication technologies enables the realization of Body Sensor Network (BSN) applications for remote physiological and multi-parameter monitoring [3]. These types of wireless sensor applications are also referred to as body area network (BAN) or Wireless Body Area Network (WBAN) [4].

In terms of their implementation, wireless sensor nodes generally consist of an application specific sensor or sensors that measure one or more physical or environmental parameters such as temperature, pressure, acceleration etc. The sensor output is interfaced with a digital processor. The controller is capable of processing the sensor output, either analog or digital, and may store intermediate data using the processor's on-chip memory. A low date-rate radio transceiver and antenna are generally included to provide low power wireless functionality.

At the present time, although wireless sensor network technology has great potential for a wide range of applications, a number of key research challenges exist. One of the most important challenges for sensor nodes is the low power consumption requirement as these devices are generally powered with irreplaceable, low capacity batteries [5]. WSN devices therefore tend to use very low power methods to maximize the lifetime of the node in a deployed scenario. The power requirement for the radio transceiver is a particularly important factor as the radio typically consumes a large portion of the system's total power budget, both in transmit and receive mode.

Wireless sensor networks most generally operate in the license free industrial, scientific, and medical (ISM) radio bands. These frequency bands are reserved internationally for short-range device (SRD) wireless communications. In Europe, these frequency bands include the 433 MHz, 868 MHz and 2.45 GHz bands [6]. The lower frequency ISM bands can offer advantages in terms of reduced free space path loss when compared with the higher frequency bands. For example the free space path loss at 433 MHz is approximately 15 dB less than at 2.45 GHz [7]. Another issue with the high frequency ISM bands concerns human body absorption of EM radiation. The depth of penetration of EM energy into the human body decreases with increasing frequency [8]. This is due to the skin effect phenomenon that causes RF currents to flow on the surface (skin) of a conductor as the frequency is increased [9]. The conductivity of human tissue also increases significantly with increasing frequency, and together with the skin effect, leads to increased overall attenuation at higher frequencies [10]. The need for improved performance in biotelemetry applications has therefore led to the introduction of the Medical Implant Communication Services (MICS) band (402-405 MHz) as an alternative to the 2.45 GHz band for bio-implantable applications [11].

In terms of their physical implementation, small and lightweight wireless sensors are a key requirement for unobtrusive monitoring in wearable BSN applications [12] and highly integrated antenna realizations are therefore required. Several types of 433 MHz antennas are available commercially, including whip [13], dipole [14], helical [15] and small-sized

chip-type antennas [16]. Chip-type antennas have the advantage that they can be realized in a very small size and are easily integrated into the target application as Surface Mount Device (SMD) components. The small antenna size is a clear benefit from a system integration point of view. However, decreasing the size of the antenna leads to a negative impact on the efficiency, gain and bandwidth performance [17] and realizing small, high-performance antennas is therefore extremely challenging.

These negative antenna-related effects can create a number of performance issues for the end-application. These issues include reduced communications range, increased bit-error-rate (BER) as well as increased sensitivity to the effects of nearby printed circuit board (PCB) components. With respect to PCB layout, these effects may also result in the requirement for non-standard or customized PCB layout designs to meet the recommended PCB layout design guidelines for the antenna. The need for antenna impedance matching networks is also a common requirement. All of the preceeding issues are undesirable as they lead to increased design and characterization requirements that ultimately result in increased design and product costs. These issues highlight the need for new types of small, low cost antenna that can maintain an acceptable degree of performance for the chosen application.

Another issue arises in wearable applications when wireless sensors are placed close to the human body. The electromagnetic coupling between the antenna and body can affect key antenna performance parameters such as resonant frequency, impedance, efficiency, radiation, and polarization characteristics [18, 19]. The presence of the human body can lead to a detuning of the antenna's resonant frequency as well as a change in the antenna impedance. The resulting impedance mismatch results in the reflection of electromagnetic energy from the antenna that ultimately leads to a reduction in radiated power from the antenna. In order to maintain a specific link budget, the transmitter Power Amplifier (PA) output power may need to be increased if this is an option but this can be an issue since increasing the transmit power also leads to increased power consumption.

In most wireless sensor devices, an impedance matching network is required to match the radio transceiver impedance to that of the antenna. This is typically achieved using an impedance matching network that is implemented using lumped element networks. A common assumption during the design phase is that the antenna impedance is fixed and has a nominal impedance or range of impedances that does not vary with time. In reality however, placing an antenna close to an object such as the human body can significantly alter the antenna impedance from its nominal value. The inability of current wireless sensor technology to deal with changing antenna environments is therefore a challenge. This is especially the case in specific types of wearable applications where the reliability of wireless communications is critical, such as in health monitoring applications [20-22]. Antenna tuning technology is only recently beginning to emerge in cellular applications. However, very little has been reported in the literature regarding the performance issues associated with antenna detuning for wireless sensor applications in particular. Another key issue at present relates to the reliability or quality-of-service (QoS) of the wireless connection. The vast majority of current WSN devices use a *single frequency band* to communicate in a wireless network. If the network fails or is adversely affected by interference due to another wireless device operating at the same frequency, this can negatively affect the reliability of the wireless connection. Therefore, there is a need for improved data reliability and QoS compared to the state-of-the-art.

The motivation of the research presented in this thesis is to address a number of specific design challenges with a particular focus on antenna-related design challenges. These challenges relate to antenna size issues, antenna detuning and the need for improved wireless network reliability. The work focuses in particular on a specific type of wireless sensor network device called the Tyndall mote platform [23].

An outline of this thesis is summarized in Figure 1-1. Chapter 2 outlines fundamental parameters, definitions and concepts relating to antenna and impedance matching network design and characterization. Chapter 3 presents an overview of state-of-the art wireless sensor platforms including the Tyndall mote platform as well as highlighting a number of

issues relating to antenna performance. A review of state-of-the art antenna and tuning solutions for WSN applications is then presented.

Some key design and performance issues and technology gaps are then identified and the requirements for new antenna designs are defined. Chapter 4 presents the design of a custom antenna matching system. The chapter begins with an experimental investigation of antenna detuning effects associated with the human wrist, using a 433 MHz Tyndall mote and a commercial 433 MHz antenna. The design and characterization of a custom antenna tuning system is then described. This solution is a system-level, first-generation adaptive antenna tuning solution that is later used as the basis for the development of a more integrated and higher performance tunable antenna in Chapter 6. Chapter 5 describes the design of a 433 MHz antenna that is compatible with the size requirements of the Tyndall mote platform. The design of the antenna is presented and the results of detailed on-body impedance characterization are described. A transmission line antenna model that allows rapid determination of total antenna impedance variation on the human body is also described. Chapter 6 combines the antenna tuner design of Chapter 4 together with the antenna design of Chapter 5 in the realization of a compact, fully integrated tunable 433 MHz antenna. Chapter 7 describes the design of a small-sized, dual-band antenna that can operate on both the 433 MHz and 2.45 GHz ISM bands. This antenna has applications for QoS improvement in WSN applications. Chapter 8 concludes the thesis with a summary of the important outcomes and contributions of the work as well as suggestions for future research.

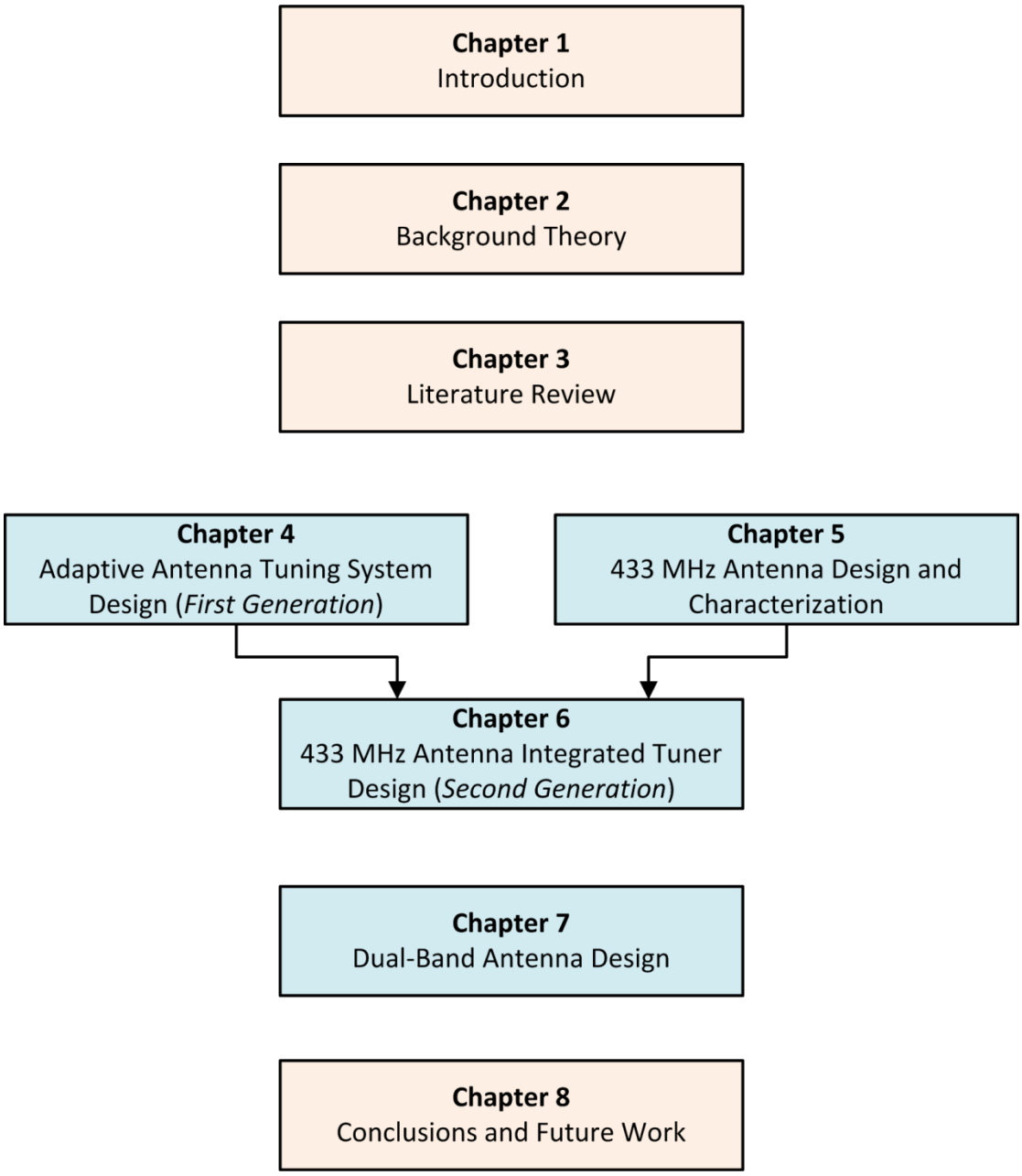


Figure 1-1 Thesis outline

Chapter 2. Background

In this section, a number of the most important definitions are introduced in relation to antenna and matching circuit design. Fundamental quantities that describe both the radiation and impedance characteristics of the antenna are first described followed by some important definitions, terms and design approaches for impedance matching networks. Finally, a number of simple impedance matching network designs are presented that illustrate key concepts used in later chapters of the thesis. Note that only brief descriptions of the most important parameters are presented here but a more detailed discussion of this material may be found in references [24-26].

2.1 Antenna Parameters

2.1.1 *Antenna Definition*

The IEEE Standard Definitions of Terms (IEEE Std 145-1983) defines an antenna as "a means for radiating or receiving radio waves" [24]. An antenna can be regarded as a transitional structure or transducer that can convert between a guided and a radiating electromagnetic wave. Antennas are typically reciprocal in nature meaning that they have identical radiation characteristics while transmitting and receiving.

2.1.2 *Antenna Impedance*

One of the most important antenna parameters, especially in the context of this work, concerns the impedance of the antenna.

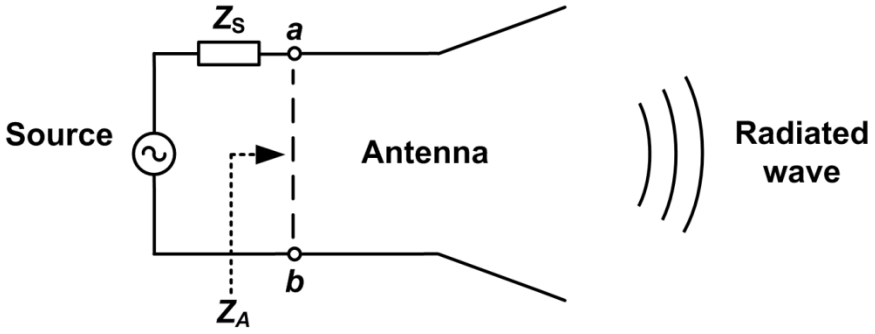


Figure 2-1 Transmitting source connected to an antenna

More specifically, the input impedance of the antenna is defined as the impedance presented by the antenna at its terminals *a-b* [24] as shown in Figure 2-1. The ratio of voltage to current at terminals *a-b* defines the input impedance of the antenna. The antenna impedance is generally a complex or vector quantity with real and imaginary components, and can be expressed as

$$Z_{\mathrm{A}} = R_{\mathrm{A}} + j\,X_{\mathrm{A}}, \tag{2.1}$$

where Z_{A} is the antenna impedance (Ω) measured at terminals *a-b*, R_{A} is the antenna resistance (Ω) and X_{A} is the antenna reactance (Ω). The quantities R_{A} and X_{A} generally vary with frequency. In a typical transmitting configuration, the antenna is connected to the RF transmitter as illustrated in Figure 2-2. In the configuration shown, the radio frequency (*RF*) source V_{s} is connected directly to transmission line T_1 that conveys electromagnetic energy from the transmitting source to the antenna. The impedance of the source is denoted Z_{S} and is shown as an arbitrary, complex quantity. The transmission line characteristic impedance Z_0 is generally chosen to match the output impedance of the source in order to ensure maximum power transfer to the load.

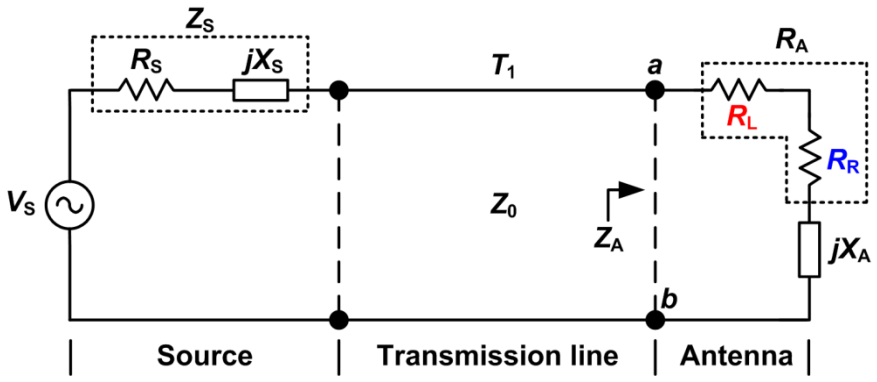


Figure 2-2 Transmitting source connected to a transmission line and antenna

The transmission line is chosen to exhibit low loss at the operating frequency and its implementation can vary from co-axial, to co-planar-waveguide to microstrip structures that are generally dictated by the requirements of the final application. As shown in Figure 2-2, the antenna resistance R_A has two components and is defined as

$$R_A = R_R + R_L \tag{2.2}$$

where R_R is the radiation resistance (Ω) and R_L is the loss resistance of the antenna (Ω). The radiation resistance R_R is a key antenna parameter as it denotes the equivalent resistance that is attributed to radiation of RF power from the antenna. In contrast, the loss resistance R_L represents unwanted ohmic losses in the antenna itself. These losses do not contribute to radiation of energy from the antenna but are instead dissipated as heat. Note that for this simplified case, losses other than ohmic losses (e.g. dielectric losses in an antenna substrate) are not considered.

2.1.3 *Antenna Co-Ordinate System*

The radiation characteristics of antennas are generally expressed using a spherical co-ordinate system [24] as shown in Figure 2-3. This co-ordinate system allows the antenna radiation properties to be defined in three dimensions as a function of the azimuthal angle Φ and elevation angle θ as shown.

In practice, the full spherical patterns are generally not required and the key antenna radiation characteristics can be determined using three principal planes (*x-y, x-z, y-z*) only.

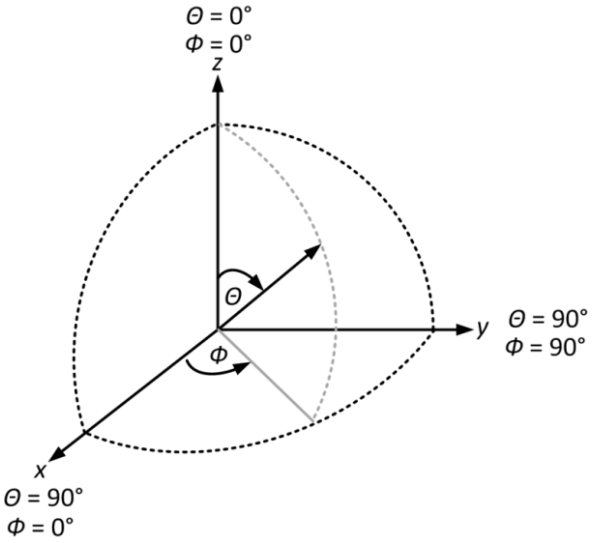


Figure 2-3 Spherical co-ordinate system

2.1.4 *Antenna Gain and Directivity*

The gain and directivity of an antenna are two of the most important parameters that describe the performance of an antenna. The directivity D of an antenna under test (AUT) is defined as the ratio of the maximum power density P (W/m^2) in a given direction (specified by the spherical co-ordinates Φ and θ) to the average value over a sphere as observed in the far field [25] and can be expressed as

$$D = \frac{P(\theta, \Phi)_{\mathrm{MAX}}}{P(\theta, \Phi)_{\mathrm{AVG}}}. \tag{2.3}$$

Antenna directivity, being a ratio of two power quantities, is a unitless value that can vary between $0 \leq D \leq 1$ and, in practice, is typically expressed in units of dBi or dB relative to an idealized isotropic antenna that radiates equally well in all directions.

The gain of an AUT is denoted G and is defined as the ratio of maximum power density P_{MAX} (W/m^2) of the AUT to that of a standard or reference antenna of known gain G_{REF} [25] or

$$G = \frac{P_{\mathrm{MAX}}\ (\mathrm{AUT})}{P_{\mathrm{MAX}}\ (\mathrm{Ref\ Ant})} \times G_{\mathrm{REF}} \tag{2.4}$$

In practice, the quantity G may also be expressed as a quantity G_{R} called the *Realized Gain* that also takes into account the inherent losses in the antenna due to conductor and dielectric losses as well as impedance mismatch losses [24]. Similar to directivity, antenna gain is generally expressed in units of dBi, or dB relative to an ideal, isotropic radiating antenna.

2.1.5 *Radiation Efficiency*

Antenna efficiency is an important figure-of-merit for an antenna as it measures the fraction of input power that is delivered to the radiation resistance for dissipation as radiation from the antenna [27]. Referring to Figure 2-2, the radiation efficiency of an antenna is defined as the ratio of the power delivered to the radiation resistance R_{R} to the total power delivered to both R_{R} and R_{L} [24]. The radiation efficiency is defined as

$$\varepsilon_{RAD} = \frac{R_{\mathrm{R}}}{R_{\mathrm{R}} + R_{\mathrm{L}}} \tag{2.5}$$

and ranges in value from $0 \leq \varepsilon_{\mathrm{RAD}} \leq 1$ but in practice is always less than unity due to inherent losses within the antenna. The antenna gain, directivity and radiation efficiency are also related by the following expression [25]

$$G = \varepsilon_{RAD} D \tag{2.6}$$

For electrically small antennas, it is common for the radiation efficiency to be much less than unity with a corresponding gain that is much less than 0 dBi.

2.1.6 *Reflection Coefficient*

The reflection coefficient of an antenna measures the degree of RF energy reflection from the antenna. For the antennas discussed in this thesis, it can be considered using the 1-port circuit of Figure 2-4 where a transmission line of characteristic impedance Z_0 is terminated with a load impedance $Z_{L,}$ representing the antenna impedance. The quantity V_1^+ is defined as the amplitude of the voltage wave incident on *Port* 1 and V_1^- is the amplitude of the voltage wave that is reflected from *Port* 1. The *voltage reflection coefficient* Γ_L at the antenna is defined as the ratio of the amplitude of the reflected voltage wave V_1^- to the amplitude of the incident voltage wave V_1^+ [26] and is expressed as

$$\Gamma_L = \frac{V_1^-}{V_1^+} = \frac{Z_L - Z_0}{Z_L + Z_0} \tag{2.7}$$

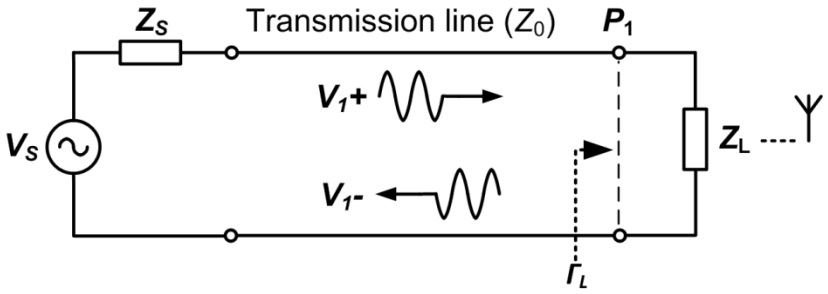


Figure 2-4 Transmission line terminated in a load impedance Z_L

The quantity Γ_L varies from $\Gamma_L = 0$ (no reflection) to $\Gamma_L = \pm 1$ (full reflection with the phase of Γ_L dependent on whether the load is a short or open circuit). For the case of an antenna load, it is clear that for maximum signal delivery to the antenna, it necessary to minimize the quantity Γ_L during normal operation. This is one of the key design goals throughout this work in terms of designing both antennas and antenna matching circuits.

2.1.7 *Return Loss*

Another parameter that is used to describe the performance of the antenna is return loss. Return loss (*RL*) is a measure of the degree of signal reflection from the antenna [28]. This quantity is derived from the voltage reflection coefficient Γ_{L} and is defined as

$$RL(\mathrm{dB}) = -20\log_{10}\left(\left|\Gamma_{\mathrm{L}}\right|\right). \tag{2.8}$$

A common design constraint in antenna and matching network design is to achieve a maximum of 10% reflected power from the antenna or 90% power delivery to the antenna. In practice, in order to maximize performance, a more common requirement is to specify a minimum return loss of 20 dB or better that translates to less than 1 % reflection. When the transmitted (or incident) power and the reflected power levels are known, for example via direct measurement using an RF power meter, then the return loss in dB can be calculated as the difference between the incident power P_{INC} (in dBm) and the reflected power P_{REF} (in dBm),

$$RL(\mathrm{dB}) = P_{\mathrm{INC}} - P_{\mathrm{REF}}. \tag{2.9}$$

2.1.8 *Mismatch Loss*

Mismatch loss (*ML*) describes antenna performance in terms of the amount of power that is lost from the generator due to impedance mismatch [29]. It is important to note that mismatch loss relates to the power lost due to reflections rather than dissipative, resistive losses and is defined such that

$$ML(\mathrm{dB}) = -10\log_{10}\left(1 - \left|\Gamma_{\mathrm{L}}\right|^{2}\right), \tag{2.10}$$

where Γ_{L} is the previously defined reflection coefficient at the load.

Throughout this thesis, *ML* is defined as a positive quantity. Considering that a return loss of 10 dB is a typical minimum acceptable figure, the corresponding minimum acceptable figure for mismatch loss is calculated as 0.45 dB using (2.10).

2.1.9 *Scattering parameters*

Scattering parameters are used at high frequencies to characterize an electrical network and are employed to avoid the difficulties that are experienced at lower frequencies where short and open-circuits are used to characterize a network. At higher frequencies, it is difficult to realize a perfect open or short-circuit and instead, S-parameters are specified with the circuit port(s) terminated in the characteristic impedance Z_0 of the system that is typically 50 Ω [9] and they describe a network in terms of forward and reflected wave quantities. Considering the arbitrary 2-port network shown in Figure 2-5, the quantity S_{11} is defined as the ratio of the reflected wave b_1 to the incident wave a_1 at port P_1 with the other port P_2 terminated in Z_0 or

$$S_{11} = \frac{b_1}{a_1} \text{ with } a_2 = 0 \tag{2.11}$$

The transmission coefficient S_{21} is defined as the ratio of the quantity b_2 at P_2 to the quantity a_1 at P_1 with port P_2 terminated in Z_0 or

$$S_{21} = \frac{b_2}{a_1} \text{ with } a_2 = 0 \tag{2.12}$$

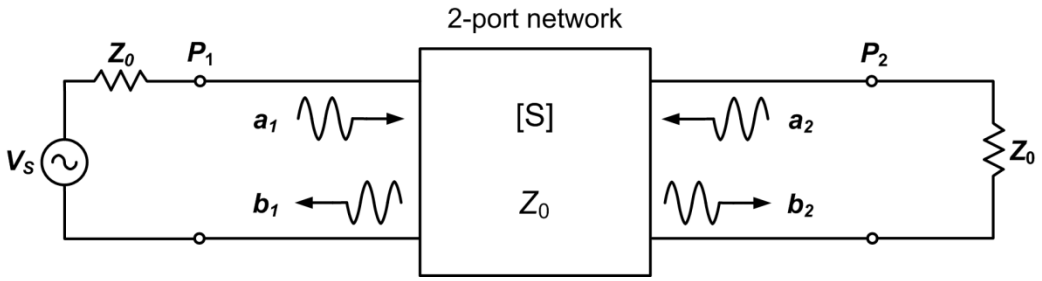


Figure 2-5 Two-port Scattering parameter definition

Throughout this thesis, all measured and simulated antenna reflection coefficients are evaluated in terms of the S_{11} parameter and expressed in units of dB.

2.1.10 *Maximum Power Transfer Theorem*

In AC circuits, the maximum power transfer theorem [26, 30] states that the maximum average power that can be delivered to a load impedance $Z_L = R_L + j\,X_L$ only occurs when the load impedance is equal to the complex conjugate of the source impedance. If the impedance of the source is taken as the quantity $Z_S = R_S + j\,X_S$, then maximum power is delivered to a load when $Z_L = R_S - j\,X_S$ or when a conjugate match $Z_L = Z_S^*$ exists. The condition for maximum power transfer is an important requirement for many types of RF circuits but there are other practical reasons for this type of impedance matching as discussed in the following chapter.

2.1.11 *Antenna Bandwidth and Quality factor*

The bandwidth of an antenna is defined as "the range of frequencies over which the performance of the antenna, with respect to some characteristic, conforms to a specified standard" [24]. Because the impedance of an antenna is never perfectly matched to that of a source for varying frequency, then a certain amount of power is reflected from the antenna across a particular frequency range. The antenna impedance bandwidth is typically expressed as the range of frequencies for which the reflection coefficient is less than some agreed value. A commonly used specification in the literature is the -10 dB bandwidth or S_{11} (-10 dB) and represents the frequency range over which 90 % of the power is delivered to the antenna [31]. The quality factor of an antenna is intimately related to the bandwidth as discussed next. The quality factor of an antenna Q_A is similar to that of a resonant circuit and for the case of an antenna, is a measure of how much energy is stored in the near-field of the antenna compared to the quantity that is dissipated via radiation and resistive losses. Quality factor can refer to a loaded quantity Q_L when connected to an external circuit such

as a source or alternatively can refer to an unloaded quantity Q_U when no external circuit is connected [26]. The unloaded quality factor is defined as

$$Q_U = \omega \frac{\text{average energy stored}}{\text{average energy lost/second}} \tag{2.13}$$

The quality factor of an antenna is generally desired to be low such that energy is radiated rather than being stored near the antenna. A useful approximation for the antenna quality factor at the resonant frequency can also be expressed as

$$Q_0 = \frac{f_0}{f_2 - f_1} \tag{2.14}$$

where f_1 and f_2 are the lower and upper -3 dB frequencies respectively and f_0 is the center frequency [32]. Although, this relation strictly only applies for simple, single resonance RLC circuits, it can be used to provide a first-order approximation in many instances.

2.1.12 *Transducer Power Gain*

Unlike the calculation of mismatch loss as defined in equation (2.10), when a 2-port network, such as an impedance matching network, is connected between arbitrary source and load impedances (i.e. Z_L and $Z_S \neq Z_0$), it is also necessary to consider the additional *losses* in the matching network itself as well as the effect of reflections at the source and load. These effects can be considered by defining a quantity known as the 2-Port Transducer Power Gain G_T [26]. Figure 2-6 shows an arbitrary two-port network that is connected to a source impedance Z_S and load impedance Z_L. The network is characterized by its two-port *S*-parameters as defined earlier. The quantity G_T of a 2-port network is defined as the power delivered to the load P_L divided by the available power from the source P_{AVS} [26] and is given as

$$G_T = \frac{P_L}{P_{AVS}} = \left[\frac{1 - |\Gamma_S|^2}{|1 - \Gamma_{IN}\Gamma_S|^2}\right] |S_{21}|^2 \left[\frac{1 - |\Gamma_L|^2}{|1 - S_{22}\Gamma_L|^2}\right] \tag{2.15}$$

where Γ_S is the source reflection coefficient, Γ_{IN} is the input reflection coefficient, Γ_L is the load reflection coefficient, and S_{mn} are the scattering parameters of the matching network. For the work described in this thesis, the input port (Port 1) of the matching network is always terminated in a characteristic impedance of 50 Ω as dictated by the radio transceiver used [33]. In this case, as shown in Figure 2-6, since $Z_S = Z_0 = 50\ \Omega$, then $|\Gamma_S| = 0$ and (2.16) can be simplified since the left bracketed terms equate to unity.

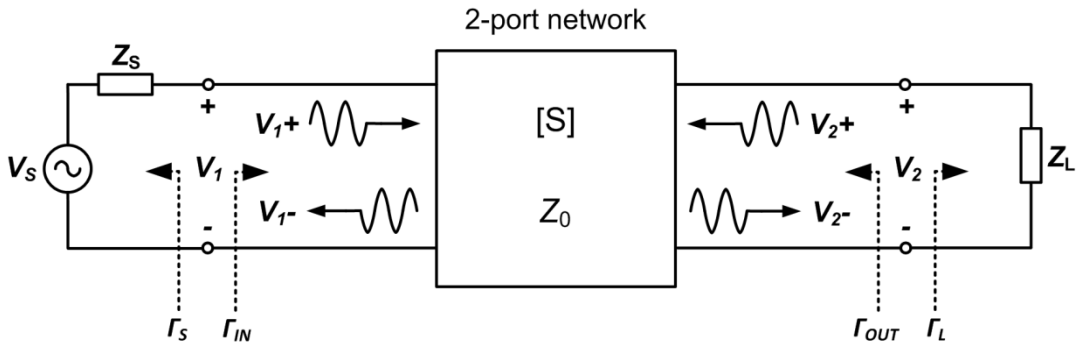


Figure 2-6 Two-port network with arbitrary source and load impedances

2.1.13 *Relative Transducer Gain*

Another useful performance parameter for antenna tuners is the relative transducer gain ΔG_T. The quantity ΔG_T is defined as the difference in transducer gain, with and without the matching network present [34] and is given as

$$\Delta G_T = \frac{|S_{21}|^2}{|1 - S_{22}\Gamma_L|^2}. \tag{2.16}$$

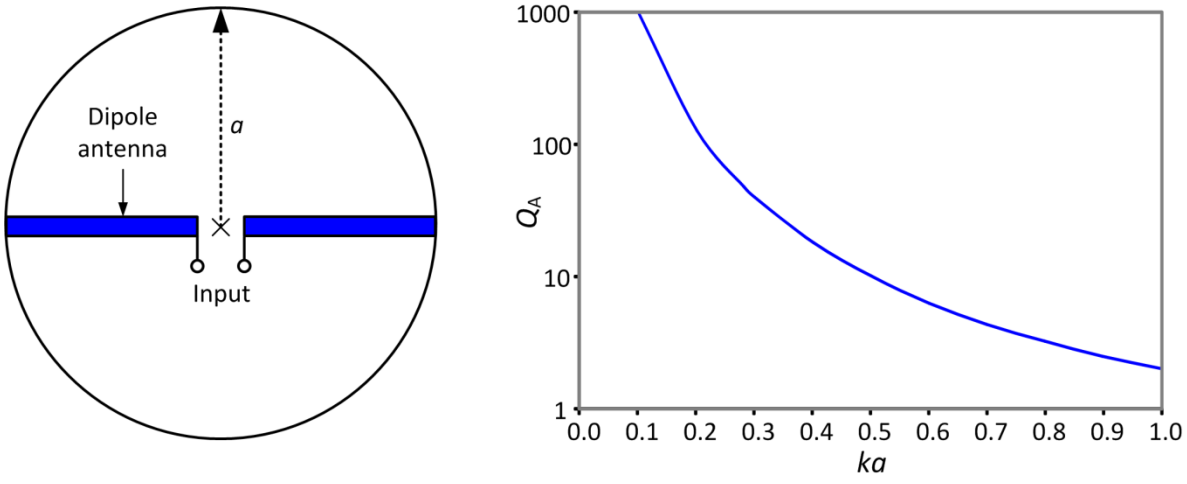
This quantity is used to specify the performance improvement that is possible when an impedance matching network is added between a matched source ($Z_S = Z_0$) and a mismatched antenna ($Z_A \neq Z_0$).

2.1.14 *Electrically Small Antennas*

This thesis incorporates the design of compact or electrically small antenna structures. An electrically small antenna is defined [17, 24, 35] as an antenna whose dimensions are small compared to the wavelength of operation. For these types of antennas, there are fundamental limits on the achievable impedance bandwidth as first addressed by Wheeler in 1947 [17]. Wheeler described an electrically small antenna as one whose maximum dimensions were less than $2\pi / \lambda$ in size with the relationship often expressed as:

$$ka < 1 \tag{2.17}$$

where $k = \lambda/2\pi$, λ is the free-space wavelength (metres) and a is the radius of a sphere (metres) that encloses the antenna. This situation is shown in Figure 2-7 (a) where a dipole antenna is surrounded by a sphere of radius a. The quality factor of the antenna can then be estimated as a function of the quantity ka. Later work by McClean [36] led to an accurate expression for calculating the minimum achievable quality factor Q_A of an electrically small, linearly polarized antenna.



(a) **(b)**

Figure 2-7 (a) Electrically small antenna definition, (b) Calculated Q_A versus ka [36]

The minimum achievable quality factor Q_A is defined as

$$Q_A = \frac{1}{k^3 a^3} + \frac{1}{ka} \tag{2.18}$$

Equation (2.18) is illustrated in Figure 2-7 (b) for varying antenna size, as expressed in terms of the factor *ka*. It can be seen that as the dimensions of the antenna decrease, the theoretical value for the minimum Q_A increases significantly. Since antenna bandwidth and *Q*-factor are intimately linked as seen earlier in equation (2.14), decreasing antenna dimensions also leads to bandwidth reduction.

2.2 Impedance Matching

This section introduces the fundamental concept of impedance matching that is a very common requirement in RF and microwave circuit design. Impedance matching is used to ensure maximum power delivery between different stages comprising a circuit. It was mentioned earlier that conjugate matching between the source and load impedances results in maximum power transfer to the load device. In relation to an antenna system, when the antenna impedance is matched to a source, reflections in the antenna feed are minimized and maximum power is delivered to the antenna. Apart from maximizing power delivery between cascaded RF stages, impedance matching is also used to optimize other performance parameters such as power amplifier (PA) efficiency, dynamic range as well as improving the signal-to-noise ratio (SNR) performance of the receiver [26, 30]. Many types of matching network topologies are available and the final choice depends on several factors including the range of impedances to be matched, the required bandwidth, circuit complexity, losses, and the cost of the final solution. In the following sections, a number of impedance matching examples are presented using the most commonly employed impedance matching network topologies.

2.2.1 *L-type matching network design using the Q-Based Method*

In order to illustrate the process of impedance matching, this example uses a matching circuit topology called the *L*-type matching network using lossless, lumped elements. Although it is one of the simplest types of matching network, it can be used to explain the impedance matching process. Impedance matching using lumped elements can have a number of advantages when compared to distributed types in certain applications. For example, lumped element designs allow for the design and implementation of low cost and wideband matching networks at UHF frequencies. This is especially critical where small size requirements are of prime importance [37]. Lumped elements however, tend to have greater losses than distributed circuits.

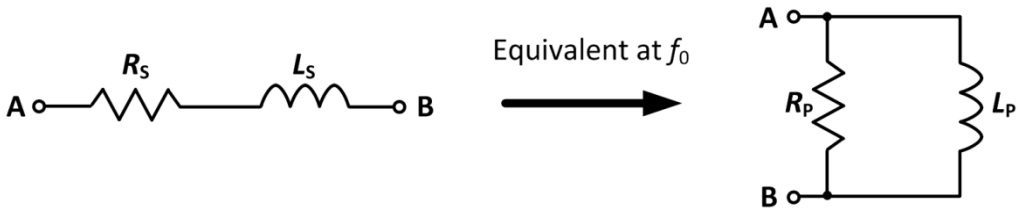


Figure 2-8 Series to parallel equivalent circuit

The *Q*-based method is a commonly used technique for designing matching networks [9, 38, 39]. Figure 2-8 shows a series *RL* circuit, comprising a resistor R_S in series with an inductor L_S. It can be shown [9] that an equivalent parallel *RL* circuit exists with resistance R_P in parallel with inductance L_P where the impedance at terminals A and B is identical in both cases at the design frequency f_0. The parallel equivalent components are calculated as

$$R_P = (Q^2 + 1)R_S \tag{2.19}$$

and

$$L_P = \frac{(Q^2 + 1)}{Q^2} L_S \tag{2.20}$$

where Q is defined as

$$Q = \frac{\omega_0 L_S}{R_S} = \frac{R_P}{\omega_0 L_P} \tag{2.21}$$

Equations (2.19) and (2.20) show the impedance transformation properties that result from voltage and current magnification in resonant LC circuits. This key property then allows impedances to be transformed to larger or smaller values depending on the Q-factor of the network as will be shown by way of example in the following section.

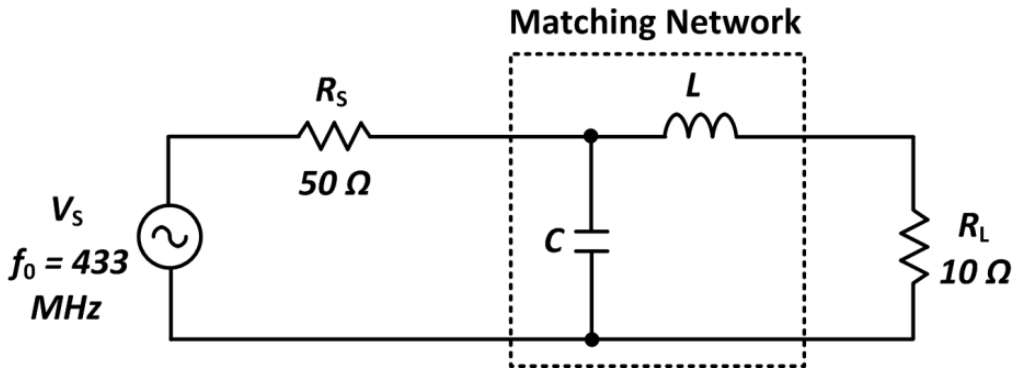


Figure 2-9 *L*-matching network using the *Q*-Based method

The Q-based method is now demonstrated using the example shown in Figure 2-9 where a load resistance R_L = 10 Ω is to be matched to a source resistance R_S of 50 Ω at a frequency of f_0 = 433 MHz. Since $R_L < R_S$, a matching element is required in series with R_L to raise the impedance towards the source resistance R_S. This component can be an inductor or capacitor depending on whether a low-pass or high-pass function is required. In this case, a low-pass topology is chosen using an inductor L in series with the load followed by a shunt capacitance C. In order to analyze the circuit, the series combination of the load resistance R_L and inductor L is transformed to a parallel equivalent giving the RLC [9] circuit of Figure 2-10. The parallel equivalent circuit comprises resistance R_P and inductance L_P as determined from equations (2.19) and (2.20). Shunt capacitance C is then chosen to resonate with L_P at the frequency f_0, such that the total impedance Z_{IN}, looking into the parallel equivalent circuit will equal R_P at resonance.

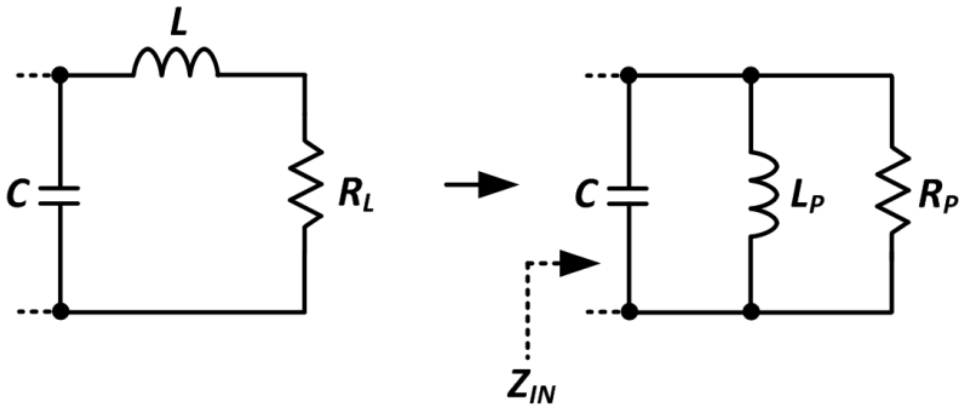


Figure 2-10 Transformation of series to parallel equivalent circuit

Since the value of R_S and R_L are given design quantities, then the loaded quality factor of the network can be determined as

$$Q = \sqrt{\frac{R_S}{R_L} - 1} = \sqrt{\frac{50}{10} - 1} = 2. \tag{2.22}$$

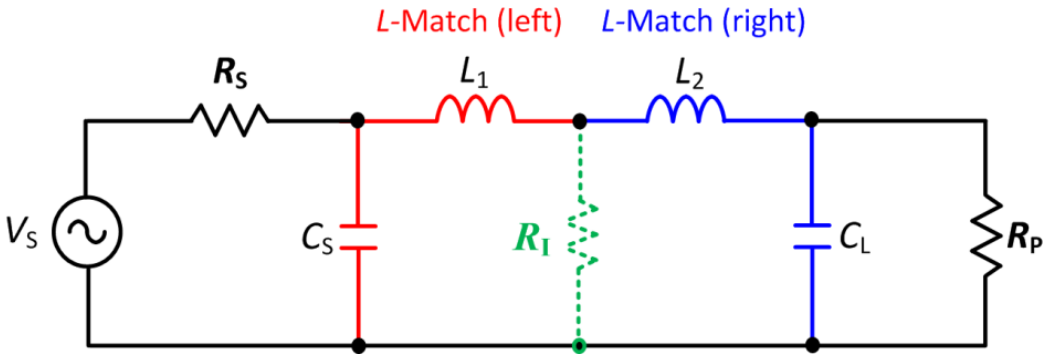
The values of L and C are then calculated as

$$X_C = \frac{R_S}{Q} = \frac{50}{2} = -j\,25\ \Omega \Rightarrow C = \frac{1}{\omega_0 X_C} = 14.7\ \text{pF} \tag{2.23}$$

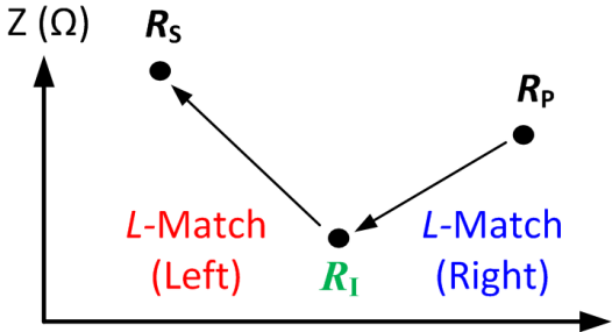
$$X_L = QR_L \Rightarrow L = \frac{QR_L}{\omega_0} = 7.35\ \text{nH} \tag{2.24}$$

2.2.2 *Π-type matching network design using the Q-Based Method*

The method to design the *Π*-type matching network is very similar to the *Q*-based design method for *L*-type matching networks as described previously. The circuit is analyzed as the series connection of two individual *L*-type matching networks (left and right) as shown in Figure 2-11 (a). The right-hand *L*-network first transforms the load resistance R_A to a lower value intermediate resistance denoted R_I. The left-hand *L*-network then transforms resistance R_I to match the source resistance R_S. Resistance R_I is not a physical resistance but rather a virtual resistance that can be chosen by the designer.



(a)



(b)

Figure 2-11 (a) *Π*-type matching network, (b) Resulting impedance transformation

Using the same method for designing *L*-type matching networks, the quality factor of the left-hand circuit is calculated as

$$Q_{\mathrm{LEFT}} = \frac{\omega_0 L_1}{R_{\mathrm{I}}} = \sqrt{\frac{R_{\mathrm{S}}}{R_{\mathrm{I}}} - 1}\,. \tag{2.25}$$

Similarly, the quality factor of the right-hand is calculated as

$$Q_{\mathrm{RIGHT}} = \frac{\omega_0 L_2}{R_{\mathrm{I}}} = \sqrt{\frac{R_{\mathrm{P}}}{R_{\mathrm{I}}} - 1}\,. \tag{2.26}$$

The overall circuit *Q* can then be calculated as

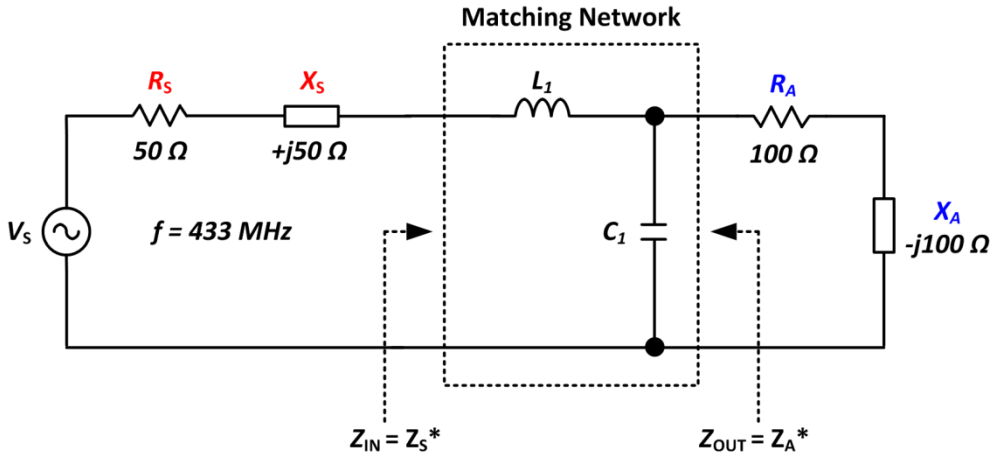
$$Q = \frac{\omega_0 (L_1 + L_2)}{R_{\mathrm{I}}} = \frac{Q_{\mathrm{LEFT}} + Q_{\mathrm{RIGHT}}}{R_{\mathrm{I}}} = \sqrt{\frac{R_{\mathrm{S}}}{R_{\mathrm{I}}} - 1} + \sqrt{\frac{R_{\mathrm{P}}}{R_{\mathrm{I}}} - 1} \tag{2.27}$$

Since for the *Π*-type matching network, the value of the circuit *Q* is specified at the start of the design process and the values of R_S and R_P are also known, then the value of R_I has to be determined. This is generally accomplished using iteration [9], by testing different values of R_I to yield a specified value of *Q*.

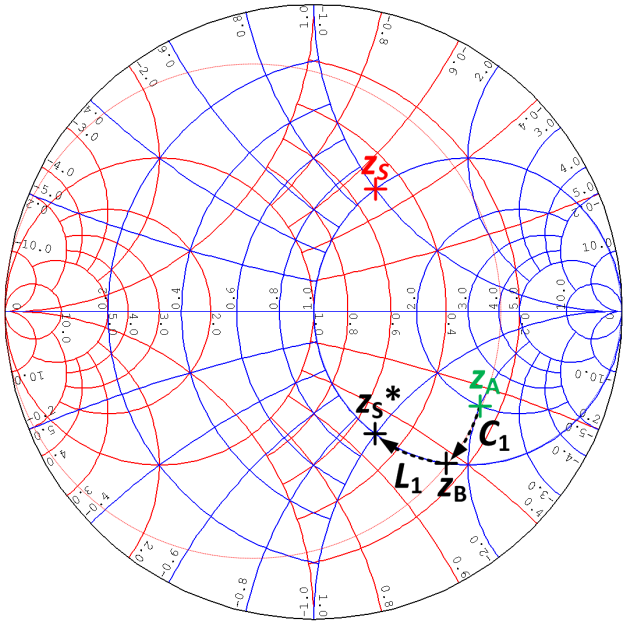
2.2.3 *L-Matching Network Example (Smith Chart Method)*

In this method, the Smith chart is used to determine the required component values for the *L*-matching network of the previous example. The Smith chart was invented in 1939 by P.H. Smith [40] and is a graphical representation of reflection coefficient in the complex plane that allows a wide range of transmission line and other circuit configurations to be analyzed in a simplified and intuitive manner.

In the following example, a practical matching problem is presented where complex source and load impedances are to be matched at a design frequency of 433 MHz as illustrated in Figure 2-12 (a). The CAD program Microwave Office [41] is used to generate the Smith chart and illustrate the design process.



(a)



(b)

Figure 2-12 Impedance matching example, (a) Circuit, (b) Smith chart

Assuming a characteristic impedance of $Z_0 = 50\ \Omega$, the normalized antenna impedance $z_A = Z_A / 50 = 2 - j\,2\ \Omega$ is first drawn on the chart as shown in Figure 2-12 (b). Because the real part of the load impedance z_A is larger than the source impedance z_S, capacitance C_1 is added in shunt with z_A to decrease the real component of the combined impedance. The addition of this shunt susceptance B_{C1} moves the combined impedance clockwise from z_A along a circle of constant conductance until the circle of constant resistance $1 + j\,X$ is reached at z_A. At point z_A, the real part of the combined impedance of C_1 and Z_A has been matched to R_S. For maximum power transfer between the source and antenna load, the input impedance of the matching network must equal the complex conjugate of the normalized source impedance or z_S*. This is achieved by adding the series inductance L_1 as shown that moves the impedance from z_B to z_{S*}. Finally, the component values for L_1 and C_1 are determined from the normalized impedances and admittances read from the chart and calculated using (2.28) and (2.29).

$$C_1 = \frac{B_{C1}}{\omega_0 Z_0} = 1.3\ pF \tag{2.28}$$

and

$$L_1 = \frac{X_{L1} Z_0}{\omega_0} = 31.6\ nH \tag{2.29}$$

It is important to note that for the *L*-type matching circuit, the quality factor of the network from (2.22) is defined exclusively by the source and load impedances and is a key limitation of this topology. As will be seen in Chapter 4, other types of matching network topologies can be used to overcome this limitation.

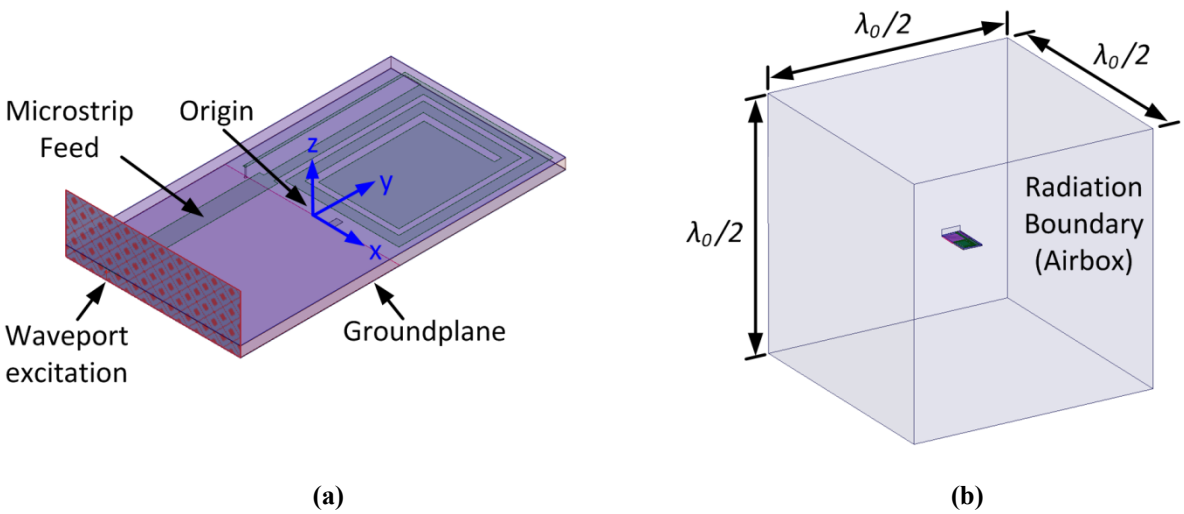
2.2.4 *Practical matching network design*

It is important to note that for simplicity, the preceeding examples assumed the use of lossless components. In reality, practical matching network components have finite losses attributed to both the matching network components and the PCB interconnect that is used to implement the circuit. Practical matching circuits also consist of distributed elements such as transmission lines, SMA connectors, as well as lumped elements including SMD component pads. In general, the combination of all these effects has a significant effect on the values of the impedances to be matched as well as the calculated optimal component values. Circuit simulation techniques are therefore used to design practical circuits where all of these effects can be specified and modelled.

2.3 **Design and Measurement Methodology**

The High Frequency Structure Simulator V14.0 (HFSS) from ANSYS [42] was used to model and analyze the antenna designs throughout the thesis. This is a finite-element-method (FEM) solver that is used to create the antenna geometry, specify material properties and boundary conditions and compute key antenna parameters of interest. These parameters include antenna input impedance, reflection coefficient, gain, efficiency, far-field E and H-plane radiation patterns as well as near-field parameters.

All HFSS antenna designs were modelled as shown in Figure 2-13 (a) with a waveport excitation used to excite a quasi-TEM mode in the microstrip feed at the input terminals of the antenna structure. The far-field behaviour of the antenna is modelled by assigning a radiation boundary or airbox as shown in Figure 2-13 (b) in order to simulate an absorbing or non-reflecting free-space volume surrounding the antenna. The distance between antenna radiating structures and nearest faces of the airbox is an important consideration for simulation accuracy in order to avoid influencing the final solution [43]. In order to satisfy this requirement, each face of the airbox was placed at a minimum distance of $\lambda_0/4$ from the origin of the antenna element with λ_0 calculated at the design frequency.



(a) **(b)**

Figure 2-13 HFSS model setup (a) Waveport, (b) Airbox boundary conditions

Circuit simulation was carried out using Microwave Office AWR [41] and the Advanced Design System (ADS) from Keysight [44]. In order to verify the proposed designs, prototype PCBs were fabricated using a LPKF ProtoMat C60 milling machine [45] or were fabricated using a commercial PCB manufacturing process [46]. Throughout this thesis, all one and two port vector network analysis (VNA) measurements were carried out using a 9 MHz to 4 GHz, Rohde & Schwarz ZVRE VNA [47] that was calibrated using a Rohde & Schwarz, ZV-Z32, 3.5 mm manual calibration kit [48].

Antenna radiation characteristics were measured in an off-site facility where there was access to a 7.8 m × 3.8 m × 3.5 m semi-anechoic, shielded test facility [49]. Antenna radiation characteristics were measured using an Anritsu Model 2038C VNA [50] that was interfaced with a Model 2090, Multi-Device Positioning Controller [51] and a 1.2 m, Model 2188 Turntable [52]. VNA and turntable control were achieved by means of a custom Labview graphical user interface [53]. Far-field measurements were conducted using a 1 - 18 GHz Model BBHA 9120 D (1201) standard gain horn antenna [54] and measurements at 433 MHz were performed using a Model ANT-418-YG5-N, Yagi Antenna [55].

2.3.1 *Antenna measurements*

During practical antenna measurements, many types of electrically small antennas can be sensitive to groundplane effects and the groundplane itself may also form part of the radiating structure [56, 57]. A coaxial feed cable is commonly used to connect an AUT to RF test equipment during the measurement of electrically small antennas. However, the presence of a cable in the near-field of the antenna can significantly affect performance. This is especially true when a finite groundplane is used as the smaller the antenna, the greater the effect of the coaxial feed [58]. This effect is illustrated in Figure 2-14 (a) where a balanced dipole antenna is fed by a balanced line. In this case, a current I_1 flows on the left conductor with an equal return current I_2 on the right conductor, leading to balanced currents I_1 and I_2 on the both dipole arms A and B that are equal in magnitude and opposite in phase. Figure 2-14 (b) shows a second configuration, where an un-balanced coaxial cable now feeds the dipole antenna. In this case, a current I_1 flows on the inner core of the coaxial cable and current I_2 returns on the inside surface of the ground shield. An issue arises however at Point P, as part of the return current I_3 can now return to ground on the outer surface of the coaxial cable due to the skin effect.

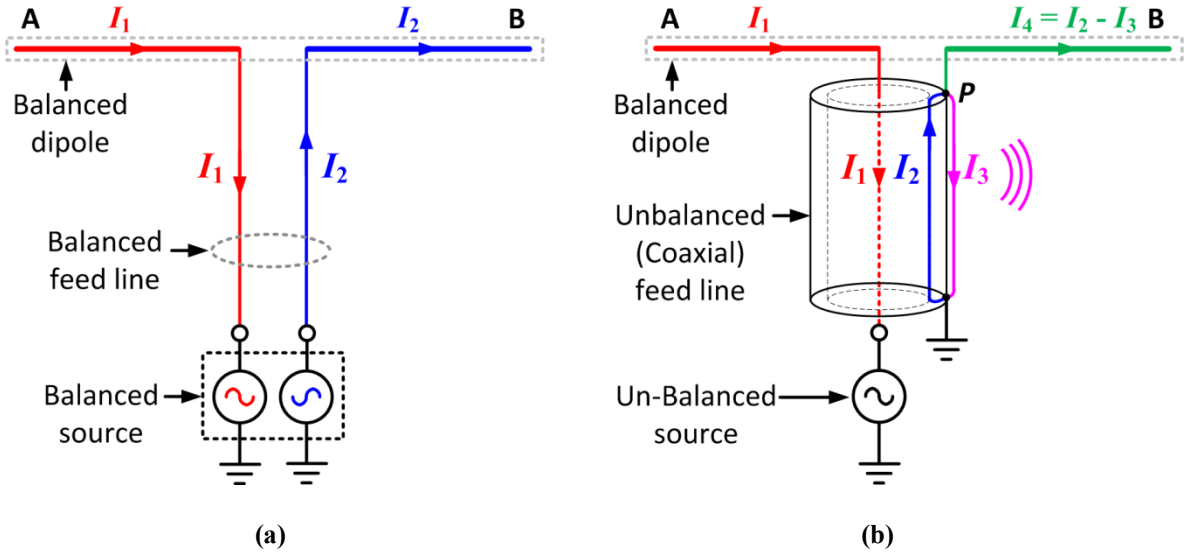


Figure 2-14 Dipole fed antenna (a) Balanced, (b) Unbalanced

In this case, the current I_4 on element B is reduced by an amount I_3 leading to less radiation from element B as well as unwanted radiation from the outer surface of the feed cable. To measure both the impedance and radiation characteristics of electrically small antennas in practice, a *balun* is required in many cases. A balun is a transformer device that performs a balanced-to-unbalanced function. Figure 2-15 (a) shows a sleeve-type balun that consists of a cylindrical metal tube placed around the coaxial cable, thus creating a coaxial transmission line with the outer shield of the coaxial cable. The sleeve is designed to have an electrical length of λ/4 at the operating frequency and acts as a quarter-wave transformer. The sleeve is shorted to the outer shield of the coaxial cable at point *S* shown and this creates an open-circuit at point *P*, thereby suppressing the unwanted current I_3 on the outer surface of the coaxial cable.

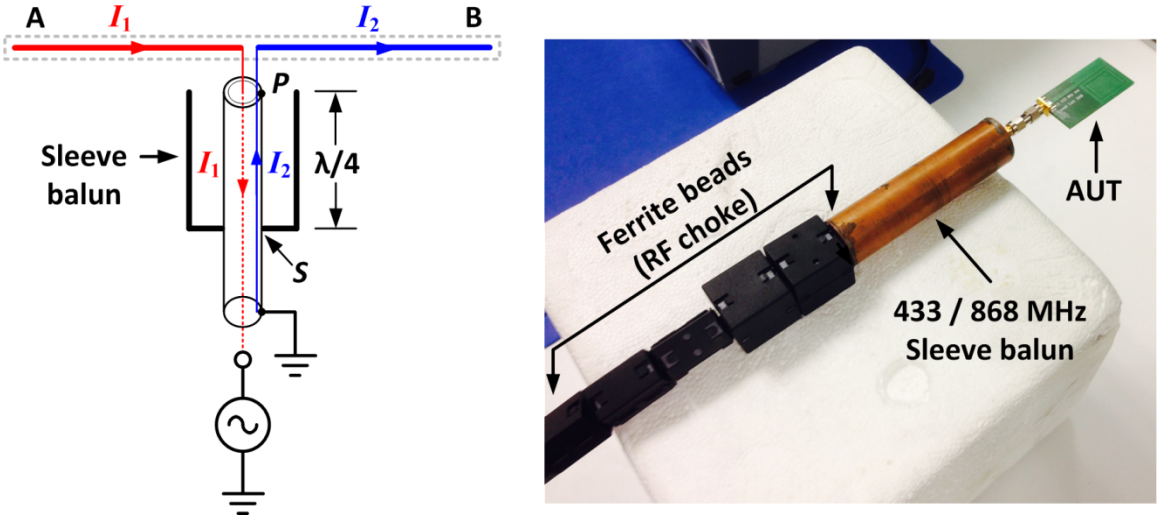


Figure 2-15 (a) Sleeve balun, (b) Dual-Band sleeve balun and ferrite beads

A dual-band sleeve balun [59] is shown in Figure 2-15 (b) and was used for 433 MHz AUT characterization. A number of ferrite-beads [60] are also shown on the feed cable and are used to further suppress feed-cable currents during antenna impedance measurements as well as radiation pattern measurements [61].

2.4 Conclusions

This chapter has presented a number of fundamental concepts relating to antenna and matching circuit design. The chapter began by outlining several important parameters that are used to specify the performance of antennas and matching networks. A short introduction to impedance matching was discussed using examples of an *L*-type and *Π*-type matching network. The circuit and EM simulation methodology as well as the RF and antenna measurement methodology that was used throughout this work was also introduced and the material in this chapter is referenced throughout the following chapters.

Chapter 3. Literature review

This chapter reviews the evolution of wireless sensor networks and then reviews modern wireless sensor network devices in terms of their architecture. Key emerging applications that are driving the design of next-generation wireless sensor devices, are then outlined. A survey of wireless sensor network platforms is then conducted and the Tyndall mote platform, which is a key focus of this thesis, is described. Some of the common characteristics and performance requirements for these systems are then reviewed and a number of key design challenges are identified with a strong focus on antenna related issues. Design challenges that relate to antenna size, antenna detuning effects and wireless network reliability are then discussed. The literature is also reviewed to determine how these issues are currently being addressed. Some open research issues are identified for current WSN technology and a number of proposed solutions are then explored in later chapters. Some of the material that is cited in this chapter has been published in [62-67].

3.1 Wireless Sensor Networks (WSN)

The first use of wireless sensor networks was for military applications such as the SOund SUrveillance System (SOSUS) that was used during the 1950s to detect and track Soviet submarines [68]. SOSUS used a network of acoustic hydrophones that were deployed on the ocean bottom to sense submarine activity. In the early 1980s, modern research on wireless sensors started with the Distributed Sensor Networks (DSN) program at the Defense Advanced Research Projects Agency (DARPA) [68] for environmental monitoring using a spatially distributed network of sensors. At this time, minicomputers were used for information processing and the size and cost of this solution limited DSN development.

During the 1980s, governments and universities began using wireless sensors for non-military, environmental monitoring applications. The term 'Networked Microsensors' was used in an article from Business Week in September 1999 [69] to describe a future technology where cheap, smart devices with multiple onboard sensors would be networked through wireless links and the Internet. The article predicted that wireless sensors would be one of the most important technologies to emerge in the 21st century and would be deployed in large numbers to provide unprecedented opportunities for instrumenting and controlling homes, cities, and the environment.

In the intervening period, there have been enormous advances in the areas of digital electronics, wireless communications and micro-electro-mechanical systems (MEMS) technology [5] that has led to the proliferation of wireless sensor network technology for a vast range of applications. A commonly used modern definition of a Wireless Sensor Network is a collection of sensor nodes organized into a co-operative network which can sense and control the environment, enabling communication between persons or embedded computers and the surrounding environment [70].

3.1.1 *WSN Node Architecture*

The main functional components of a typical, modern-day WSN device are shown in Figure 3-1. The node consists of an application specific sensor or sensors that sense one or more physical parameters and converts these measured parameters to an analog or digital output. For the case of an analog sensor, an extra signal-conditioning block (not shown) may also be required. The sensor output is then interfaced with a digital processor that is commonly implemented using a low-power micro-controller (MCU).

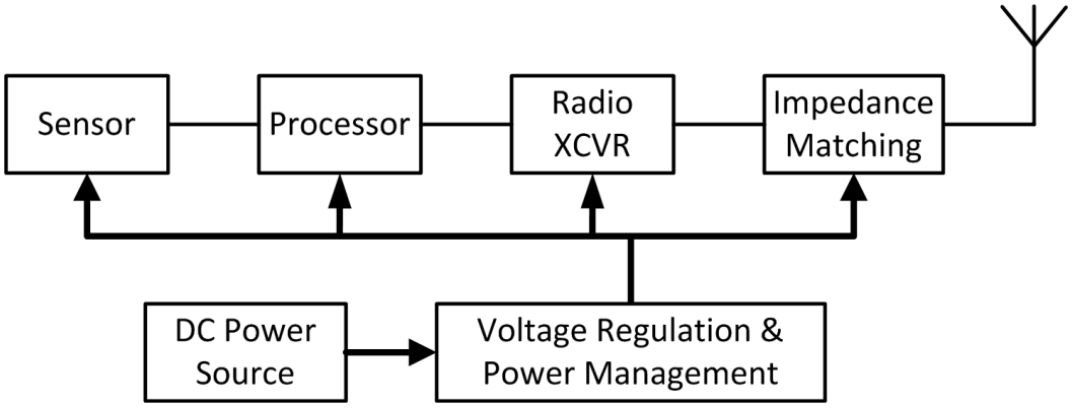


Figure 3-1 Block diagram of typical WSN node

The micro-controller is capable of processing the sensor output, either analog or digital, and may store intermediate data using the processor's on-chip memory. The amount of on-chip memory (RAM and ROM) is generally limited for the majority of low-cost, low-power WSN applications. Wireless functionality is provided using a radio transceiver (XCVR) and antenna. The wireless transceiver generally operates in the license-free 433, 868, 915 MHz or in the 2.45 GHz ISM bands. The power requirements for the radio transceiver are critical since the radio consumes a large portion of the system power, especially during wireless transmission. Radio transceivers for WSN applications are generally optimized for low power operation. For ease of implementation in a target application, they are designed to require very few external components to make the device functional.

An impedance matching network is generally placed between the antenna and radio transceiver in order to match the antenna and radio transceiver impedances. The impedance matching network may also provide additional filtering and balanced-to-unbalanced (BALUN) functionality. A power source, such as a small capacity battery, is most commonly used to provide power to the node. Energy conservation is one of the most critical aspects of WSN node design and some means of power control and management is generally provided at the hardware level to enable the DC power consumption to be minimized [4].

3.1.2 *Wireless Sensor Network Applications*

Technological advances in digital electronics, sensor design and wireless communications have enabled the development of low-cost, low-power, highly-integrated and multi-functional sensor nodes that are used in an increasing number of applications such as BSN applications in sports and fitness monitoring [63, 65, 71]. Figure 3-2 shows a BSN application for tennis stroke recognition using Tyndall's 2.45 GHz, Zigbee wireless inertial measurement units. One of the key challenges for this type of application is mitigating the effects of the user on the reliability of the measured data due to antenna-body interaction.

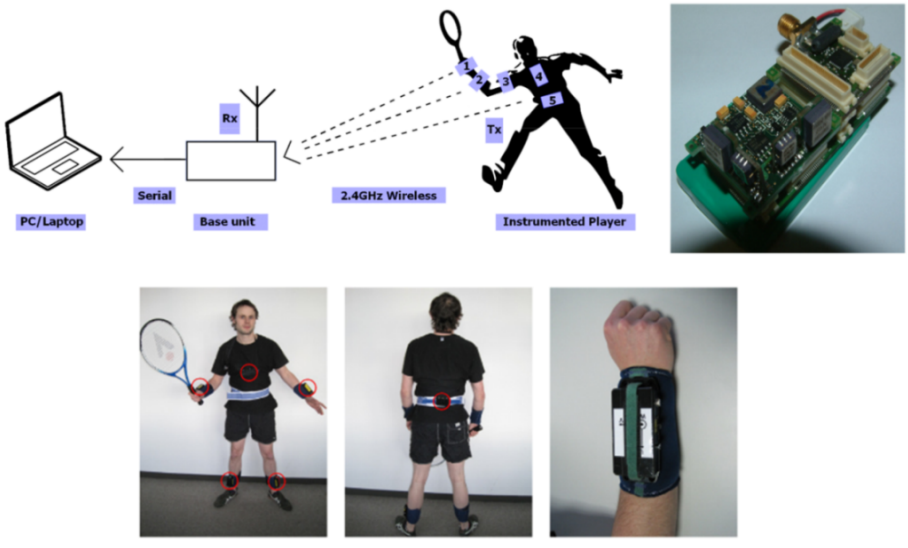


Figure 3-2 Example of a BSN tennis application [63, 65]

Other emerging applications include intelligent building energy management [72-74] where wireless sensors are used to replace traditional wired networks that are very expensive to install. Wireless sensors can also be used in applications to monitor the structural health of buildings [75]. Figure 3-3 shows an example of a miniaturized 433 MHz wireless sensor that is capable of being embedded in concrete to monitor curing properties and transmit live data from the embedded sensor to a remote data acquisition system. It was also shown in [75] that high levels of relative humidity during initial curing have a detrimental effect on the reliability of wireless communications in terms of the measured packet loss.

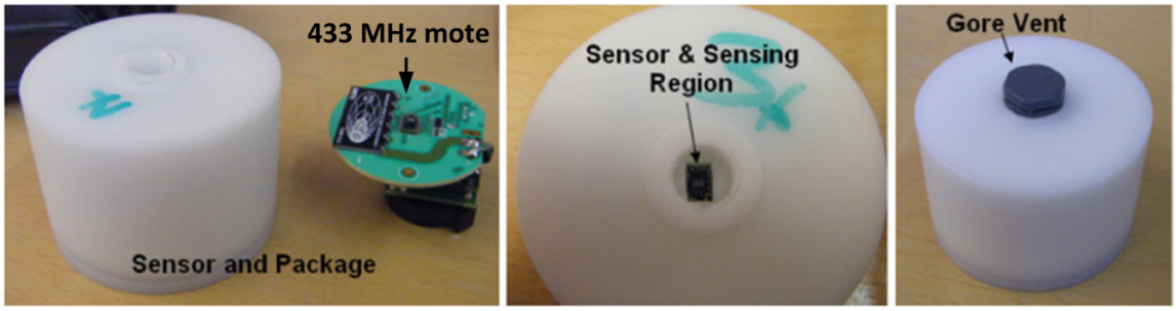


Figure 3-3 433 MHz wireless sensor to monitor concrete curing [75]

There has also been a rapid emergence of WSN applications in the field of health monitoring. In these applications, various types of wearable sensors can be attached to the patient's body to monitor and collect physiological data using BSN solutions that are designed to connect and operate sensors within, on or at close proximity to the human body [76]. An example of a BSN health application is shown in Figure 3-4 where a number of ISM-band sensor nodes are placed on the patient's body in a wearable configuration to monitor parameters such as sweat pH and skin temperature [77] as well as movement [78]. The measured sensor data can then be stored and processed locally or sent wirelessly via the cloud to a physician or hospital for analysis. Wireless sensor devices provide a number of advantages that enable improved healthcare for patients.

The need for more sustainable healthcare systems is a key societal problem across the world and the use of wireless health monitoring can offer a number of potential advantages compared to existing solutions [79-81].

Wireless monitoring is also a comfortable and unobtrusive means to monitor a patient and enables the healthcare professional to have 24-hour access to the patient's data. The incurred expenses are also much lower when clinical tests are performed using automated, wearable devices that can continuously monitor the patient [82].

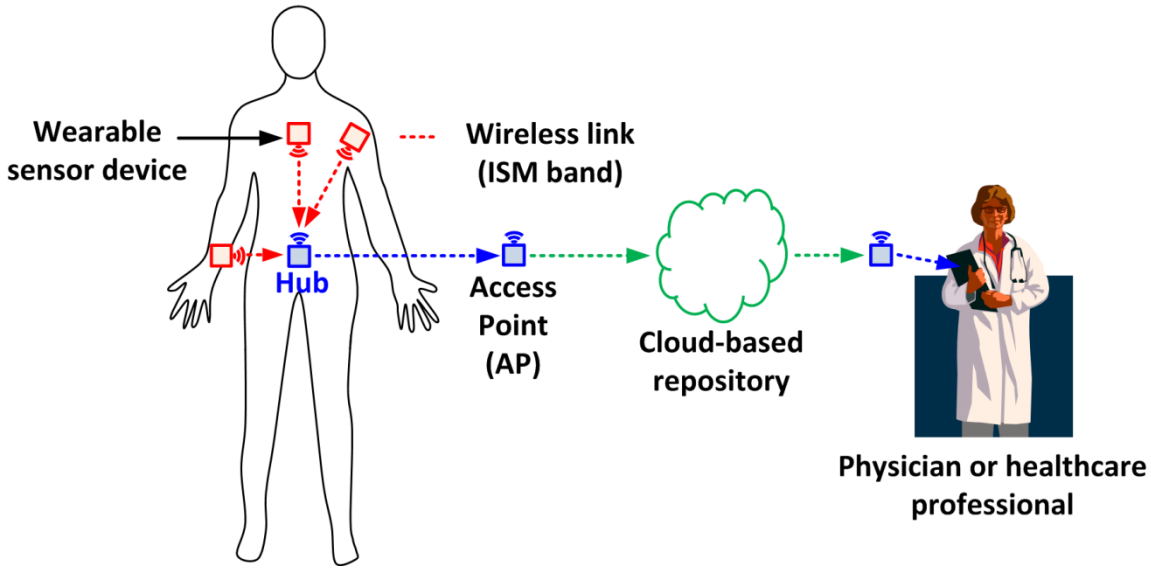


Figure 3-4 Example of body sensor network for health applications

3.1.3 *Wireless sensor network platforms*

This section surveys a number of wireless sensor network research platforms that are currently in use as summarized in Figure 3-5. The Mica 2 platform [83] shown in Figure 3-5 (a) is a commercially available solution from Crossbow (Moog-Crossbow as of June, 2011) and is widely used in the research community. The platform comes in a rectangular form factor as shown and is powered by two AA batteries.

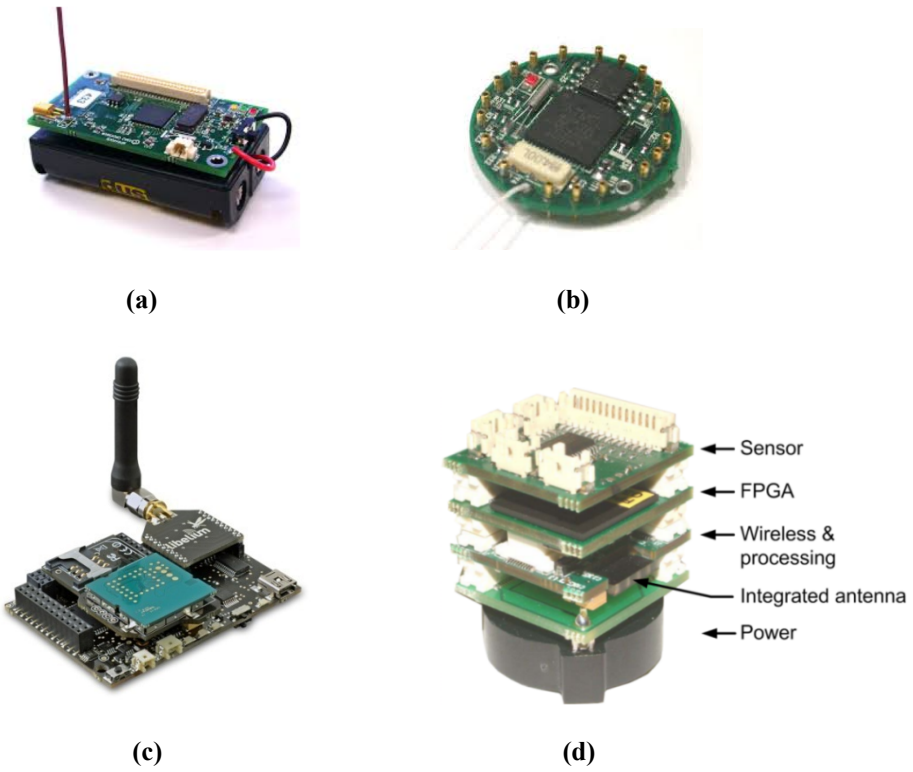


Figure 3-5 Platforms (a) Mica [83], (b) Mica Dot [84], (c) Wasp [85], (d) Tyndall [23]

A smaller device from Moog-Crossbow called the Mica Dot [84] is shown in Figure 3-5 (b) and has a smaller, circular form factor and is designed to run from a 3V coin-cell battery. The MICA platform uses a low-power RISC-based ATmega128L microcontroller [86] that runs at a clock speed of 4 MHz. Various types of sensor boards can be added using the connector interfaces shown and these boards enable the sensing of parameters such as light, temperature, relative humidity, and acceleration. Another popular wireless sensor platform is the Wasp Mote from Libelium [85] shown in Figure 3-5 (c). This mote features an ultra low power mode with the capability to interface up to 100 types of different sensors and 18 different radio transceiver modules.

The Tyndall mote platform [23] is shown in Figure 3-5 (d). This is a highly integrated research platform and has been tailored for a wide range of applications. A novel aspect of the design is the modular nature of the platform. This enables a wireless sensor network system to be quickly evaluated using a wide range of available functional layers including sensing, actuation, power, processing and wireless layers. The mote platform is also optimized for low-power operation using a variety of low-power RISC-based microcontrollers. In addition, the platform can also work in conjunction with a high specification FPGA layer for high specification signal processing tasks if required. In terms of wireless communications, the platform can be configured to operate using the 433 MHz, 868 MHz, 915 MHz or the 2.45 GHz ISM Bands.

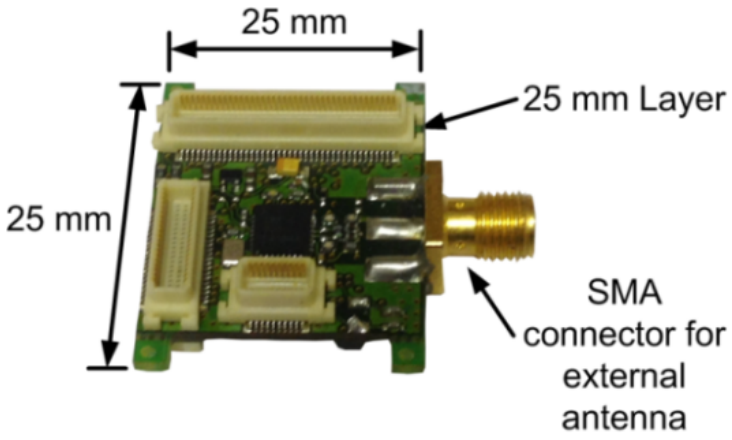


Figure 3-6 Tyndall mote size specifications [23]

Figure 3-6 shows a photograph of a 433 MHz wireless sensor mote later. This layer has a small size of 25 × 25 mm and features a stackable connector system to allow various layers to be combined. The main components of this layer are a RISC-based ATmega128L low-power microcontroller [86] and a Nordic NRF905 radio transceiver [33] for 433/868/915 MHz ISM band operation and provides an SMA connector to allow a wide range of 50 Ω antenna types to be employed, depending on the application. Table 3-1 compares some important features with respect to the physical size and ISM-Band capability for the four different platforms shown in Figure 3-5.

Platform	Size (mm)	ISM Frequency Band (MHz)		
		433	868	2450
Wasp [85]	73.5 × 51 × 13	✓	✓	✓
Mica 2 [83]	57 × 31.8 × 6.4	✓	✓	×
Mica Dot [84]	25 (diameter) × 6.4	✓	✓	×
Tyndall Mote [23]	25 × 25 × 7	✓	✓	✓

Table 3-1 Summary of mote platform size and frequency performance

3.2 Antenna Size Issues For WSN Devices

It can be seen from Table 3-1 that the realization of extremely compact wireless sensors is possible. However, in general, the use of external antennas places a limit on the minimum achievable size. This is especially true for wireless sensors that operate in the 433 MHz (ISM) band that are now becoming a popular choice for wearable WSN applications mainly because of their reduced RF attenuation by the human body and reduced path loss when compared to higher 2.45 GHz frequencies [87-89].

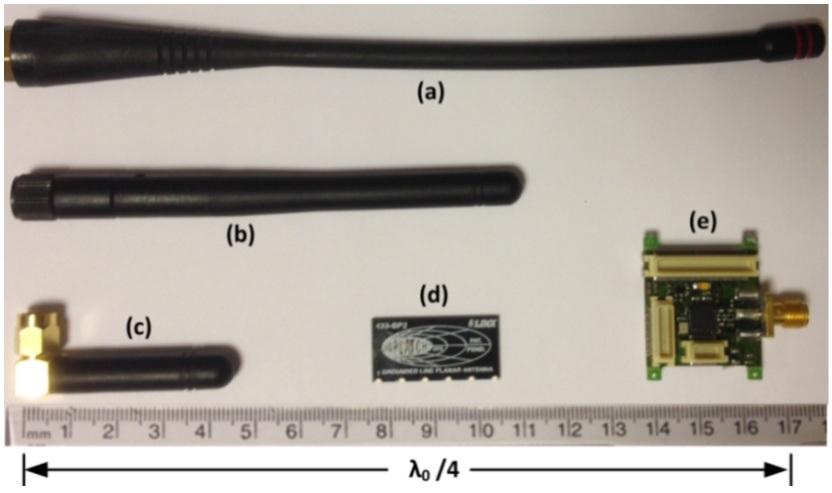
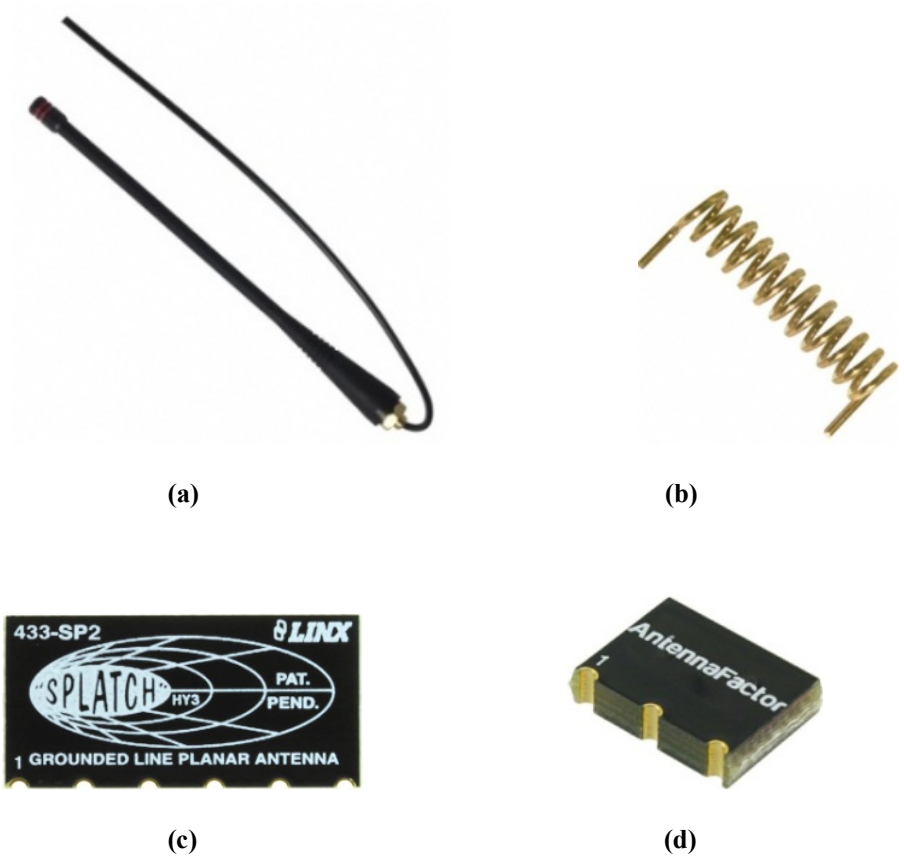


Figure 3-7 Commercial antenna size versus 25 mm mote platform

As depicted in Figure 3-7 (a), a free-space resonant whip antenna [90] at 433 MHz requires dimensions of $\lambda_0/4$ or approximately 17 cm, excluding a groundplane. Smaller antennas sometimes referred to as 'stub' types are commercially available as in Figure 3-7 (b-c) but there is a clear incompatibility in terms of the size of the whip-type antennas in comparison to the size of the mote. More integrated types of antennas are available commercially such as the small, planar antenna structure shown in Figure 3-7 (d) [91]. However, it was shown in Chapter 2 that electrically small antennas have fundamental performance limits in terms of efficiency, gain and bandwidth [17] and in practice, realizing small, high-performance antennas is therefore a challenging task.



(a) **(b)**

(c) **(d)**

Figure 3-8 Commercial antenna examples (a) 1/4-Wave Whip [90], (b) Helical [92], (c) SMD [91], (d) Chip [93]

A number of commercial 433 MHz antennas are shown in Figure 3-8 and Table 3-2 compares these antennas in terms of their size, bandwidth, peak gain and the minimum groundplane size required as specified by the manufacturer. It can be seen that reducing the antenna dimensions leads to a decrease in both gain and bandwidth. The minimum groundplane size specified by the manufacturer is also a key design requirement that needs to be met to ensure that the antenna performance meets the datasheet specifications.

Antenna Type	**f_0 (MHz)**	**BW (MHz)**	**Size (mm)**	**Peak Gain at f_0 (dBi)**	**Groundplane area (mm)**
Whip [94]	433	70	173 × 4.5	+3.3	101.6 × 101.6
Helical [92]	433	40	38.1 × 8.9	+1.9	190 × 7.6
Planar [91]	433	8	27.9 × 13.7 × 1.2	-6.4	84 × 38
Chip [93]	433	7	12.7 × 0.36 × 1.2	-9.8	80 × 39

Table 3-2 Specification summary of commercial-type 433 MHz antennas

One of the key requirements for developing appropriate antenna designs for the Tyndall mote relates to the physical space that is occupied by the mote layers. This is equal to an area of 25 × 25 mm as shown in Figure 3-9 and is generically used for the majority of mote layers. Because of the stackable configuration of the mote layers to accommodate sensor, processing, wireless communications and other functionality, the maximum available size to realize the antenna element is shown in Figure 3-10. This space provides a maximum total area of approximately 50 × 25 mm +/- 10 % for both the radiating element and groundplane.

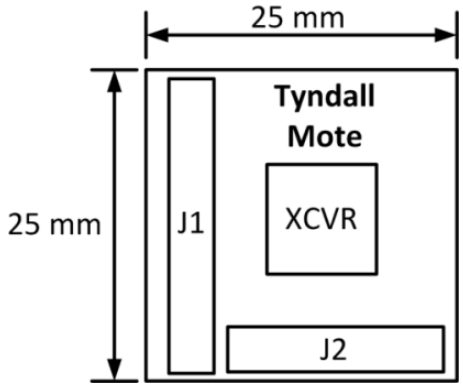


Figure 3-9 Tyndall mote layer physical size requirements

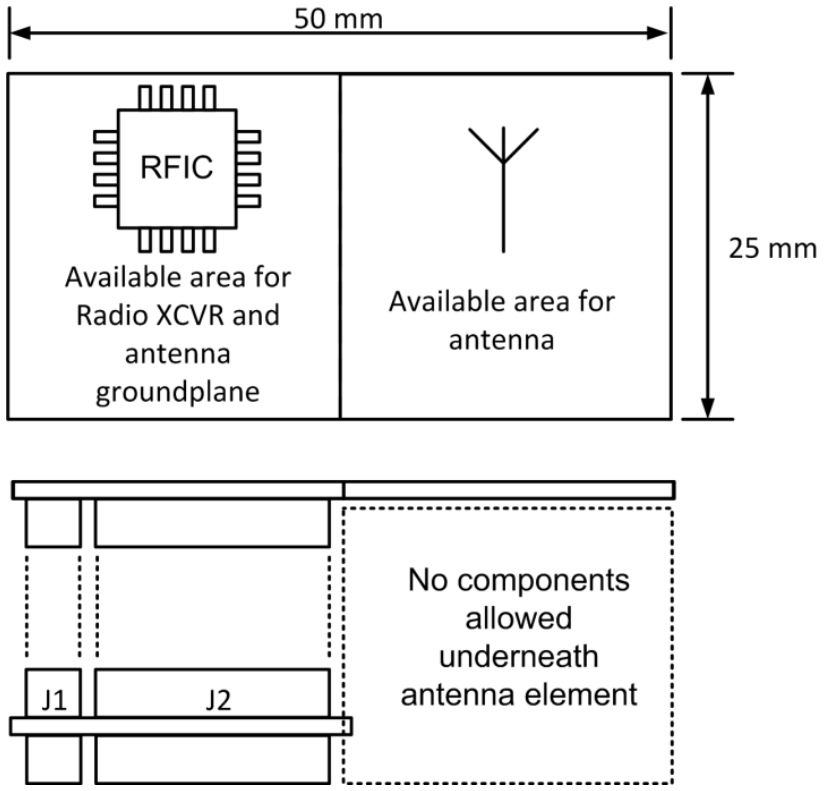


Figure 3-10 Antenna physical size requirements

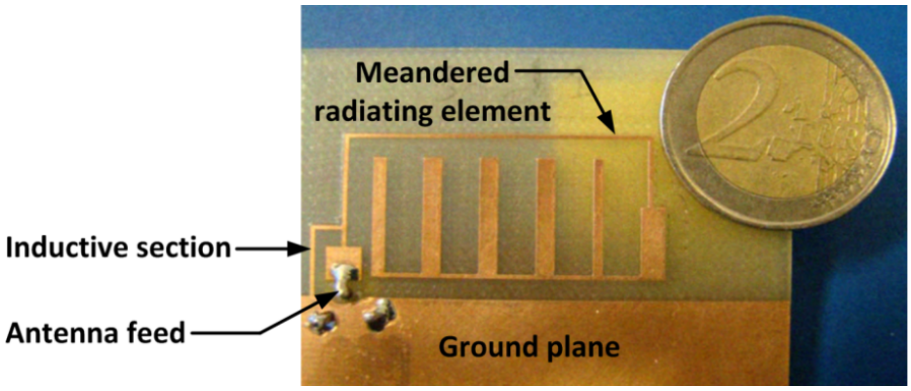


Figure 3-11 433 MHz meandered IFA antenna [95]

Apart from commercial antenna solutions described previously, several small-sized 433 MHz antennas have been reported by researchers in recent times, using a number of different antenna miniaturization techniques. A 433 MHz antenna is reported in [95] and is shown in Figure 3-11. Size reduction is achieved using an Inverted-F (IFA) topology comprising a meandered radiator together with an inductive section and is fabricated using standard FR-4 laminate material. The radiating element has a size of 37 × 20 mm and the antenna achieves a peak realized gain figure of -6.1 dBi at 433 MHz but also requires a minimum groundplane size of 37 × 30 mm and makes this topology unsuitable for the chosen application.

A miniaturized RFID tag antenna for an active 433.92 MHz RFID system is reported in [43]. The antenna is shown in Figure 3-12 and uses a spiral shaped radiator for size reduction. The radiator is placed above a square groundplane. The antenna has a reported peak realized gain of -3.48 dBi but requires a 700 × 700 mm groundplane and requires the radiating element to be displaced from the groundplane using a 20 mm foam material.

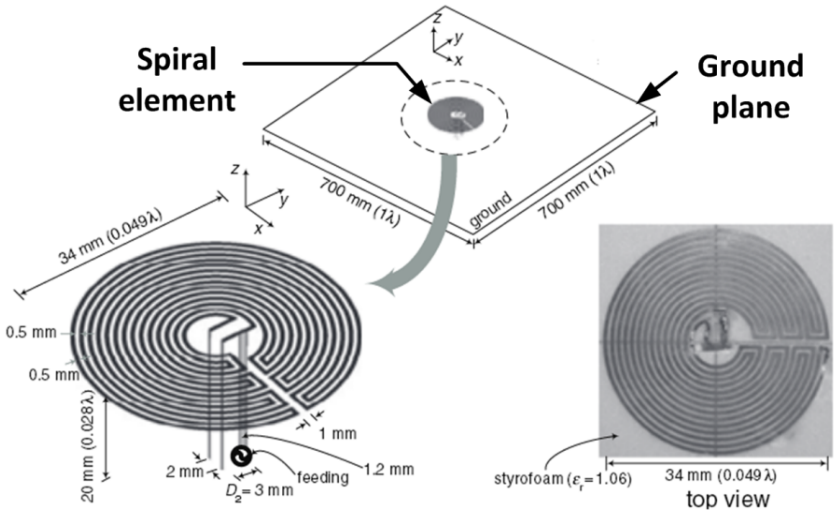


Figure 3-12 Spiral shaped meander-line 433 MHz antenna [43]

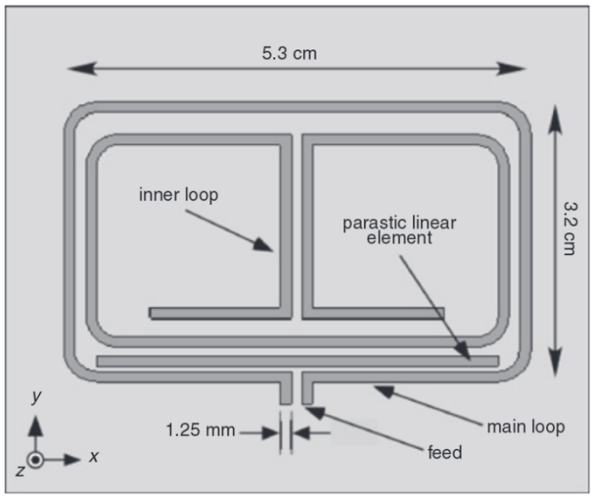


Figure 3-13 Double loop 433/ 868 MHz antenna [96]

Loop antennas are also a commonly used solution in applications where small size is one of the key requirements. In particular, electrically small loop antennas, whose overall length is less than a tenth of a wavelength [24] are frequently used in automotive applications such as remote keyless entry (RKE) systems [7]. A dual-band, double-loop antenna is proposed in [96] for 433 MHz and 868 MHz operation with application in wireless tyre pressure monitoring. The antenna is shown in Figure 3-13 and is implemented using FR-4 material with a thickness of 1.25 mm and dimensions of 53 × 32 mm.

A balanced feed is connected to the outer loop that encloses a smaller parasitic loop and parasitic linear element. The outer loop is resonant at 433 MHz and the inner loop is resonant at 868 MHz with the linear element used to tune the antenna at both frequencies. The antenna has reported gain figures of -20.9 dBi at 433 MHz and -9.19 dBi at 868 MHz as derived from simulation. The low gain figures are expected for electrically small loop structures whose radiation resistance are generally much smaller than their loss resistances [24].

A large number of small-sized bio-implantable antennas are also described in the literature including the antenna reported in [97]. This antenna is shown in Figure 3-14 and covers both the 402-405 MHz Medical Implant Communication Services (MICS) band as well as the 433 MHz and 2.45 GHz ISM bands. This antenna uses a Planar Inverted-F (PIFA) topology with a slotted groundplane technique to provide closely spaced resonances at 402 MHz and 433 MHz that are combined to provide wideband coverage from 356 to 610 MHz. Although the antenna size is extremely compact and has a wide bandwidth, because it is embedded in lossy tissue, the antenna gain is limited.

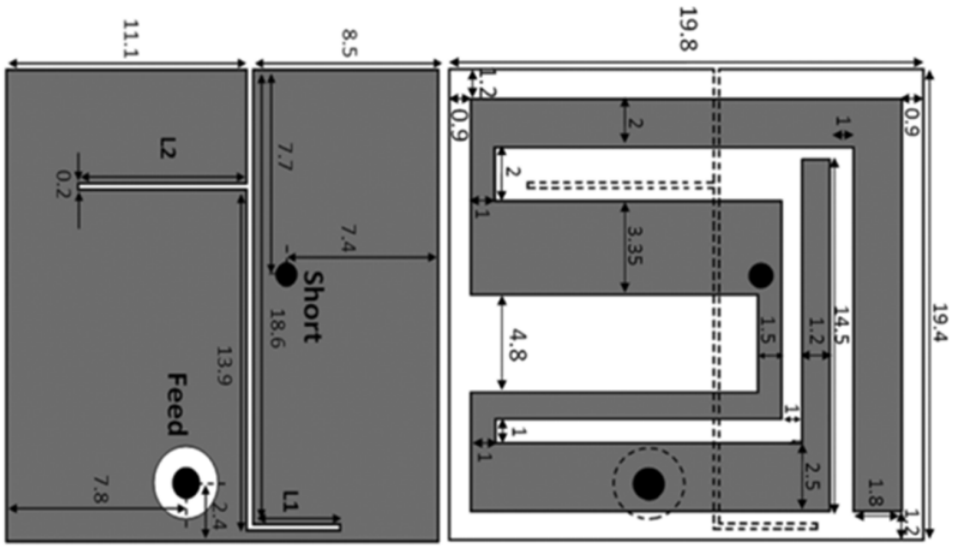


Figure 3-14 Slotted PIFA for bio-implantable applications [97]

Antenna Type	f_0 (MHz)	BW (MHz)	Size (mm)	Peak Gain at f_0 (dBi)	Required Groundplane area (mm)
PIFA [43]	433.92	3.52	34 × 20	-3.48	700 × 700
IFA [95]	433	6	37 × 20	-6.1	37 × 30
Loop [96]	433/868	Not available	53 × 32	-20.9	Not required
PIFA [97]	356 - 610	127	19 × 19.4 × 1.27	-27.6	Not required

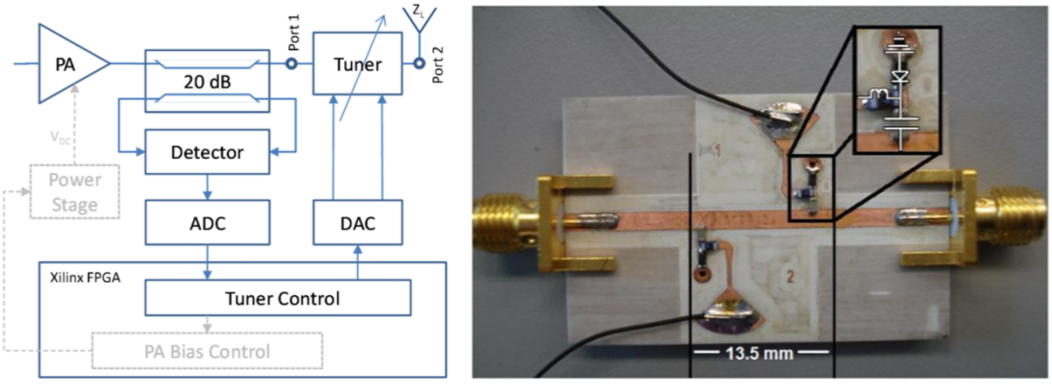
Table 3-3 Specification summary of several 433 MHz antennas in the literature

3.3 Antenna Detuning Issues for WSN Devices

When wireless devices are placed close to the human body, the electromagnetic coupling between antenna and body can affect antenna parameters such as impedance, efficiency, gain, radiation and polarization characteristics [18, 19]. In [10], the propagation losses of a body implanted dipole antenna were studied using EM simulation methods for the 433 MHz, 915 MHz, 2450 MHz and 5800 MHz ISM bands. It was shown that the high permittivity of human body tissue leads to an increase in the electrical length of the antenna and the large conductivity of the human body results in increased antenna losses. The change in antenna resonant frequency, or detuning effect, due to human body loading implies a change in antenna impedance and any impedance mismatch that exists, can lead to a reduction in radiated power. It was previously discussed in Chapter 2 that an impedance matching circuit is generally required to match the radio transceiver impedance to that of the antenna. The most common design approach for wireless sensor network devices at present is the use of *fixed* impedance matching networks using lumped elements. However, this design approach assumes that the antenna impedance remains constant and does not vary due to environmental factors. This is one of the main drawbacks of current WSN technology in terms of not having the capability to deal with varying antenna impedance.

One solution to the problem of antenna detuning is the use of an impedance matching system that adaptively corrects for changes in antenna impedance. Adaptive antenna tuning networks are extremely desirable and have been investigated by many researchers in recent times. Cellular handset applications in particular have been the key driver for the development of antenna tuning solutions because of performance issues associated with user effects. The effects of the user's hand and head have been studied by researchers in [27, 98] and it has been shown that the antenna impedance can vary considerably, especially for small-sized antennas that are integrated within the handset. Apart from antenna mismatch issues, the power amplifier (PA) of a cellular handset is typically designed to operate with a fixed impedance in order to maximize PA efficiency [99] and thereby reduce power consumption. Another key benefit of adaptive impedance matching that is being currently being exploited for handset applications is a desirable characteristic in which the operation frequency and bandwidth of an antenna can be adjusted automatically. For example in a cellular handset application where the available space for the antenna is extremely limited, a small-sized, non-resonant antenna may be brought to resonance over a range of frequencies using a suitable matching network [100].

Reconfigurable RF front-ends for cellular handset applications have been implemented using various types of tunable components including barium strontium titanate (BST) technology [101], CMOS SOI [102-105] as well as micro-electro-mechanical systems (MEMS) solutions [106-110]. The use of reconfigurable RF components poses strict requirements in terms of small size components with low loss, large tuning range, high linearity and low power consumption [111]. Substantial progress has been made in recent years with the commercial availability of high-performance tunable RF elements. These components are now in widespread use within mobile handsets to improve performance, compensate for environmental influences, shrink antenna volumes and shorten design cycles [112]. These types of tunable components include SOS capacitors [113, 114] as well as tunable RF MEMs capacitors [115, 116].

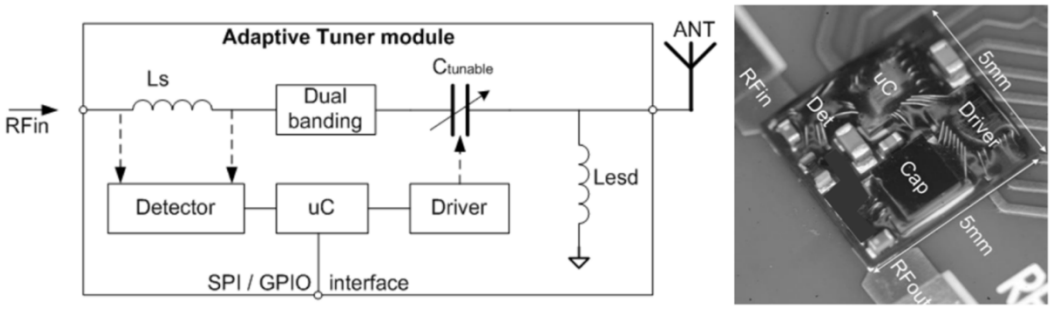


(a) (b)

Figure 3-15 CDMA antenna tuner [117], (a) Block diagram, (b) Double stub tuner

Several adaptive tuners for handset applications have been demonstrated in academic works. In [117], a closed-loop impedance tuner is proposed for WCDMA applications at 1.95 GHz using a double-stub varactor-based tuner as shown in Figure 3-15 (a). The double-stub varactor tuner is shown in Figure 3-15 (b). Tuner control is achieved using a Xilinx FPGA and uses a dual-output DAC for varactor bias. A coupler is used to sample antenna forward and reflected RF power that is then detected using ADCs as shown.

A completed design and measurement methodology for a tunable RF Impedance-Matching network is described in [118]. This paper reports on the use of a *Π*-structure with tunable components made of varactors in series with inductors for 1 GHz operation. The matching network can provide 80 % coverage of the Smith chart but only the details of the matching network are reported. A broadband reconfigurable RF impedance tuner is reported in [119] using varactor diodes that provides broadband coverage from 4 to 7 GHz for a wide range of load conditions but only the details of the RF impedance tuner are reported. A highly-integrated, self-contained adaptive antenna tuner is reported in [120] that enables low-loss cellular handset antenna tuning over the frequency ranges 698-960 MHz and 1710-2690 MHz. Figure 3-16 shows a block diagram of the System in Package (SiP) tuner module that allows autonomous, closed-loop control of a MEMS tunable capacitor. Antenna mismatch detection is achieved using a phase detector and a microcontroller for tuning control.



(a) **(b)**

Figure 3-16 Cellular antenna tuner, (a) Block diagram, (b) Tuner module [120]

Aperture tunable methods for [121, 122] are also reported that place a tunable component on the antenna element to enable the antenna to be reconfigured. Balanced antenna structures [123] can also be used for cases where the antenna is placed close to the human body as they have good immunity to detuning effects [76] but tend to be large in size. The above survey indicates that antenna tuning is currently a rapidly emerging area of research, driven by the need for smaller, more compact cellular handset devices. High performance RF tunable components are now commercially available but WSN applications have not yet benefited from the use of this technology. One of the main goals of this work was to explore how the above tuning technology could be applied to WSN devices to mitigate detuning issues.

3.4 Wireless Reliability Issues for WSN Devices

A large number of WSN devices currently use the 2.45 GHz ISM band using the IEEE 802.15.4 standard [62, 67]. However, the availability of other license-free bands such as the 433 MHz ISM band in Europe provides potential for Quality of Service (QoS) improvements. For example, the ability to switch from the 2.45 GHz to the 433 MHz ISM band can provide potential such as reduced signal attenuation in biological monitoring applications as well as reduced path loss and improved immunity to interference and congestion. Band switching can also offer improvements in data reliability, availability, and security when compared with existing solutions.

There are currently a large number of multi-band antennas reported in the literature for applications in ISM band communications, Wireless LAN, WiMax etc. The rapid growth in wireless communication applications, especially mobile wireless applications, has increased the need for antennas with multi-band capability in order to provide additional wireless features in devices whose size continues to decrease. However, the available space for multiple antennas within these devices is generally extremely limited and antennas that can provide multi-band operation are therefore extremely attractive.

Many modern ISM-band wireless sensor devices have the requirement for small size in applications where size and weight are critical. The requirement to switch between frequency bands poses a number of design challenges however, because small, low-cost antenna structures with multi-band capability are necessary. This area has been the subject of intense research in recent years with a large number of multi-band antennas reported in the literature. These include a dual-band, inverted-F antenna (IFA) for 433/868 MHz [66], a printed-loop for 433/868 MHz vehicular applications [96] and a triple-band inverted-L topology for 2.4/5.2/5.8 GHz WLAN applications [124]. Other approaches use reconfigurable antennas where the antenna topology can be controlled electronically, for example using active RF switches [125.]. Most passive, multi-band antennas are generally resonant at a fundamental and a harmonic, or near harmonic, of the fundamental frequency. Only a limited number of small sized, passive-type antennas are described in the literature that can cover both the lower and upper extents of the ISM bands, such as dual-band operation at 433 MHz and 2.45 GHz. A commercial antenna that covers the 440 MHz, 850 MHz, 900 MHz, 1.575 GHz, 1.8 GHz and 2.4 GHz bands is available from Abracon [126] but is a large in size, measuring 153 × 154 × 99 mm and is designed for automotive applications. Examples of small-sized, multi-band topologies are described in [127] [97] [128] but are designed for bio-implantable applications. A small-sized antenna design is reported in [129] using a capacitively loaded IFA topology and a parasitic element to achieve dual-band operation at 930 MHz and 1.7 GHz. A conventional IFA requires a minimum size of $\lambda/4$ and this antenna is realized in a small size of $0.109\lambda \times 0.025\lambda$ but does

not include a groundplane. The above highlights the potential for developing small-sized, multi-band antennas that have the ability to cover both the lower and upper extents of the UHF ISM bands for applications in short-range, wireless applications.

3.5 Conclusions

This chapter has shown that there is a growing trend for the development of highly integrated WSN devices such as the Tyndall mote. The realization of extremely compact wireless sensors is possible but antenna integration remains an issue and places a limit on the minimum achievable size. This is especially true for wireless sensors that operate in the 433 MHz (ISM) band. There are a growing number of applications where WSN devices have great potential. However the sensitivity of antennas to environmental effects in BSN applications can have a considerable effect on wireless performance. It was also shown that antenna tuning technology is rapidly emerging for cellular applications, driven by the recent availability of high-performance tunable components. However, to date, wireless sensors are relatively simple in design, with no capacity to deal with changing antenna environments such as in BSN applications and an opportunity therefore exists to use the latest tunable technology in these types of applications. Finally, most current WSN devices operate on a single ISM band only and there is potential to improve QoS performance by using a multi-band approach. However, this requires the development of new types of antennas that meet the small size requirements of these applications while still maintaining acceptable levels of antenna performance. The focus of this thesis is to develop a number of antenna solutions that address each of the above challenges for WSN devices and several novel antenna designs are reported that advance the state-of-the-art in the area.

Chapter 4.
First-Generation Adaptive Antenna Tuning System

4.1 Background

This chapter presents the design of the initial adaptive antenna tuning system developed during this research, which is referred to as the 'first-generation' system. The chapter begins with an investigation of the effects of antenna detuning on wireless sensor performance due to the presence of the human body, particularly the wrist. The aim is to investigate some of the potential benefits of adaptive antenna tuning as well as identify key challenges and requirements in implementing an automated antenna tuning solution for a wrist-wearable antenna configuration. Effects such as antenna detuning and matching network losses as well as wireless sensor power consumption are first determined experimentally in a practical application. Modeling and simulation results for a reconfigurable *Π*-type impedance matching network are then presented. The design of a digitally tunable capacitor is then outlined using discrete component Silicon-On-Sapphire (SOS)-based RF switches. As a first step towards the development of a more integrated, second-generation solution as described in Chapter 6, a discrete-component prototype, first-generation antenna measurement and tuning system is presented that allows the antenna S_{11} parameter (magnitude) to be measured and displayed using a graphical user interface (GUI) and implements a tuning algorithm by means of a full code search. Some of the key results of this chapter have been published in [130, 131].

4.2 Example of Antenna Detuning for a Wrist-Mounted Antenna

As described briefly in Chapter 3.3, when wireless devices including motes, are placed in close proximity to the human body, the electromagnetic coupling between antenna and body can affect antenna parameters such as impedance, efficiency, radiation and polarization characteristics [19, 132]. This investigation focuses on the degree of antenna impedance variation caused by the presence of the human wrist. Antenna detuning leads to increased antenna mismatch losses that ultimately result in a decrease in power delivery to the antenna. Without some means of adaptively tuning the antenna, the only option is to increase the RF output power of the transmitter in order to maintain a specified radiated power level. However, this leads to increased power consumption and reduced battery lifetime. The addition of a tunable matching network can allow the varying antenna impedance to be tuned adaptively. However, the design of a suitable matching network requires accurate knowledge of the range of antenna impedances that are possible when an antenna is positioned close to the human body. It can be difficult to obtain consistent antenna impedance measurements in practice using real human bodies due to problems of movement, repeatability, and traceability. Accurate phantoms that mimic the human body are commercially available such as [133] that use a silicone-carbon-based outer structure and a conductive inner structure to simulate human tissue over the frequency range 0.3 – 3 GHz. These phantoms are designed to evaluate the performance of wireless devices that may be affected by the presence of the forearm and hand. One of the disadvantages with commercial phantoms is the cost. An alternative approach is presented here in the development and characterization of a low cost human phantom that uses a homogenous liquid-filled solution.

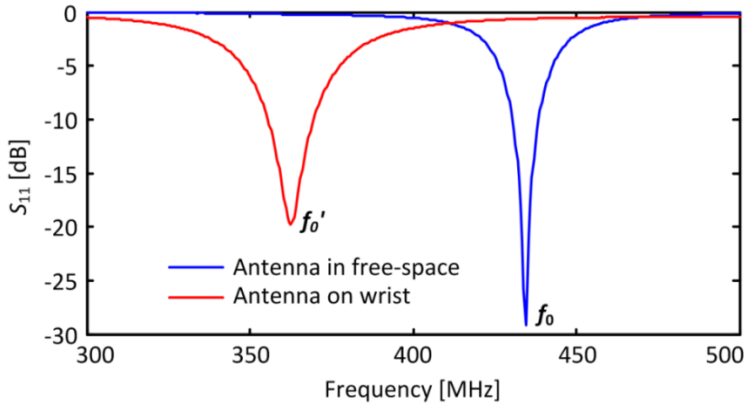
4.2.1 *Homogenous Phantom Arm Design and Characterization*

In order to facilitate repeatable and consistent antenna impedance measurements, a low cost human phantom arm that simulates human tissue at 433 MHz was investigated. Different materials have been used to simulate human tissue at microwave frequencies [134, 135].

One approach uses a sucrose (sugar) and saline solution where the ingredients are inexpensive and readily available. These liquids can be used to mimic the dielectric properties, particularly the relative permittivity and conductivity of human tissue over a limited frequency range. The sucrose ingredient is used to control the permittivity of the solution while sodium chloride is used to control the conductivity. For this study, the proportions (by weight) of water, sucrose and sodium chloride were selected as 52.4%, 46.2% and 1.4% respectively, based on similar work at frequencies of 100 MHz to 1 GHz reported in [136]. A hollow fiberglass mannequin shell of thickness 3 mm was selected to contain the liquid solution and has a physical size and shape that closely resembles that of a human arm. The AUT for this test was a commercial 50 Ω planar type that has a specified resonant frequency of 433 MHz in free-space [91]. The antenna was mounted on a 25 x 25 mm^2 printed circuit board as shown in Figure 4-1 (a). The antenna was fed via an SMA connector and 50 Ω co-planar waveguide, printed on an FR-4 substrate [137] of thickness 1.52 mm, with a relative permittivity of 4.5 and a loss tangent of 0.02. Several ferrite-beads [60] were also placed on the 50 Ω feed-cable in order to help suppress cable shield currents to improve measurement accuracy as discussed in Chapter 2.3. The detuning effects of the human wrist were first evaluated by first measuring the AUT S_{11} in free-space, followed by a measurement with the antenna placed on the human wrist as shown in Figure 4-1 (b). The measured results are shown in Figure 4-1 (c). It can be seen that with the antenna placed in a free-space environment, the antenna was tuned to the nominal operating frequency f_0 = 433 MHz with a corresponding measured value of S_{11} close to -30 dB. However, when the antenna was then placed on the human wrist, the resonant frequency decreased to a value of 363 MHz with a measured S_{11} of close to 0 dB at f_0, representing a large impedance mismatch condition.



(a) (b)



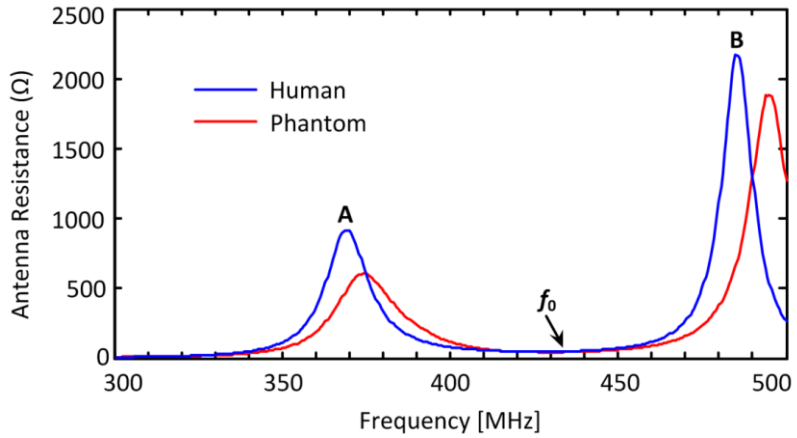
(c)

Figure 4-1 (a) 433 MHz AUT, (b) AUT on human wrist , (c) Measured S_{11}

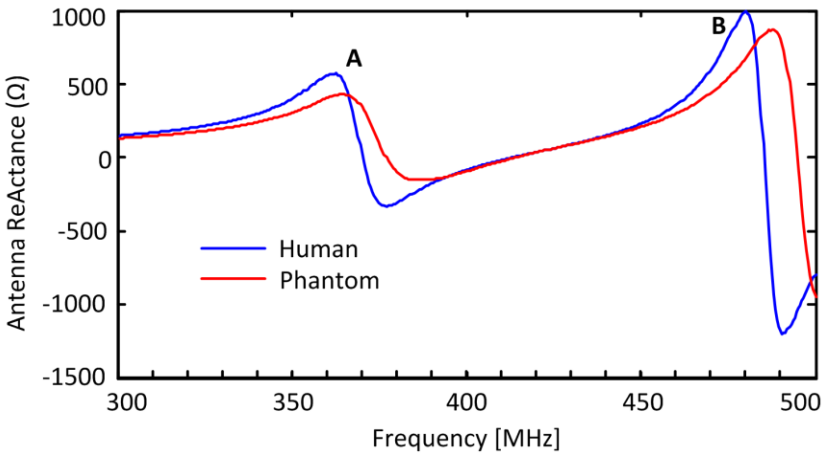
The phantom test case was measured using the test setup of Figure 4-2. The test antenna was then placed on the human arm but in this case, a 3 mm Plexiglass insulator was used to model the phantom arm shell thickness and prevent contact with the back side of the antenna. Without the insulator present, placing the antenna in direct skin contact results in an effective short-circuit at the antenna terminals due to the high conductivity of the skin tissue. In practice, this property of the skin is not easily simulated for physical human phantoms [138] and for the following measurements, the skin properties are not considered. However, in Chapter 5, these effects are considered using a heterogeneous human phantom model. The impedance and reactance of the test antenna were then measured on both the phantom and human wrists and the measured results are shown in Figure 4-3.



Figure 4-2 Phantom measurement setup



(a)



(b)

Figure 4-3 Measured antenna characteristics for human and phantom test cases:

(a) Antenna impedance, (b) Antenna reactance

It can be seen in Figure 4-3 (b) that the measured antenna resistance and reactance for the human and phantom wrists agree at frequencies close to the nominal antenna resonant frequency of 433 MHz, denoted f_0. Note that two resonances (A and B) were observed in the antenna resistance and reactance graphs occurring at frequencies of approximately 370 MHz and 490 MHz. The antenna impedance at these frequencies is much greater than the system characteristic impedance of 50 Ω and therefore the resonant effects are not reflected in the S_{11} measurements. Figure 4-4 compares the measured antenna S_{11} for the human and phantom cases. There is a shift in frequency between the two cases but the difference is less than 5 MHz. Exact agreement between the two test cases is not expected since the simulation model and physical test setup using the homogenous phantom are not anatomically identical.

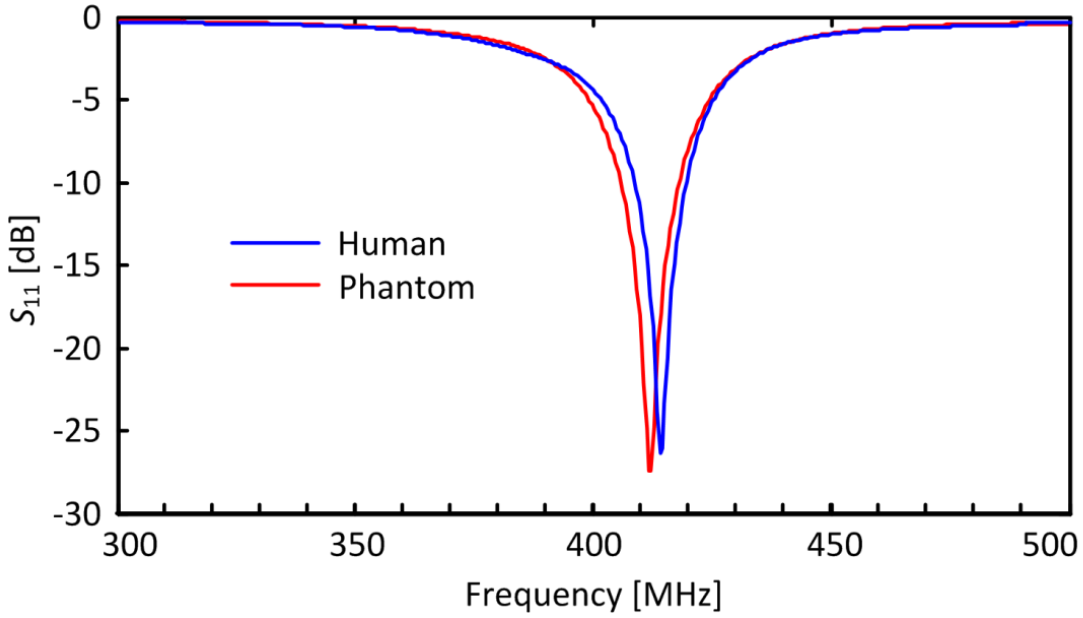
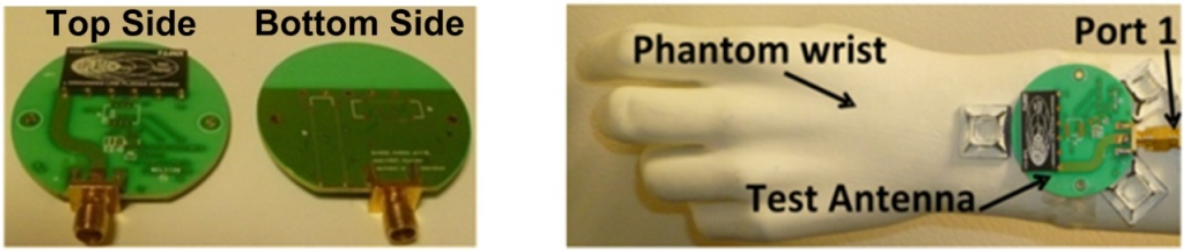


Figure 4-4 Comparing measured AUT S_{11} characteristics on human and phantom

4.2.2 *Antenna detuning for varying distance to phantom arm*

The objective of the following investigation was to determine the impedance variation of a commercial test antenna placed in varying proximity to the phantom wrist. The AUT for this test case is shown in Figure 4-5 (a) and is the same, small-sized, commercial antenna [91] as described previously. In this case, the antenna was placed on a 45 mm circular PCB to allow the antenna to be evaluated in different shaped PCB configurations for related project work [75]. The goal here was to investigate how a different shaped PCB and substrate would affect detuning. The PCB was implemented using low-loss, 1.6 mm RO4003C substrate [139] with ε_R = 3.35 and loss tangent of 0.0027. The antenna was fed via a 50 Ω microstrip trace with a groundplane placed on the bottom side of the PCB as shown. The reference port location for the S_{11} measurements is designated Port 1 in Figure 4-5 (b).



(a) **(b)**

Figure 4-5 (a) 433 MHz AUT, (b) AUT placed on phantom arm

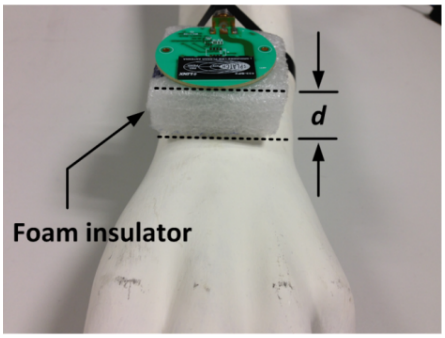


Figure 4-6 AUT to phantom distance *d* using foam insulating material

For subsequent measurements, the distance d between the antenna and phantom arm was varied in 5 mm steps using foam spacers as shown in Figure 4-6. This material was first verified to have no measurable effect on the measured antenna impedance. The antenna S_{11} characteristics were then measured using a Rohde & Schwarz ZVRE vector network analyzer [47] and the mismatch loss for each case was also determined using equation (2.10). Figure 4-7 presents the measured S_{11} and calculated mismatch loss of the antenna, specified at the design centre frequency f_0 = 433 MHz for varying distance d. For the case where d = 0 mm (antenna touching phantom surface), the antenna impedance was measured as Z_A = 45 + j 115 Ω. This antenna impedance corresponds to a load VSWR of approximately 7.8:1. It can also be observed that there is a significant mismatch loss of approximately 4 dB approximately due to impedance mismatch effects. For distances of 20 mm or more, the S_{11} magnitude does not vary significantly and is within 5 % of its free-space value.

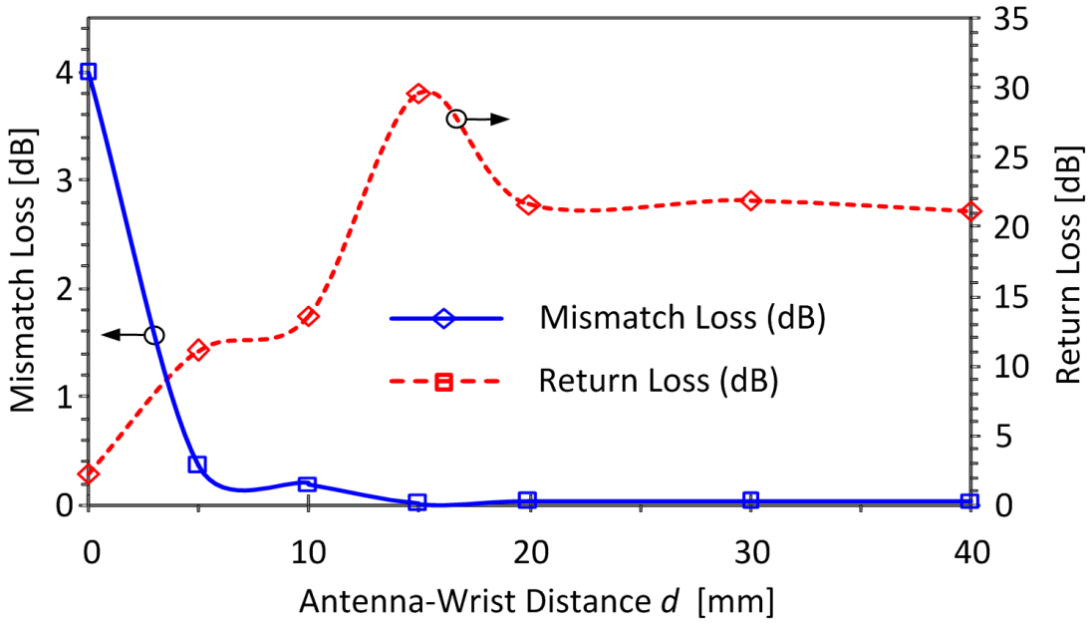


Figure 4-7 Measured antenna S_{11} and mismatch loss for varying distance d

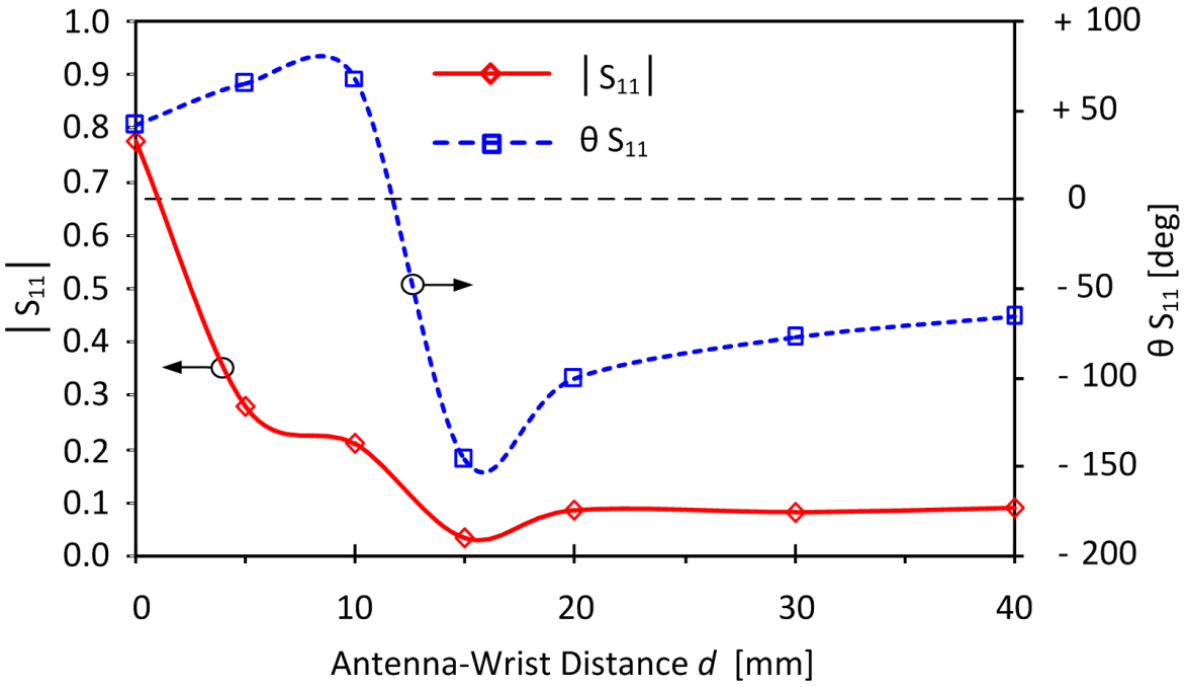


Figure 4-8 Measured S_{11} (magnitude and phase) versus distance d at f_0

Figure 4-8 shows the magnitude and phase of S_{11} versus distance d with the measured antenna impedance exhibiting an inductive reactance for values of $d \leq 12$ mm approximately and then becomes capacitive for $d > 12$ mm.

4.2.3 *Matching network implementation*

In this section, the goal is to investigate the performance improvements possible when an impedance matching circuit is used to correct the impedance mismatch of the detuned antenna using a manually tunable, discrete component antenna matching network. A low-pass, *Π*-type matching topology was chosen as it is widely used in narrow-band wireless sensor applications due to its harmonic rejection capability and wide matching range [140]. Unlike the *L*-type network where the loaded quality factor Q is determined by the required impedance transformation ratio, the additional tuning component provides an extra degree of freedom in choosing a value of Q as described in Chapter 2.

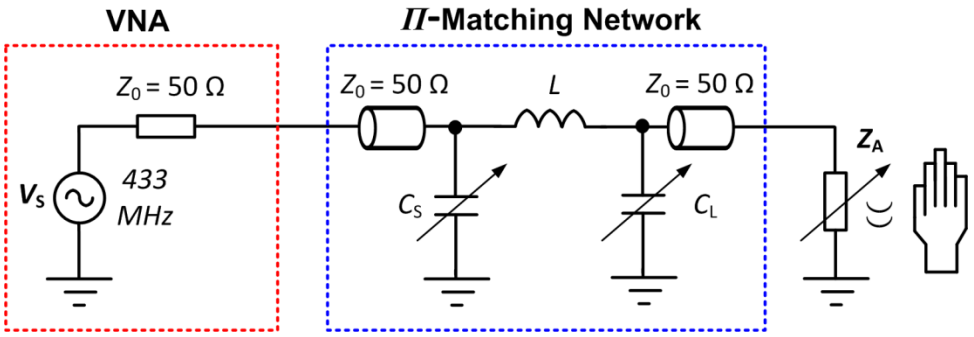
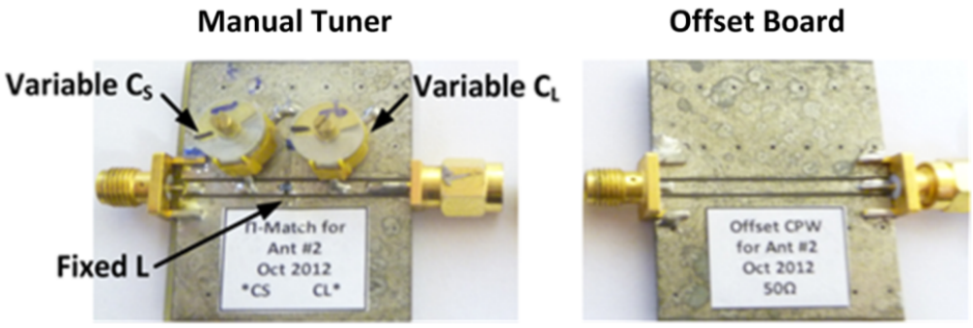


Figure 4-9 *Π*-type matching circuit connected to VNA

Figure 4-9 shows a schematic of the matching network connected between the detuned antenna and the 50 Ω source impedance of the VNA [47]. The *Π*-type matching network is composed of three reactive elements: a source-side shunt variable capacitance C_S, a series inductor L, and a load-side shunt capacitance C_L. For this case, the load or antenna impedance was specified as the measured value of $Z_A = 45 + j\ 115\ \Omega$ for the case where the antenna is placed directly on the surface of the phantom wrist (d = 0 mm). The required values of L, C_S and C_L were determined in simulation using the *iMatch* filter and matching network tool [141] that is integrated within the AWR Microwave Office Suite [41]. The source impedance was specified as Z_0 = 50 Ω with a network Q of 10 and a centre frequency f_0 = 433 MHz with the required component values determined as C_S = 27.4 pF, C_L = 13.6 pF and L = 16.9 nH.

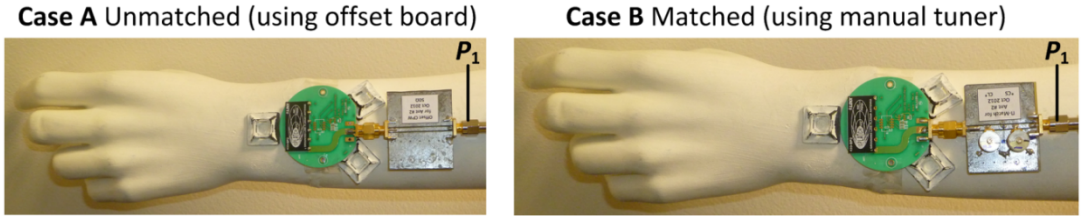


(a) **(b)**

Figure 4-10 (a) Manual tuner, (b) Offset board

For test purposes, a manually tunable matching network was implemented as shown in Figure 4-10 (a). Variable capacitors [142] ranging from 6 to 80 pF were used for C_S and C_L to enable fine-tuning of the network. This was necessary to compensate for the effects of losses in the lumped elements as well as the effects of the finite length CPW traces that lead to slightly different component values to those calculated earlier. For inductor L, the nearest available value of 17 nH was chosen, using a high-Q inductor (Q_L = 50) 0603WL170JT from American Technical Ceramics [143]. The tunable matching network was then implemented on a 1.6 mm FR-4 substrate of size 33 mm × 42 mm with ε_R = 4.5 and loss tangent of 0.02 [137] using 50 Ω grounded co-planar waveguide (GCPW) lines as shown in Figure 4-10 (a). In order to test the antenna on the phantom arm without a matching network present, an offset board was used to connect the antenna directly to the VNA during measurements. The offset board is shown in Figure 4-10 (b) and the CPW used has identical electrical properties and physical dimensions as the matching circuit and provides identical placement of the VNA reference for measurements.

A close-up of the measurement configuration for the two test cases A and B is illustrated in Figure 4-11. In Case A (unmatched), the offset board is present and in Case B (matched) the manual tuner is used. The VNA reference plane at the end of the feed cable is shown as port P_1 in both cases. Figure 4-12 shows the measured antenna S_{11} parameters for both cases. It can be seen that without matching, the antenna has a measured S_{11_U} (unmatched) of approximately -2.2 dB and is also resonant at a frequency lower than f_0 = 433 MHz. When the matching circuit is added and tuned, the antenna is made resonant at f_0 and the measured S_{11_M} (matched) = -28 dB approximately, i.e. an improvement of 26 dB.



(a) **(b)**

Figure 4-11 Photograph of test setup (a) Unmatched, (b) Matched

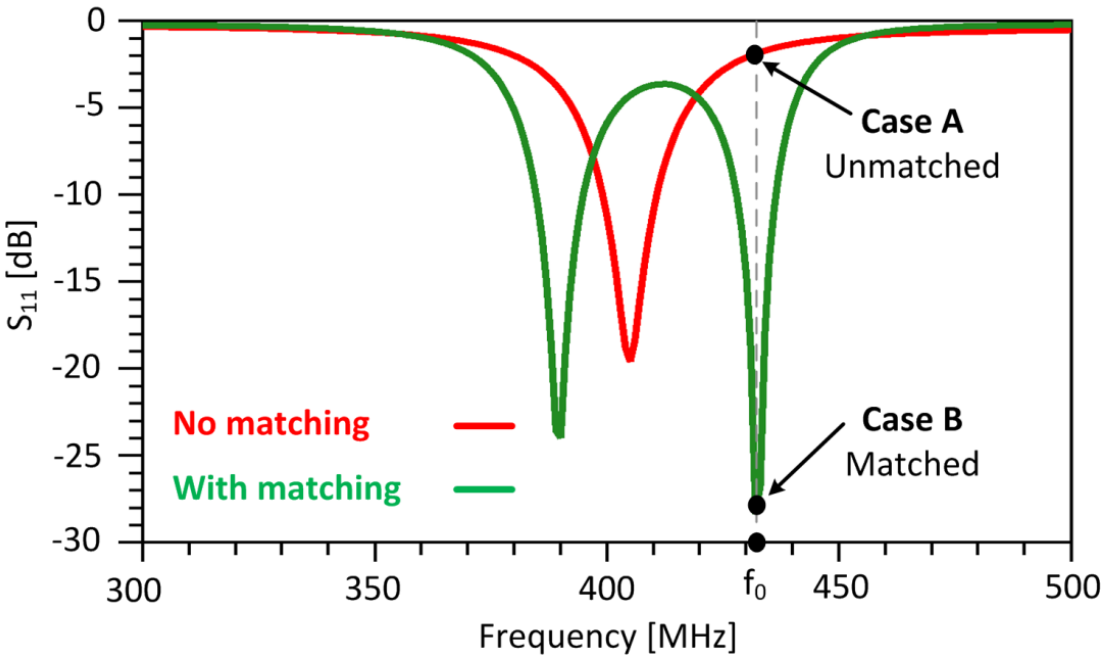


Figure 4-12 Measured antenna S_{11} in matched and unmatched cases

It can also be seen from Figure 4-12 that two resonances are present for the case where the matching circuit is included. This extra resonance is caused by the addition of the matching network and the reason for the observed effects is discussed in detail in Section 6.4.

Having measured the antenna S_{11} with and without the matching network present, the values of the reflection coefficient magnitudes $|\Gamma_M|$ (matched) and $|\Gamma_U|$ (unmatched) are calculated for both cases as

$$|\Gamma_M| = 10^{(-S_{11_M}/20)} = 0.78 \quad (4.1)$$

and

$$|\Gamma_U| = 10^{(-S_{11_U}/20)} = 0.04 \quad (4.2)$$

The resulting mismatch losses for the matched case ML_M and the unmatched case denoted ML_M are then calculated using (2.10), leading to the following values

$$ML_U\ (\text{dB}) = 10\log_{10}(\,1 - \ |\Gamma_U|^2\,) = \ 4\ \text{dB} \tag{4.3}$$

$$ML_M\ (\text{dB}) = 10\log_{10}(\,1 - \ |\Gamma_M|^2\,) = \ 0.01\ \text{dB} \tag{4.4}$$

The estimated improvement in power delivery to the antenna, with the matching circuit included, denoted P_{CALC} is therefore

$$P_{CALC}\ (\text{dB}) = ML_U - \ ML_M \approx 4\ \text{dB}. \tag{4.5}$$

Equation (4.5) shows that in theory, the addition of the matching circuit results in a 4 dB reduction in mismatch loss. However, it is important to point out that P_{CALC} accounts solely for losses due to antenna impedance mismatch and does not include any inherent losses in the matching network itself.

4.2.4 *Antenna detuning effects on wireless sensor performance*

This section investigates the effects of antenna detuning caused by the human body based on physical testing of a wireless sensor device in a wearable scenario. The platform used for this work is the 433 MHz mote [23] as shown in Figure 4-13.

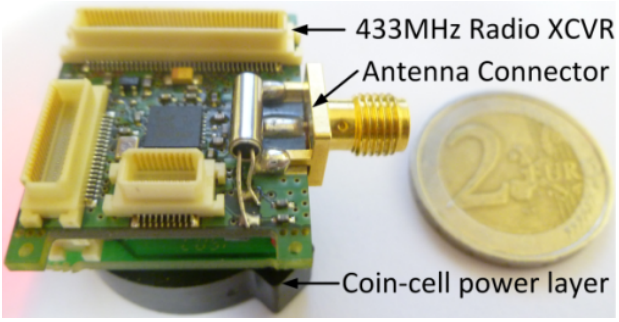
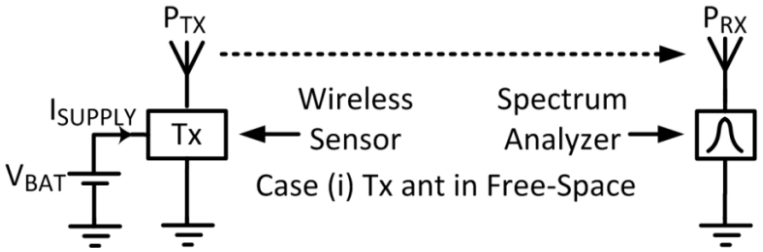


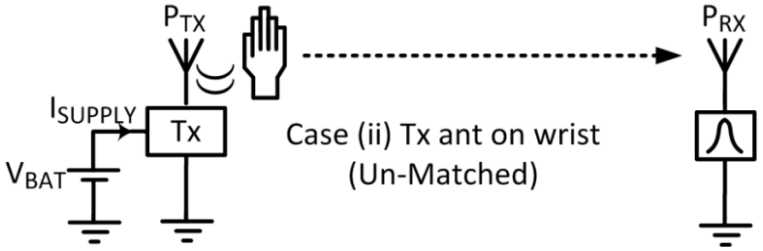
Figure 4-13 433 MHz WSN mote

The following tests were performed for three different configurations of the transmitting wireless sensor antenna as illustrated in Figure 4-14. In the first case shown in Figure 4-14 (a), the transmit (*Tx*) antenna was placed in free-space and the received power (denoted P_{RX}) was measured with a remote receiving antenna connected to a Rohde & Schwarz ® FSUP Signal Source Analyzer [144]. This test was conducted in order to provide a free-space reference to compare with subsequent measurements.

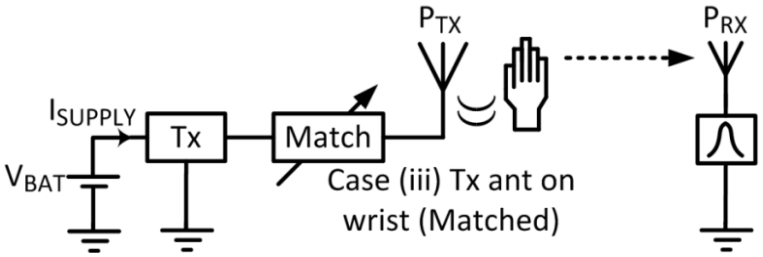
In the second case shown in Figure 4-14 (b), the *Tx* antenna was placed on the phantom wrist, with no impedance matching. Finally, in the third case as shown in Figure 4-14 (c), the *Tx* antenna was placed on the phantom wrist and the discrete-component matching circuit (pre-tuned) was connected between the transmitter and the antenna. The lab setup is shown in Figure 4-13 (d). The FSUP analyzer shown in the foreground was used to monitor received power P_{RX} at a distance of approximately 2.5 m from the transmitting mote using a 433 MHz quarter-wave antenna. During these measurements, the battery powered wireless mote was programmed to output an un-modulated carrier with a frequency f_0 = 433 MHz at a power level of +10 dBm as measured into a 50 Ω load using the FSUP analyzer. This power level was used to maximize the receive power at the receiving end in order to increase the repeatability of these, and subsequent measurements in a non-ideal (non-anechoic) laboratory environment, the average of a series of ten measurements of P_{RX} was calculated for each test case.



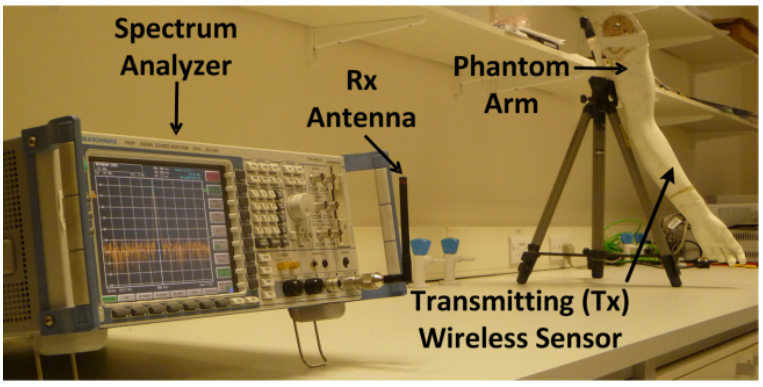
(a)



(b)



(c)



(d)

Figure 4-14 Test cases (a) Free-Space, (b) No match, (c) Manual tuner, (d) Test setup

The measured results are shown in Figure 4-15. On this graph, the left-hand y-axis is used to indicate received power and mote supply current while a 'pseudo-x-axis' is used to indicate the three measurement conditions. When the antenna was placed in free-space, the average received power P_{RX} was measured as -49.42 dBm. When the antenna was then placed on the phantom wrist with no matching network, a significant decrease of over 10 dB was observed in the value of P_{RX}. This reduction in received power is attributed to a combination of antenna impedance mismatch and losses associated with RF absorption and polarization effects caused by the phantom [17-18].

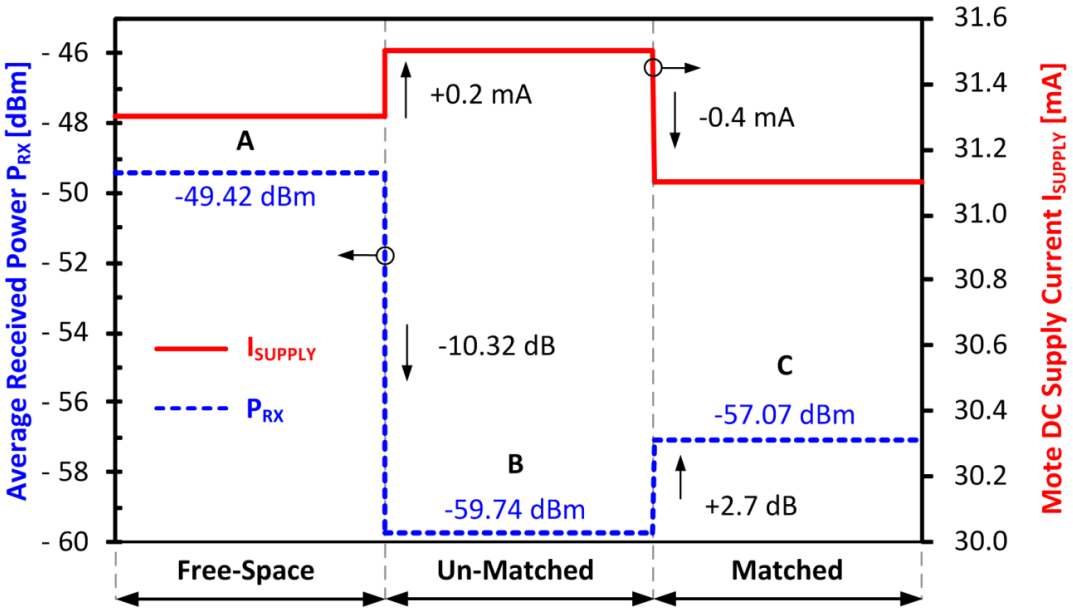


Figure 4-15 Measured P_{RX} and I_{SUPPLY} for the three configurations of Tx antenna

Finally, when the discrete component matching network was connected, the value of P_{RX} increased by 2.7 dB compared to the unmatched case. The results show that the measured increase in received power denoted P_{MEAS} was less than the calculated value P_{CALC} from equation (4.5) where an ideal (lossless) matching network was assumed. In reality, the discrete component matching network exhibits a loss denoted P_{LOSS} of

$$P_{LOSS}\ (\text{dB}) = P_{CALC} - P_{MEAS} \approx 4\ \text{dB} - 2.7\ \text{dB} \approx 1.3\ \text{dB}. \qquad (4.6)$$

The supply current of the mote denoted I_{SUPPLY} was also measured for the three test cases. Note that for these measurements, I_{SUPPLY} is the total current for the entire mote rather than just the radio transceiver itself and it is the relative changes in I_{SUPPLY} that are of interest as the only changing parameter is the antenna loading. It is important to note that microcontroller activity does not contribute to changes in I_{SUPPLY} during these measurements. Figure 4-15 shows that when the antenna is placed on the phantom arm in the unmatched case, the wireless sensor consumes maximum current coinciding with a minimum value of P_{RX}. Then, when the matching network is added, the value of I_{SUPPLY} is reduced by 0.4 mA with a 2.7 dB measured increase in P_{RX} compared to the unmatched case.

4.2.5 *Radio transceiver current consumption versus transmit power*

The current consumption of the wireless mote was also measured for varying transmitter PA output power and the results are shown in Figure 4-16. The results show that as the Tx power is increased, there is a substantial increase in the mote DC supply current, especially for high output power settings. For example, increasing the transmit power by 4 dB, from +6 dBm to +10 dBm, requires an additional 12.54 mA of supply current. In practice, many wireless sensor applications operate the radio near maximum transmit power in order to maximize range, link quality and throughput but there is a substantial increase in the resulting current consumption and this is an important consideration for low-power wireless sensor devices. These results show an important potential benefit of antenna matching for wireless sensors in terms of power consumption. The use of antenna tuning has been shown to enable a reduction in the losses associated with antenna mismatch. This decrease in antenna mismatch loss creates the potential to reduce the PA output power of the mote leading to decreased DC power consumption and increased battery life which is one of the key goals for WSN development at the present time.

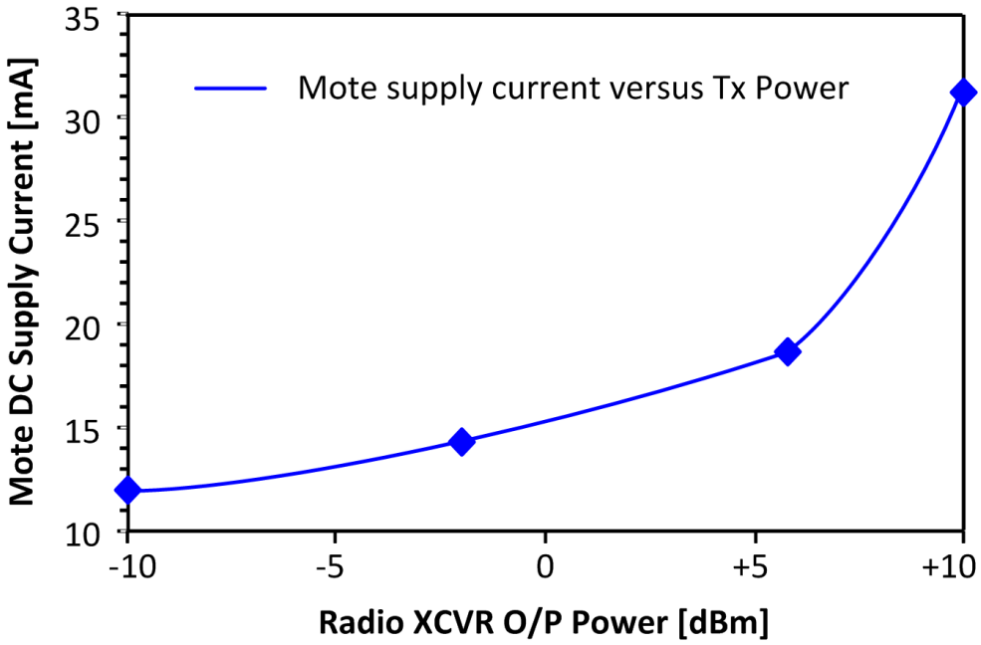


Figure 4-16 Measured Tx mote current consumption versus transmit power

(Under a 50 Ω Load condition)

4.3 Antenna Tuner System Design

This section discusses the design of a first-generation antenna tuner system that incorporates antenna S_{11} parameter measurement. The motivation was to develop and characterize a discrete component antenna tuning system to achieve the best possible power delivery to the antenna and this design also serves as the basis for a more integrated solution that is described in Chapter 6. A block diagram of the system is shown in Figure 4-17. The radio transceiver (in this case the wireless sensor mote) is used as the source of RF power. During antenna measurements or tuning operations, the transceiver provides an un-modulated RF output at a frequency of 433 MHz and a power level of +10 dBm. As discussed in Chapter 3.3, a popular method to measure the degree of power reflection from an antenna is the use of a reflectometer or directional coupler and the same method is used here. In this case, the transceiver output drives the input port of a commercial ZFBDC20-62H bi-directional coupler from Mini-Circuits [145]. The chosen coupler for this application has a bandwidth of 10 to 600 MHz, a low insertion loss of 0.3 dB at 433 MHz with coupling and directivity figures of 20 dB and 25 dB respectively and a maximum voltage standing wave ratio (VSWR) of 1.05:1. The directional coupler is the main component that determines both the frequency range of the system and the minimum value of S_{11} that can be measured. For this work a 433 MHz coupler was chosen but the same principle can be use for higher frequencies by utilizing a higher frequency coupler. The output port of the coupler (denoted P_1) in Figure 4-17 is connected to the input of the reconfigurable tuning circuit or can also be directly connected to an antenna for direct measurement of antenna S_{11} without any matching network.

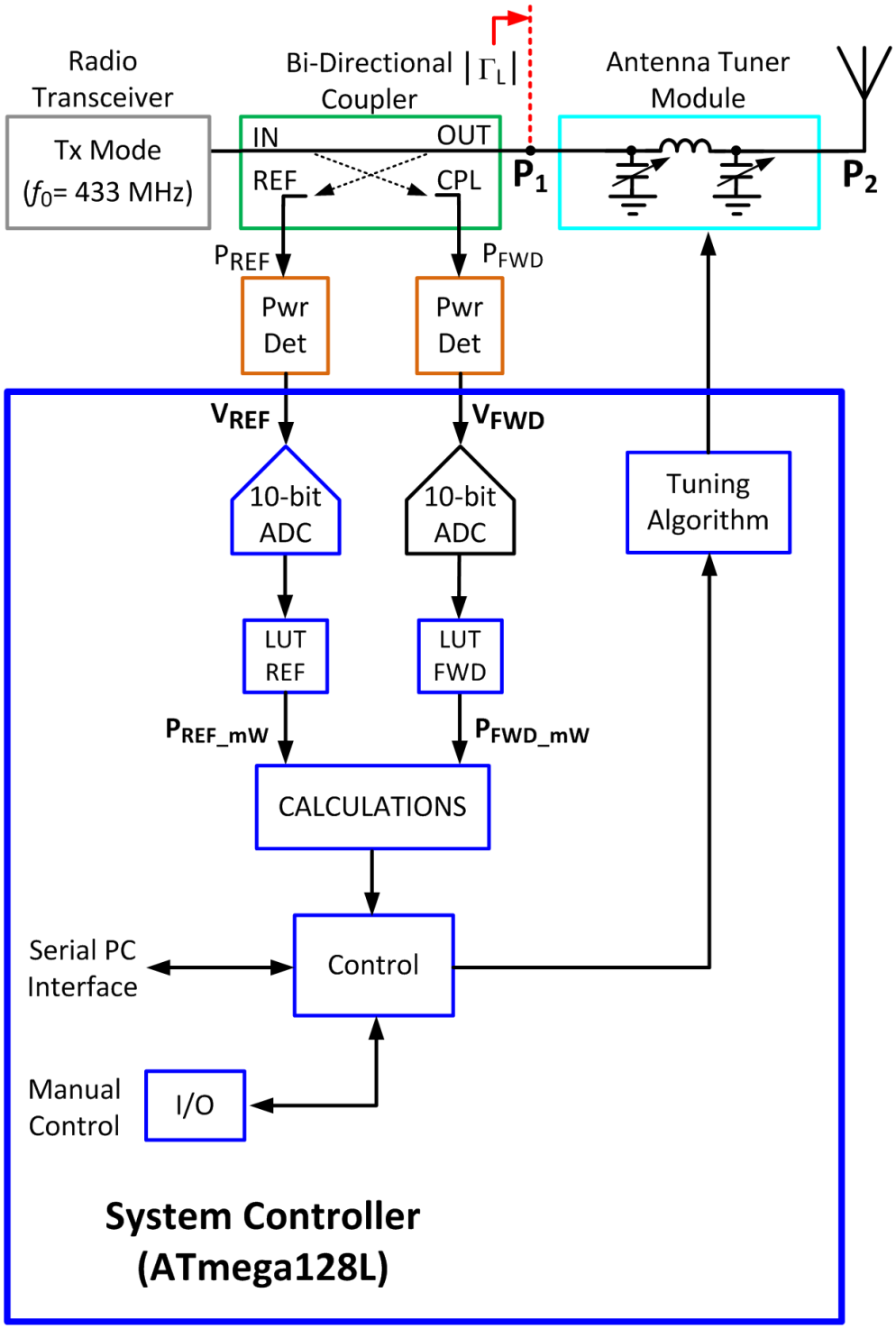


Figure 4-17 Block diagram of antenna tuner system

The coupler provides a sample of the coupled forward power P_{FWD} as well as the coupled reflected power P_{REF} from P_1. The coupled forward and reflected powers are then measured using two commercial ZX47-55 RF power detectors from Mini-Circuits [146]. These detectors have a wide bandwidth of 10 MHz to 8 GHz, with a dynamic range of -55 dBm to +20 dBm with a maximum VSWR of 1.05:1. The power detector outputs are then digitized by the system controller using two, on-chip, 10-bit analog to digital converters (ADC). The system controller is implemented using a low-power, high-performance, 8-bit RISC based AtMega128L microcontroller from Atmel [86]. During initial calibration, the power detector outputs are pre-calibrated from physical measurements to generate lookup table (LUT) values to allow the values of P_{FWD} and P_{REF} to be determined.

The test setup for characterization of the RF power detectors is shown in Figure 4-18. RF input power was applied to each of the power detectors individually using a Rohde & Schwarz SML-03 [147] signal generator (A) and a 50 Ω coaxial cable (B) as shown. The output voltage (C) of the power detectors (D) was measured using the 10-bit ADCs for V_{FWD} and V_{REF} for RF input power levels varying from -60 dBm to +10 dBm as measured using a Rohde & Schwarz FSUP Signal Source analyzer [144]. The measured responses of the two power detectors are shown in Figure 4-19. The negative slope of these detectors shows that the detector output voltage decreases for increasing RF input power. The measured data was then used to generate LUT values for RF power versus measured voltage and this data was then stored in firmware on the system controller (E). The LUT was then used in firmware to compute values for P_{FWD} and P_{REF} in the final system. Once the values of P_{FWD} and P_{REF} are known, the magnitude of the reflection coefficient $|\Gamma_L|$ at P_1 is then calculated using (2.9). Other measurement parameters of interest such as VSWR and Mismatch Loss can then be readily derived and knowledge of $|\Gamma_L|$ enables the tuning algorithm to determine when the matching network has been adjusted for minimum reflection.

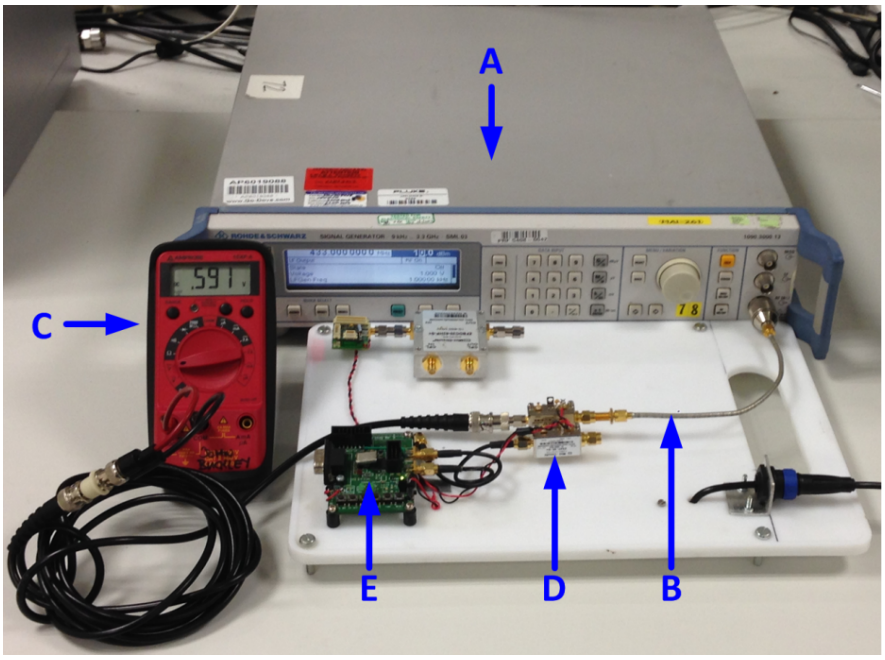


Figure 4-18 Test setup for RF power detector characterization

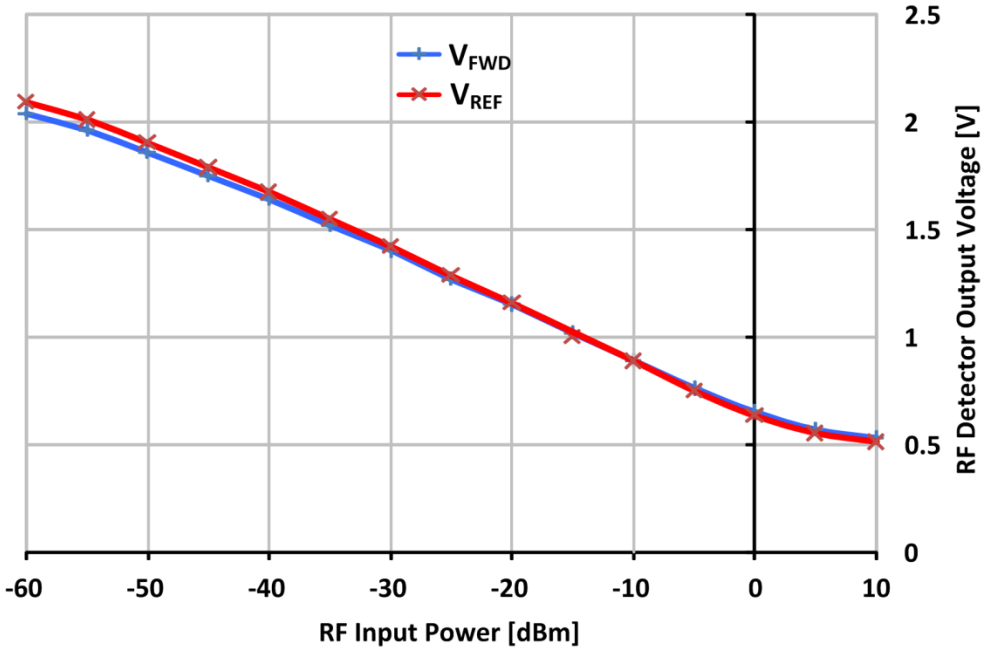


Figure 4-19 Measured power detector response

4.4 Prototype and Measured Results

A photograph of the prototype antenna tuner system is shown in Figure 4-20. The system controller interfaces with the tuner module and other system components as shown and performs S_{11} measurements and tuning control as well as data transfer to a PC for display and analysis.

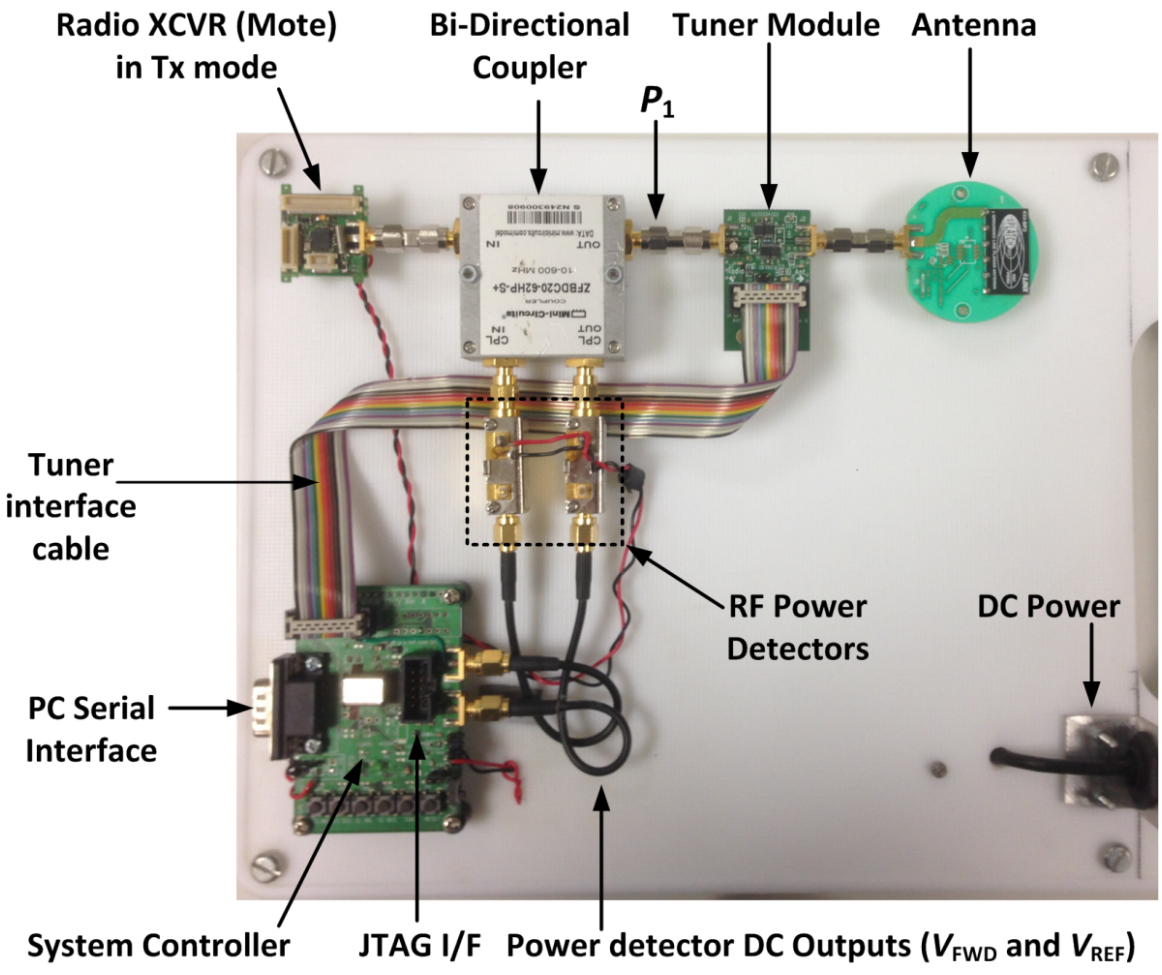


Figure 4-20 Photograph of antenna tuner system

In order to test the accuracy of the measurement system, the load VSWR (at Port P_1) was swept from a value of 1:1 to 10:1 using a Maury model 1878G triple-stub tuner [148] that was connected to P_1 in Figure 4-20 instead of the tuner module and antenna. For each value of load VSWR, the S_{11} parameter was measured using the prototype system denoted $|S_{11A}|$ followed by a calibrated VNA measurement denoted $|S_{11B}|$ on the same triple-stub tuner. All measurements were performed at a frequency of 433 MHz and Table 4-1 tabulates the results. The prototype S_{11} measurements agree with the VNA measurements to within 0.3 dB or less across a wide range of load VSWR values. However, for values of VSWR close to 1:1, the measurement error increased significantly and is attributed to the finite directivity of the bi-directional coupler or 25 dB in this case.

Load VSWR	**Prototype**	**VNA**	**Error**
	$\|S_{11A}\|$ (dB)	$\|S_{11B}\|$ (dB)	$\|S_{11B}\|$ - $\|S_{11A}\|$ (dB)
1:1	-33.01	-30.26	2.75
1.5:1	-14.01	-14.11	-0.10
2:1	-9.08	-9.27	-0.19
4:1	-4.54	-4.38	0.16
6:1	-3.03	-2.85	0.18
8:1	-2.43	-2.16	0.27
10:1	-1.99	-1.73	0.26

Table 4-1 S_{11} accuracy measurements for the antenna tuner system

4.5 Design of Tuner Module

This section describes the design of the *Π*-type antenna tuner module used in the prototype system. The matching network is realized using an array of binary-weighted, switched capacitances. The use of CMOS Silicon-On-Sapphire (SOS) PE4210 RF switches [149] is investigated as a means of implementing a digitally controllable capacitor bank in order to realize a reconfigurable antenna tuner. Unlike tuners implemented using discrete components such as *PIN* diodes [150] or Varactor diodes [100] that require additional mixed-signal circuitry and increased DC power consumption, these devices require very little DC power which is desirable for WSN applications. The RF switches that were used for this application are PE4210, SOS single-pole-double-throw (SPDT) based discrete devices that operate from DC to 3 GHz [149]. These components were chosen primarily due to their low insertion loss, high isolation and linearity. In addition, these devices have extremely low power consumption and require a DC supply current of less than 0.001 mA which is a key advantage for low power wireless sensor applications.

Figure 4-21 shows a simplified schematic of the reconfigurable, *Π*-type matching network which is placed between the source impedance Z_S and the antenna impedance Z_A. In this case, capacitors C_S and C_L in Figure 4-21 provide the tuning capability and a high-Q inductor (Q_L = 50) 0603WL170JT from American Technical Ceramics [143] was chosen. A more detailed view of the source-side tunable capacitance C_S is also shown and was implemented using four, discrete RF switches, SW_0 to SW_3, and four binary-weighted capacitances, C_{S0} to $8C_{S0}$ as shown that are discussed in more detail later in this section. The SPDT switch enables the common pin (RFC) to be switched between either of the two other pins (RF1 or RF2). The 4-bit implementation provides a total of $N = 2^4 = 16$ individual tuning combinations for each capacitance C_S and C_L, or 256 combinations in total for the two capacitances.

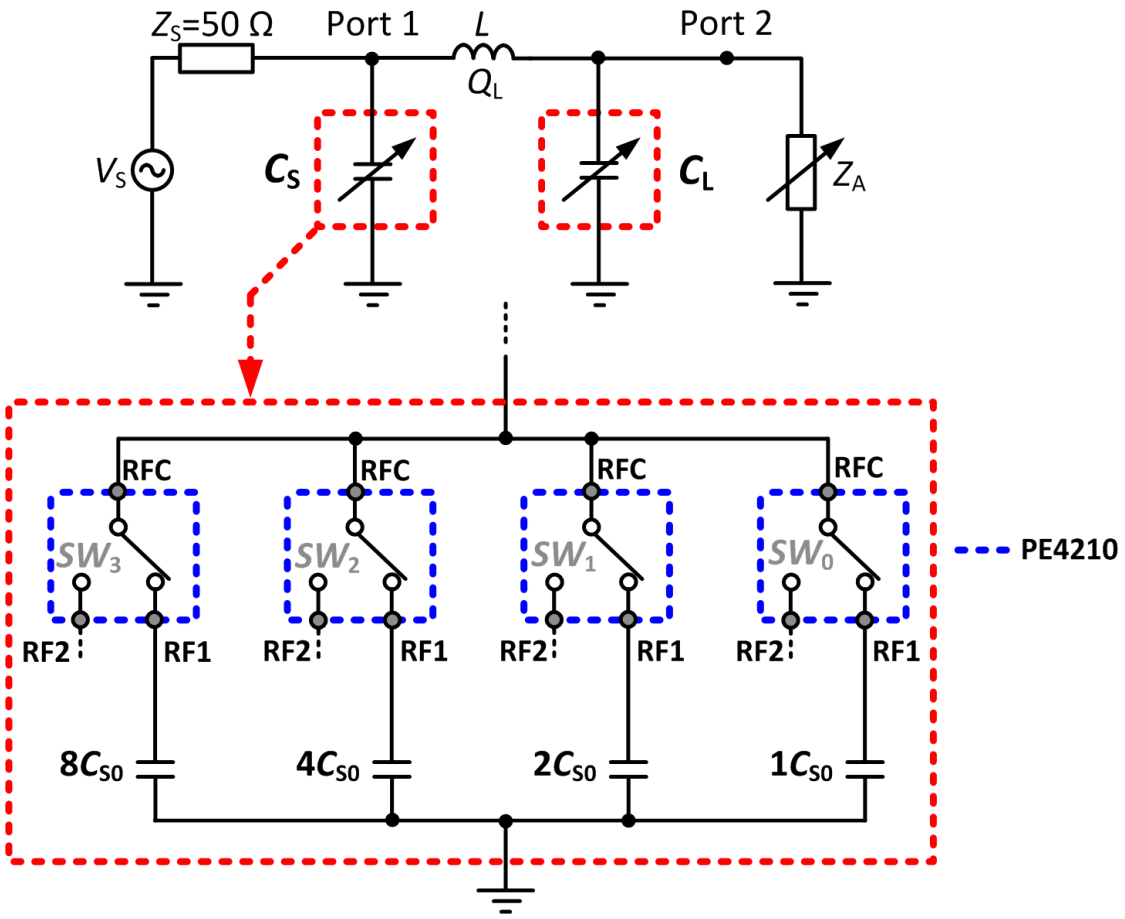


Figure 4-21 Simplified tuner schematic and details of tunable capacitor implementation

In Figure 4-21, the switches are shown as idealized, lossless elements with no switch or package parasitics but, in reality, there are a number of parasitics associated with the device. A functional model of the PE4210 switch is shown in Figure 4-22 (a). The RFC pin connects to either RF1 or RF2 depending on the logic state of the CTRL signal (1 = H, 0 = L). With CTRL = 1, denoted the ON-state as shown in Figure 4-22 (b), the RFC pin is connected to the RF1 pin. The RF1 pin is in turn, connected to an external capacitor C_{EXT}, representing a binary weighted capacitance. The RF2 pin is not connected externally. Resistor R_{ON} denotes the parasitic resistance of the switch in the ON-state and L_P denotes the bond-wire inductance associated with each of the three RF pins internal to the 8-lead MSOP package [149].

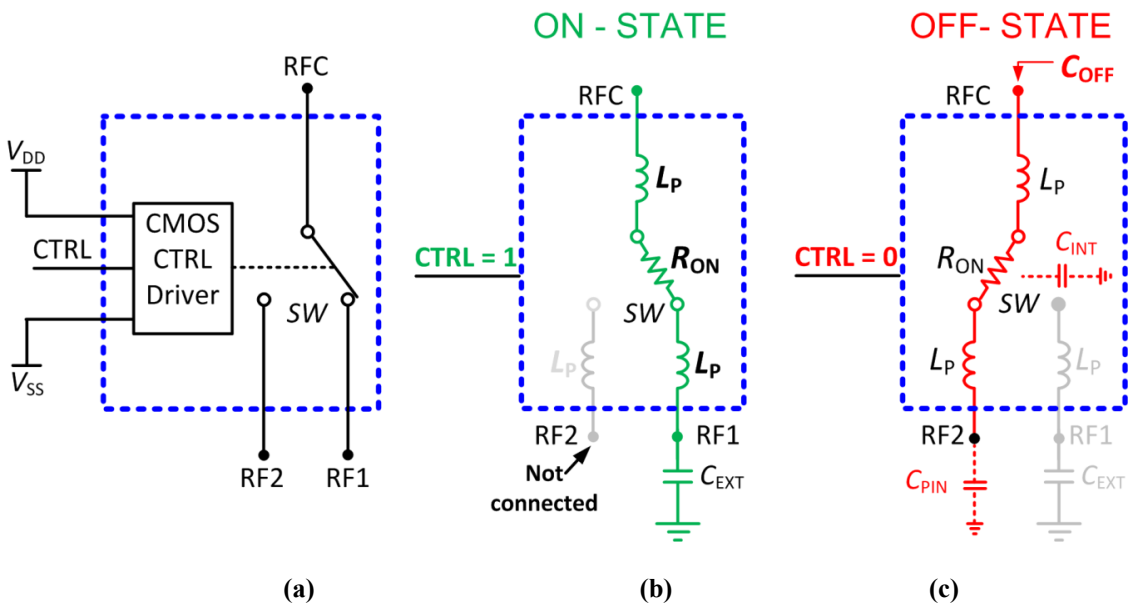


Figure 4-22 RF switch (a) Functional view, (b) ON-parasitics, (c) OFF-parasitics

In the opposite switch state when CTRL = 0, denoted the OFF-state as shown in Figure 4-22 (c), the RFC pin now connects to the RF2 pin. Capacitance C_{OFF} is used to denote the total capacitance that arises internal to the device (C_{INT}) in addition to the external package capacitance associated with the RF2 pin, C_{PIN}, and the capacitance of the surface mount PCB pad for this pin. Device parameters L_P, R_{ON} and C_{OFF} were measured using the test fixture shown in Figure 4-23. The PCB was implemented on an FR-4 substrate of thickness t_{SUB} = 1.6 mm with ε_R = 4.5 and $tan\delta$ = 0.02 [137] and a 4-layer stackup with details in [151]. A short-open-load (SOL) calibration structure was designed to allow a 1-port VNA measurement to be made directly at the RFC pin of the PE4210 RF switch. The RF1 pin was short-circuited to V_{SS} to enable R_{ON} and the total package inductance of $2L_P$ to be measured with CTRL = 1. The RF2 pin was left disconnected to allow the off-capacitance of the switch C_{OFF} to be measured with CTRL = 0. A DC supply voltage of V_{DD} = 3.0 V was applied to the device during the measurements and is the same voltage as the regulated supply on the tuner system. A SOL calibration was first performed from DC to 500 MHz using the calibration structures shown.

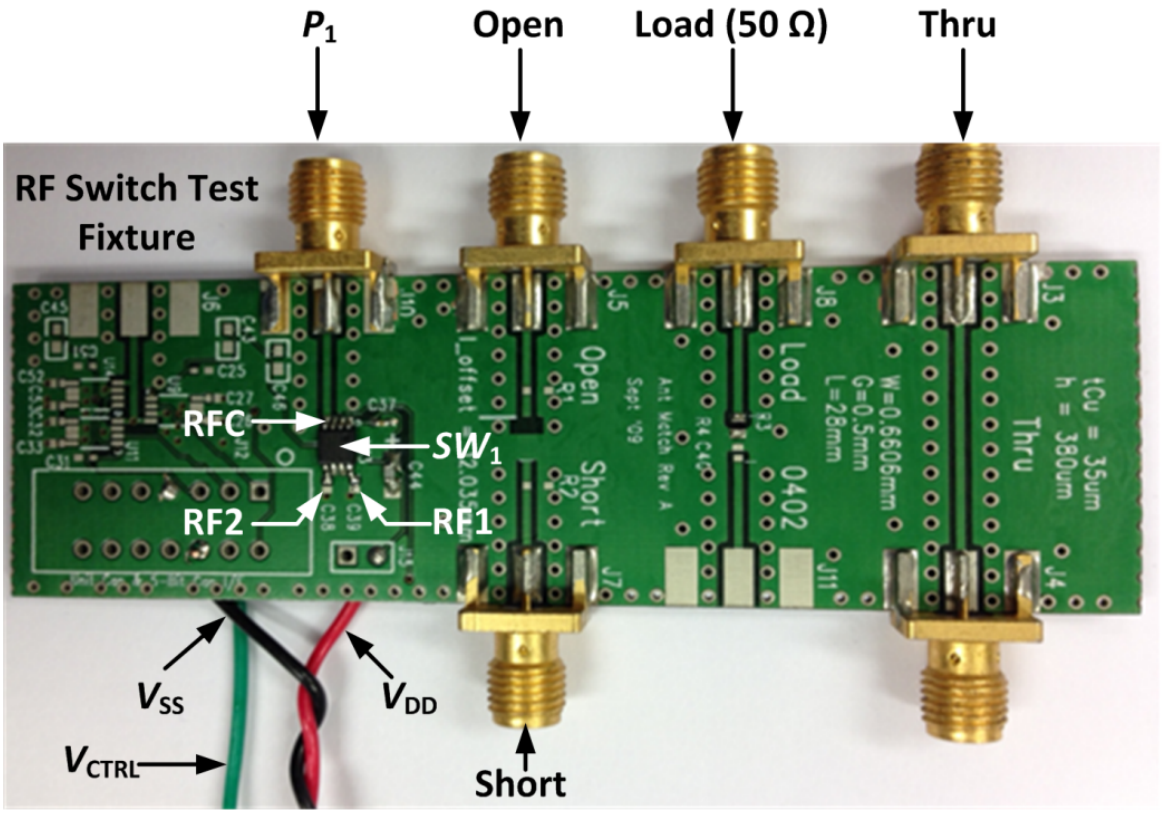


Figure 4-23 Test fixture to measure RF switch parasitics

A 1-port S-Parameter measurement was then performed for both the ON and OFF states using a Model ZVRE Rohde and Schwarz VNA [47] that was connected to port P_1 using a 50 Ω coaxial cable. The resulting S-parameter measurements are de-embedded to the RFC pin of the RF switch. The measured results are shown in Figure 4-24 where the frequency was swept from 9 kHz to 500 MHz and the measured impedance profiles for the ON (green) and OFF (red) cases are shown. The corresponding values of R_{ON} and L_P were determined from the measured impedance value at 433 MHz in the ON state. Similarly, the value of C_{OFF} was extracted from the measured impedance in the OFF-state also measured at 433 MHz. The final values for the extracted parameters are listed in Table 4-2.

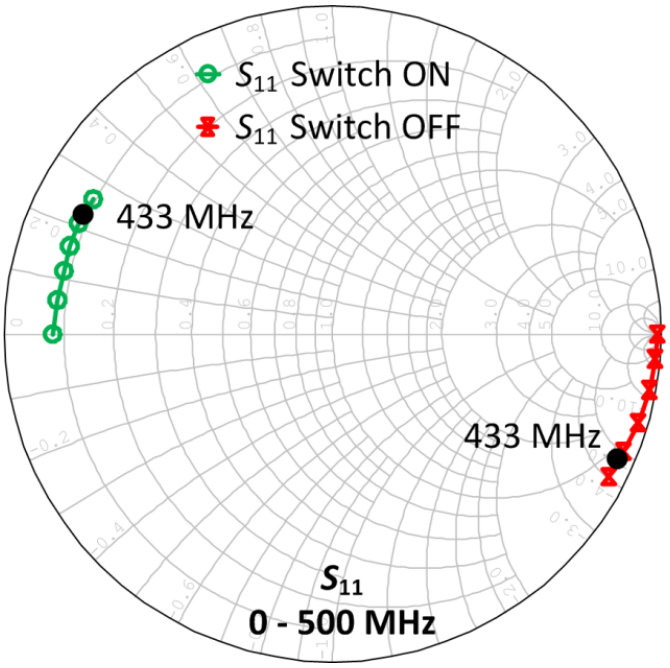


Figure 4-24 Measured S_{11} of RF switch in ON and OFF states

Parameter	Extracted switch parasitics (433 MHz)	Unit
R_{ON}	4.4	Ω
C_{OFF}	1.9	pF
L_P	2.1	nH

Table 4-2 Summary of PE4210 RF switch parasitics

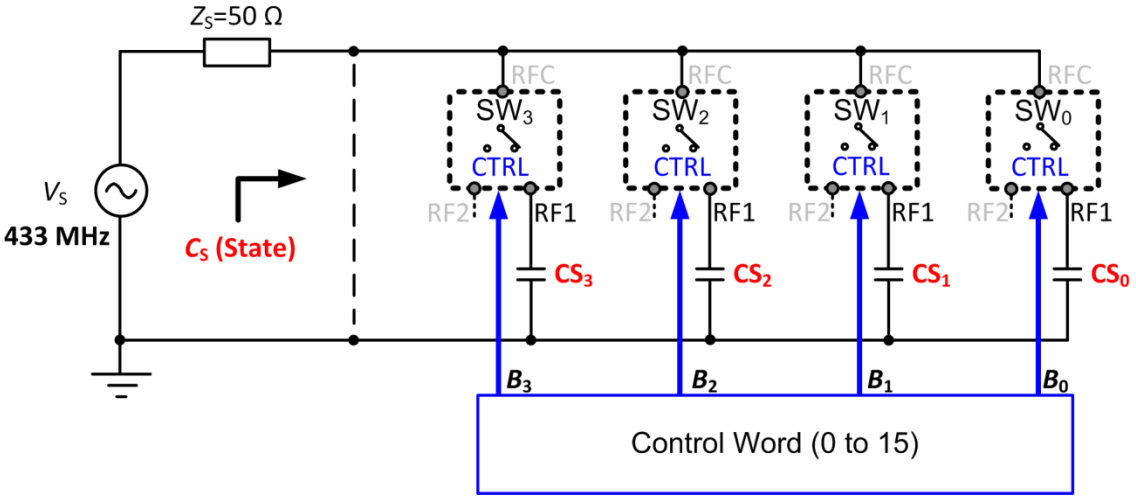


Figure 4-25 Simulation model for the 4-bit tunable capacitor C_S

A circuit model was created in ADS [44] to simulate a 4-bit tunable capacitor as shown in Figure 4-25. The four switches are modelled using the sub-circuits SW_0 to SW_3. These sub-circuits model the RF switch in both the ON and OFF-states defined in Figure 4-22 (b) and (c) along with the parasitic values of Table 4-2. During simulation, the four switch CTRL inputs are driven by a 4-bit control word or counter to provide 16 different switch states (0 to 15) as shown. Four binary-weighted capacitances CS_0 to CS_3 are shown connected to the RF1 pins for SW_0 to SW_3. These values were determined iteratively in simulation to yield a linearized variable capacitance as a function of the switch states at a frequency of 433 MHz and are listed in Table 4-3. Note that if the parasitic capacitances were all zero, this would lead to an ideal binary-weighted set of capacitance values.

Model capacitance parameter	Value (pF)
C_{S0}	1.0
C_{S1}	2.0
C_{S2}	3.9
C_{S3}	6.3

Table 4-3 Simulated capacitance values for CS_0 to CS_3

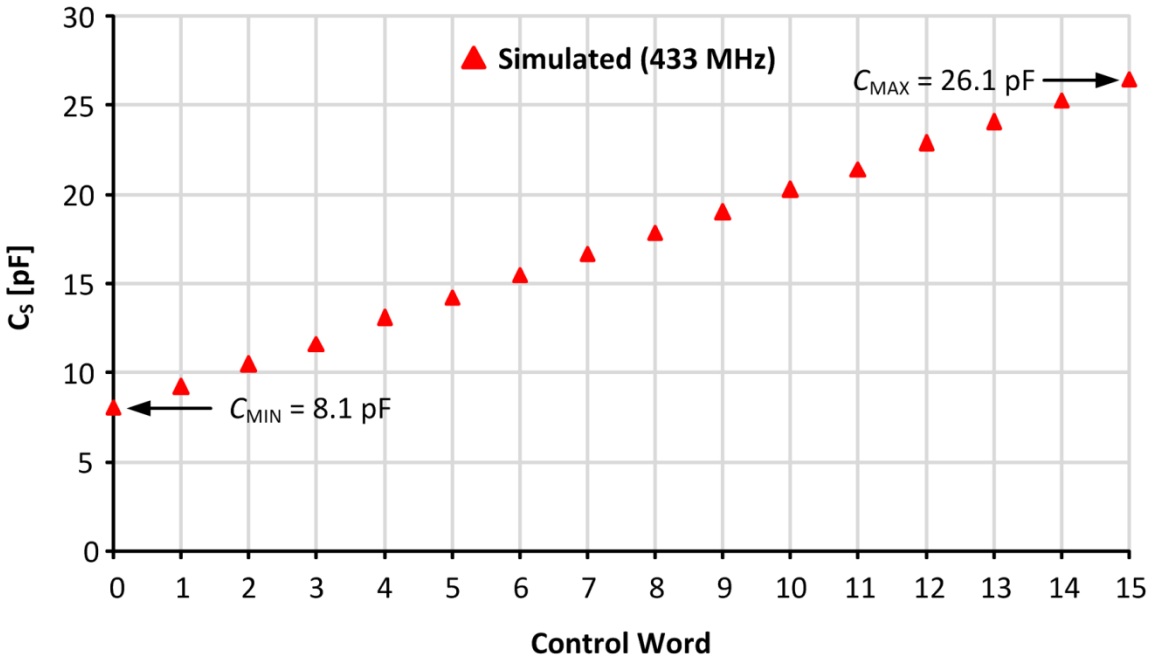
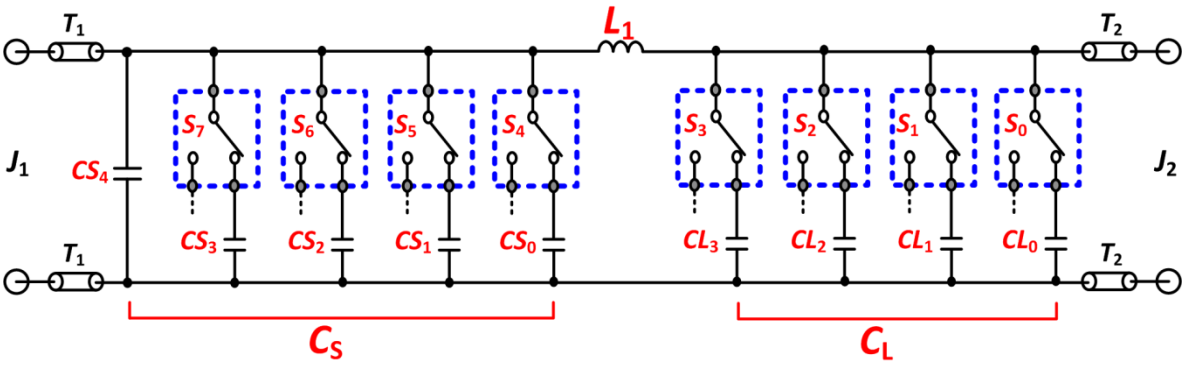
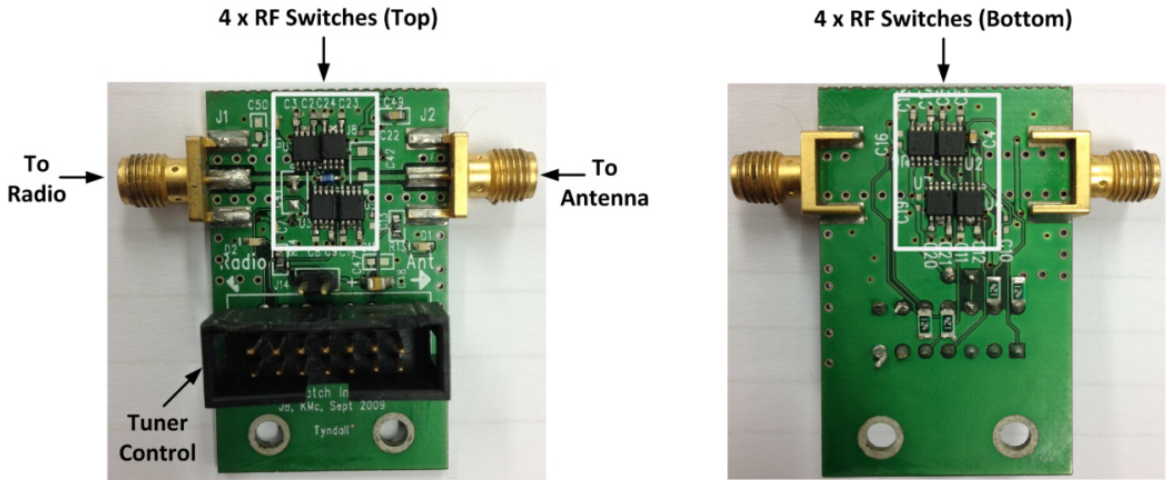


Figure 4-26 Simulated capacitance C_S versus control word

The simulated capacitance C_S is shown in Figure 4-26. The tunable capacitor produces a linear response that varies from C_{MIN} = 8.1 pF in state 0 to C_{MAX} = 26.1 pF in state 15, i.e. a tunable range of 18 pF. It is also observed that C_{MIN} is approximately $4C_{OFF}$. The value of C_{OFF} sets an important lower limit for the minimum capacitance that can be achieved using the 4-switch design. In order to validate the design, a tuner module was designed to allow the value of C_S to be measured as well as implementing a Π-type antenna tuner. A schematic of the tuner module is shown Figure 4-27 (a). A source capacitance C_S of 27.4 pF is required to match the detuned antenna impedance. The maximum achievable capacitance of the 4-bit capacitor was limited to 26 pF approximately, therefore an extra fixed capacitance CS_4 = 10 pF was added to the source-side to set the mid-scale value of C_S to approximately 27 pF and enabling a relative tuning range of +/- 9 pF about the mid-scale value.



(a)



(b)

Figure 4-27 Prototype tuner, (a) Schematic, (b) Prototype

The tuner module PCB was implemented on the same panel as the SOL test fixture PCB and has identical material [137] and stackup properties [151]. A schematic of the tuner is shown in Figure 4-27 (a) and a photograph of the prototype is shown in Figure 4-27 (b). The associated tuning component values for the prototype tuner module are listed in Table 4-4.

Component	Value	Unit	Manufacturer	Part Number	Reference
CS_0, CL_0	1.0	pF	ATC Ceramics	600L1R0JT	[152]
CS_1, CL_1	2.0	pF	ATC Ceramics	600L2R0JT	[152]
CS_2, CL_2	3.9	pF	ATC Ceramics	600L3R9JT	[152]
CS_3, CL_3	6.3	pF	ATC Ceramics	600L6R3JT	[152]
CS_4	10	pF	ATC Ceramics	600L200JT	[152]
L_1	17	nH	ATC Ceramics	0603WL170JT	[143]

Table 4-4 Prototype tuner component values

4.5.1 *Tuner Module Capacitance Measurements*

Figure 4-28 shows the measured and simulated values of C_S for the 4-bit tunable capacitor. Note that a 1-port SOL (Short-Open-Load) calibration at 433 MHz was performed as described earlier. For this measurement, inductor L_1 and capacitor CS_4 were removed from the circuit such that the only contribution to the measured capacitance is due to CS_0 to CS_3. It can be seen in Figure 4-28 that the measured and simulated capacitance has a linear response from states 0 to 7 but a deviation is observed for states 8 to 15. This effect is caused by a small mismatch in the total on-capacitance for the least-significant three bits of C_S compared to the on-capacitance of most-significant bit. In this case, a standard component value of 6.3 pF was used for the most-significant bit CS_3 but the response can be further linearized from states 8 to 15 by further fine-tuning the values of CS_0 - CS_3. It can also be observed that the measured capacitance C_S ranges from a value of C_{MIN} = 7.65 pF to a value of C_{MAX} = 27.6 pF, measured at 433 MHz.

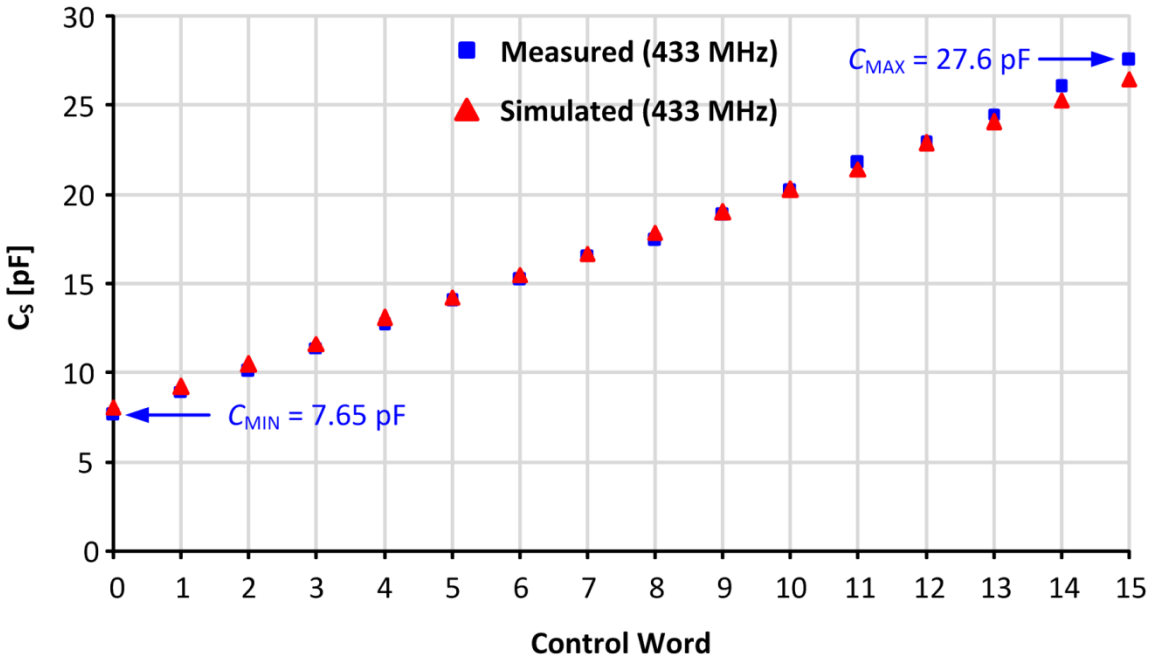


Figure 4-28 Comparing measured and simulated 4-bit capacitance *C*S

The programmable capacitance C_L is implemented in the same manner as C_S and uses the same components and layout and is thus expected to show the same performance characteristics as C_S but in this case, a fixed capacitance is not required.

4.6 Tuning Algorithm

The system controller is used to implement a tuning algorithm as illustrated in Figure 4-29. The system controller interfaces with the tuner module via the 8-bit TUNE_CTRL register that simultaneously writes 4-bit switch control words to capacitor arrays C_S and C_L. During a tuning command, the algorithm performs a sequential search for values of C_S and C_L that minimize the measured antenna S_{11} value. The tuning algorithm first assumes a worst case reflection coefficient for the antenna or $|\Gamma_{MAX}| = 1$. Since the number of discrete capacitances $nc = 8$, a sequential search of $N = 2^{nc} = 256$ states is performed.

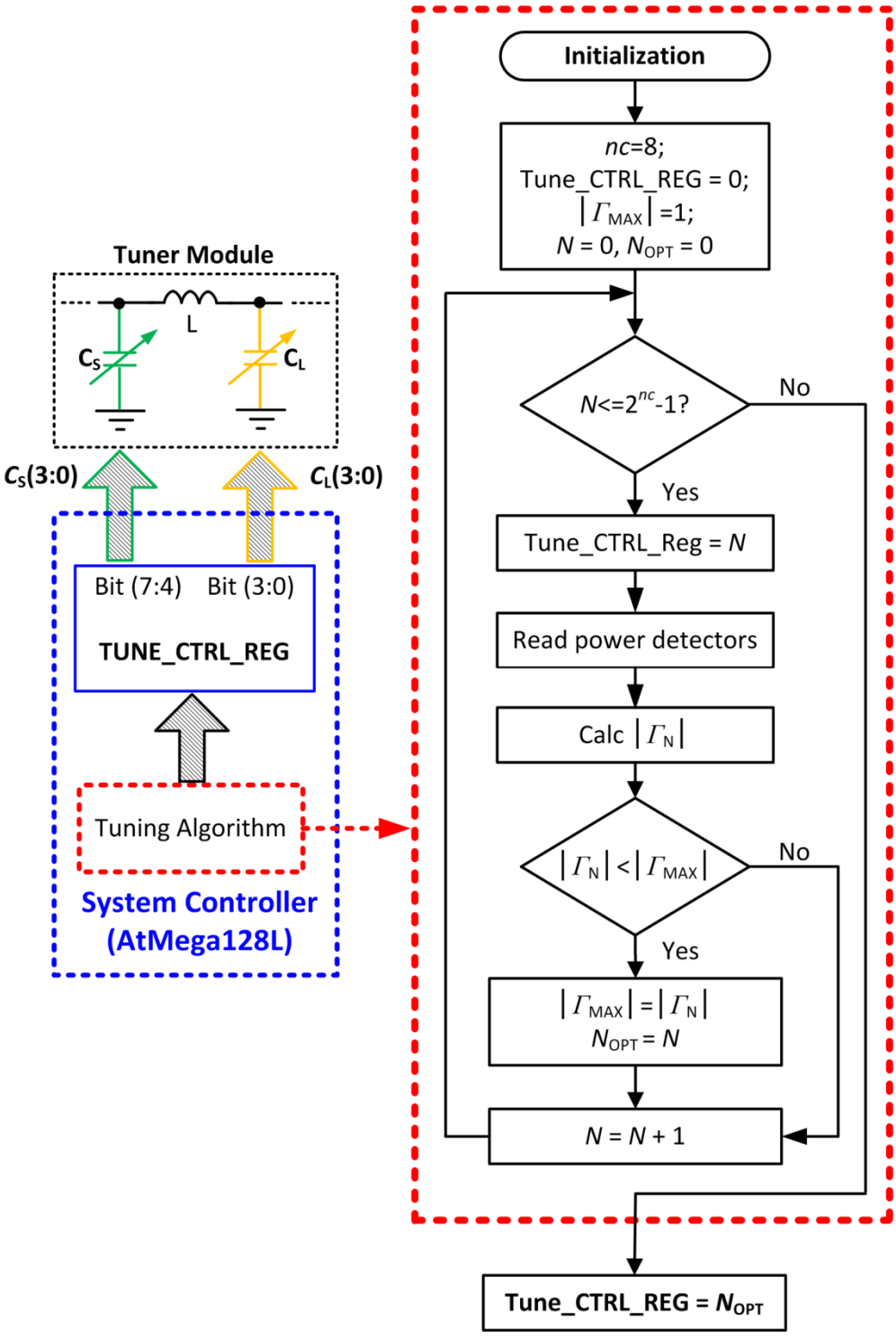


Figure 4-29 Flow chart of the antenna tuning algorithm

For each state, the current value N is written to the capacitor bank via register TUNE_CTRL_REG to select the desired capacitor combinations. The power detector outputs are then read and the lookup tables are used to determine the values of P_{FWD} and P_{REF} from which the value of $|\Gamma_N|$ is determined. The algorithm sequentially searches all 256 states to determine the optimal state N_{OPT} that minimizes $|\Gamma_N|$. At the end of the tuning process, the optimum state TUNE_CTRL_REG is then written to the capacitor bank. Other types of tuning algorithm may be easily implemented by modifying the embedded code within the microcontroller.

4.6.1 *Graphical User Interface*

Control and monitoring of the tuner is achieved using the Graphical User Interface (GUI) shown in Figure 4-30 and is implemented in Labview® [53]. The GUI displays real-time parameters such as measured coupler power levels, antenna VSWR, reflection coefficient magnitude and mismatch loss by communicating directly with the microcontroller using the PC serial interface. Figure 4-30 shows the case where a finger is placed on the antenna to detune it and the tuning algorithm is then executed.

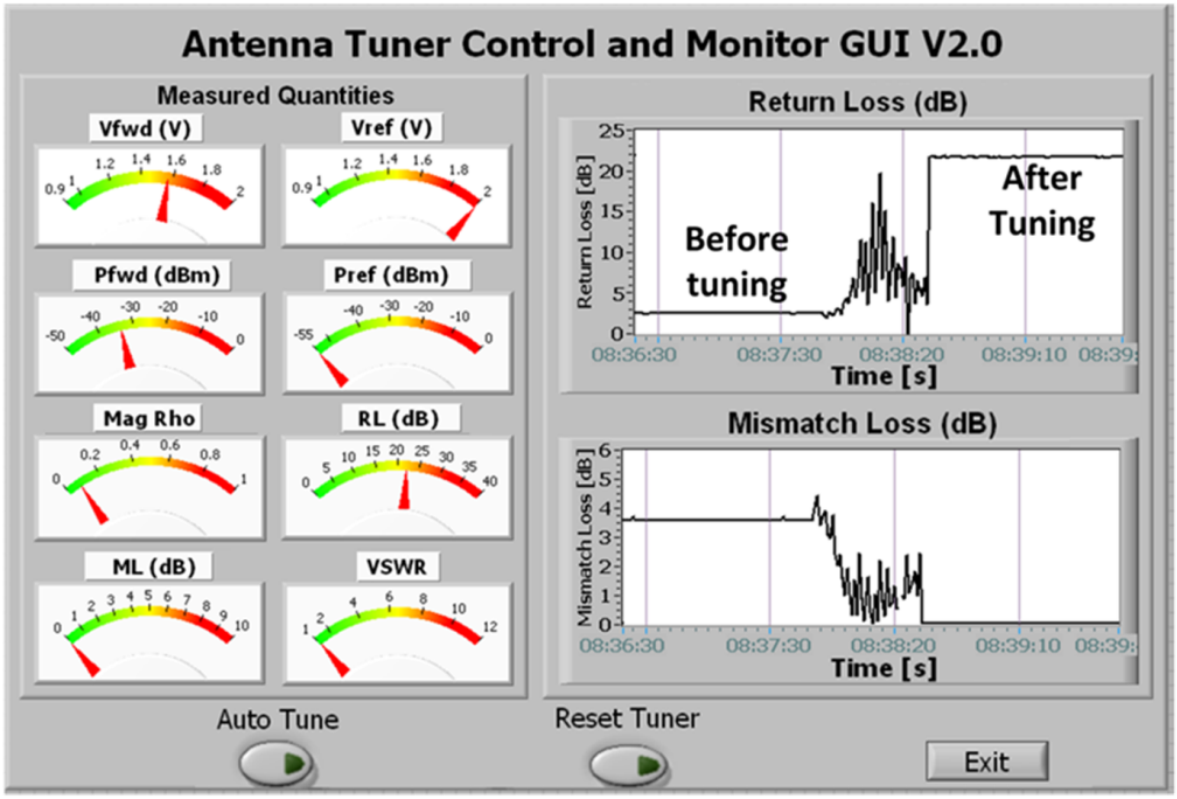


Figure 4-30 Screenshot of the antenna tuner GUI

When the tuning algorithm is executed, the antenna tuning process can be observed in real-time directly from the hardware by monitoring the V_{REF} signal and an oscilloscope trace of the tuning process is shown in Figure 4-31. It can be seen that prior to tuning the antenna (Point A), V_{REF} is at a minimum, denoting maximum reflected power P_{REF} from the input of the tuner. Once initiated, the tuning algorithm sequentially monitors the V_{REF} signal for all 256 switch combinations. The maximum value of V_{REF}, corresponding to minimum reflected power from the antenna, occurs after a time of approximately 150 ms. When the search sequence is completed at Point B, the tuning algorithm sets the tuner state for minimum reflected power using the previously determined optimal codeword corresponding to the capacitor combination giving minimum reflected power. The maximum current consumption for the tuner module is extremely low and was measured at 0.025 mA DC while the tuning algorithm was being executed.

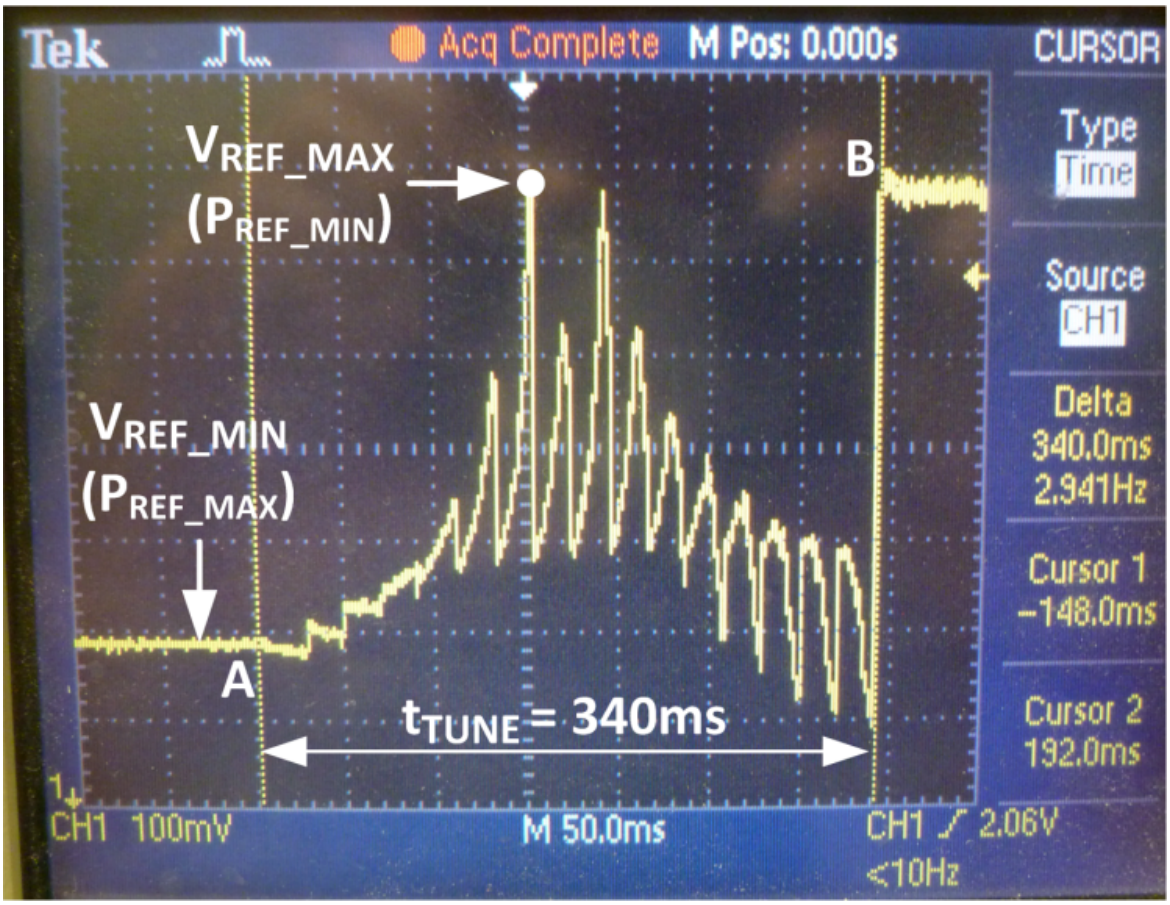


Figure 4-31 Oscilloscope measurement of V_{REF} signal during tuning

The DC current consumption of the individual functional modules was measured during execution of the tuning algorithm and the results are tabulated in Table 4-5. The two RF power detectors consume a total DC current of approximately 130 mA. The power detectors employed in this case are high-performance devices that allow accurate power detection over a large dynamic range of 70 dB with an 8 GHz bandwidth [146]. It is therefore possible that the most dramatic current saving can be made by the choice of lower power detectors and this possibility is investigated in Chapter 6. The radio transceiver (in *Tx* mode) consumes approximately 31 mA DC and the system controller has a peak current of approximately 20 mA while executing the tuning algorithm. This power consumption is mainly attributed to microcontroller activity during execution of the tuning algorithm

including data acquisition (256 ADC samples of RF forward and reflected power at f_{CPU} = 8 MHz), as well as data logging to the PC and LED driver activity.

Device	Peak DC Current (mA)
RF Power Detectors	127.6
Radio XCVR (TX mode, PTX = +10 dBm)	31.3
System Controller (during tuning)	19.8
Tuner Module (during tuning)	0.0025

Table 4-5 DC current consumption for individual tuner system blocks

The measured antenna S_{11} and transducer gain G_T are shown in Figure 4-32. When a finger is first placed on the antenna to deliberately detune it and the tuning algorithm is then executed, it can be observed that the tuning system correctly tunes the antenna for minimum S_{11} at a frequency of f_{S11_MIN} = 433 MHz with S_{11} ≈ -23 dB at f_{S11_MIN}.

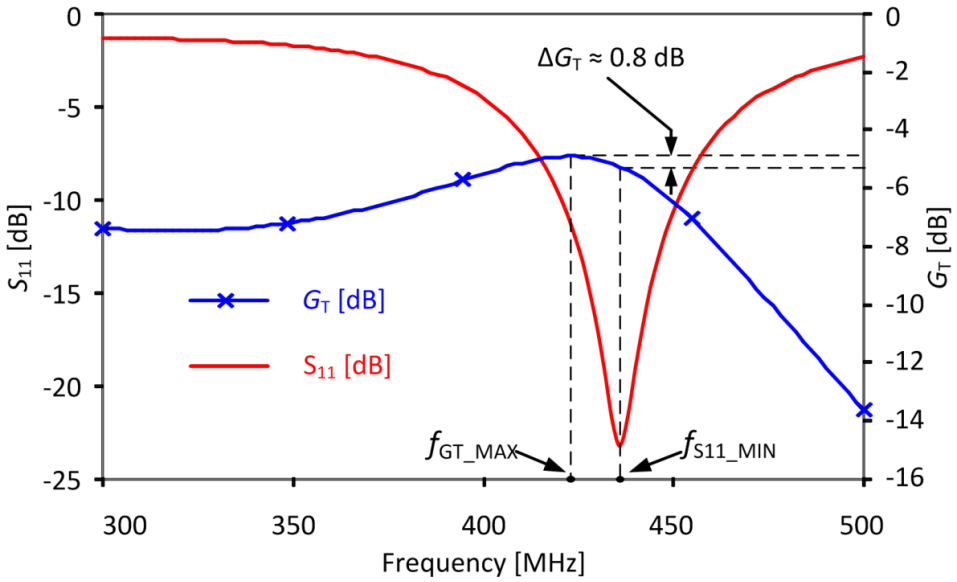


Figure 4-32 Measured S_{11} and G_T of the tuner module

The transducer gain G_T is also shown in Figure 4-32 with a measured value of 4.9 dB at 433 MHz after tuning. This value of G_T represents a significant loss. It can also be observed that maximum power is delivered to the load at a frequency less than f_{S11_MIN}.

In this case, a difference in ΔG_T of approximately 0.8 dB is observed at these two frequencies. A detailed analysis revealed that approximately 4 dB losses were attributed to the switches. It was also determined that the inductor contributes to the remaining losses of 0.9 dB. A second-generation tuner design is described in Chapter 6 that addresses the above issues by taking advantage of low-loss, high performance tunable components that have since become available.

4.7 **Conclusions**

This chapter first investigated the effects of antenna detuning caused by the presence of the human wrist on the performance of various commercial 433 MHz antennas. It was shown that antenna detuning in the presence of the human body is a significant challenge and can lead to a substantial loss in power delivered to the antenna or up to 4 dB for the AUT case considered. A number of potential benefits of using antenna tuning for BSN applications was then investigated. It was first shown, using a 433 MHz mote, that manual antenna tuning led to additional 2.7 dB of power being delivered to the antenna when compared to the unmatched case as well as a reduction of 0.4 mA in supply current. A fully automated, first-generation antenna tuning system for 433 MHz BSN applications was then demonstrated. A number of performance issues associated with RF switch and inductor losses were also highlighted as well as the requirement for higher performance tunable and fixed components. These issues are addressed in Chapter 6 with significant performance improvements demonstrated. Some of the key results of this chapter have been published in [130, 131].

Chapter 5. 433 MHz Antenna Design and Characterization

5.1 Background

This chapter presents a compact, low-cost, custom 433 MHz antenna as an alternative to commercial antenna solutions. As outlined in Chapter 3, the main limitations of commercial antennas relate to integration and performance issues as well as cost. Integration issues include the need for a specific target PCB design in order that the antenna meet the manufacturer's performance figures relating to the gain, bandwidth and radiation characteristics of the antenna. Even though a large number of commercial antennas may have a small physical size, their performance in the target application depends to a large degree on factors such as PCB size, groundplane size, PCB materials and the effects of nearby components. In practice, if the recommended groundplane size and other requirements of the manufacturer are not met, this may lead to sub-optimal performance of the antenna in the target application. A number of candidate antenna topologies reported in the literature were reviewed in Chapter 3 in terms of their suitability for 433 MHz BSN applications. However, it was determined that the reported solutions did not meet the specific requirements of the Tyndall mote. In particular, for the intended application, size considerations were paramount and required the development of a custom antenna design.

In the following section, a compact, planar antenna operating at 433 MHz is proposed. This antenna has dimensions of 51 × 28 mm including the groundplane and is printed on low-cost FR4 material. Significant size reduction is achieved using a variation of an inverted-F (IFA) configuration with a square-spiral section and rectangular patch element.

Fine-tuning of the antenna's resonant frequency is also investigated using a small capacitive stub. Sensor and radio transceiver electronics can be accommodated above the groundplane. This antenna was then used as a test case for more detailed analysis of antenna detuning behaviour in proximity to the entire human body rather than just the wrist as in Chapter 4. In addition, an equivalent circuit model of the antenna was developed to allow fast computation of total antenna impedance variation across eleven different body positions. The measured data from this analysis provided key information for the design of a tunable 433 MHz antenna that is described in Chapter 6. The antenna design outlined in this chapter was published in [153].

5.2 Antenna Design

The configuration of the proposed antenna is shown in Figure 5-1 and is printed on 1 Oz, double-sided *FR-4* substrate of thickness t_{SUB} = 1.6 mm with ε_R = 4.5 and $tan\delta$ = 0.02 [137].

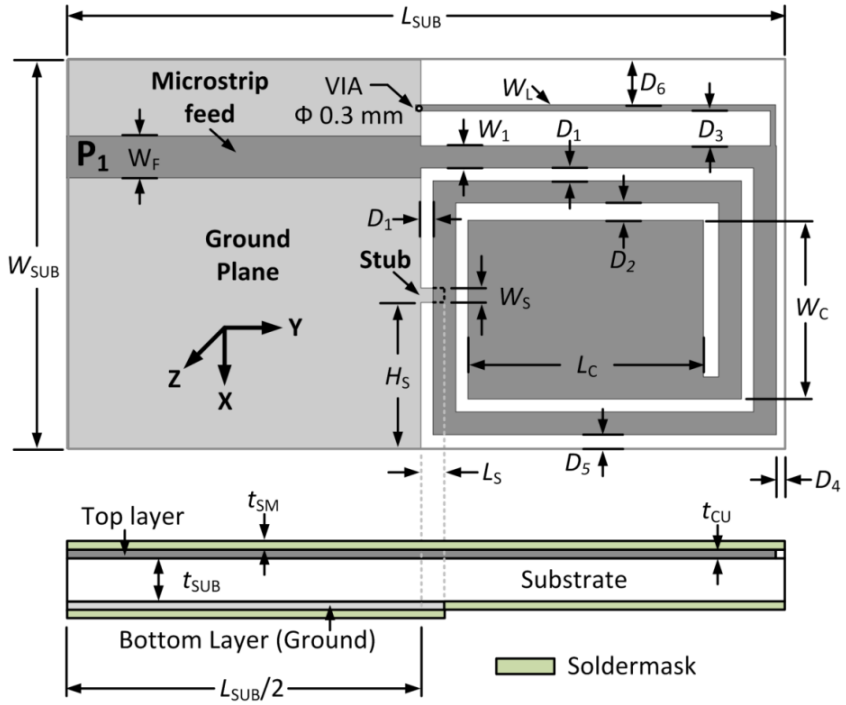


Figure 5-1 Outline of 433 MHz Antenna Topology

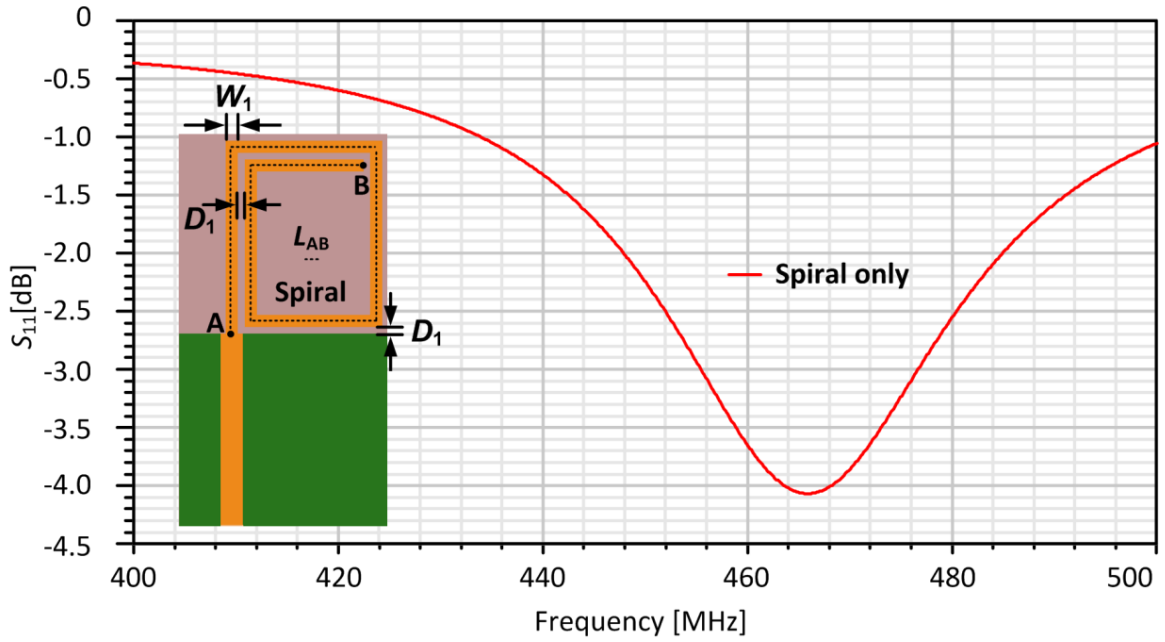


Figure 5-2 Effects of spiral element length L_{AB} on antenna resonant frequency

The antenna PCB has a size of L_{SUB} (51 mm) × W_{SUB} (27.4 mm) and is designed to be compatible with a low cost *FR-4* manufacturing process with soldermask layers on the top and bottom sides with t_{SM} = 0.1 mm, ε_R = 4.0 and $tan\delta$ = 0.02 [154]. The antenna is excited at port P_1 using a 50 Ω microstrip of length $L_{SUB}/2$ that is referenced to the groundplane on the bottom layer. The starting point for the design was the structure shown in Figure 5-2 and was analyzed using HFSS [42]. The length and width of the groundplane were chosen to be compatible with the Tyndall mote with dimensions of $L_{SUB}/2$ = 25.5 mm and W_{SUB} = 27.4 mm and were maintained at a constant value throughout with all other parameters for the configuration shown listed in Table 5-1 at the end of this section. A square spiral structure of total length L_{AB}, width W_1 = 1.5 mm and a track separation D_1 = 0.9 mm was initially specified as shown in Figure 5-2. The length L_{AB} was increased until the resonant frequency decreased to less than 500 MHz. In the configuration shown, the antenna was resonant at a frequency of approximately 475 MHz and the impedance matching is not optimal in this case with a simulated -10 dB S_{11} value of only -4 dB at 475 MHz.

To further reduce the resonant frequency, a capacitive loading method was investigated. A rectangular patch element of area $L_C \times W_C$ was next introduced as shown in Figure 5-3. The effects of varying L_C and W_C were studied in simulation and the results showed that increasing either of these two parameters led to a large decrease in the resonant frequency. In order to examine the effect of maximizing the patch area, patch dimensions of L_C = 16.56 mm and W_C = 12.62 mm were specified to maximize the area of the patch within the spiral section and maintain the trace separation values listed in Table 5-1. The simulated results of Figure 5-3 show that adding the patch element leads to a large decrease in resonant frequency from 475 MHz to approximately 432 MHz as shown. It can also be observed that the impedance matching at the resonant frequency is not affected significantly by the introduction of the patch element.

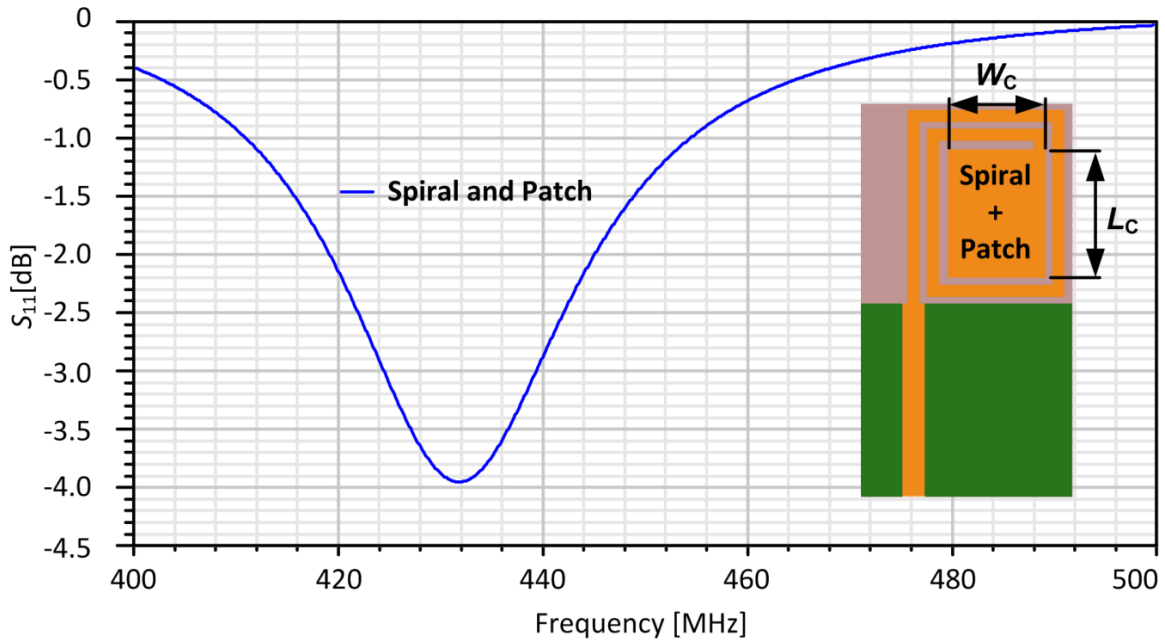


Figure 5-3 Effects of spiral and patch element on resonant frequency

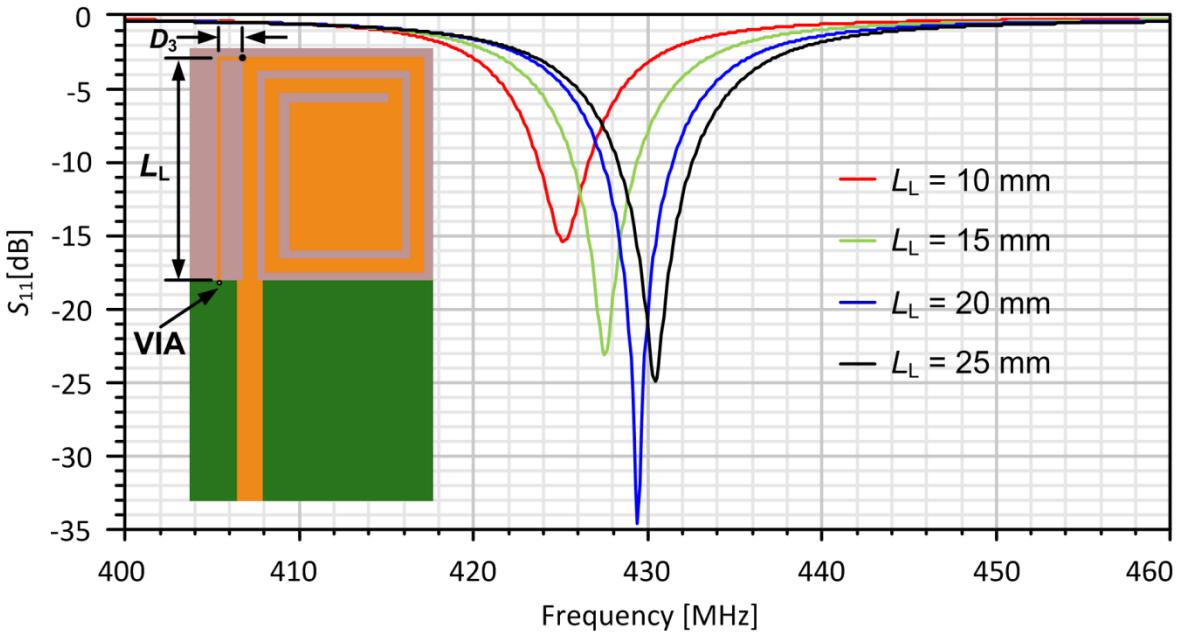


Figure 5-4 Effects of inductive length parameter L_L

In order to improve the impedance matching of the antenna, a shunt inductive element, similar to an IFA configuration, was added in order to counteract the combined capacitive reactance of the spiral and patch elements [155]. This configuration is shown in Figure 5-4. The inductive element has a length L_L, a width W_L and was placed with a spacing of D_3 from the spiral element and was connected to the ground plane on the bottom layer using a plated through-hole (PTH) via of diameter 0.3 mm. The VIA also moves with distance D_3 or along the x-axis. The value of D_3 was specified at 3.2 mm with W_L = 0.4 mm and all previous parameters unchanged. The simulated S_{11} shows that parameter L_L enables the input impedance of the antenna to be transformed to a value closer to 50 Ω with a best-case S_{11} of -35 dB achieved. In addition, the -10 dB S_{11} bandwidth increases with L_L and is maximized for L_L = 25 mm.

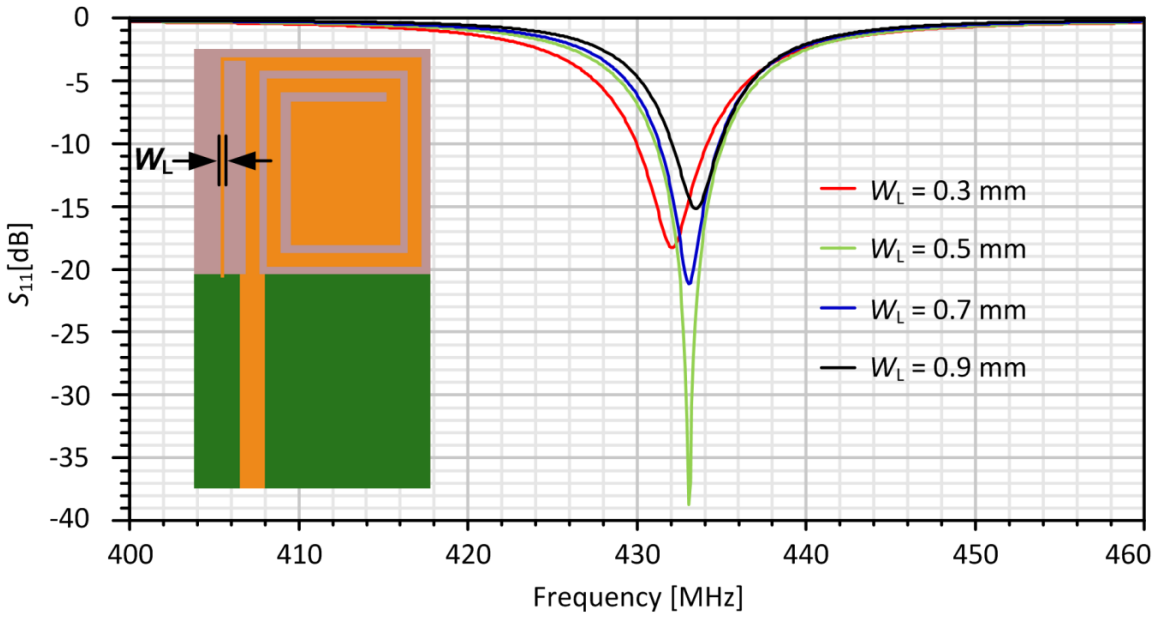


Figure 5-5 Effects of varying inductive width parameter W_L

The effects of varying the width of the inductive element W_L were next investigated while keeping parameter L_L = 25 mm and all previous parameters unchanged, with the results presented in Figure 5-5. The results show that the resonant frequency increases with increasing W_L and the input impedance of the antenna is also sensitive to this parameter. In addition, the -10 dB bandwidth increases for decreasing values of W_L.

The effects of adding a small, grounded tuning stub that was capacitively coupled to the spiral element were next investigated as a means of independently controlling the resonant frequency without affecting the antenna input impedance to a large degree as in [156]. Figure 5-6 shows the configuration with the stub positioned approximately half-way along the bottom spiral section with a distance H_S = 10.3 mm and the stub width was specified as W_S = 1.0 mm with W_L set to 0.4 mm and the other parameters as in Table 5-1.

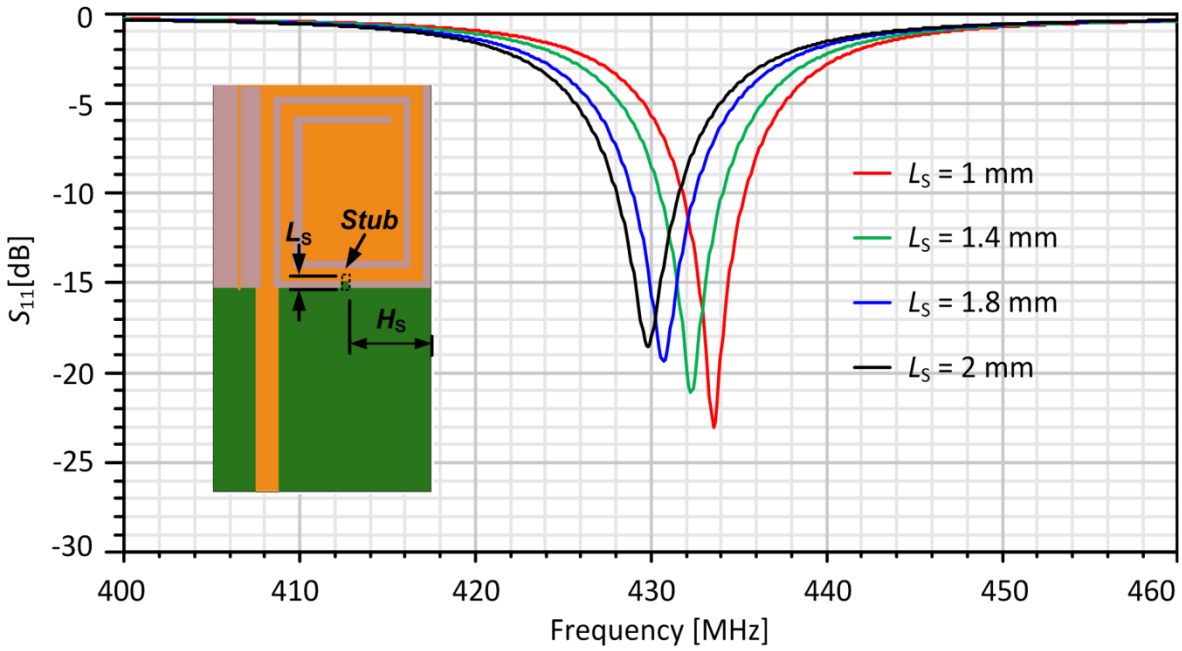


Figure 5-6 Effects of varying stub length L_S

The simulated antenna S_{11} is shown for varying stub length L_S with the results showing that the resonant frequency decreases with increasing stub length due to the capacitive loading effect of the stub. Varying the length of the stub provides a convenient means to adjust the resonant frequency of the antenna across a 4 MHz range while maintaining a value of S_{11} < -18 dB.

Figure 5-7 compares the simulated performance of the antenna with and without soldermask. Removal of the soldermask results in an increase in resonant frequency from f_0 = 433 MHz to f_0' = 448 MHz. Additional investigation of the gain characteristics of the antenna in simulation showed that removing the soldermask layer led to an increase of 1.2 dB in the value of peak realized gain from -13.8 dBi to -12.6 dBi at f_0'. This shows that the soldermask has a substantial effect both on the antenna impedance and radiation characteristics of the antenna.

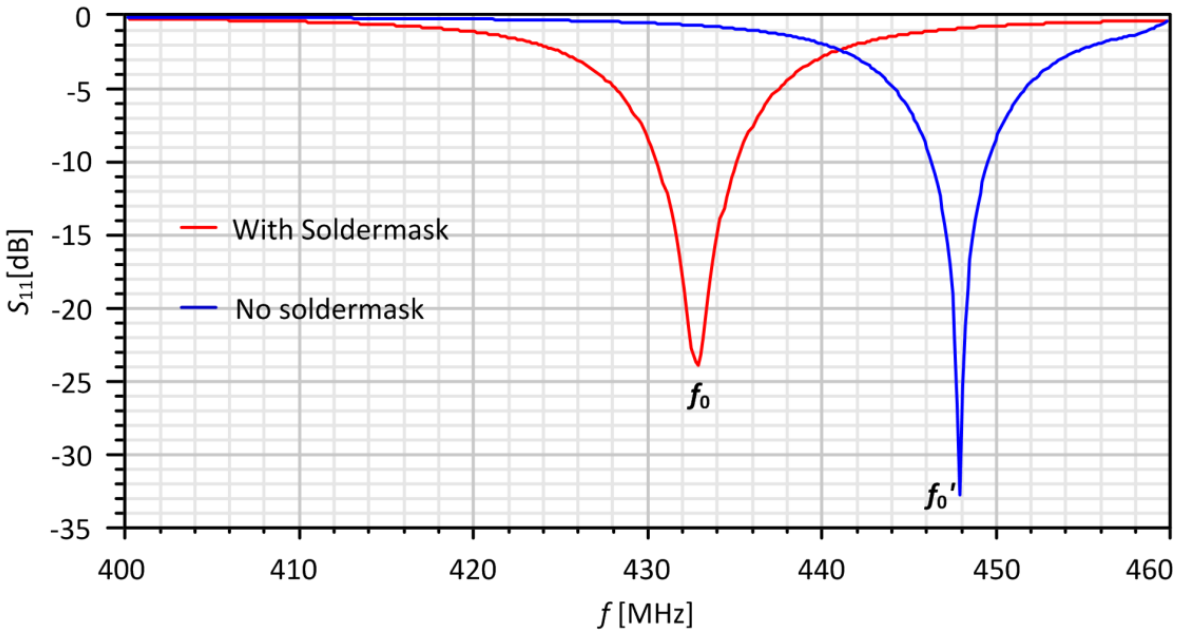


Figure 5-7 Effects of soldermask on antenna resonant frequency

The simulated surface current distribution of the final antenna design at 433 MHz is depicted in Figure 5-8. At resonance, large currents flow on the spiral and inductive sections with a smaller current flow on the capacitive stub.

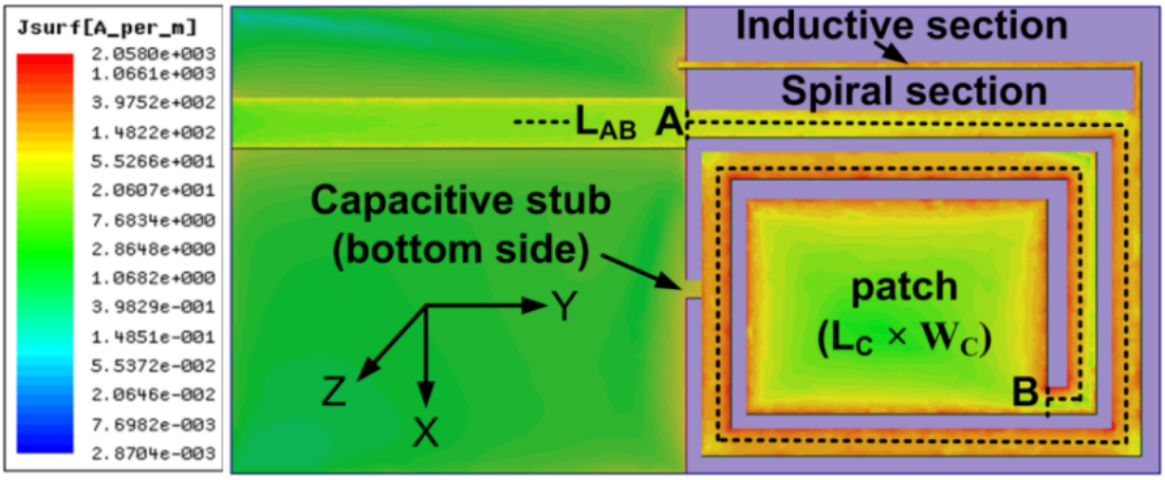


Figure 5-8 Simulated antenna surface current distribution at 433 MHz

Because this antenna is electrically small, a fundamental limit [17] exists for the achievable bandwidth and efficiency performance. Providing a good impedance match at the antenna input terminals over the specified bandwidth was a key challenge during the design and optimization phase. However, in addition to optimizing the antenna bandwidth, it is also possible in some cases, to optimize the radiation efficiency performance of an electrically small antenna assuming sufficient bandwidth exists. For example in [69], the radiation efficiency optimization of a 433 MHz 3D folded dipole antenna is described where the effects of wire diameter and material properties are investigated. It is shown that when the antenna size is maintained at a constant value, the antenna efficiency can be traded for bandwidth by adjusting the antenna geometry (wire diameter) or the material conductivity. It this work, that flexibility was not present since the bandwidth requirement was challenging to meet and the antenna design parameters were instead optimized to meet the resonant frequency and bandwidth target specifications with the final optimized antenna design parameters listed in Table 5-1.

Parameter Name	Value (mm)
L_{SUB}	51.0
W_{SUB}	27.4
W_F	2.91
W_1	1.57
W_L	0.40
L_L	25.0
W_C	12.62
L_C	16.56
W_S	1.0
L_S	1.4
H_S	10.3
D_1	0.9
D_2	1.2
D_3	2.47
D_4	1.0
D_5	1.0
D_6	3.2
Φ_{VIA}	0.3
t_{SUB}	1.6
t_{SM}	0.1
t_{CU}	0.035

Table 5-1 Optimized antenna design parameters

5.3 Antenna Prototype and Measured Results

The prototype antenna was fabricated using a commercial PCB manufacturing process [46] and a photograph of the final structure is shown in Figure 5-9. The top side of the antenna is shown in Figure 5-9 (a) and is fed using an SMA connector. The bottom side of the antenna is shown in Figure 5-9 (b) and the capacitive stub that is used for fine-tuning of the antenna's resonant frequency can be seen protruding from the groundplane.

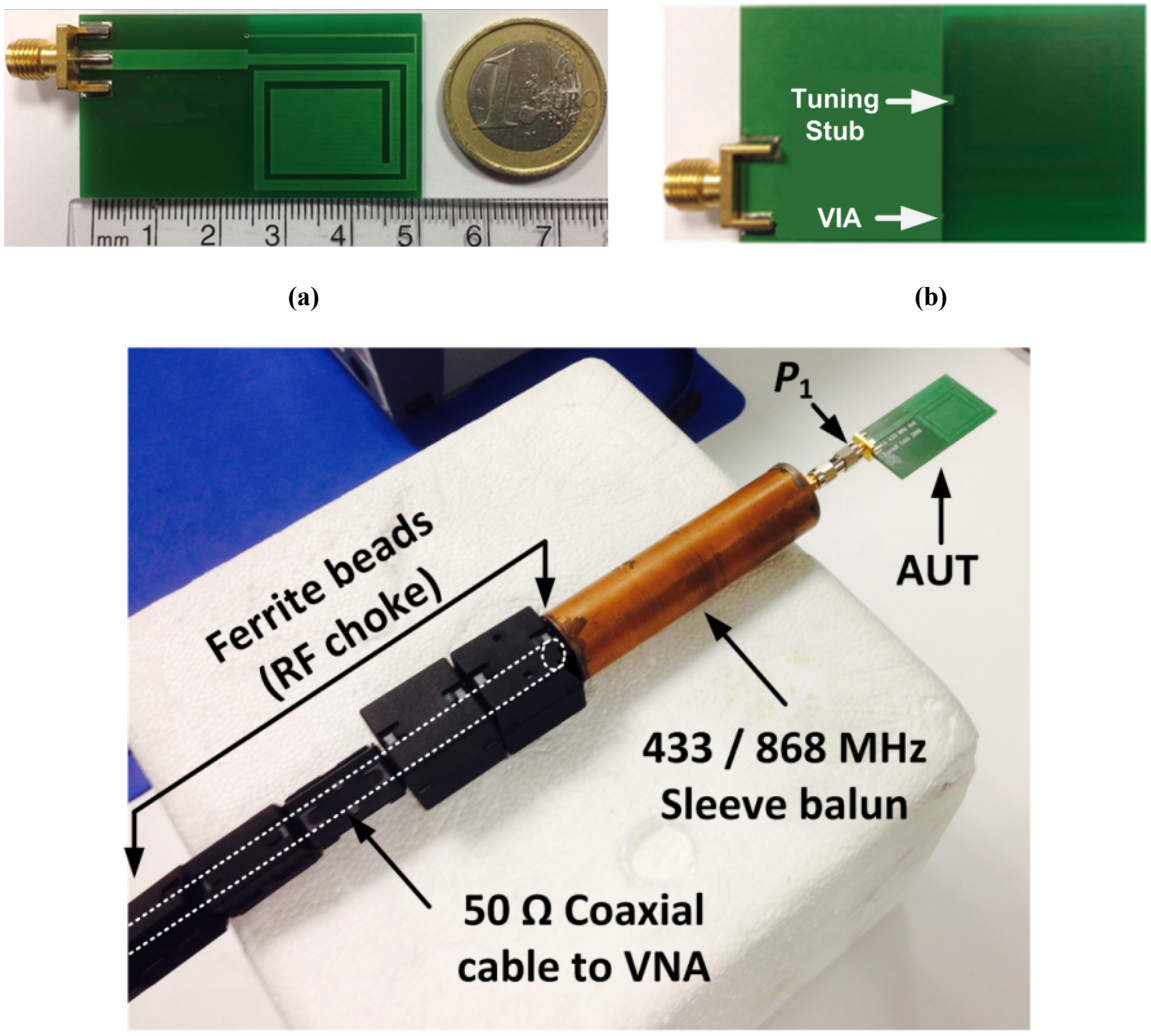


Figure 5-9 Prototype 433 MHz antenna (a) Top side, (b) Bottom side, (c) Test setup

The antenna S_{11} was measured using the test setup of Figure 5-9 (c). A Rohde & Schwarz ZVRE vector network analyzer [47] was used to perform the measurement.

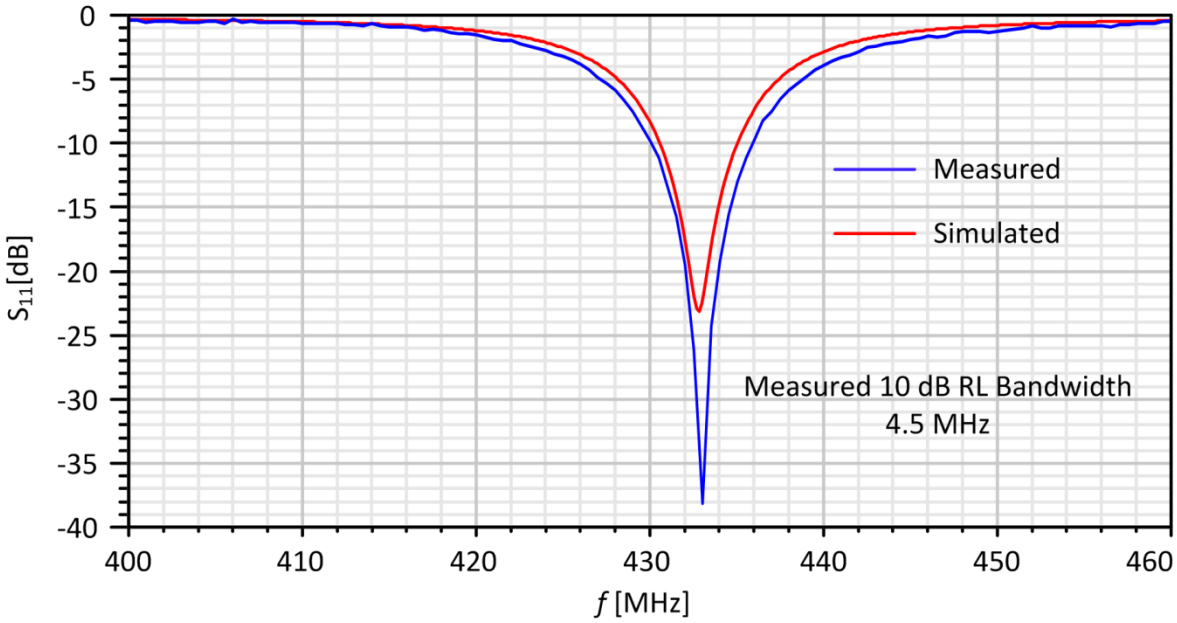
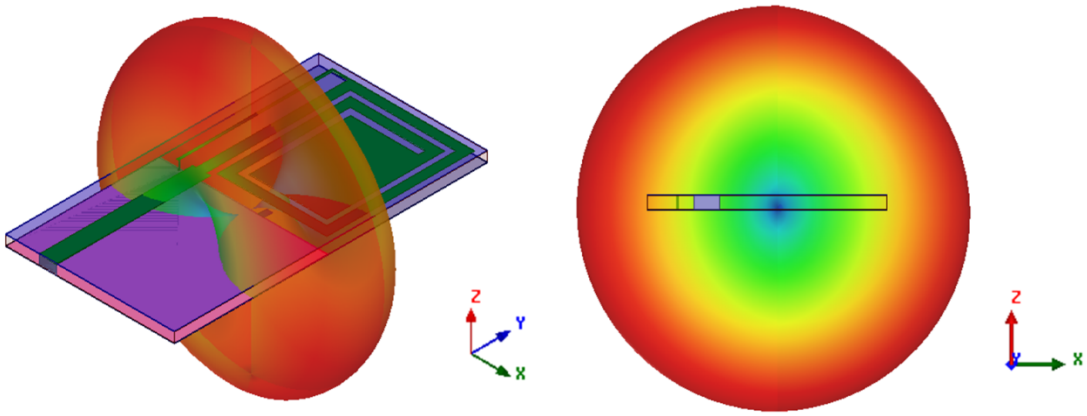
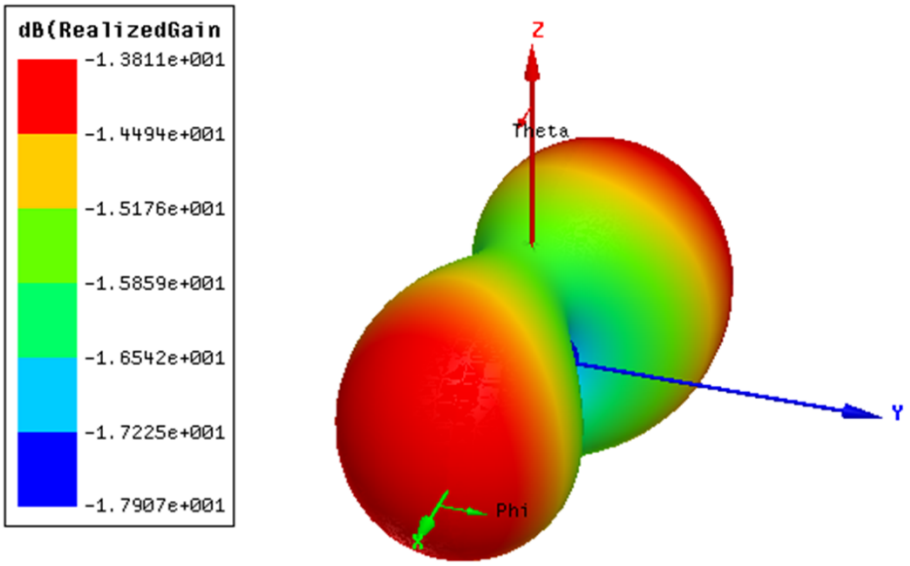


Figure 5-10 Measured and simulated antenna S_{11}

A balun [157] and several ferrite beads [60] were used to suppress coaxial cable currents as described in Chapter 2.3 with the VNA calibrated to the port P_1 position as shown in Figure 5-9 (c). The measured and simulated antenna S_{11} values are presented in Figure 5-10. It can be observed that the measured S_{11} (-10 dB) is approximately 5.5 MHz, adequately covering the required 1.75 MHz range for the 433.05 to 434.79 MHz ISM Band that is the focus of the application. The measured bandwidth is slightly larger than the simulated case and is likely due to effects in the measurement setup such as losses in the balun and ferrite-beaded cables that are not included in simulation. Figure 5-11 (a) shows the 3D realized gain patterns for the antenna at 433 MHz as derived in simulation. It can be seen that the antenna exhibits omni-directional radiation characteristics in the *x-z* plane. Figure 5-11 (b) shows that the simulated value of peak realized gain is -13.8 dBi.



(a)



(b)

Figure 5-11 Simulated 433 MHz 3D Gain, (a) Normalized, (b) Un-normalized

The antenna radiation patterns were then measured in a semi-anechoic chamber facility [49] and the normalized radiation patterns for the measured and simulated cases are shown in Figure 5-12. The observed differences between the measured and simulated cases are due to non-idealities in the measurement setup that are examined in detail in Chapter 7.

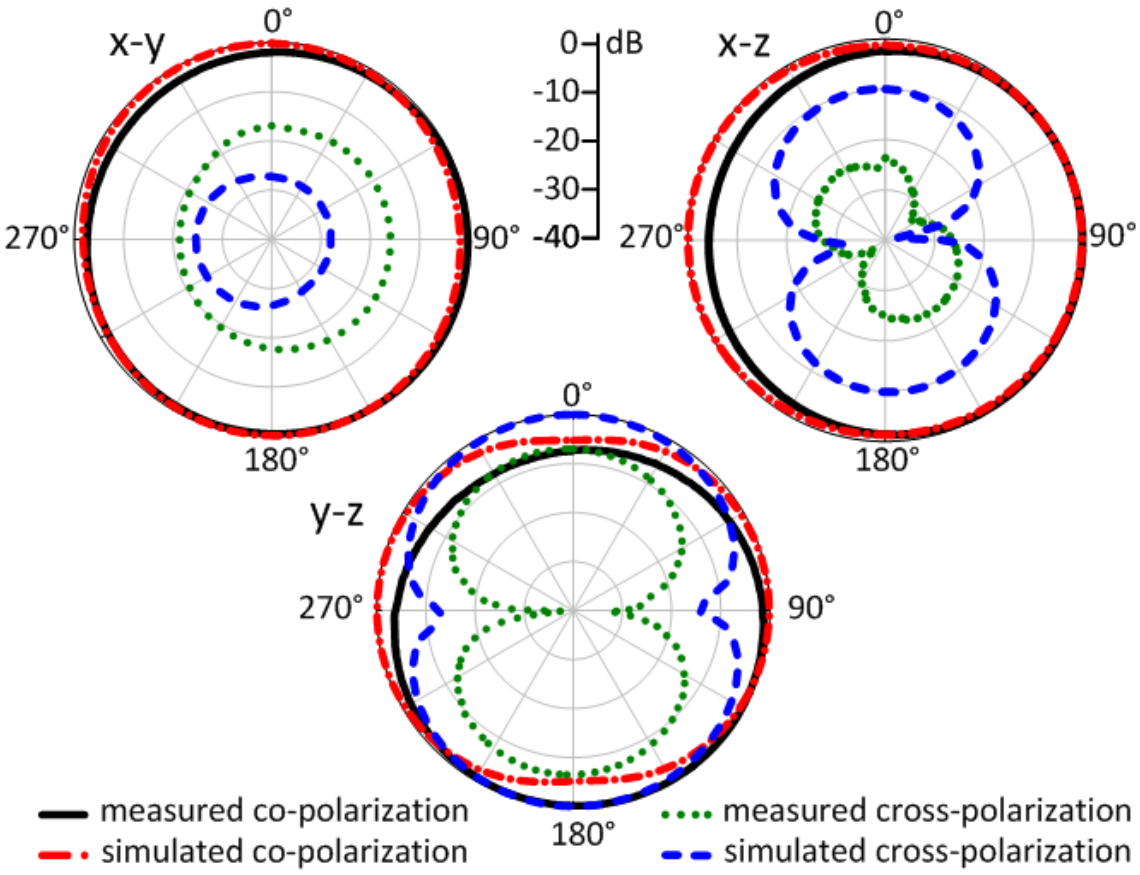


Figure 5-12 Normalized measured and simulated radiation patterns at 433 MHz

The measured and simulated gain and radiation efficiency figures for the antenna are listed in Table 5-2 and are specified at a frequency of 433 MHz.

Test Case	Peak Realized Gain (dBi)	Radiation Efficiency (%)
Simulated	-13.8	6.8
Measured	-13.0	NA

Table 5-2 Summary of antenna Gain and Efficiency parameters at 433 MHz

The measured peak realized gain figures are in good agreement with the simulated case and a difference of less than 1 dB was observed. Due to limitations in the measurement setup, it was not possible to measure the radiation efficiency of the antenna but the simulated value was determined to be 6.8 % and is primarily limited by the antenna size constraints [17].

The performance of the developed antenna solution was next compared to that of commercially available antennas with the gain figures listed in decreasing order. Table 5-3 shows that the proposed antenna has the lowest gain and bandwidth figures. However, it can also be seen that all the other antennas require significantly larger ground planes. It can also be observed that the commercial antennas investigated do not meet the size requirements of the Tyndall mote and this issue was one of the key motivations for carrying out this research in developing appropriate antenna solutions for highly miniaturized WSN devices.

Antenna Type	**f_0 (MHz)**	**BW (MHz)**	**Size (mm)**	**Peak Gain at f_0 (dBi)**	**Required Groundplane area (mm)**
Whip [94]	433	70	173 × 4.5	+3.3	101.6 × 101.6
Helical [92]	433	40	38.1 × 8.9	+1.9	190 × 7.6
Planar [91]	433	8	27.9 × 13.7 × 1.2	-6.4	84 × 38
Chip [93]	433	7	12.7 × 0.36 × 1.2	-9.8	80 × 39
This work	433	4.5	51 × 27.4 x 1.6	-13.8	Not required

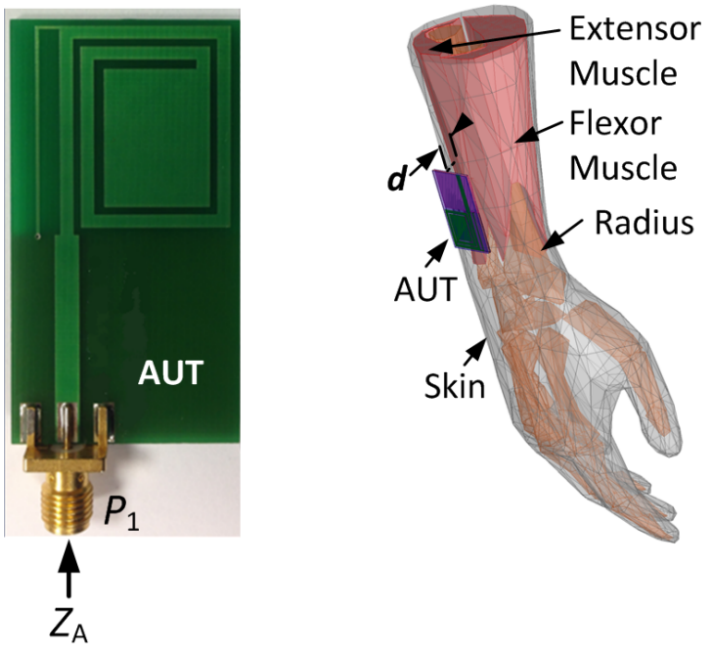
Table 5-3 Comparing proposed antenna performance to commercial solutions

Table 5-4 compares the proposed solution to antennas reported in academic works. This antenna has mid-range performance in terms of gain and bandwidth but has the advantage of not requiring additional groundplane area. Although the gain and bandwidth of the antenna is limited by its small electrical size [17], it can be seen that the proposed topology does offer a gain improvement of 7.9 dB when compared to a loop topology of similar size [96]. It also has to be pointed out that the PIFA antenna [97] is designed for bio-implantable applications in lossy tissue which limits the achievable gain but also leads to a large bandwidth as shown.

Antenna Type	**f_0 (MHz)**	**BW (MHz)**	**Size (mm)**	**Peak Gain at f_0 (dBi)**	**Required Groundplane area (mm)**
PIFA [43]	433.92	3.52	34 × 20	-3.48	700 × 700
IFA [95]	433	6	37 × 20	-6.1	37 × 30
This work	433	4.5	51 × 27.4 x 1.6	-13.8	Not required
Loop [96]	433/868	NA	53 × 32	-20.9	Not required
PIFA [97]	356 - 610	127	19 × 19.4 × 1.27	-27.6	Not required

Table 5-4 Comparing proposed antenna performance to the literature

5.4 Human Body Effects on Antenna Performance



(a) **(b)**

Figure 5-13 (a) Photograph of AUT, (b) Heterogeneous phantom arm model [42]

It was shown in Chapters 3 and 4 that the presence of the human body in the vicinity of the antenna can greatly affect the measured impedance characteristics of the antenna. The goal of this section was to determine, using measurement and EM simulation methods, the total antenna impedance variation that occurs when the previously described 433 MHz AUT is placed in close proximity to different parts of the human body. For subsequent measurements and simulations in this section, the antenna impedance Z_A refers to the impedance measured at port P_1 in Figure 5-13 (a). In order to design an antenna tuner for an application where it is in varying proximity to the human body, it is first necessary to determine the total range of antenna impedance that the antenna can experience in use [120, 158]. The relationship between Z_A and the distance to the human body was first investigated using a numerical simulation with the AUT model placed close to an anatomical model of the human arm as shown in Figure 5-13 (b) in the wrist position.

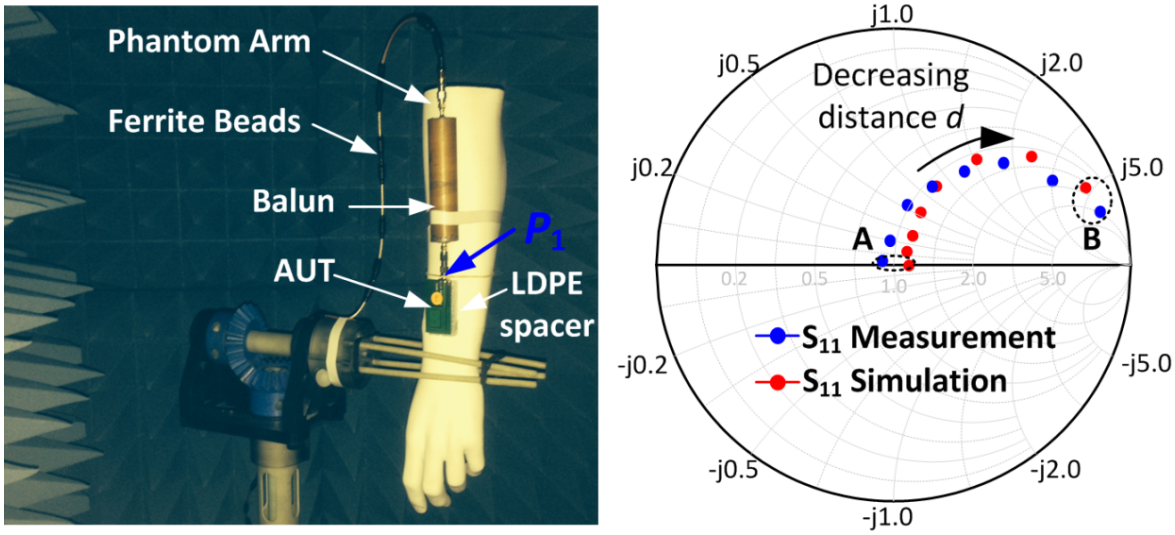
This heterogeneous phantom arm model includes important anatomical features of cortical bone, muscle and a thin outer layer of skin and fat that can accurately model the effects of the human body on antenna performance. Homogenous human body phantom models can also be used to simplify the simulation process and reduce simulation time. These models are typically based on simple geometrical shapes such as rectangles and cylinders with homogeneous dielectric properties used to model skin and muscle for example [18, 159]. The relative trade-off between accuracy and computation for homogenous and heterogeneous phantoms has been studied in the literature. For example in [99], a 2.45 GHz patch antenna is studied in close proximity to both a homogenous and heterogeneous human head model and the resulting radiation characteristics are compared. The results show that the homogenous model solves 5 times faster than the heterogeneous model and average gain figures differ by a maximum of 0.5 dB. In this work, the simulation goal was to study antenna-body interaction for eight different antenna positions relative to the human arm. Since the computational requirement was low, the heterogeneous phantom arm model was therefore used to maximize simulation accuracy. Figure 5-13 (b) shows the anatomical human arm model whose dielectric properties [160] are specified in Table 5-5.

Tissue	Relative Permittivity (ε_R)	Conductivity σ (S/m)
Cortical Bone	13.07	0.094
Muscle	56.87	0.804
Skin/Fat (Avg)	47.75	0.69

Table 5-5 Numerical model dielectric characteristics specified at 433 MHz

A full-wave EM simulation was then performed using ANSYS HFSS [42] to analyze antenna performance for varying distance *d* above the phantom skin surface with *d* varied from 3 to 59 mm in steps of 8 mm. Validation of the simulation model was then performed using the physical phantom arm described in Chapter 4. The measurements were performed in an AMS8050 anechoic chamber [161] using the test setup shown in Figure 5-14 (a).

The AUT was then connected to a Rohde & Schwarz ZVRE vector network analyzer [47] via a 50 Ω cable with ferrite beads [60] and BALUN to suppress unwanted feed cable radiation during measurements. Distance d was varied in the same sized steps as for the simulated case using 8 mm thick foam spacers. Figure 5-14 (b) shows that the measured and simulated values of S_{11} at f_0 with a similar impedance variation observed in both cases for changing values of d.



(a) **(b)**

Figure 5-14 (a) Photograph of test setup, (b) Measured and simulated S_{11} at f_0

The measured and simulated results show that the antenna behaves as though it were in a free-space environment for values of d greater than 6 cm approximately, with the measured and simulated values of Z_A both close to the centre of the Smith chart shown at point A. For decreasing values of d, the measured and simulated values of Z_A both move in a clockwise direction and converge at point B as shown. Exact agreement is not expected between the measured and simulated cases since the simulation model and physical test setup, using the homogenous phantom, are not anatomically identical. Moreover, it is the measured antenna impedance data that is of key interest as described in the following section.

5.5 Human-Body Antenna Impedance Measurements

A detailed study of total AUT impedance variation across the entire human body was conducted to determine how the quantity Z_A varied in its entirety. Because of the simulation complexity and large computational time required for this type of scenario, this work focused instead on a measurement-based approach, using a human test subject. Figure 5-15 illustrates the on-body antenna measurement setup adopted.

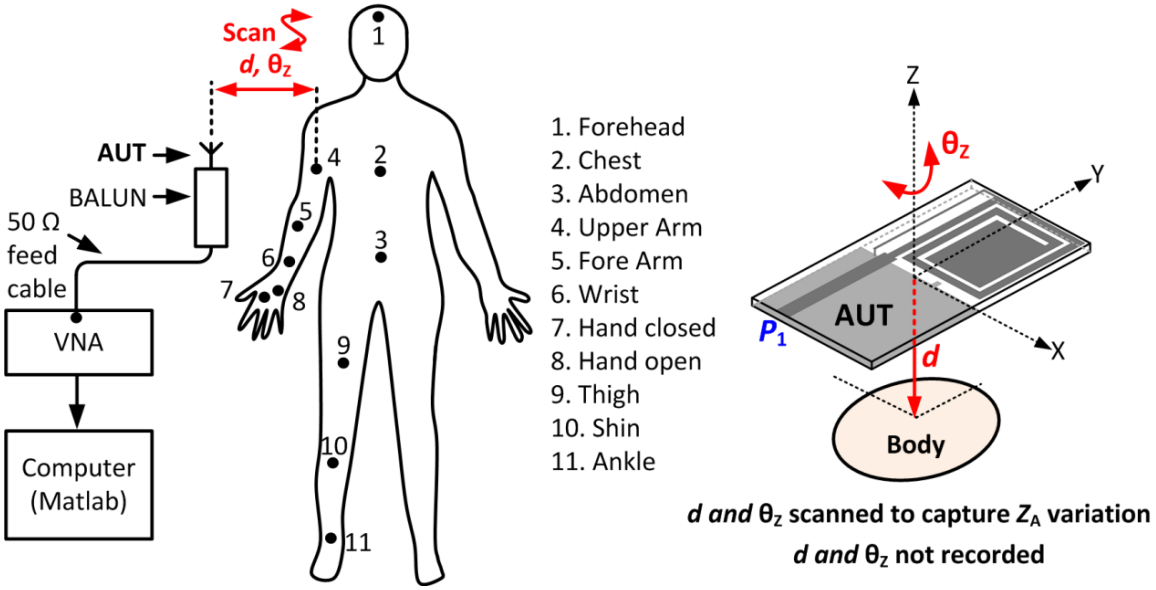


Figure 5-15 Overview of measurement setup for on-body AUT characterization

The AUT was placed at one of eleven different body locations shown with the human test subject clothed and in a standing position. In this case, the antenna-body distance d was then scanned repeatedly from a maximum distance d_{MAX} of greater than 6 cm approximately, representing the distance beyond which the antenna impedance does not noticeably change, to a minimum distance d_{MIN} = 1 mm. Minimum distance d_{MIN} was set to 1 mm because the AUT is not designed to be in contact with human skin whose high conductivity would effectively create a short circuit at the antenna terminals. Distance d_{MIN} was set by attaching a 1 mm LDPE spacer [162] to the bottom side of the AUT. The x-y plane of the antenna was positioned parallel to the skin surface during measurements.

In addition to repeatedly moving the antenna uni-laterally along the *z*-axis, the antenna was also rotated about the *z*-axis by an angle denoted θ_Z that was rotated in the range $0° \leq \theta_Z \leq 360°$ in order to capture any impedance variation due to orientation in this configuration. A computer running a Matlab [163] script was used to continuously measure and record all values of S_{11} at Port P_1. The values of d and θ_Z were not recorded, as the measured impedance data is of interest for later work. Each of the body position measurements was performed for a 90 s period, resulting in approximately 750 discrete measurements per body position for all variations of distance d and angle θ_Z. The measured values of S_{11} for the eleven different body positions are shown in Figure 5-16 showing the measured upper and lower body antenna responses.

It is apparent from the measured results that different body locations produce different impedance responses for the AUT. It is therefore necessary to carefully consider the effects of the entire human body to determine the total range of possible antenna impedance values. It was also determined that rotation of the antenna about the z-axis does not have a pronounced effect on the measured impedance. The effects of pocket objects such as a wallet, coin, car keys and iPhone 5 was also investigated as shown in Figure 5-16 (c). It can be seen that these items all produce different responses and it appears that more conductive metal objects lead to higher measured VSWR values, with the trajectory of the measured impedance moving towards the right-hand side of the Smith chart. Figure 5-16 (d) shows the superposition of all measured data on the same graph denoted Z_{A_TOT}. This impedance data represents the total antenna impedance variation that was measured for all distances d and θ_Z across eleven body positions. The measured data shows that the antenna impedance behaves in a predictable manner with both the inductive and resistive components of Z_A increasing with decreasing values of d. To better understand the observed behaviour of the antenna in varying proximity to the human body, a transmission line antenna model was developed as described in the following section.

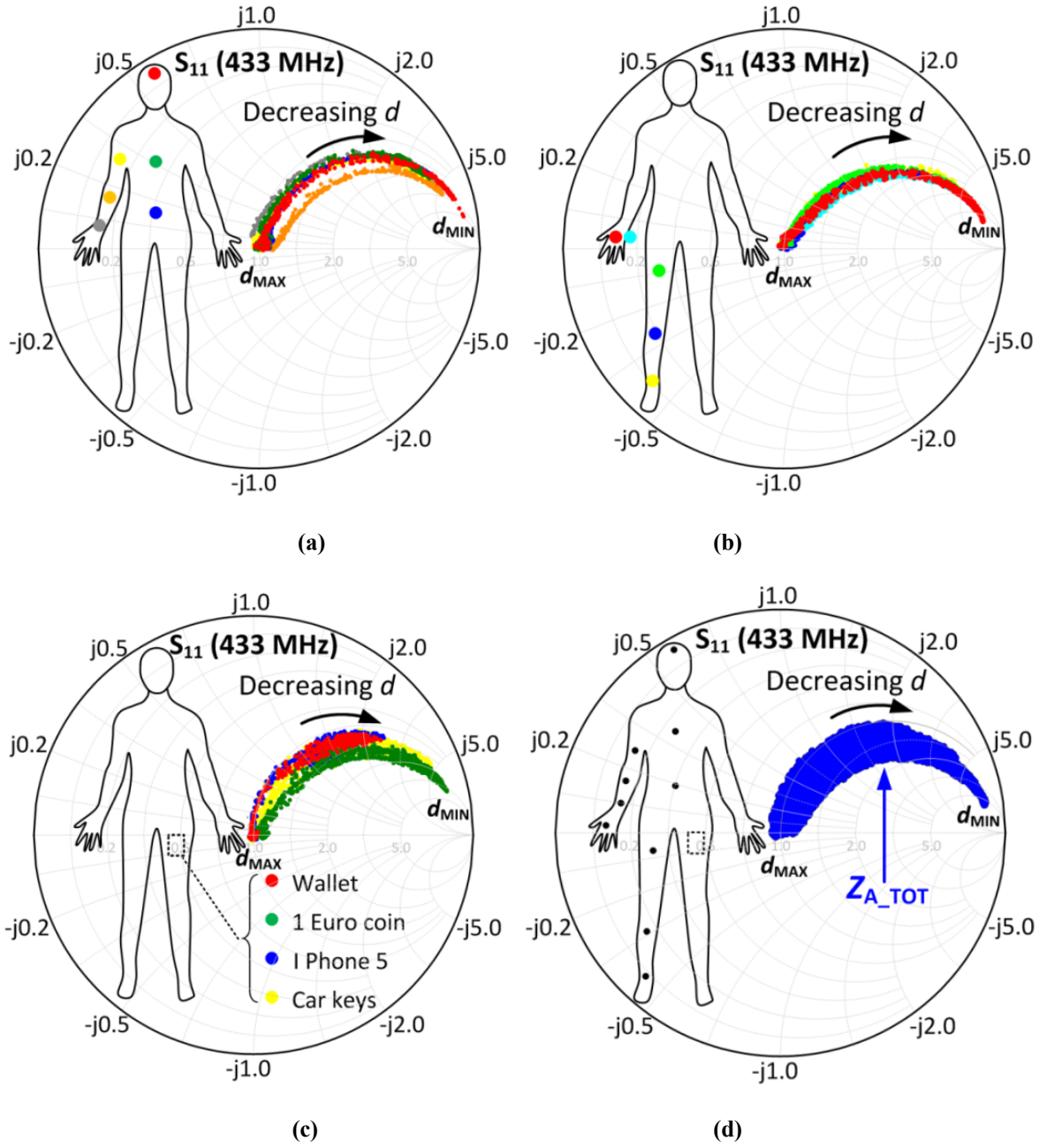


Figure 5-16 Summary of AUT measurements (a) Upper body, (b) Lower body, (c) Pocket items, (d) Superposition of all measurements (Z_{A_TOT})

5.6 Antenna Transmission Line Model

Equivalent transmission line models for IFA antennas in free-space have been reported previously in the literature [66, 164]. In this work, the motivation was to present a transmission line antenna model of the 433 MHz antenna that models the free-space case but also accounts for the observed effects of human body loading on the input impedance of the antenna. A simplified schematic of the antenna is depicted in Figure 5-17 showing the SMA input at Port P_1 and microstrip line with all the other antenna elements labeled from Point A to Point D. An equivalent circuit for the antenna was then developed using AWR Microwave Office [41] as shown in Figure 5-18. The antenna feed at Port P_1 is connected to a 50 Ω coaxial transmission line T_{SMA} representing the on-board SMA connector with characteristic impedance Z_{0SMA} = 50 Ω and electrical length Θ_{SMA} = 3 ° at 433 MHz.

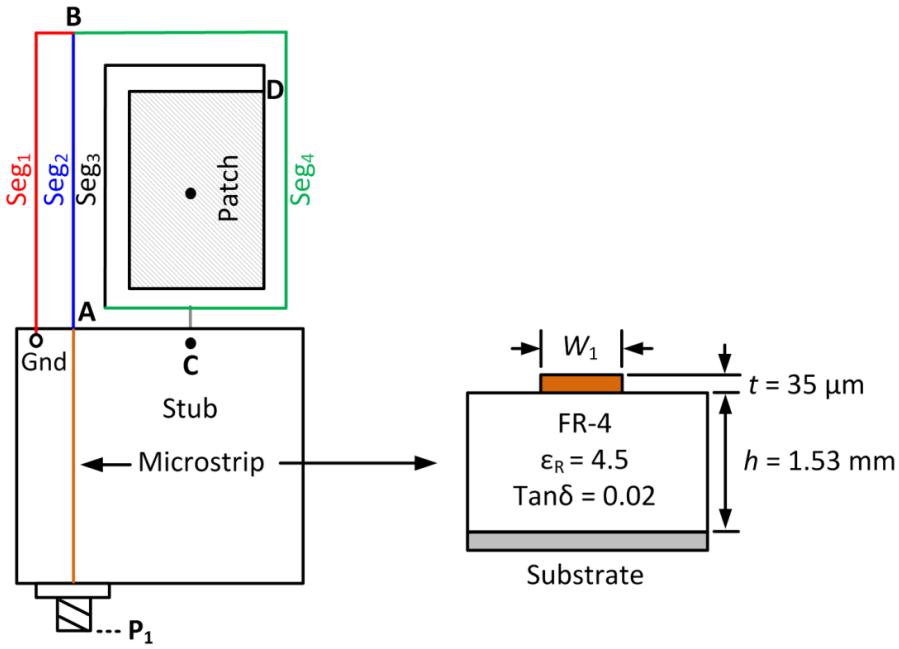


Figure 5-17 Simplified schematic of the 433 MHz antenna

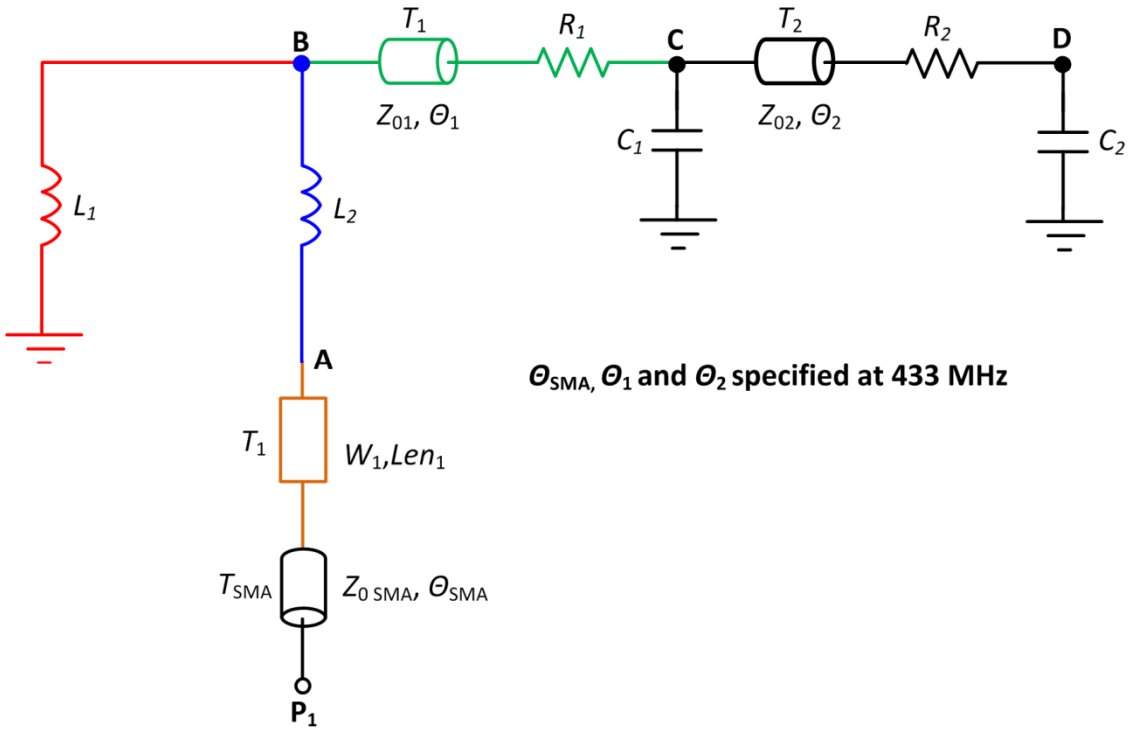


Figure 5-18 Equivalent circuit of the 433 MHz antenna

T_{SMA} is connected to a 50 Ω microstrip line T_1 of width W_1 = 2.91 mm and physical length Len_1 = 25 mm. The shunt inductive loop comprising segments Seg_1 and Seg_2 was modeled as a series combination of inductors L_1 and L_2. Spiral arms Seg_3 and Seg_4 were modeled as two transmission lines T_1 and T_2 with characteristic impedance Z_{01} and Z_{02} and electrical length Θ_1 and Θ_2 respectively. Series resistances R_1 and R_2 were used to model the distributed radiation and loss resistances (e.g. conduction and dielectric losses) associated with Seg_3 and Seg_4. Lumped capacitance C_1 was used to account for the capacitive stub at Point *C*. Finally, the end-capacitance of the patch at Point *D* was modeled as a lumped capacitance C_2 to Ground. The equivalent circuit model parameters, except those for the SMA connector and microstrip line which were fixed, were then optimized against measured 1-port antenna measured data over the range 400 to 500 MHz using AWR Microwave Office [41]. The final optimized parameter values are listed in Table 5-6.

Parameter Name	Value
R_1	9.57 Ω
R_2	11.1 Ω
C_1	0.14 pF
C_2	0.31 pF
L_1	10.48 nH
L_2	29.23 nH
Z_{0SMA}	50 Ω
θ_{SMA}	3° (433 MHz)
Z_{01}	166.2 Ω
Θ_1	55.08° (433 MHz)
Z_{02}	443.4 Ω
Θ_2	30.13° (433 MHz)

Table 5-6 Final optimized equivalent circuit model parameters

The optimized parameters show that the combined electrical length of the main spiral sections is $\Theta_2 + \Theta_3 \approx 85°$ or slightly less than a resonant $\lambda_0/4$ length at f_0 which is similar to the results in [164]. Figure 5-19 compares S_{11} responses of the measured AUT and equivalent circuit and good correlation is observed, in both magnitude and phase across a 100 MHz frequency range.

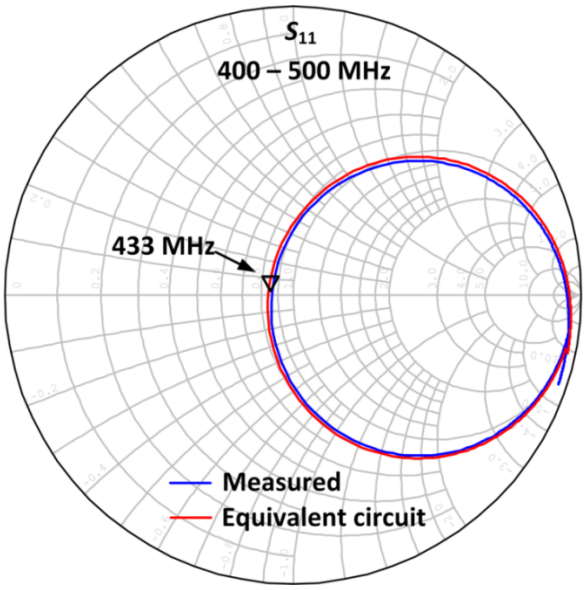


Figure 5-19 Equivalent circuit model versus measured data

Incorporation of human-body loading effects in the equivalent circuit model was also investigated to help explain the previously measured antenna impedance variation in proximity to the human body. Since the patch element and ground-plane have the largest cross-sectional-area, when compared to the other antenna features, it was therefore assumed that the majority of the capacitive coupling between the antenna and human body occurs via the patch capacitance C_P and ground capacitance C_G. This is illustrated in Figure 5-20 with both C_P and C_G assumed to be inversely proportional to the antenna-body distance d. In addition to the above, it is also assumed that the human body has a variable conductance G_B, depending on the body-position in question. The series equivalent of C_P, C_G and G_B is then modeled as a simple parallel equivalent of C_3 and R_3 that is added to the equivalent circuit of Figure 5-18 at point D, as illustrated in Figure 5-20.

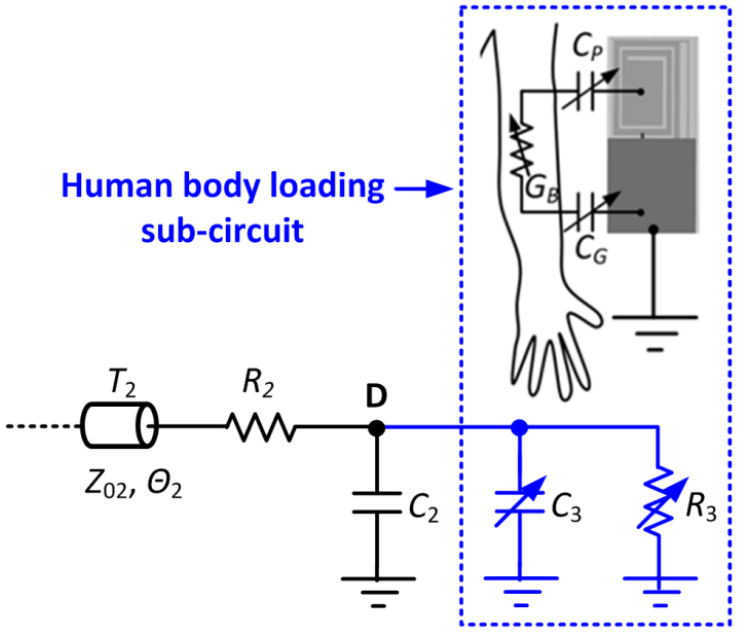


Figure 5-20 Human body loading effects added to antenna equivalent circuit

Figure 5-21 compares the simulated values of S_{11} using the equivalent circuit model versus measurements on the AUT where $S_{11_ANT_TOT}$ denotes the total measured impedance variation of the AUT for eleven body positions or approximately 11 × 750 = 8,250 individual measurements. For the equivalent circuit model, the range of parameters C_3 and R_5 were determined experimentally in simulation, with C_3 varied from 0 to 0.2 pF in steps of 2 fF and R_5 was varied from 29.5 kΩ to 300 kΩ in steps of 20 kΩ. Figure 5-21 shows that the simulation model is capable of estimating the total range of possible antenna impedances when compared with the measured case. Accounting for human body antenna loading effects using an equivalent circuit model, rather than using EM methods also has significant benefits in terms of computation time. For example, the FEM model of Figure 5-13 (b) requires 1.5 hours to compute Z_{ANT} for 8 discrete values of d using a machine with 24 GB of RAM and an Intel® Xeon® 8-core CPU running at 1.6 GHz. In contrast, the equivalent circuit model allows 1,350 discrete S_{11} antenna values to be computed in a time of 0.54 seconds.

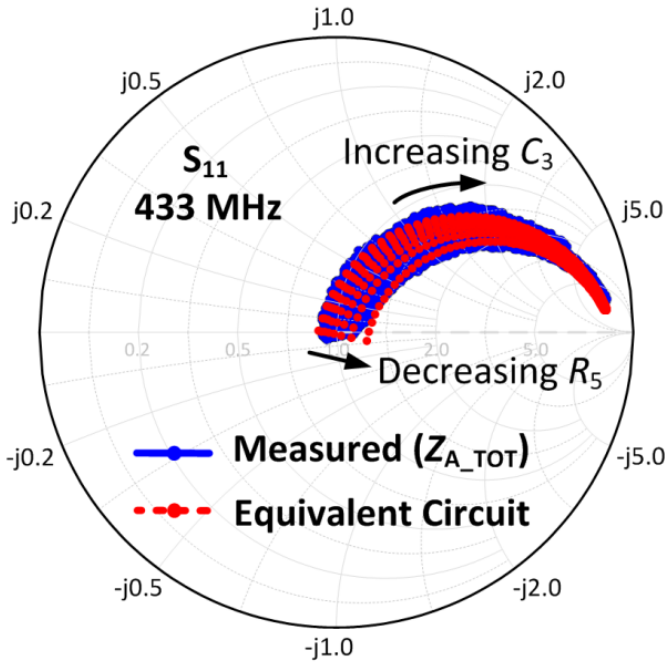


Figure 5-21 On-body equivalent circuit versus measured data

5.7 Conclusions

A compact and low-cost planar antenna operating at 433 MHz has been presented. Significant reduction of the antenna's resonant frequency is achieved using a variation of an IFA configuration with a square-spiral section together with a rectangular patch element and a small capacitive stub. It was shown that this antenna has a number of advantages over commercial types [91-94] in that it meets the size requirements for the Tyndall mote application and does not require an additional groundplane. In addition, the proposed antenna is implemented using low-cost FR-4 material and provides sufficient area for the integration of additional wireless sensor support circuitry in the groundplane area. Extensive characterization of antenna-body proximity effects were carried out with the new antenna. An equivalent transmission line model of the antenna was also described that predicts the free-space impedance characteristics. Furthermore, the model can also be used to estimate the impedance variation of the antenna in proximity with the human body.

This model can consider human body effects and allows rapid determination of the total antenna impedance variation when the antenna is placed at different positions and distances from the human body. It was also shown that the equivalent circuit model had the advantage of being able to solve much faster than the FEM-based model of Figure 5-13 (b) that was used for comparison and validation. The proposed equivalent circuit is not intended to replace EM modelling methods but has the advantage of enabling a fast analysis to be performed while also providing insight into the detuning behaviour of the AUT in proximity to the human body. Results outlined in this chapter have given rise to publication in [153].

Chapter 6. Second-Generation Antenna-Integrated Tuner Design

6.1 Background

In Chapter 4, a first-generation antenna tuner was proposed and demonstrated. The potential benefits of antenna tuning were shown both experimentally and in simulation for a reconfigurable, low-pass, *Π*-type matching topology. For the first-generation system, the implementation was large and the power consumption was not optimized for low power operation. In this chapter, the design of a second-generation, antenna-integrated tuner is presented. As summarized in Figure 6-1, the design combines key aspects of the first-generation tuner of Chapter 4 with the 433 MHz antenna design of Chapter 5. Improved modeling techniques are described that take into account the total antenna impedance variation of the antenna in proximity to the human body. The new tuner implementation takes advantage of higher performance tunable and fixed RF components that have become available commercially since the design of the first-generation system. Other key design improvements have also been made in terms of power consumption and tuning time. The described system is now substantially miniaturized compared to the previous generation and can now be integrated onto the antenna substrate, leading to a lower-loss, lower-power implementation.

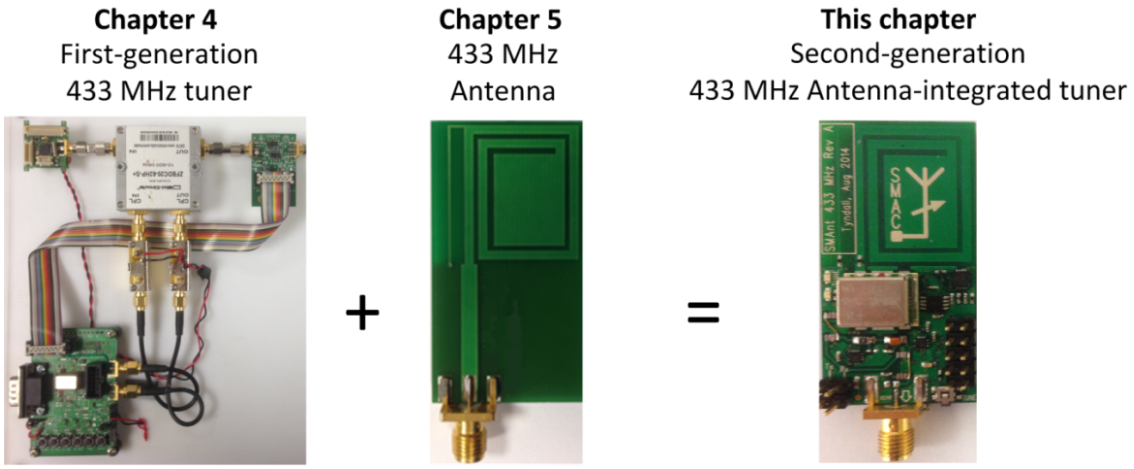


Figure 6-1 Summary of this chapter

6.2 Reconfigurable Matching Network Design

In Chapter 5, Section 5.5, the total impedance variation of the 433 MHz antenna, denoted Z_{A_TOT}, was measured in proximity to the human body. This measured information represents the total range of impedances that are possible at the input terminals of the antenna and is next used in the analysis and design of a reconfigurable antenna matching network. In order to determine the potential benefits of impedance matching, the losses due to impedance mismatch are first evaluated when *no matching network is present*. This is achieved by calculating the antenna Mismatch loss (*ML*) using (2.10). Figure 6-2 shows the previously measured values of Z_{A_TOT} superimposed on the calculated contours of *ML* for varying S_{11} at 433 MHz with a source impedance $Z_S = Z_0 = 50\ \Omega$. A significant, worst-case loss of approximately 6 dB is observed without matching for this AUT.

In order to reduce the above losses due to impedance mismatch, the following presents the design of a reconfigurable impedance matching network. The main requirements for the matching network are that it provides the required impedance coverage to match all possible antenna load impedances or Z_{A_TOT}, with minimal loss. Several different types of low-pass matching network topologies were investigated including *L*, Double-*L*, *T* and *Π*-type networks.

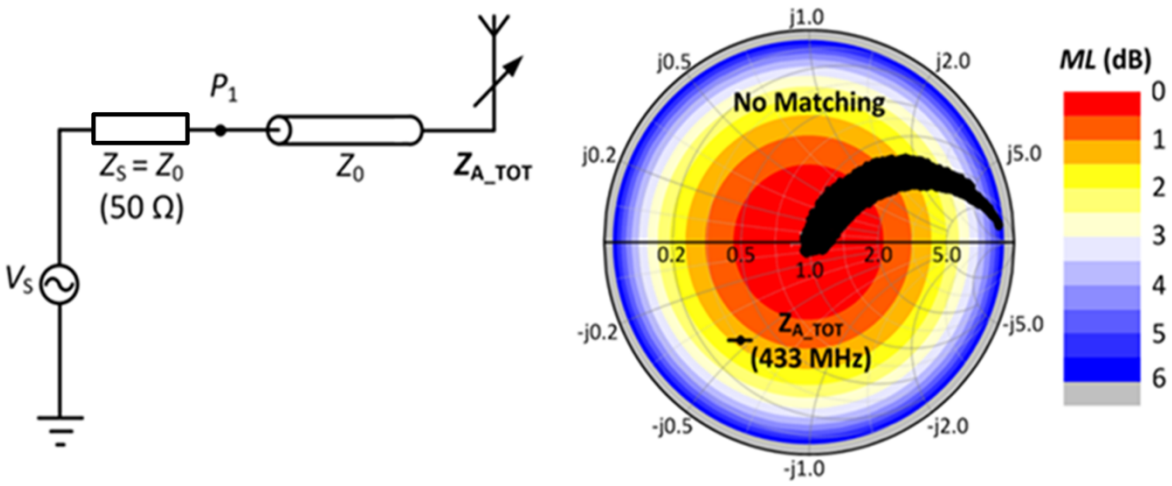


Figure 6-2 Total measured impedance variation and *ML* with no tuning

The main disadvantages of the *L*-network are limited loaded quality factor and bandwidth. and conjugate matching is possible only for a limited area of the Smith chart [34], even when ideal, lossless components are used. The Double-*L*, low-pass network can offer increased coverage and bandwidth but has the disadvantage of requiring an extra series inductor, which leads to increased losses. The low-pass *T*-network has only one tunable component and therefore has limited impedance coverage. The *Π*-structure was eventually chosen for this application as this topology minimizes the effect of finite-*Q*-factor tunable and fixed components that are used to implement the network and provides the necessary Smith chart coverage. In terms of choosing a suitable impedance mismatch sensor, a number of solutions were investigated in the literature. A popular approach is to place a directional coupler between the power amplifier (*PA*) and matching circuit where the sensed forward and reflected powers are then used to tune the circuit [117, 130, 165]. However, as observed in Chapter 4 and as also reported in [166], tuning circuit losses using this topology can result in non-optimal power delivery. An alternative approach is to place the coupler at the output of the matching network and during tuning, maximize the power delivery through the matching network. It is the latter approach that has been determined to work best for this application as the tuning components have finite loss.

This method also allows the antenna S_{11} magnitude to be measured directly at the antenna port during tuning. A simplified representation of the *Π*-type matching network is shown in Figure 6-3. Reconfigurability is achieved using variable capacitances C_1 and C_2 using a commercial PE64102 device [167]. This is a 5-bit device that allows the capacitance between the RF+ and RF- terminals to be digitally tuned from C_{MIN} = 1.88 pF to C_{MAX} = 14.0 pF in 32, discrete steps of 391 fF. This device was not available during the design of the first-generation system. It offers a number of performance advantages in terms of lower RF losses, wider tuning range and increased resolution. The device is also highly integrated and leads to greatly reduced PCB parasitics in comparison to what was achievable with the first-generation system.

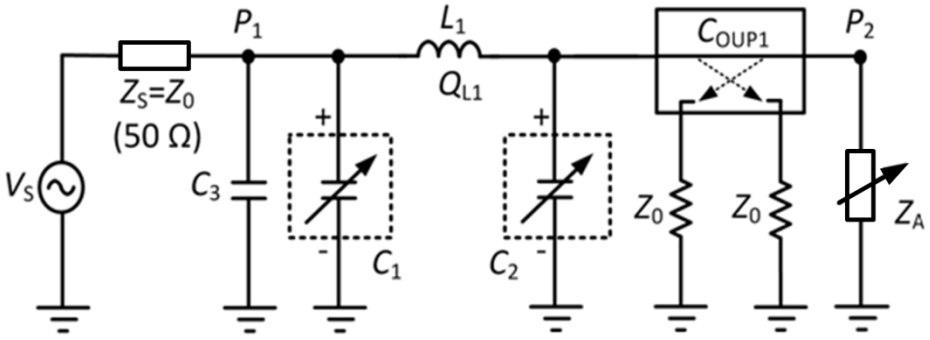


Figure 6-3 Simplified circuit for the *Π* -type matching network

In terms of accurately predicting the performance of the matching network, the component parasitics of C_1 and C_2 are essential to model and an equivalent circuit model of the component was employed [167]. The manufacturer recommended DTC Equivalent Circuit Model is shown in Figure 6-4 and includes all the parasitic elements required for accurate modeling of the physical device. Variable quantities such as the tuning core capacitance C_S between RF+ and RF- ports of the device are modelled using an equation-based method as listed in Table 6-1.

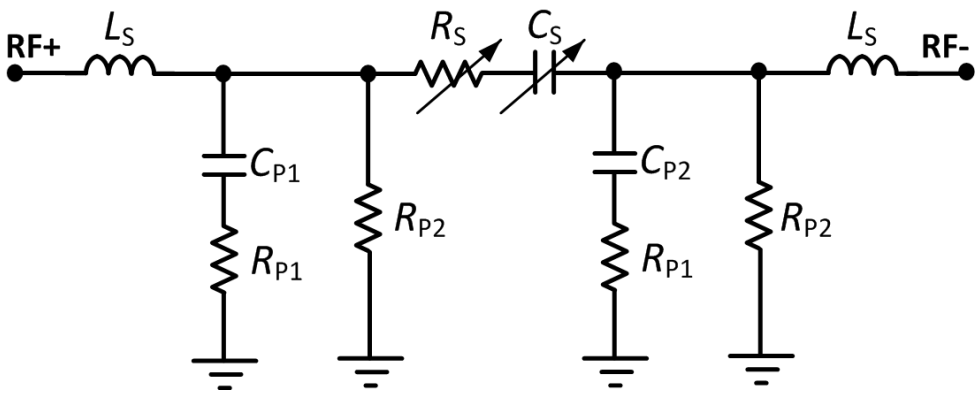


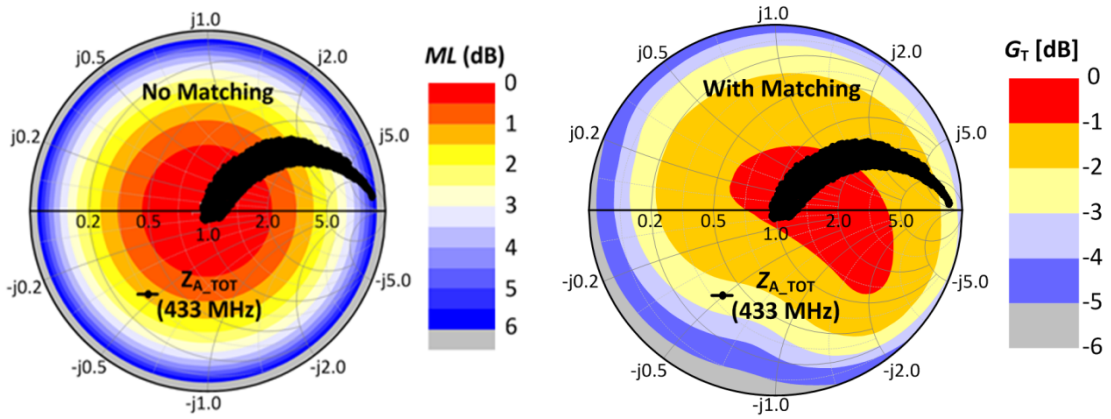
Figure 6-4 Equivalent circuit of PE64102 DTC capacitance [167]

Parameter	Value	Parameter
C_S	(0.394 × State) + 1.456	*p*F
R_S	15/(State + 15/(State + 0.4)) + 0.4	Ω
C_{P1}	-0.0026 × State + 0.4155	pF
C_{P2}	0.0029 × State + 0.4914	pF
R_{P1}	4	Ω
R_{P2}	22000 + 6 × $(State)^3$	Ω
L_S	0.4	nH

Table 6-1 DTC equivalent model parameters [167]

A high *Q*-factor, 14 nH air-core inductor was chosen for L_1 using an 0807SQ-14NJLB part from Coilcraft with Q_{L1} = 110 [168]. Fixed capacitor C_3 was used to provide additional capacitance at the source side of the matching network to enable high VSWR load impedances to be matched. The values of L_1 and C_3 were optimized in simulation as described later in this section. A bi-directional coupler C_{OUP1} was employed at the output of the matching network. The chosen coupler was a SYDC-20-62HP+ from Min-Circuits [169]. This component has a coupling factor of 20 dB with a high directivity of 30 dB and an insertion loss of 0.34 dB at 433 MHz. This coupler is also substantially smaller compared to the first-generation solution.

The measured *S*-Parameters of the coupler were included in the simulation model as well as a vendor model for inductor L_1. The antenna connector, feed, PCB substrate, and all interconnect for the RF paths were included in the simulation model. A load-pull analysis and optimization of the simulation model was then performed using the Advanced Design System (ADS) from Keysight [110] in order to optimize L_1 and C_3 to maximize G_T of the matching network, over the range of antenna impedances defined by Z_{A_TOT}. The resulting G_T contours with matching are shown in Figure 6-5 (b) and the previously simulated *ML* contours without matching are shown for comparison in Figure 6-5 (a). It can be seen from Figure 6-5 (b) that the *Π*-type matching network provides significant improvement in power delivery to the antenna for high antenna VSWR when compared with the unmatched case. For example, as outlined previously, the worst-case *ML* without matching was 6 dB. However, with matching, the worst-case G_T is approximately -2.5 dB maximum, or a 3.5 dB improvement in power delivery to the antenna. For values of Z_A towards the centre of the Smith chart, the simulation model predicts losses of approximately 0.8 dB, mainly attributed to component losses in C_1, C_2, L_1 and C_{OUP1}.



(a) **(b)**

Figure 6-5 (a) *ML* no matching, (b) G_T with matching

6.3 Antenna Tuner Implementation

In this section, the hardware implementation details of the second-generation antenna integrated tuner are presented. A dedicated tuner module was first developed for characterization purposes and a block diagram is shown in Figure 6-6 with a photograph of the fabricated module also shown for reference. Port P_1 of the matching network is the interface to the radio transceiver and Port P_2 is the antenna interface. The matching network comprises variable capacitors C_1 and C_2 as well as fixed capacitor C_3 and inductor L_1. The output of the matching network is connected to the input (*IN*) of C_{OUP1}. The coupler provides a sample of the coupled forward and reflected power denoted P_{FWD} and P_{REF}, allowing the reflection coefficient $|\Gamma_L|$, at the antenna port (P_2) to be determined.

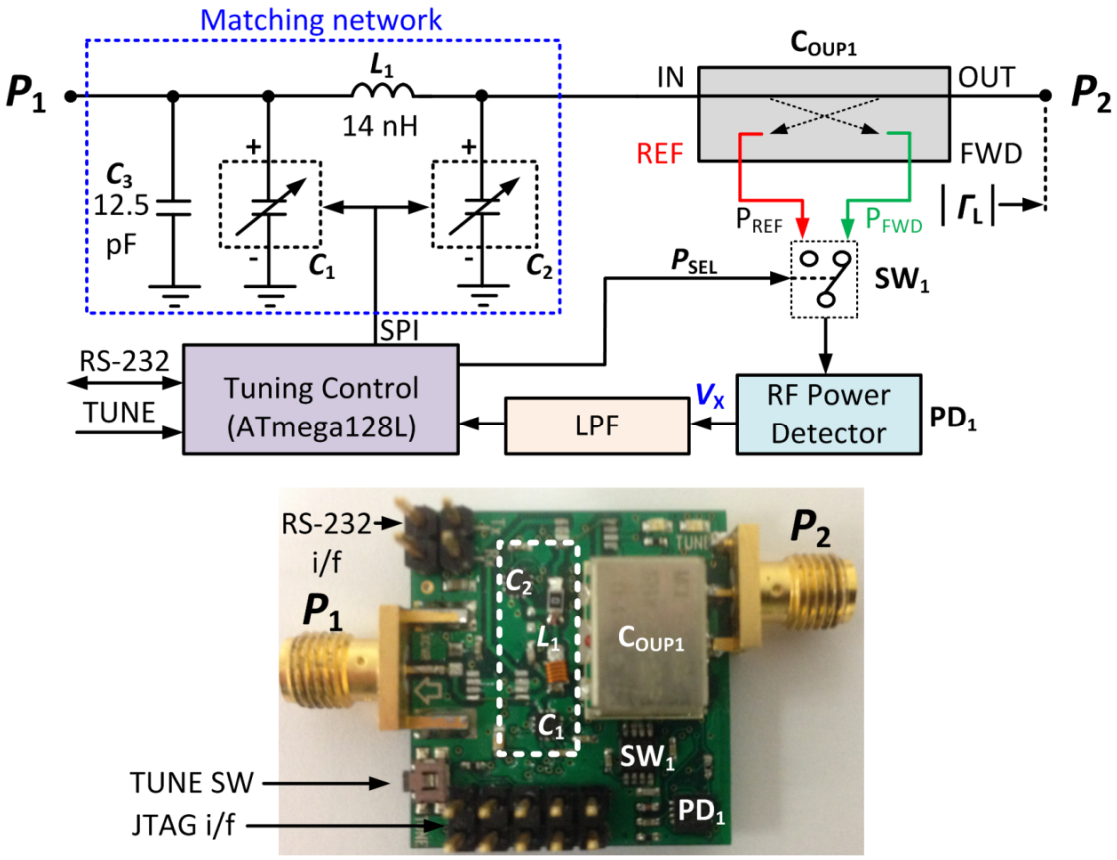
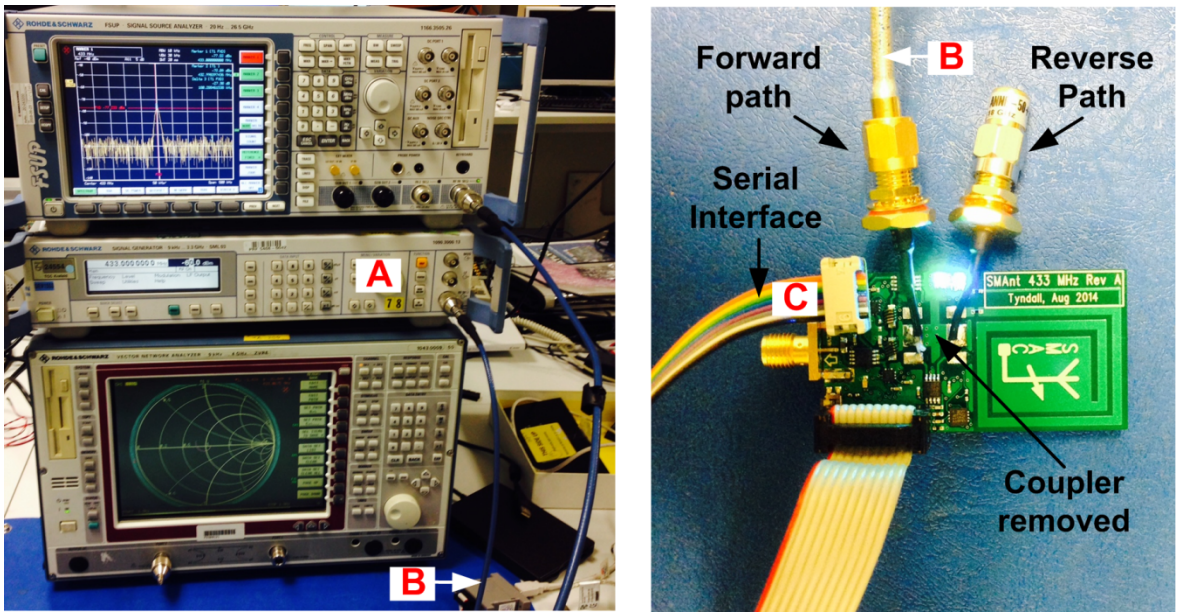


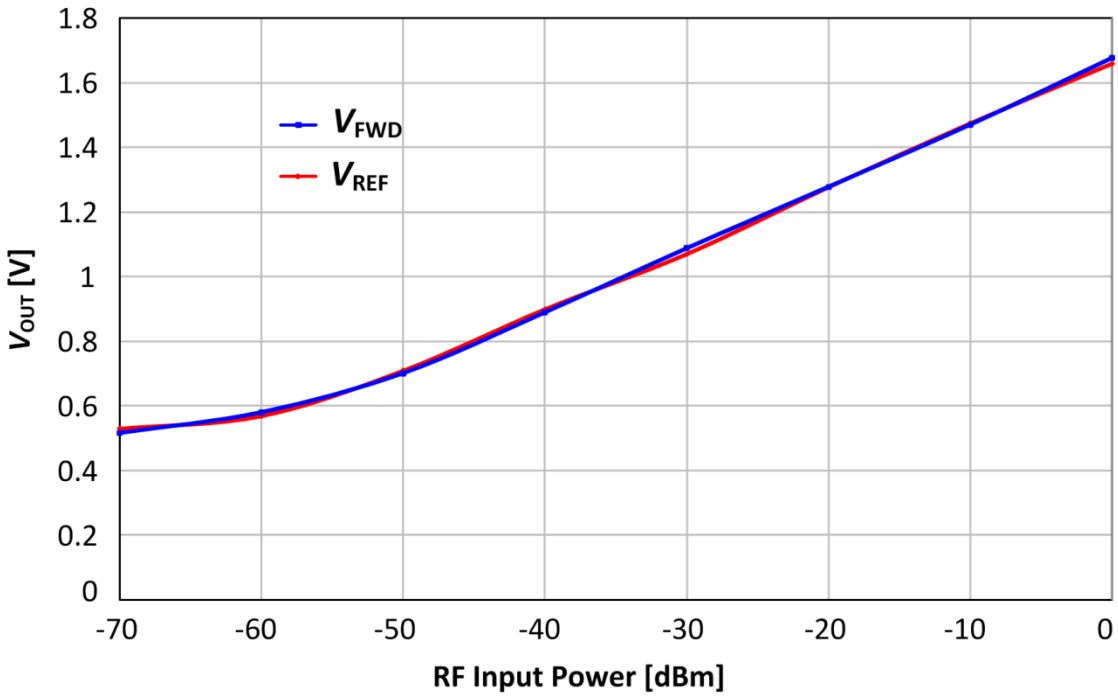
Figure 6-6 Block diagram and photograph of tuner module

Unlike the first-generation design, that used two separate RF power detectors, in this case, a lower-power configuration was adopted using a single LT5538 RF (PD_1) power detector from Linear Technology [170]. The LT5538 RF power detector is a high sensitivity device with a dynamic range from –75 dBm to +10 dBm and a frequency range of 40 MHz to 3.8 GHz. This power detector has a significantly lower supply current of 29 mA DC as opposed to 128 mA for the first-generation system. A PE4251 SPDT absorptive RF switch SW_1 from Peregrine Semiconductor [114] was then used to allow either of the P_{FWD} or P_{REF} signals to be measured independently. Note that the use of an absorptive switch ensures that the coupler ports are always terminated in 50 Ω. The DC output voltage V_X of the power detector was then filtered using a single-pole, low-pass filter and digitized by a low-power, ATmega128L micro-controller [86].

The test setup for characterization of the RF power detectors is shown in Figure 6-7 (a). RF input power was applied using a Rohde & Schwarz SML-03 [147] signal generator (A) and a 50 Ω coaxial cable (B) as shown. Note that for the measurements described, a separate tuner module was used with the coupler removed to allow RF power to be fed directly to the RF power detector via the RF switch SW_1. The P_{FWD} and P_{REF} paths were then characterized separately using the P_{SEL} signal to select individual paths. The digitized output voltage of the power detector was read using the serial interface (C) for RF input power levels varying from -70 dBm to 0 dBm at 433 MHz as measured using a Rohde & Schwarz FSUP Signal Source analyzer [144]. The measured results for both the P_{FWD} and P_{REF} paths are shown in Figure 6-7 (b). Similar to Chapter 4, the measured data was then used to generate LUT values of calculated power versus measured voltage and this data was then stored in firmware to allow $|\Gamma_L|$ at P_2 to be calculated. An RS-232 interface allows real-time monitoring of measured data via a graphical user interface (GUI) similar to the methods used in Chapter 4. The tuner module was implemented using standard, 1.6 mm *FR-4* material ($\varepsilon_R = 4.5$, $\tan\delta = 0.02$), with a 6-layer stackup [70] and was integrated in a small area of 25 × 28 mm. The tuning circuitry was placed on the top layer of the PCB with the tuning controller placed on the bottom layer.



(a)



(b)

Figure 6-7 RF power detector characterization (a) Test setup, (b) Measured results

6.3.1 *Antenna Tuning Algorithm*

For this design, two types of tuning algorithms were investigated. The first algorithm (*Type A*) used an exhaustive search of all 1,024 combinations of variable capacitances C_1 and C_2 to maximize P_{FWD}, the power delivered to the antenna. At the end of the tuning process, the optimum tuning states were written to capacitors C_1 and C_2 using the serial peripheral interface (*SPI*) bus. The second algorithm (*Type B*) used the pre-characterized AUT impedance data Z_{A_TOT} to enable faster tuning as now described.

Figure 6-8 shows the previously measured total impedance variation Z_{A_TOT} for the AUT in proximity to the human body. It can be seen that the majority of measured AUT impedances are confined to the right-hand quadrant of the Smith Chart, where the phase of Γ_L is limited to $0° \leq \Theta_L \leq 90°$. Investigation of the simulation model of Figure 6-3 revealed that 344 optimal tuner states denoted C_{1_OPT} and C_{2_OPT} occupied this 90° quadrant or approximately 34 % of all 1,024 possible states. Further reduction in the number of searchable states is possible by noting that only those states that occupy the area within the Z_{A_TOT} boundary or dashed white line illustrated in Figure 6-8 need to be searched.

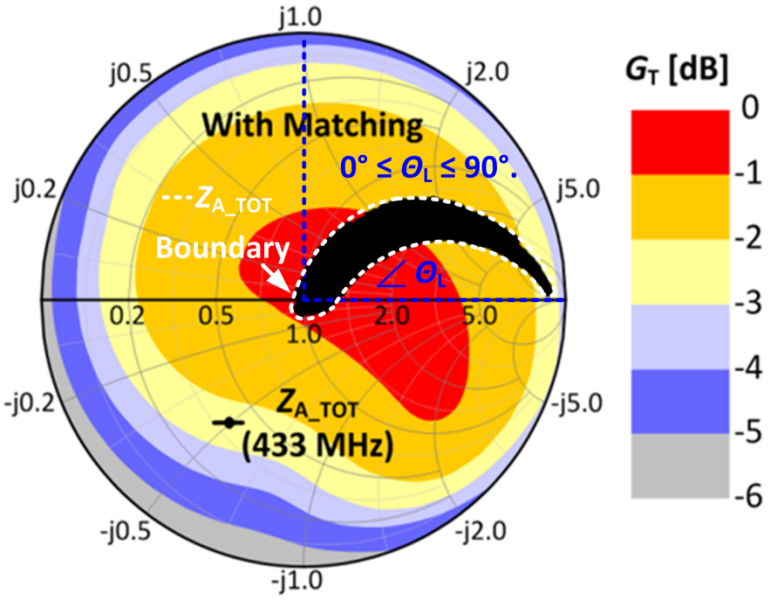


Figure 6-8 Total measured on-body antenna impedance variation

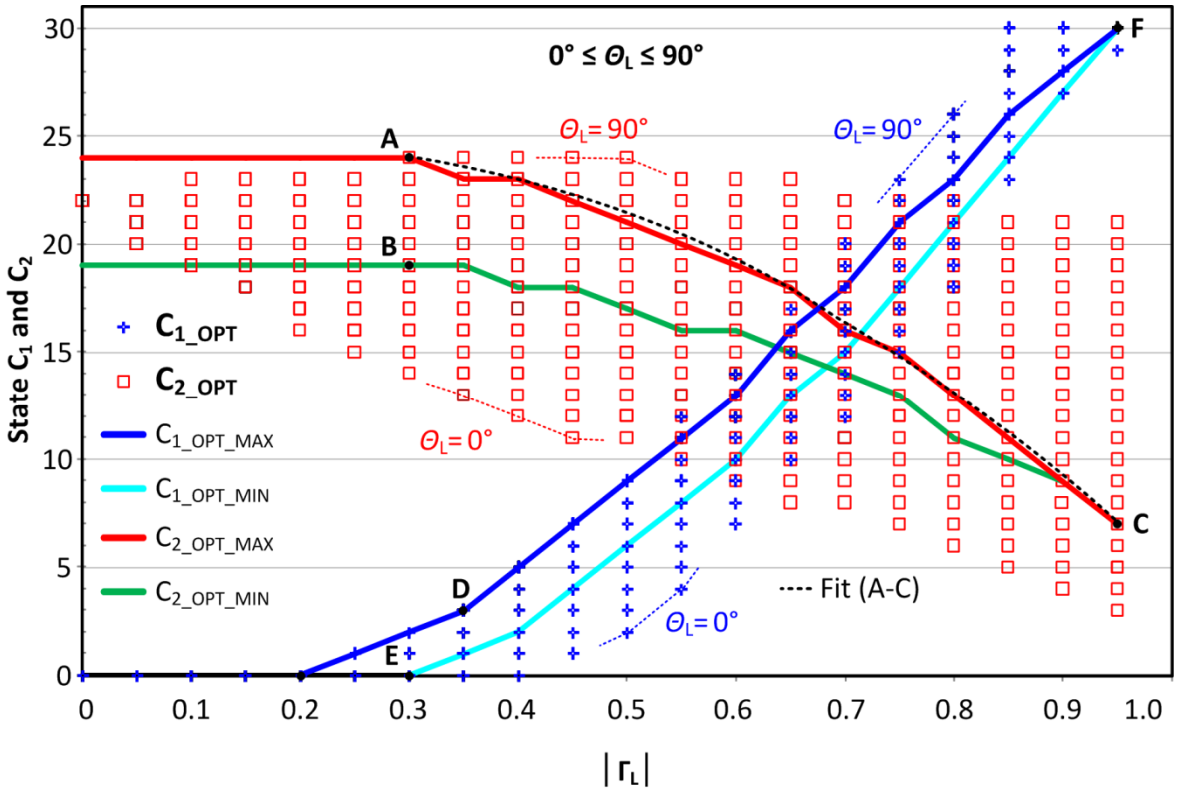


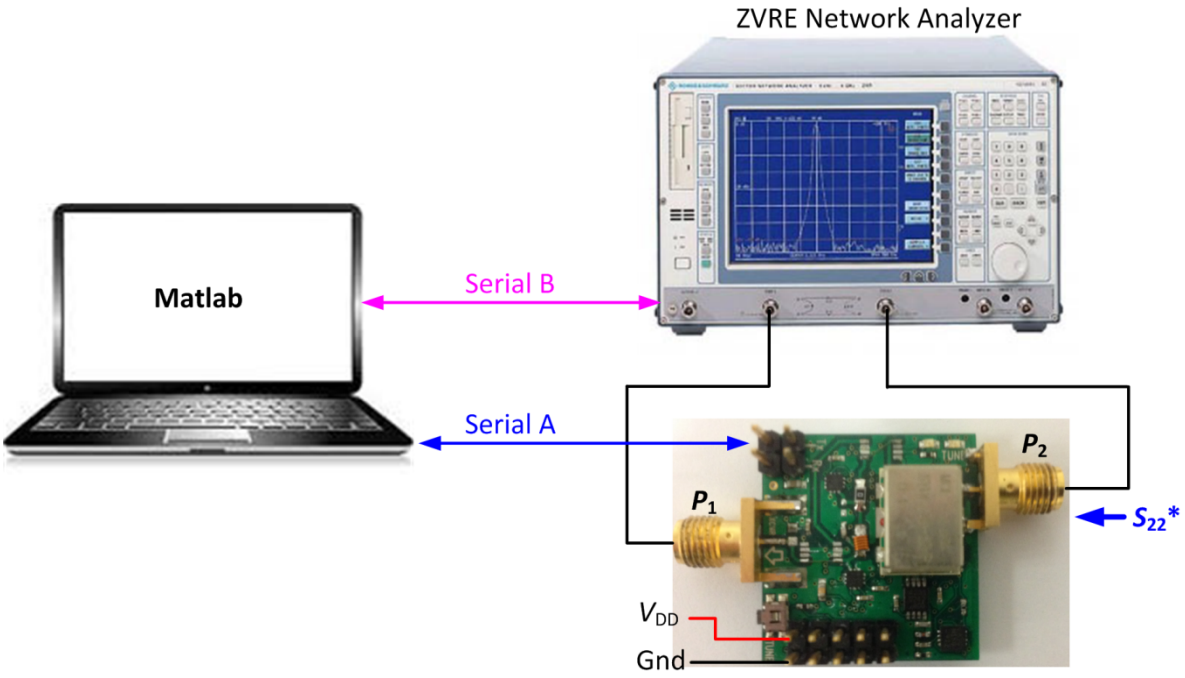
Figure 6-9 Simulated optimal states for C_1 and C_2 vs $|\Gamma_L|$ for $0° \le \Theta_L \le 90°$

These 344 optimal states are shown in Figure 6-9 as a function of $|\Gamma_L|$. The extents of these searchable state boundaries for C_1 and C_2 are denoted $C_{1_OPT_MAX}$, $C_{1_OPT_MIN}$, $C_{2_OPT_MAX}$ and $C_{2_OPT_MIN}$ and are shown as solid lines in Figure 6-9 and are determined from analysis of the pre-characterized Z_{A_TOT} data. Thus, for a measured value of $|\Gamma_L|$, only a limited set of optimal tuning states for C_1 and C_2 need to be searched. The minimum and maximum boundary values for C_1 and C_2, extracted from the measured data, are then defined using a combination of linear and quadratic equations, depending on the measured value of $|\Gamma_L|$. Quadratic equations are used to define the minimum and maximum values $C_{x_OPT_MIN}$ and $C_{x_OPT_MAX}$ for $0.3 < |\Gamma_L| < 0.95$, having the form $a|\Gamma_L|^2 + b|\Gamma_L| + c$ and $x = 1, 2$. The coefficients a, b and c were determined by curve fitting of the measured Z_{A_TOT} boundary data values, with the boundary values then quantized to the nearest integer (e.g. $C_{2_OPT_MAX}$ shown as the dashed line A-C).

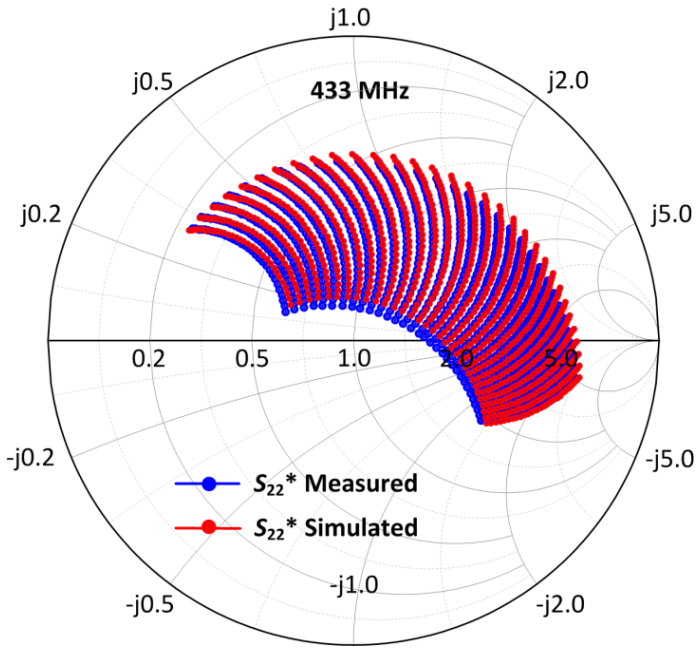
The same approach was used to define the boundaries *B-C, D-F and E-F*. Based on the measured value of $|\Gamma_L|$, the tuning algorithm performs a search of all states for C_1 and C_2 that lie between the calculated $C_{x_OPT_MIN}$ and $C_{x_OPT_MAX}$ values resulting in a significant reduction in tuning time. For example, a measured value of $|\Gamma_L| = 0.5$, requires 4 values of C_1 and 5 values of C_2 to be searched or a total of $4 \times 5 = 20$ iterations required, compared to 1,024 for an exhaustive search, thus significantly reducing both the time and power consumption required during the tuning process. Using this tuning method, the procedure to determine the appropriate search space for the matching algorithm only has to be completed once, for a given antenna type that has been pre-characterized.

6.4 Prototype Measurement and Verification

The tuner module was first characterized by measuring the range of impedances that could be conjugately matched to 50 Ω at P_2 at a frequency of 433 MHz with P_1 terminated in 50 Ω, using the test setup of Figure 6-10 (a). A ZVRE VNA [47] was connected as shown in a 2-port configuration and DC power was applied to the tuner module with $V_{DD} = 3.0$ V. A Matlab script [163] was then written to control the tuner as well and acquire the measured S-parameters from the VNA. The Matlab script was used to write each of the 1,024 states for variable capacitances C_1 and C_2 via laptop-tuner interface Serial A. For each state, the measured value of S_{22}* on the VNA was recorded via the Serial B interface and all results were stored for subsequent analysis. Figure 6-10 (b) compares the measured and simulated values of S_{22}*. It can be seen that there is good agreement between the measured and simulated results in terms of the range of S_{22}* impedances predicted by the model. Good impedance coverage is also observed at *Port* P_2 indicating that the tuner can match a wide range of antenna impedances.



(a)



(b)

Figure 6-10 (a) Tuner module test setup, (b) S_{22}* at 433 MHz

A key performance parameter of the tuner is its ability to match impedances with low loss. The relative transducer power gain ΔG_T was therefore measured with a manually adjusted, 2-port, load-pull setup using a ZVRE VNA [47] and Maury Model 1878G [148] triple stub tuner to adjust the load VSWR at P_2. The measured and simulated results are shown in Figure 6-11 with the VSWR at P_2 applied along trajectory *P*-*Q*-*R* as shown.

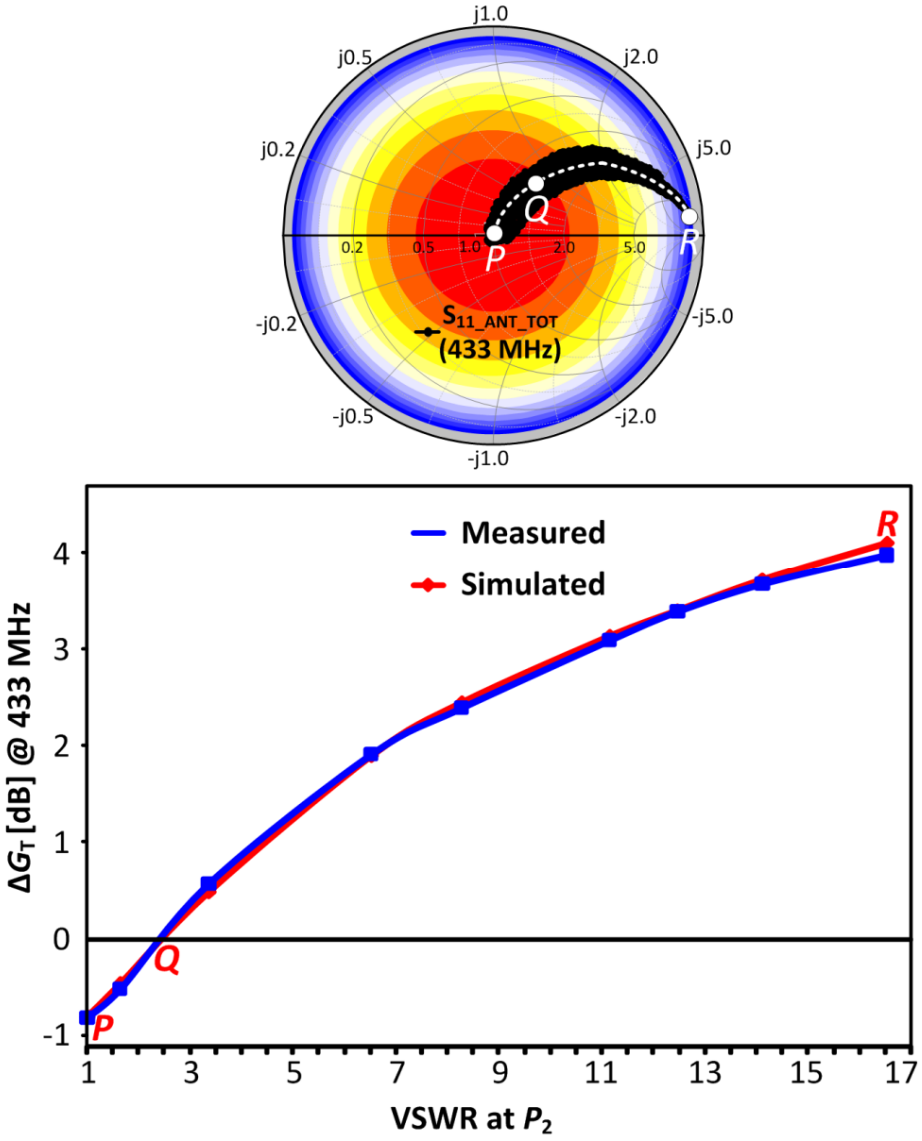


Figure 6-11 Measured and simulated values of ΔG_T at 433 MHz

The measured results show that the matching network provides increased power delivery to P_2 for a large span of VSWR values ranging from 1.7:1 to 16.5:1, with approximately 3.9 dB improvement for worst-case VSWR at P_2. For load VSWR = 1:1, the matching network has a maximum measured loss of 0.84 dB that is a substantial improvement compared to the value of 4.9 dB for the first-generation tuner. This improvement is attributed mainly to the low loss tunable capacitors employed for this design.

The final tunable antenna is shown in Figure 6-12 and measures 51 × 28 × 8 mm. The antenna uses identical PCB stackup and materials as the tuner module of Figure 6-6 and incorporates both the tuner and antenna in a single design. The matching circuit is placed on the top side and the tuning controller is placed on the bottom side as shown. Figure 6-13 (a) shows the measured values of S_{11} for the original 433 MHz AUT with *no tuning*, for the cases where the antenna was placed in free-space (ideal case) as well as on the human head and wrist. For the head and wrist test cases, the antenna was placed at a distance of approximately 1 mm above the skin surface using a LDPE spacer [162] to prevent skin contact. It can be seen that the AUT is correctly tuned for the free-space case but significant detuning is observed when the AUT is placed close to the human body.

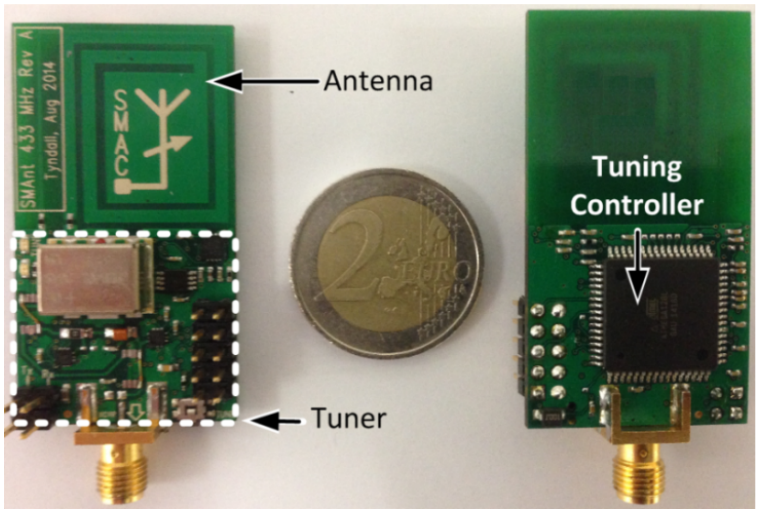
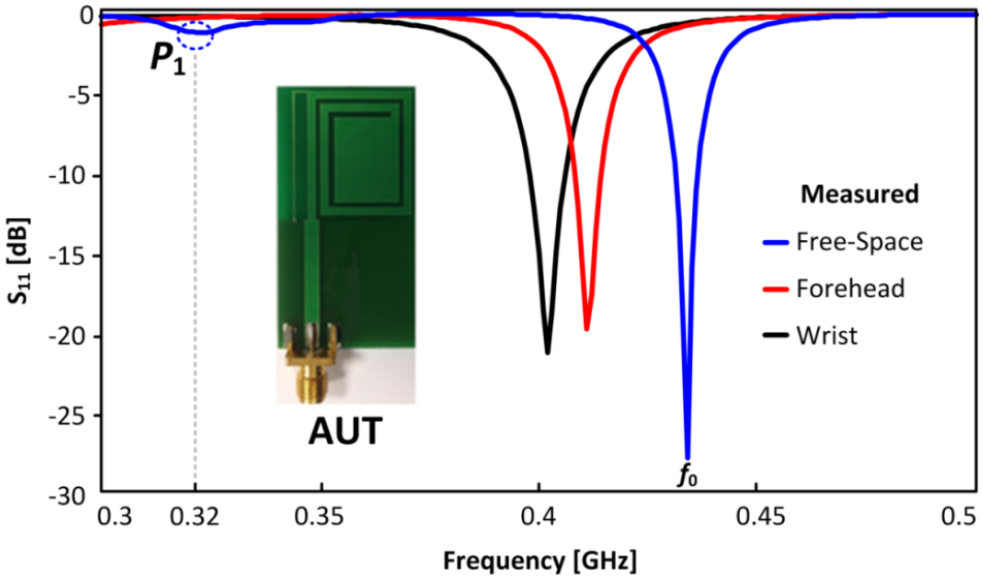
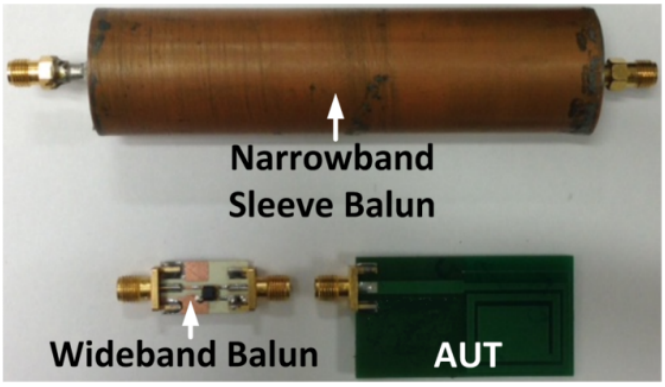


Figure 6-12 Photograph of final tunable antenna



(a)



(b)

Figure 6-13 (a) Measured AUT S_{11}, (b) Narrow and wideband balun designs

The measured AUT S_{11} results of Figure 6-13 (a) also reveal that a resonance was present in the free-space measurement. This is shown as point P_1 at occurs at a frequency of approximately 320 MHz. This resonance was determined to be due to bandwidth limitations of the sleeve balun. This balun suppresses cable shield currents over a relatively narrow bandwidth of approximately 28 MHz, centered at 433 MHz. A wideband balun design was therefore investigated and is shown in Figure 6-13 (b).

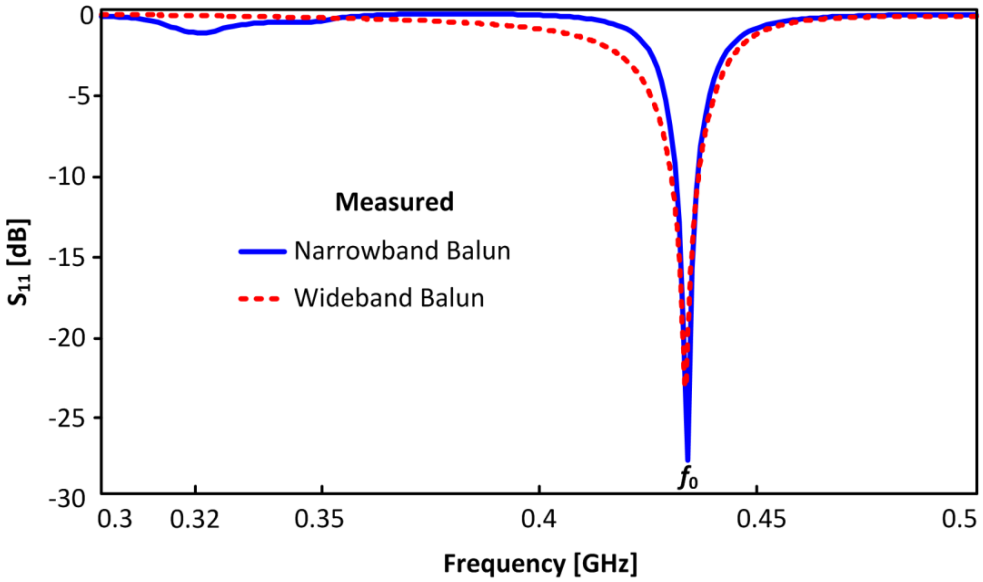


Figure 6-14 Measured AUT S_{11} response using narrow and wideband balun

This balun was implemented using a 1:1 wideband (4.5 - 3000 MHz) RF-transformer [98]. Figure 6-14 compares the measured AUT S_{11} responses of the narrow and wideband balun designs. It can be observed that the wideband balun does not exhibits resonant effects as previously. A slightly larger S_{11} (-10 dB) AUT bandwidth was also observed for the wideband balun due to greater RF transformer losses when compared to the sleeve balun case that uses a low-loss coaxial structure.

It was noted earlier that significant detuning effects were evident in Figure 6-13 (a) when the AUT was placed close to the human body. In contrast, the tunable antenna responses for the same test conditions are shown in Figure 6-15. In this case, the tunable antenna has a measured S_{11} (-10 dB) bandwidth of greater than 18 MHz for all cases. It can also be observed from Figure 6-15 that two resonances are observed in the measured S_{11} responses. For example in the free-space case, the addition of the matching network results in two resonances at frequencies of f_1 = 403 MHz and f_2 = 430 MHz approximately. This behaviour can be explained by comparing the measured S_{11} responses of the AUT and tunable antenna as shown in the Smith Chart of Figure 6-16 where the frequency is swept from 300 to 500 MHz.

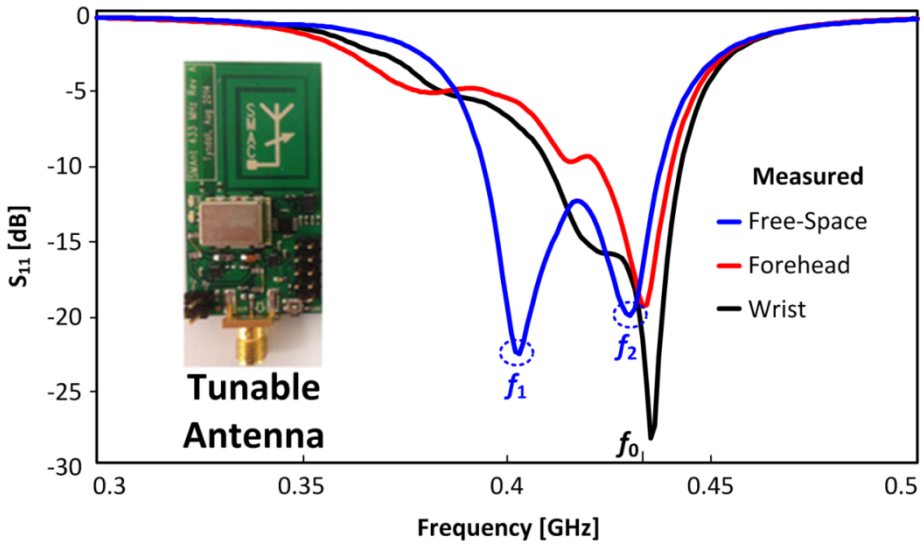


Figure 6-15 Measured antenna S_{11} for the tunable antenna

For the case of the AUT, the response shows a single resonant mode at frequency f_0 = 433 MHz. However, for the tunable antenna case, the addition of matching components C_1, C_2, C_3 and L_1 leads to an additional loop in the measured impedance profile, leading to a wider matching bandwidth and this behaviour is described in detail in similar work [171].

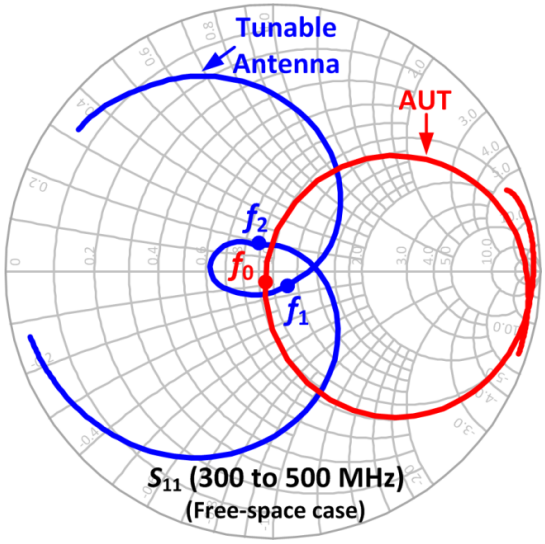


Figure 6-16 Comparing measured S_{11} of AUT and tunable antenna

The operation of the tuner during a tuning command is illustrated by referring to the oscilloscope measurement of Figure 6-17 using the tuner module shown in Figure 6-6. A load reflection coefficient of $|\Gamma_L| = 0.5$ with a phase of 0° at 433 MHz was applied to P_2 using a Maury Model 1878G [148] triple-stub tuner. The top trace shows the V_{FWD} signal during an exhaustive search (*Type A*). Prior to tuning the antenna, the measured V_{FWD} signal has a voltage $V_{FWD\text{-}A}$ which is proportional to P_{FWD}. Once initiated, the tuning algorithm searches all 1,024 states, taking a time $t_1 \approx 370$ ms to execute. Once the search is complete, the algorithm sets the final tuner state for maximum P_{FWD} corresponding to maximum voltage $V_{FWD\text{-}MAX}$. The lower traces shows that *Type B* tuning algorithm is approximately 10 times faster, taking ≈ 30 ms to execute.

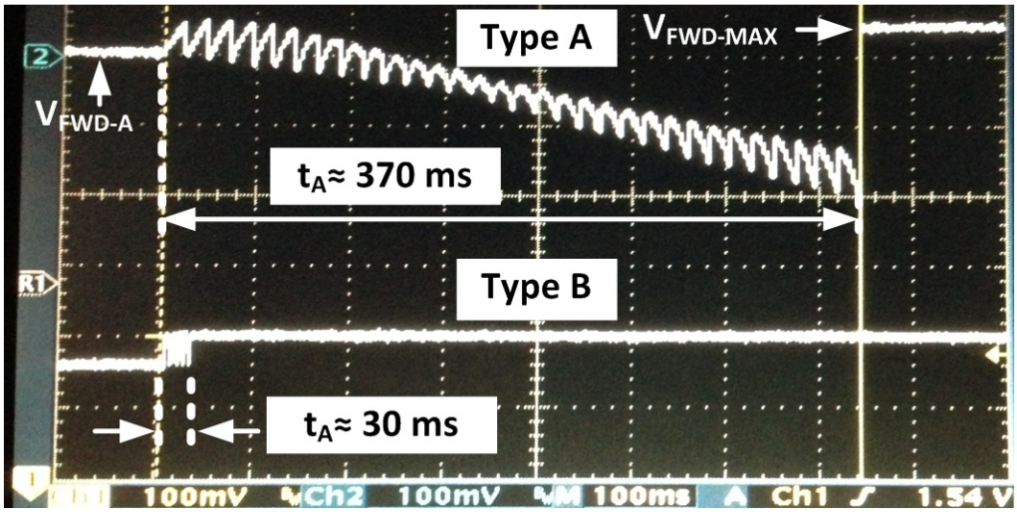


Figure 6-17 Oscilloscope measurement of V_{FWD} signal during tuning

Current consumption measurements of the prototype tunable antenna show that it requires a peak supply current of 32 mA DC during a tuning operation. Once the tuning operation is completed, the tuning controller or micro-controller is placed in standby mode and the RF power detector is placed in shutdown mode. In this mode, all current capacitor states for tunable capacitors C_1 and C_2 are maintained, thereby maintaining the current impedance match settings.

This mode also means that the DC supply current to the antenna can be significantly reduced to a value of approximately 0.25 mA. The micro-controller clock frequency used for the above measurements was 8 MHz.

As discussed in Section 4.2.5, the benefits of antenna impedance matching were investigated in relation to power consumption of wireless sensors that use fixed (non-tunable) antenna matching circuits. It was shown that recovering 4 dB of link budget using a commercial radio transceiver, without matching, requires a 4 dB increase in *PA* transmit power. At maximum PA output power, this requires an additional 12.54 *m*A of DC supply current, for the duration of each radio transmission. In contrast, the proposed tunable antenna, when placed within a wearable device that is securely attached to the body during use, would only need to be tuned once, after placement, with only periodic tuning required thereafter. In such cases, there is a clear benefit in terms of improving RF link quality and reducing power consumption, especially for battery-operated WSN devices with limited capacity.

6.5 **Conclusions**

In this chapter, a compact 433 MHz antenna-integrated tuner was demonstrated. Prototype measurements show up to 3.9 dB of improvement in power delivery to the antenna for a VSWR of 17:1 with a maximum loss of 0.84 dB and -10 dB bandwidth of ≥ 18 MHz. The proposed solution offers particular performance advantages for wearable BSN devices in terms of improving RF power delivery to the antenna, reducing current consumption, and providing longer battery life. Improved RF link quality and the need for less data re-transmissions is also a critical advantage for health-related applications. The prototype tunable antenna was developed as a stand-alone device but could also be integrated into existing wearable BSN devices using a host CPU for tuning control. Although the work focuses on the 433 MHz ISM band, the same methods can be applied to other frequency bands. In order to compare the performance of the first and second-generation antenna tuning solutions, Table 6-2 tabulates a number of important performance criteria. It can be

seen that in terms of size, the second-generation has approximately 1 % the volume of the original solution. The current consumption of the second-generation tuning solution is reduced by 78 % with a 91 % improvement in tuning time.

Parameter	Unit	First Generation	Second Generation
Size (L × W × H)	mm	300 × 200 × 25	51 × 28 × 8
Peak DC supply current	mA	147.7	32
Maximum tuning time	ms	340	30
Maximum tuner loss @ 433 MHz	dB	4.9	0.84
Number of tunable states	--	256	1024

Table 6-2 Performance comparison between first and second-generation tuners

It can also be seen from Table 6-1 that a significant 4 dB reduction in tuner loss was achieved using high performance tunable capacitors [167] that have become available since the development of the first-generation solution as well as a High-Q inductor [168]. Continuing advances in tunable component technology will mean that the above tuner losses can be decreased with the adoption of the latest available tunable component technology.

Chapter 7. Dual-Band Antenna Design

7.1 Background

This chapter presents the design of a low-cost, dual-band antenna topology with small dimensions. The motivation behind this design was to develop a single-feed antenna that could cover both the 433 MHz and 2.45 GHz ISM bands. The ability to switch between both frequency bands opens up new possibilities in improving Quality of Service (QoS) for WSN applications. It was noted in Chapter 3 that very few compact antenna structures are reported in the literature that can provide Multi-ISM-band coverage in the case where the frequency separation between both frequency bands is large. An example of such a case is dual-band operation in both the 433 MHz and 2.45 GHz ISM bands in Europe. The goal of this chapter is to develop an antenna design that addresses this technology gap.

In this chapter, the single-band 433 MHz antenna [153] of Chapter 5 is used as a starting point for the design. A key motivation was to make a number of improvements to certain aspects of the original design while, at the same time, developing a new antenna topology that adds a second resonant mode for the 2.45 GHz band. The new design achieves dual-band operation without increasing the size of the original antenna. Details of the design, implementation, and characterization of the antenna are presented in this chapter and have been published in [172].

7.2 Review of the original 433 MHz antenna design

The first stage of the design process for the dual-band antenna was to re-evaluate the 433 MHz antenna design [153]. As shown in Figure 7-1, the simulated surface current distribution showed that very little current flowed at the centre of the patch element shown as region A, and it was only at the edges of the patch element that the current density was largest. It was also shown that the capacitive stub at point B increased the total capacitance of the radiating element with respect to ground and that a large shunt inductance was required to cancel the net capacitance of the patch and stub. This was achieved in the original design by maximizing the length *L* of the inductive section as well as decreasing its width *W* by using a long, narrow element as shown. The design methodology for this antenna was to remove the patch element to reduce the total capacitance of the radiating element and achieve 433 MHz resonance using a spiral element only, together with a lower loss inductive section. An additional goal was to convert the capacitive stub of the previous design into a resonant element at 2.45 GHz.

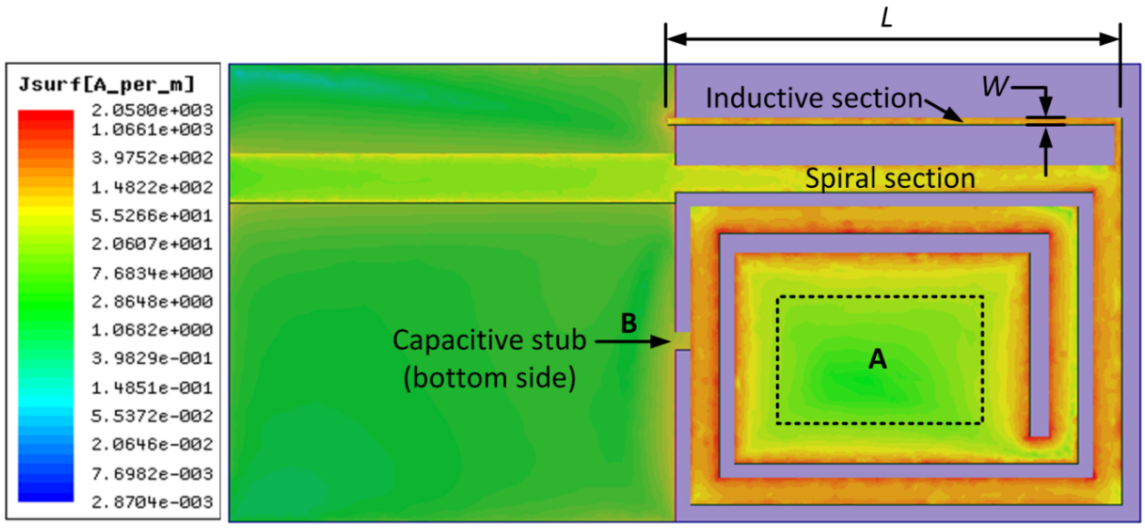
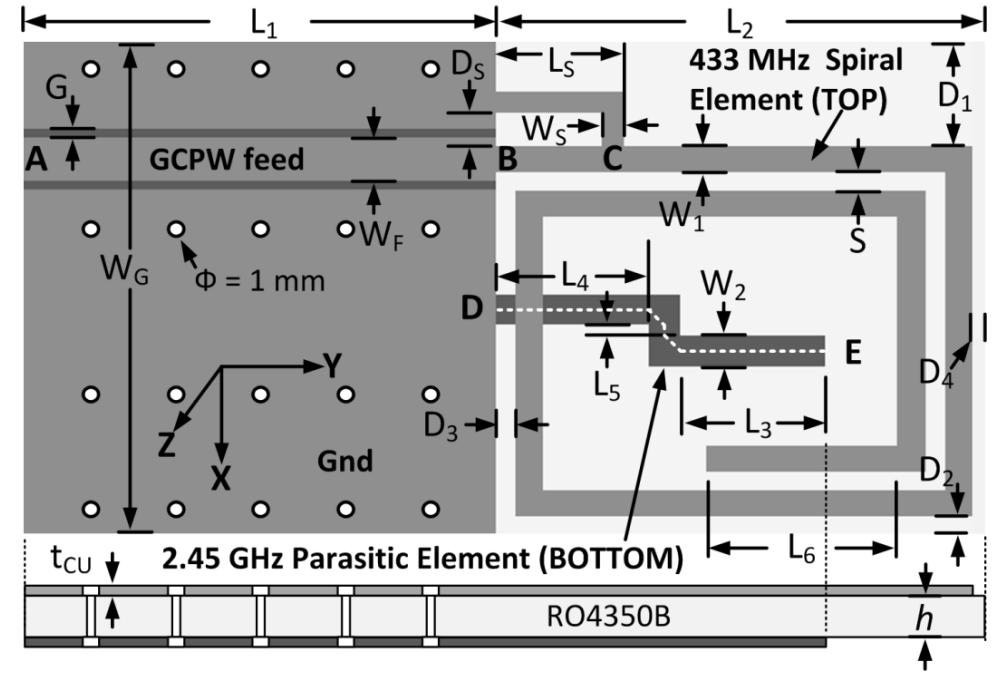
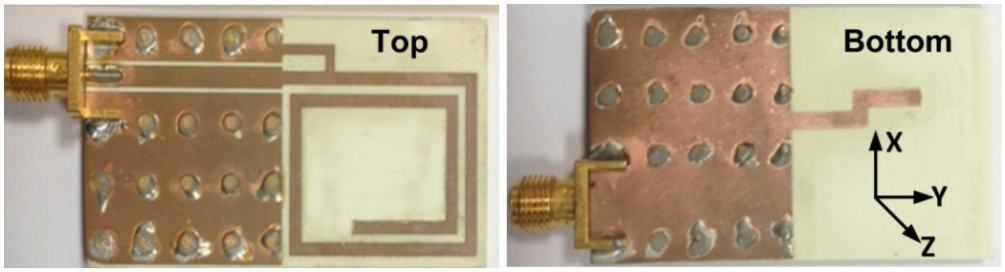


Figure 7-1 Simulated surface currents of 433 MHz antenna [153]

7.3 Antenna Design



(a)



(b)

Figure 7-2 (a) Configuration of proposed antenna, (b) Photograph (top and bottom)

Figure 7-2 shows the configuration of the proposed dual-band antenna. In contrast to the antenna of [153] that was printed on FR-4 material, a lower loss RO4350B substrate [139] was used in this case to reduce the substrate losses.

This material is a double-sided laminate with a relative permittivity ε_R = 3.6 and loss tangent tanδ = 0.0031 with a copper thickness of 1 Oz (0.035 mm) with substrate height h = 1.524 mm. The total size of the antenna is 51 mm × 27.4 mm and in this case, was excited using a 50-Ω grounded-coplanar-waveguide (GCPW) feed-line at Point A shown, referenced to ground on both the top and bottom layers, and thus eliminating the requirement for placing a VIA and its associated parasitics on the radiating element, as in the previous design. A ground plane was printed on the bottom side of the substrate with dimensions of $W_G \times L_1$ and the co-planar ground structures on the top side were connected to the ground plane using a series of plated through-hole vias as shown.

Similar to the original 433 MHz antenna of [153], for the Lower Band (433 MHz), a square-spiral structure of width W_1 was printed on the top layer at the end of the feed line at Point B. This structure is a variation of an IFA topology with the spiral used to minimize the required area for this resonant section. At Point *C*, a shunt inductive element was used to allow impedance matching of the antenna impedance to 50-Ω without the need for discrete matching components. In this case, in contrast to [153], a smaller, wider and lower loss inductive section was used.

For the Upper Band (2.45 GHz), a parasitic monopole element was printed on the bottom layer, with the element shorted to the groundplane at Point *D* as shown. This element has a width W_2 and a total length of $L_3 + L_4 + L_5 + \sqrt{2}\ W_2$ as defined along the centre of the element as shown. The monopole is staggered to maximize the monopole length and at the same time, minimize the degree of end coupling to the spiral element at Point *E* as shown.

Parameter	Value (mm)
L_1	25
L_2	26
L_3	11.02
L_4	8
L_5	0.64
L_6	7.56
L_S	6.69
W_G	27.4
W_F	2.42
W_S	1.14
W_1	1.45
W_2	1.68
D_1	7.3
D_2	1.0
D_3	1.0
D_4	1.25
D_S	1.88
G	0.5
S	1.0
h	1.524
t_{CU}	0.035

Table 7-1 Final design parameters for the antenna

7.4 Antenna Simulation

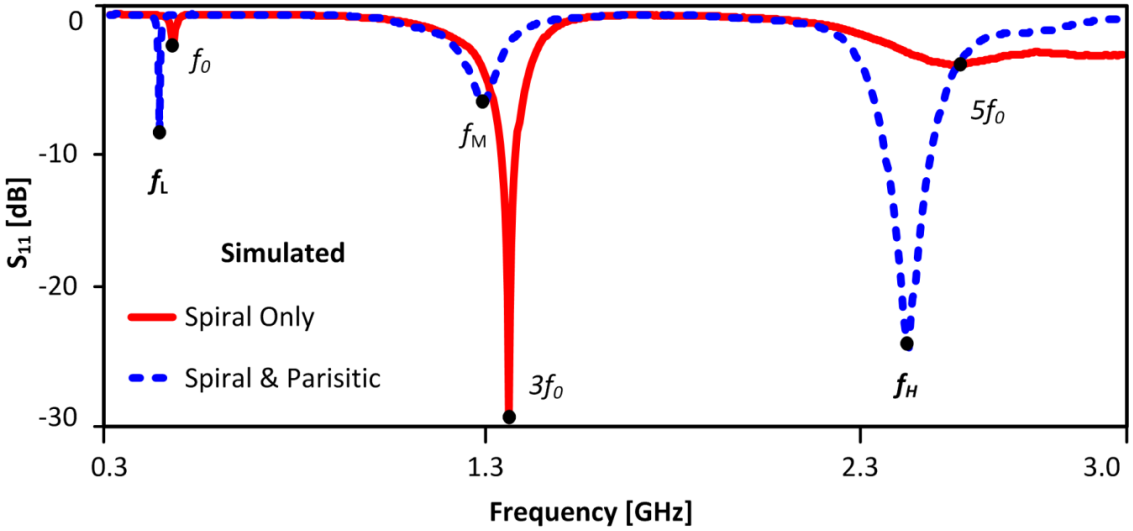


Figure 7-3 Simulated antenna S_{11} with and without the parasitic element

The generalized resonant behaviour of the antenna with and without the parasitic monopole element was first studied in simulation using a full-wave EM model of the antenna ANSYS HFSS [42]. Table 7-1 lists the parameters that were employed, except for L_6, L_3 and L_S that are specified here as L_6 = 10 mm, L_3 = 5 mm and L_S = 5 mm. Figure 7-3 shows the simulated antenna S_{11} from 300 MHz to 3 GHz. The multi-band response of the antenna relates fundamentally to the intrinsic resonant properties of the spiral element which was designed to have a total electrical length of ≈ λ/4 at f_0 =433 MHz. The simulated response in Figure 7-3 shows that with only the spiral element present, three distinct resonances are observed. The lowest resonance is shown at f_0, with two, higher frequency resonances observed at approximately odd multiples of f_0 i.e. $3f_0$ and $5f_0$. This behaviour is characteristic of a quarter-wavelength antenna structure that has harmonic resonances at odd multiples of the antenna's fundamental frequency [25]. The resonance at $3f_0$, or approximately 1.3 GHz, lies well outside both the ISM bands of interest and is therefore not considered further for this application but could possibly be explored in the future for GPS applications.

The resonances at f_0 and $5f_0$ are approximately 5% and 10% above the upper limits of the 433 MHz and 2.45 GHz ISM bands, respectively, but are not well matched to the 50-Ω source impedance. It can be seen from Figure 7-3 that adding the parasitic element leads to a similar resonant response. However, in the case where the monopole element is present, the three resonant frequencies occur at lower frequencies and the impedance matching is greatly improved at the two frequencies of interest for this application (f_L = 433 MHz and f_H = 2.45 GHz).

To understand this behaviour, the Smith Chart of Figure 7-4 shows the simulated antenna input impedance, with and without the parasitic element present, from 2 to 3 GHz. At Point A, with only the spiral element present, the antenna input impedance at 2.45 GHz is non-resonant and inductive. At Point *B*, a small resonance is also observed at a frequency of 2.55 GHz. When the parasitic monopole element is now introduced, a net capacitive loading effect is observed that results in a lowering of the resonant frequency from 2.55 to 2.45 GHz as well as enabling the antenna input impedance to be matched close to 50-Ω at 2.45 GHz. This is shown graphically as the movement of the impedance from Point *B* to Point *C* in Figure 7-4.

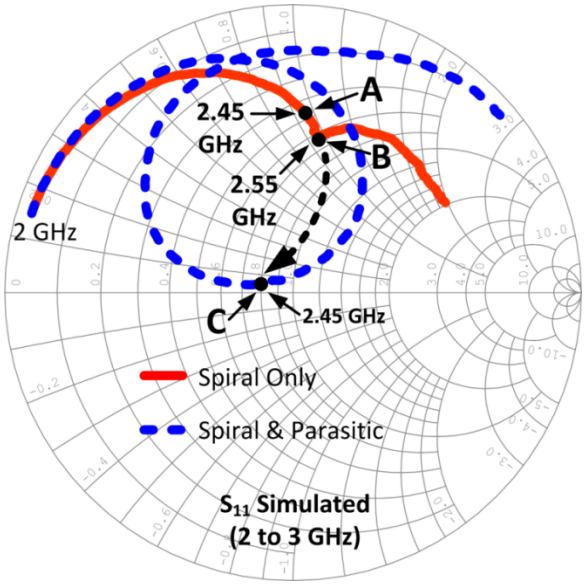
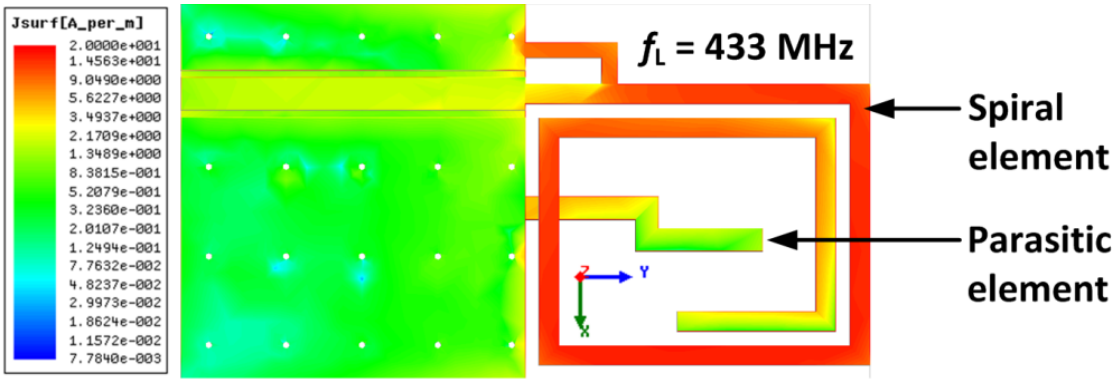
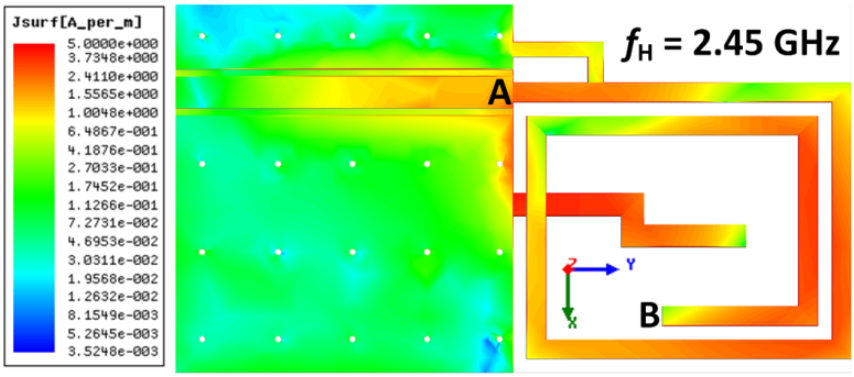


Figure 7-4 Simulated antenna S_{11} with and without the parasitic element

In order to visualize the resonant modes of the antenna, the simulated surface current distributions are shown in Figure 7-5. It can be seen from Figure 7-5 (a) that a large current flows on the spiral element at 433 MHz, with a much smaller current flow on the parasitic monopole element. Figure 7-5 (b) shows that at 2.45 GHz, the spiral has a second resonant mode, with three current maxima and two current minima present. This indicates that the spiral has an electrical length (from point A to B) of approximately 5λ/4 at 2.45 GHz. In this case, a large current is seen to flow on the parasitic element that has a resonant length of ≈ λ/4 at 2.45 GHz and is excited via mutual inductive coupling with the driven spiral element.



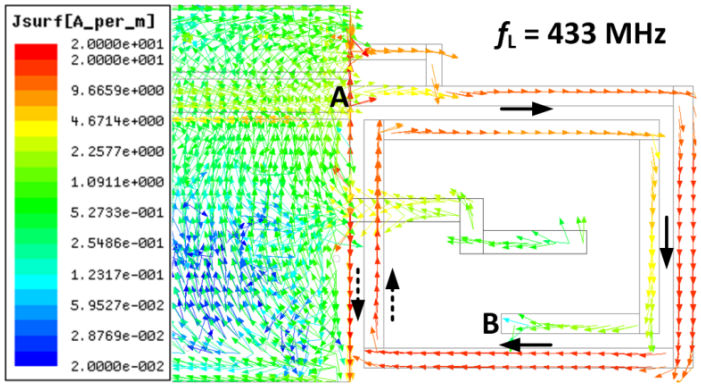
(a)



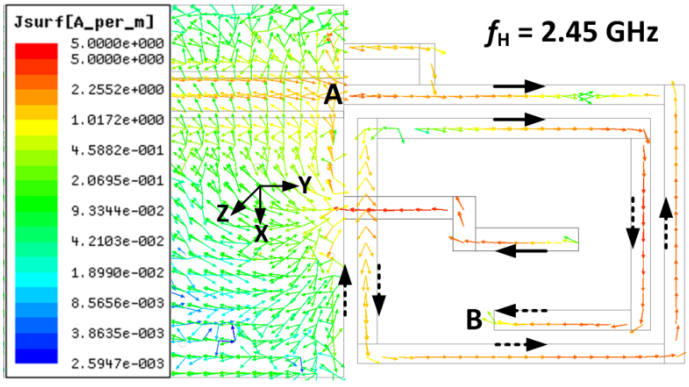
(b)

Figure 7-5 Simulated surface current distributions (a) 433 MHz, (b) 2.45 GHz

The simulated surface current distributions are shown in vector form in Figure 7-6. Figure 7-6 (a) shows that the direction of current flow on the main spiral arm at 433 MHz is uniform along the length of the spiral from point A to point B. Figure 7-6 (b) shows that at 2.45 GHz, in-phase currents (drawn as solid arrows) occur mainly on the horizontal sections of the spiral element. Out-of-phase currents (drawn as dashed arrows) are observed largely on adjacent vertical sections. The combined radiation from the spiral and parasitic elements at 2.45 GHz is therefore expected to be monopole-like, mainly due to the large currents flowing on the parasitic element, leading to enhanced radiation in the *x*-*z* plane with nulls present along the y-axis.



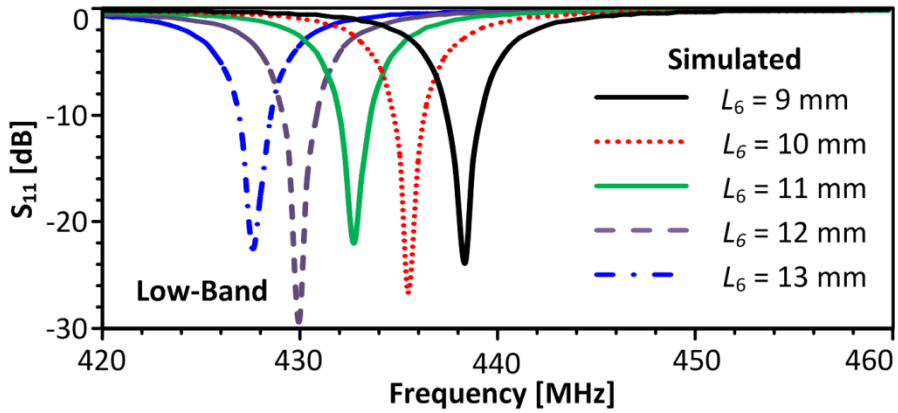
(a)



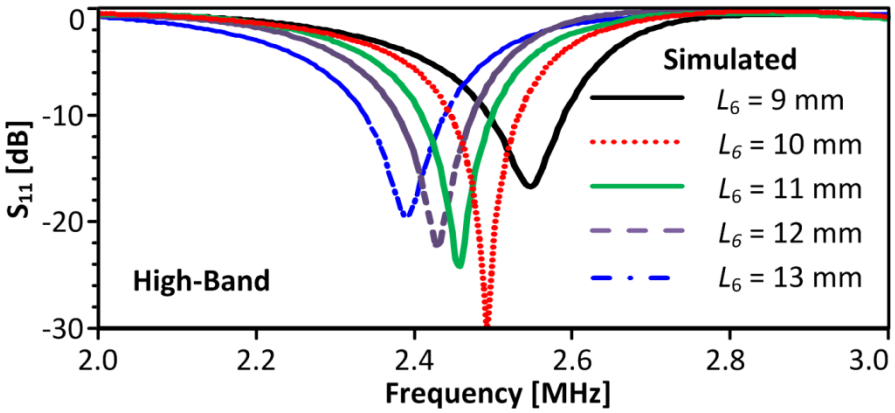
(b)

Figure 7-6 Simulated surface current distribution (a) 433 MHz, (b) 2.45 GHz

In order to optimize the antenna for dual-band operation, the effects of several key parameters were investigated. For subsequent discussion and presentation of results, only the lower and upper band responses are considered and for clarity are shown separately. The influence of the spiral length on the lower and upper bands was first studied. The spiral end-length L_6 was varied while keeping all other parameters constant according to the values listed in Table I. Figure 7-7 (a) and Figure 7-7 (b) show that the resonant frequencies for both the low and high bands decrease with increasing L_6 and the impedance matching for the upper band, in particular, is also affected.



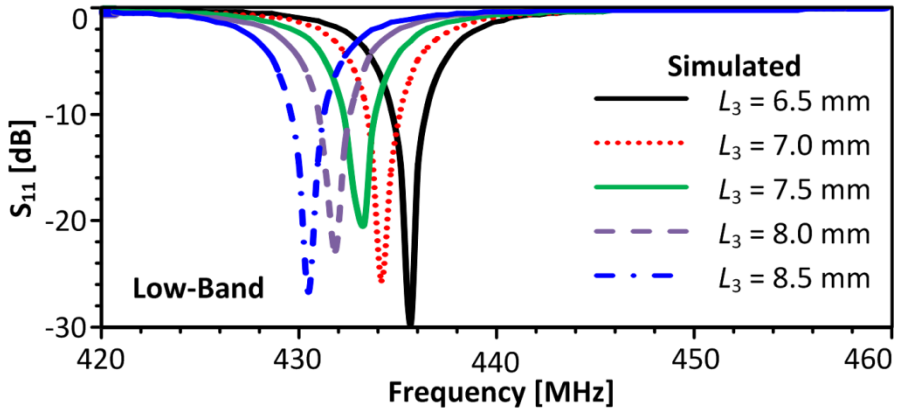
(a)



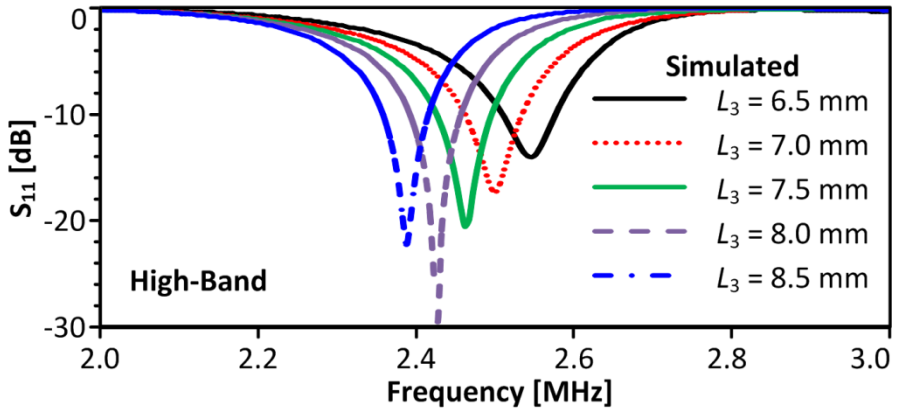
(b)

Figure 7-7 Simulated antenna S_{11} for varying L_6 (a) Low-band, (b) High-band

The influence of the parasitic monopole end-length parameter L_3 is summarized in Figure 7-8. It can be seen that the resonant frequencies for both the lower and upper bands are also seen to decrease for increasing L_3 and the impedance matching for both bands is also affected, particularly for the upper band.



(a)

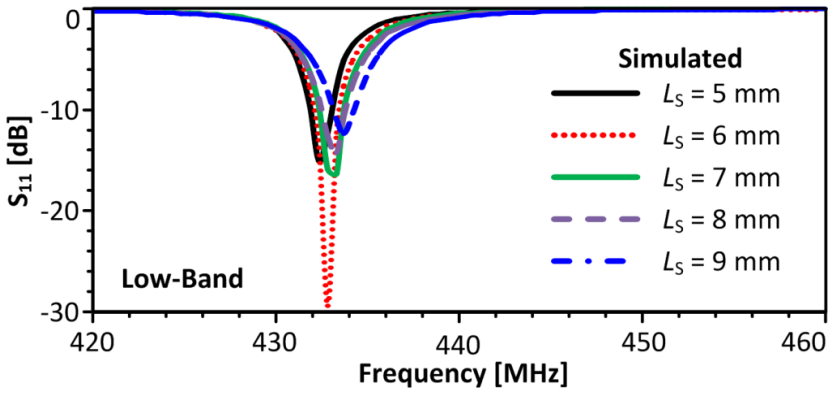


(b)

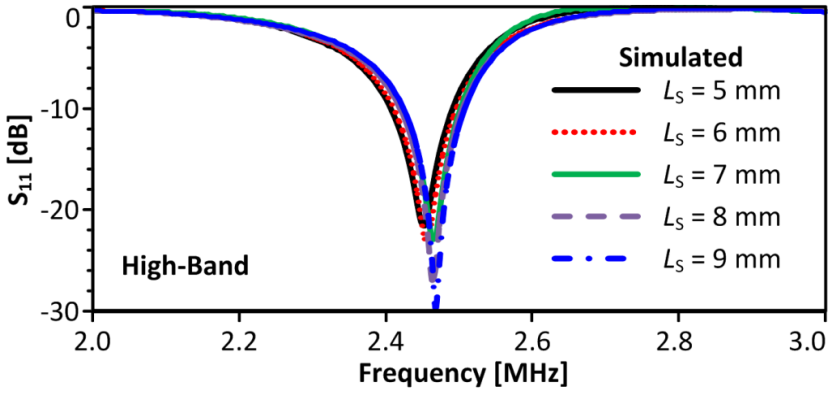
Figure 7-8 Simulated antenna S_{11} for varying L_3 (a) Low-band, (b) High-band

The mutual inductive coupling between the spiral and parasitic element accounts for the observed effects as lengthening either element leads to a decrease in resonant frequencies for both bands. The effects of varying the shunt inductance length L_S were also investigated as shown in Figure 7-9.

It can be observed that parameter L_S allows a good degree of independent control of the impedance matching for the lower band with a small effect on the resonant frequency for both bands but primarily for the low band. These parametric simulations show that frequencies f_L and f_H are primarily determined by the total length of the spiral element.



(a)



(b)

Figure 7-9 Simulated antenna S_{11} for varying L_S (a) Low-band, (b) High-band

The preceeding results also show that a sufficient degree of independent control is possible using parameters L_3, L_6 and L_S to enable the Lower and Upper frequency bands to be tuned and matched over the frequency range shown. Once the main parameters were identified, the design was then optimized using the Optimetrics feature of Ansys HFSS [173].

The parameters chosen for inclusion in the optimization process are listed in Table 7-2 with the minimum and maximum limits determined experimentally in simulation.

Parameter	Start Value (mm)	Minimum (mm)	Maximum (mm)	Min Step (mm)	Max Step (mm)
L_3	5.00	7.00	13.07	0.01	0.5
L_4	5.00	4.00	9.00	0.01	0.5
L_5	0.50	0.00	1.00	0.01	0.5
L_6	11.00	5.00	18.50	0.01	0.5
L_S	5.30	4.00	25.00	0.01	0.5
D_S	0.42	0.40	1.20	0.01	0.5
D_3	1.00	0.50	3.00	0.01	0.5
W_F	2.41	1.00	3.00	0.01	0.5
W_2	1.77	1.00	3.00	0.01	0.5
W_S	1.20	0.50	1.50	0.01	0.5

Table 7-2 Antenna design parameters included for optimization

The dimensional parameters of the antenna were optimized using the Quasi-Newton Method [174] that is an integral part of HFSS [42]. Two cost functions (*CF*) were defined. *CF_A* was used to search for the optimal dimensional parameters of the spiral element by minimizing the antenna input reflection with a target of $|\Gamma_{IN}| = 0$ at 433 MHz. Similarly, *CF_B* was used to search for the optimal parameters for the parasitic element by minimizing the antenna input reflection with a target of $|\Gamma_{IN}| = 0$ at 2.45 GHz. It was found during initial trials that the variations of the parameters of Table 7-2 had a much greater effect for the 433 MHz band in comparison to the 2.45 GHz band and the optimizer had difficulty finding a solution. The cost function *CF_A* was therefore assigned a weighting of 1.5 times that of *CF_B* as the 433 MHz spiral element was much more sensitive and narrow-band compared to the 2.45 GHz band. The optimization process took 334 iterations with a total cost of 0.05 and a total computation time of approximately 8 hours using a machine with 24 GB of RAM and an Intel® Xeon® 8-core CPU running at 1.6 GHz. The final, optimized antenna dimensions for the design are listed in Table 7-1.

7.5 Measured Results

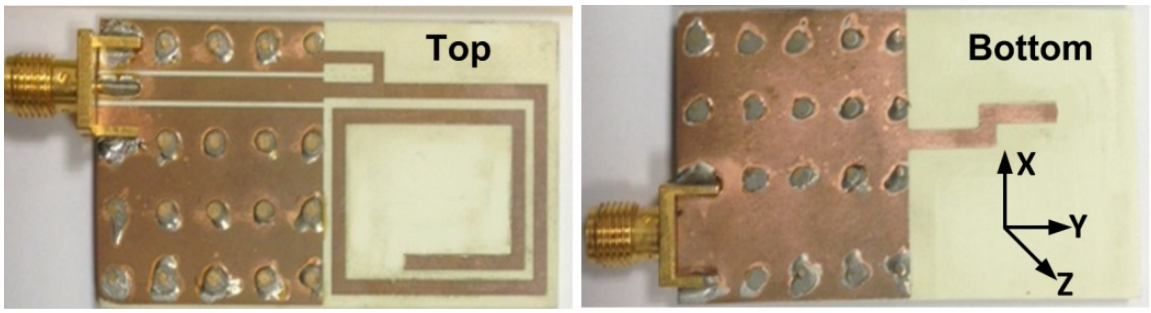


Figure 7-10 Photograph of prototype antenna

In order to verify the proposed design, a prototype antenna was fabricated as shown in Figure 7-10 using a LPKF ProtoMat C60 milling machine [45]. The top and bottom ground interconnections were made using brass pins as shown. The impedance and radiation characteristics of the antenna were then measured in a semi-anechoic chamber [49] using a Model ZVRE Rohde and Schwarz VNA [47]. In order to suppress cable current effects, the measurements were performed using a balun [66] and ferrite-beaded cable.

Figure 7-11 shows the lower band response with reasonable agreement shown between measurement and simulation. The antenna has a measured S_{11} (-10 dB) bandwidth of 2 MHz at 433 MHz. The discrepancies in resonant frequency originate from a combination of fabrication tolerances for the prototype and the use of a simplified excitation model that does not consider the effects of the balun. Figure 7-12 shows the upper band response and the antenna has S_{11} (-10 dB) bandwidth of 132 MHz at 2.45 GHz.

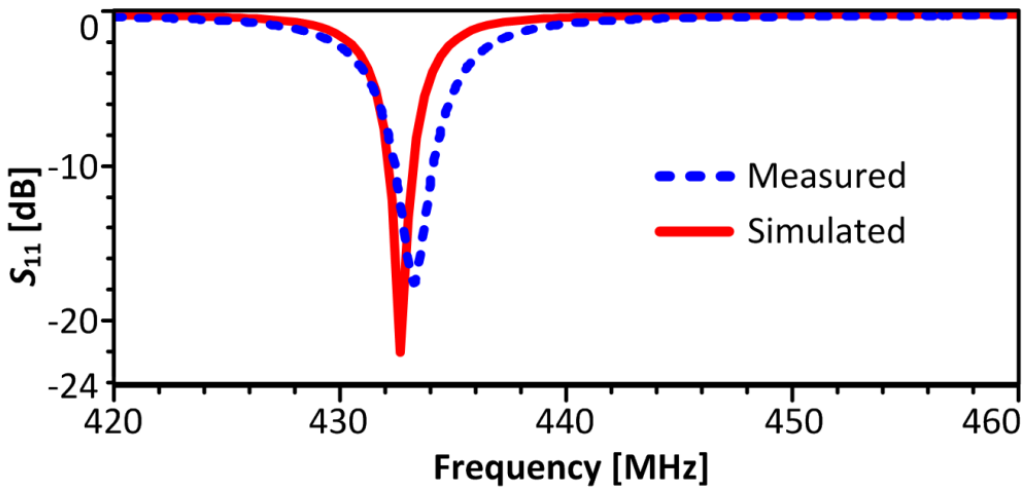


Figure 7-11 Comparing measured and simulated antenna S_{11} at 433 MHz

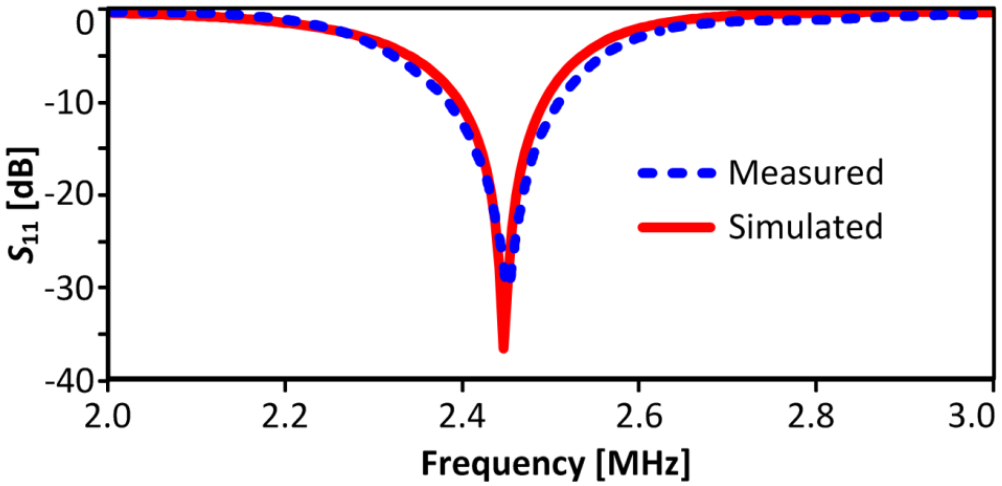
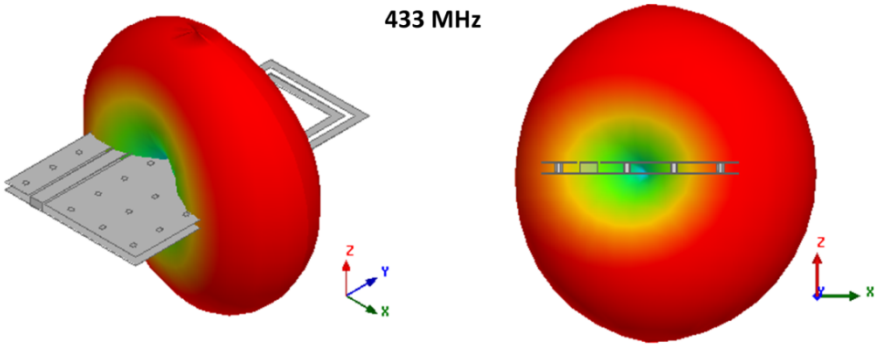
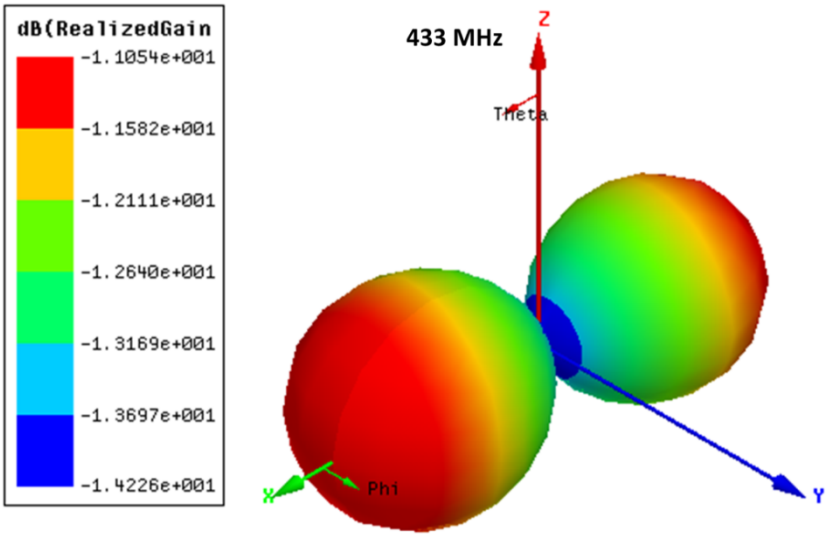


Figure 7-12 Comparing measured and simulated antenna S_{11} at 2.45 GHz

Figure 7-13 (a) shows the normalized 3D realized gain patterns for the antenna at 433 MHz as derived in simulation. The antenna has omni-directional radiation characteristics in the *x*-*z* plane. Figure 7-13 (b) shows that the simulated peak realized gain is approximately -11.1 dBi.



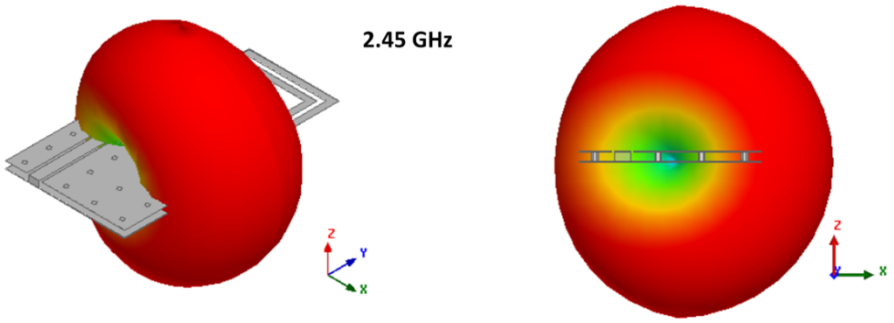
(a)



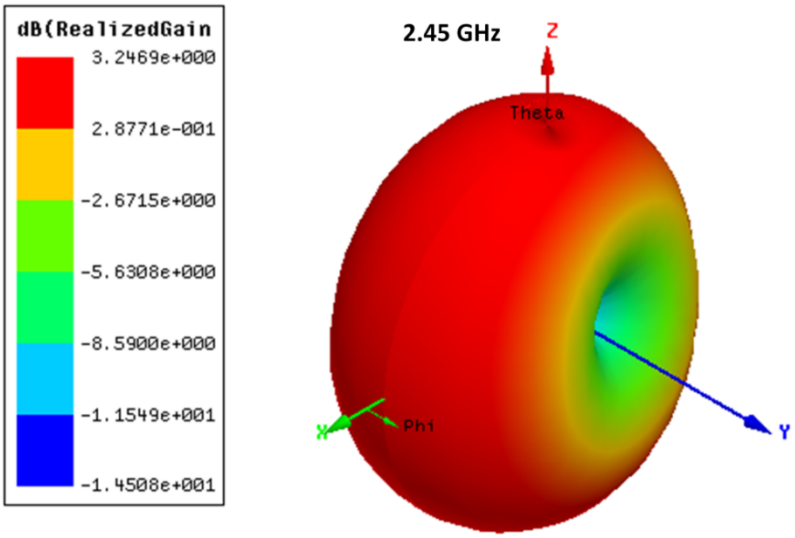
(b)

Figure 7-13 Simulated 3D gain at 433 MHz, (a) Normalized, (b) Un-normalized

Figure 7-14 (a) shows the 3D realized gain patterns for the antenna at 2.45 GHz as derived in simulation. It can be seen that the antenna also exhibits omni-directional radiation characteristics in the *x*-*z* plane at this frequency. Figure 7-14 (b) shows that the simulated value of peak realized gain is approximately +3.25 dBi.



(a)



(b)

Figure 7-14 Simulated 3D Gain at 2.45 GHz, (a) Normalized, (b) Un-normalized

The measured and simulated radiation patterns for the principal planes are shown in Figure 7-15. It can be observed from Figure 7-15 (c) and Figure 7-15 (d) that the measured and simulated co-polarized radiation patterns correlate well in the *x*-*z* plane, both at 433 MHz and 2.45 GHz. However, the measured radiation patterns in the *x*-*y* and *y*-*z* planes are in poor agreement, especially at 2.45 GHz. The reason for the discrepancy is thought to relate to the measurement setup used for radiation pattern measurements as shown in Figure 7-16. For the *x*-*z* plane measurement, the test setup of Figure 7-16 (a) was employed. The antenna was connected to a balun [66] as shown and a flexible RF absorber material was used to shield the upper 30 cm of the feed-cable and balun. The antenna was then rotated in the *x*-*z* plane, about the *y*-axis as shown, with the axis of rotation, as required, placed close to the origin of the spherical co-ordinate system that was used in simulation, shown as the cross-shape in Figure 7-16. The measured results in the *x*-*z* plane therefore correlate reasonably well with the simulated case in terms of symmetry.

However, for the *x*-*y* plane measurement and similarly for the *y*-*z* case, a different antenna configuration was necessary as shown in Figure 7-16 (b). In this case, a 90° SMA adapter was required to enable rotation of the antenna about the *z*-axis shown. However, the adapter has the effect of moving the axis of measurement away from the phase-centre of the antenna when measuring the *x*-*y* and *y*-*z* patterns as well as increasing the possibility for coupling between the antenna and the ferrite absorber material and balun, especially for the upper band at 2.45 GHz. It is believed that these effects explain the observed discrepancies as these measurement details could not be modelled in simulation. Although not ideal, improvements to the measurements setup could be made and it is considered that the radiation pattern measurements are nonetheless in sufficient agreement with the simulations for the purposes of verifying the radiation properties of the new design.

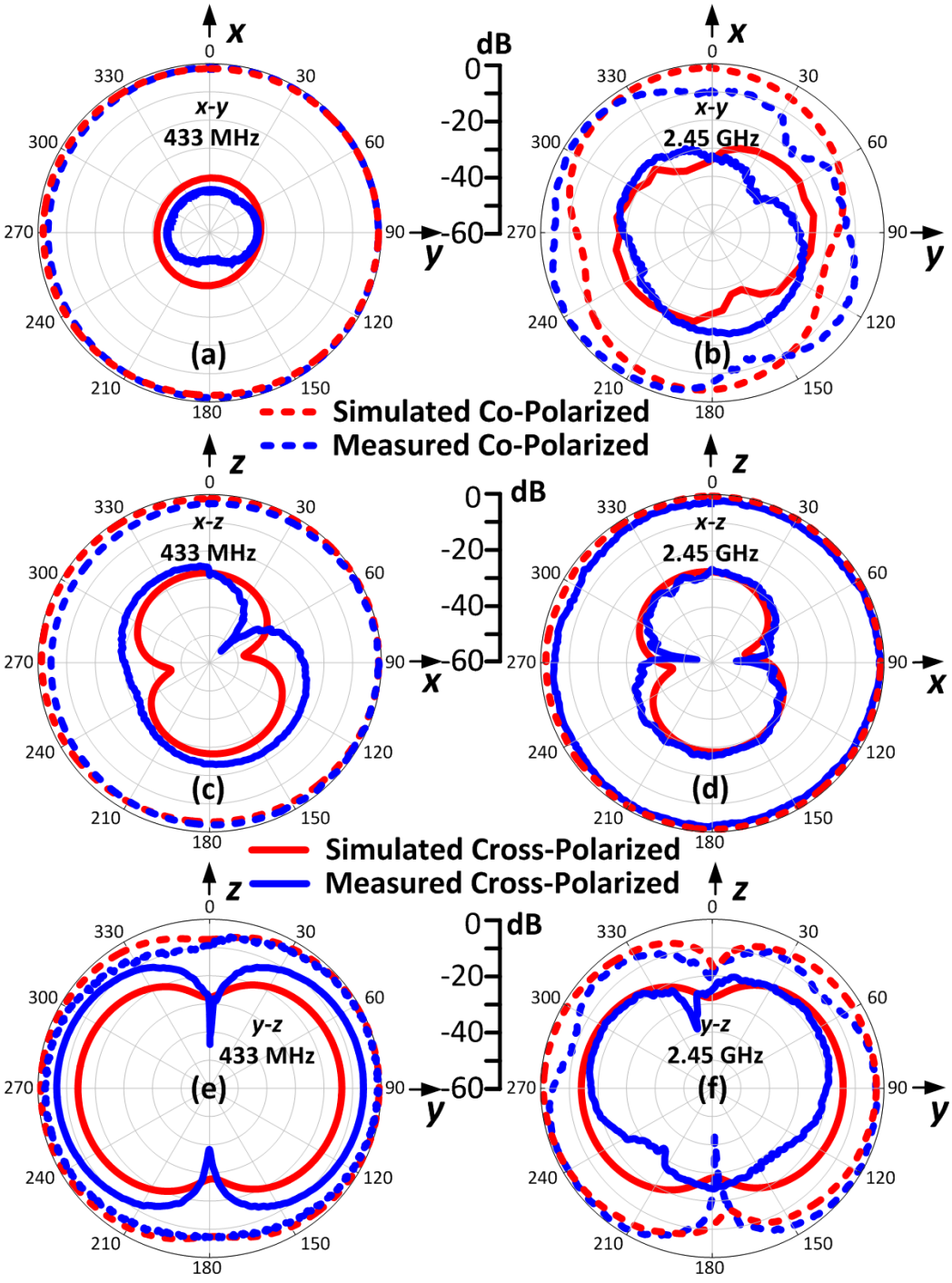
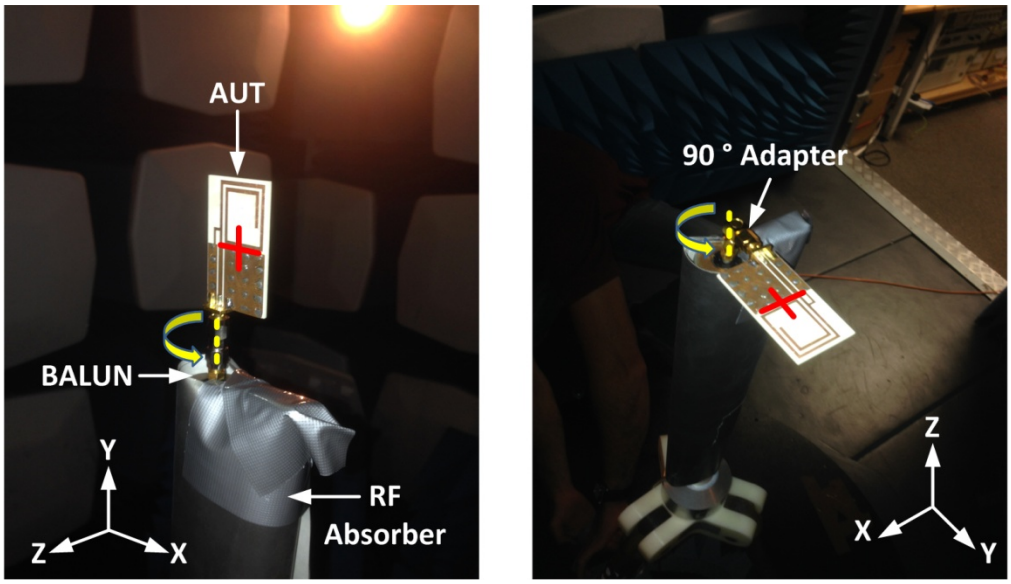


Figure 7-15 Measured and simulated radiation patterns



(a) (b)

Figure 7-16 Radiation pattern measurement setup (a) *x-z* plane, (b) *x-y* plane

The measured and simulated gain and radiation efficiency figures for the antenna are summarized in Table 5-2 and are specified at 433 MHz and 2.45 GHz. The peak realized gain was measured as -11.5 dBi at 433 MHz and +0.5 dBi at 2.45 GHz with the maximum gain measured in the *x-z* plane for both frequency bands. At 433 MHz, the measured peak realized gain figures are in good agreement with the simulated case with a difference of approximately 0.5 dB observed. At 2.45 GHz, the measured peak realized gain figure is 2.75 dB less than the simulated case and is most likely due to the previously described non-idealities in the measurement setup.

Test Case	Peak Realized Gain (dBi)	Radiation Efficiency (%)
Simulated (433 MHz)	-11.05	7.9
Measured (433 MHz)	-11.5	NA
Simulated (2.45 GHz)	3.25	89
Measured (2.45 GHz)	0.5	NA

Table 7-3 Antenna Gain and Radiation Efficiency at 433 MHz and 2.45 GHz

The antenna has a simulated radiation efficiency of 7.9 % at 433 MHz with a greatly improved efficiency of 89 % at 2.45 GHz because the parasitic element is of resonant length at 2.45 GHz.

7.6 Conclusions

A compact, low cost, single-feed planar antenna that operates in both the 433 MHz and 2.45 GHz ISM bands has been developed. Dual-band operation is achieved using a spiral element and a parasitically coupled monopole element. The antenna is realized in a compact size of $0.07\lambda \times 0.05\lambda$ at 433 MHz including the groundplane. The antenna is linearly polarized with omni-directional radiation characteristics. The dual-band feature is implemented passively with no requirement for additional active elements with associated RF losses and increased power requirements. Band switching allows adaptive control of antenna gain to suit the link requirements of the application. The relatively low gain and radiation efficiency figures at 433 MHz are expected since the antenna is electrically small [17]. However, when the Free-Space-Path-Loss L_{FS} [175] at 433 MHz versus 2.45 GHz is considered, assuming line-of-sight communications, there is approximately 15 *dB* less attenuation at 433 MHz compared to 2.45 *GHz* (for the same *Tx* power) and this can offset the low efficiency performance of the antenna at 433 MHz. In addition, comparing the gain of the proposed antenna to a loop antenna of similar size [96], it can be seen that the proposed antenna achieves approximately 9 dB more gain at 433 MHz. The ability of the antenna to cover both the lower and upper extents of the UHF ISM bands together with its small physical size and cost make it suitable for a wide variety of short-range, WSN applications. The results of this chapter have been published in [172].

Chapter 8. Conclusions and Future Work

8.1 Summary

This final chapter summarizes the contributions of the research contained in this thesis. It also highlights the main advancements made in antenna design for BSN applications as well as a description of future work. A review of the literature showed three key antenna-related design challenges that currently exist for wireless sensor networks. The first challenge relates to the continuing trend for miniaturization that is leading to the development of increasingly smaller wireless sensor devices. Commercial antenna integration is becoming increasingly difficult, especially for the lower-UHF bands and there is a need for the development of new types of compact, low-cost antenna designs to meet the requirements of current and future devices. A second challenge concerns the effects of antenna detuning in wireless sensor applications. At present, these devices are implemented using simple, fixed matching networks that have no capability to deal with changing antenna environments. This is especially problematic where the wireless sensor device is placed on or close to the human body such as in the rapidly emerging application area of wearable BSN. This represents a key limitation of current technology. The final challenge relates to wireless sensor network reliability. At present, the vast majority of ISM-band wireless sensor platforms operate on a single frequency band with very limited redundancy in terms of wireless communications in the event of wireless network failure or issues associated with interference. Multi-band operation offers potential for improved data

reliability and quality-of-service (QoS) compared to the state-of-the-art but this requires the development of new types of multi-band antenna designs.

8.2 Contributions to state-of-the-art

To address the above challenges, this work has developed two generations of antenna tuning solutions. The architecture for a first-generation antenna tuner system was developed and a fully automated, 433 MHz solution was then demonstrated. A higher performance, second-generation tuner was then developed. This solution was substantially miniaturized in comparison to the first-generation solution, allowing the tuner to be integrated into the antenna element itself with significant improvements demonstrated in tuner losses, power consumption and tuning time. Two low cost, small-sized antenna designs were also developed. The first was a 433 MHz antenna that was designed to meet the needs of highly integrated WSN devices such as the Tyndall mote, using a compact and low cost antenna topology. A second dual-band antenna was developed to cover both the 433 MHz and 2.45 GHz ISM bands using a single-feed with no requirement for an additional groundplane. The journal and conference publications that have arisen from this work are listed at the end of this chapter.

8.3 Future Work

During the course of this thesis, several topics have emerged that would be appropriate for future research. The first issue relates to RF performance. To date, one of the biggest challenges in implementing antenna tuner designs has been the tradeoff between improved performance and losses of tunable RF components. However, there has been great progress made recently with the advent of low-loss MEMs tunable capacitors. For example tunable capacitors from Cavendish Kinetics [176] are now available with a Q-factor of > 200 at 800 MHz. The use of this technology in place of the existing devices would immediately reduce the matching network losses of the 433 MHz tunable antenna described in Chapter 6 by approximately 0.5 dB, without any other design changes required.

A high-Q tunable capacitor/inductor is only part of the solution however. A key component of an adaptive antenna tuning system is the impedance mismatch sensor that allows the determination of the degree of impedance match that exists. One or more directional couplers are generally used to sample the forward and reflected power levels from the antenna in order to determine the optimum tuner settings for maximum power delivery to the antenna. However, most present coupler designs, especially for the lower UHF bands, are large, discrete component devices with limited bandwidth and introduce losses when placed in circuit. A number of techniques have been proposed in the literature that remove the requirement for the coupler in cellular applications [177, 178] [120] and these approaches could offer potential performance improvements. Apart from the above issues, the biggest challenge relates to implementation and cost. In order to develop a tuning solution that was ready for mass adoption, a fully integrated, low-cost and low-power antenna tuner IC would be required.

In Chapter 4, it was shown that the reflection coefficient of the AUT was related to the distance of the AUT to the body. It was also shown in Chapter 6 that the optimal capacitor states could easily be determined as a function of reflection coefficient. It may therefore be possible to adjust the matching network based on known proximity information of the user. This could possibly allow the optimum tuner states of the tuner to be determined without the need for measuring the reflection coefficient of the antenna using a coupler and power detector(s). Most modern power detectors use logarithmic amplification to detect RF power levels. These types of power detector have a large dynamic range with a wide-band response but are power hungry and may not be practical in some types of low power wireless sensor operations.

In terms of measuring the radiation characteristics of the antennas described in this thesis, several improvements are necessary to improve the correlation between the measurements and simulation for the antennas discussed in Chapters 5 and 7. This would include the use of a fully calibrated, anechoic test environment that was calibrated over the frequency range from 400 MHz to 3 GHz for the test cases considered in this work.

For this work, load-pull measurements were carried out manually, using a triple-stub-tuner [148]. This method proved time consuming and an automated load-pull test method would be essential to thoroughly characterize the tuner. In addition, inter-modulation distortion measurements would be useful to characterize the linearity of the tuner in future work.

Journal Publications

J. L. Buckley, K. G. McCarthy, L. Loizou, B. O. Flynn, and C. O. Mathuna, "A Dual-ISM-Band Antenna of Small Size Using a Spiral Structure With Parasitic Element," IEEE Antennas and Wireless Propagation Letters, vol. 15, pp. 630-633, 2016.

J. L. Buckley, D. Gaetano, K. G. McCarthy, L. Loizou, B. O'Flynn, and C. O'Mathuna, "Compact 433 MHz antenna for wireless smart system applications," Electronics Letters, vol. 50, pp. 572-574, 2014.

Conference Publications

J. L. Buckley, K. G. McCarthy, B. O'Flynn, and C. O'Mathuna, "The detuning effects of a wrist-worn antenna and design of a custom antenna measurement system," in Microwave Conference (EuMC), 2010 European, 2010, pp. 1738-1741.

J. L. Buckley, B. O'Flynn, P. Haigh, C. O'Mathuna, and K. G. McCarthy, "Antenna tuning for wearable wireless sensors," in Sensors, 2011 IEEE, 2011, pp. 1990-1993.

Bibliography

[1] T. Gao, D. Greenspan, M. Welsh, R. R. Juang, and A. Alm, "Vital signs monitoring and patient tracking over a wireless network," in *Engineering in Medicine and Biology Society, 2005. IEEE-EMBS 2005. 27th Annual International Conference of the*, 2006, pp. 102-105.

[2] L. Jin-hee, K. Kyeongyul, L. Sang-Chul, and S. Byeong-Seok, "Smart backpack for visually impaired person," in *ICT for Smart Society (ICISS), 2013 International Conference on*, 2013, pp. 1-4.

[3] X. Ding, W. Dai, N. Luo, J. Liu, N. Zhao, and Y. Zhang, "A flexible tonoarteriography-based body sensor network for cuffless measurement of arterial blood pressure," in *Wearable and Implantable Body Sensor Networks (BSN), 2015 IEEE 12th International Conference on*, 2015, pp. 1-4.

[4] A. Nayak and I. Stojmenovic, "Wireless sensor and actuator networks," *John-Whiley & sons,* 2010.

[5] I. F. Akyildiz, W. Su, Y. Sankarasubramaniam, and E. Cayirci, "Wireless sensor networks: a survey," *Computer networks,* vol. 38, pp. 393-422, 2002.

[6] ERC70-03, "Recommendation relating to the use of short range devices (SRD)," *Version of,* vol. 18, 2009.

[7] A. E. Kouche, H. S. Hassanein, and A. Alma'aitah, "Configuring a UHF antenna for sensor nodes in harsh environments," in *Communications (QBSC), 2014 27th Biennial Symposium on*, 2014, pp. 66-70.

[8] A. Vander Vorst, A. Rosen, and Y. Kotsuka, *RF/microwave interaction with biological tissues* vol. 181: John Wiley & Sons, 2006.

[9] T. H. Lee, "The Design of CMOS Radio-Frequency Integrated Circuits," 2nd ed: Prentice Hall, 2012, pp. 136-144.

[10] J. Gemio, J. Parron, and J. Soler, "Human body effects on implantable antennas for ISM bands applications: Models comparison and propagation losses study," *Progress In Electromagnetics Research,* vol. 110, pp. 437-452, 2010.

[11] H. S. Savci, A. Sula, W. Zheng, N. S. Dogan, and E. Arvas, "MICS transceivers: regulatory standards and applications [medical implant communications service]," in *SoutheastCon, 2005. Proceedings. IEEE*, 2005, pp. 179-182.

[12] S. C. Mukhopadhyay, "Wearable sensors for human activity monitoring: A review," *Sensors Journal, IEEE,* vol. 15, pp. 1321-1330, 2015.

[13] Linx Technologies Inc. (2015, November). *ANTEN 433MHz 1/4 Wave Whip Antenna*. Available: http://www.linxtechnologies.com, Accessed May 2016

[14] Taoglas Limited. (2015, November). *ANT 433MHz ISM Band Dipole*. Available: http://www.taoglas.com/, Accessed May 2016

[15] Taoglas. (2015, November). *ANT 433MHz, ISM Band Helical*. Available: http://www.taoglas.com/, Accessed May 2016

[16] Yaego. (2015, November). *ANT1204F002R0433A, Chip antenna 433 MHz*. Available: http://www.yaego.com, Accessed May 2016

[17] H. A. Wheeler, "Fundamental Limitations of Small Antennas," *Proceedings of the IRE,* vol. 35, pp. 1479-1484, 1947.

[18] F. Merli, L. Bolomey, J. Zurcher, G. Corradini, E. Meurville, and A. K. Skrivervik, "Design, realization and measurements of a miniature antenna for implantable wireless communication systems," *Antennas and Propagation, IEEE Transactions on,* vol. 59, pp. 3544-3555, 2011.

[19] K. L. Wong and C. I. Lin, "Characteristics of a 2.4-GHz compact shorted patch antenna in close proximity to a lossy medium," *Microwave and Optical Technology Letters,* vol. 45, pp. 480-483, 2005.

[20] D. Chen and P. K. Varshney, "QoS Support in Wireless Sensor Networks: A Survey," in *International Conference on Wireless Networks*, 2004, pp. 227-233.

[21] F. Hu and S. Kumar, "QoS considerations in wireless sensor networks for telemedicine," in *ITCom 2003*, 2003, pp. 217-227.

[22] A. Milenković, C. Otto, and E. Jovanov, "Wireless sensor networks for personal health monitoring: Issues and an implementation," *Computer communications,* vol. 29, pp. 2521-2533, 2006.

[23] B. O'Flynn, S. Bellis, K. Delaney, J. Barton, S. C. O'Mathuna, A. M. Barroso, J. Benson, U. Roedig, and C. Sreenan, "The development of a novel minaturized modular platform for

wireless sensor networks," in *Information Processing in Sensor Networks, 2005. IPSN 2005. Fourth International Symposium on*, 2005, pp. 370-375.

[24] C. A. Balanis, *Antenna theory: analysis and design* vol. 1: John Wiley & Sons, 2005.

[25] J. D. Kraus, "Antennas For All Applications," Third ed: McGraw Hill, 2002, pp. 181-183.

[26] D. M. Pozar, "Microwave Engineering," Fourth ed: John Wiley & Sons, Inc., 2012, p. 561.

[27] M. A. Christou, N. C. Papanicolaou, and A. C. Polycarpou, "A nematic liquid crystal tunable patch antenna," in *Antennas and Propagation (EuCAP), 2014 8th European Conference on*, 2014, pp. 1875-1878.

[28] T. S. Bird, "Definition and Misuse of Return Loss [Report of the Transactions Editor-in-Chief]," *Antennas and Propagation Magazine, IEEE,* vol. 51, pp. 166-167, 2009.

[29] M. Golio and J. Golio, *RF and microwave passive and active technologies*: CRC Press, 2007.

[30] J. C. McLaughlin and K. L. Kaiser, ""Deglorifying" the Maximum Power Transfer Theorem and Factors in Impedance Selection," *Education, IEEE Transactions on,* vol. 50, pp. 251-255, 2007.

[31] R. K. Saini and S. Dwari, "CPW-fed broadband circularly polarized microstrip rectangular slot antenna with triangular fractal slots in tuning stub," in *2013 IEEE Applied Electromagnetics Conference, AEMC 2013*, 2013.

[32] Y. Huang and K. Boyle, *Antennas: from theory to practice*: John Wiley & Sons, 2008.

[33] Nordic Semiconductor. (2015, November). *nRF905, Low power Multiband Sub 1-GHz RF Transceiver IC* Available: http://www.nordicsemi.com, Accessed May 2016

[34] G. Qizheng, J. R. De Luis, A. S. Morris, and J. Hilbert, "An Analytical Algorithm for Pi-Network Impedance Tuners," *Circuits and Systems I: Regular Papers, IEEE Transactions on,* vol. 58, pp. 2894-2905, 2011.

[35] P. Hurwitz, S. Chaudry, V. Blaschke, and M. Racanelli, "Foundry SOI technology for wireless front end modules," in *2013 IEEE SOI-3D-Subthreshold Microelectronics Technology Unified Conference, S3S 2013*, 2013.

[36] J. S. McLean, "A re-examination of the fundamental limits on the radiation Q of electrically small antennas," *Antennas and Propagation, IEEE Transactions on,* vol. 44, p. 672, 1996.

[37] I. J. Bahl, *Lumped elements for RF and microwave circuits*: Artech house, 2003.

[38] C. Bowick, *RF circuit design*: Newnes, 2011.

[39] R. Ludwig, Bogdanov. G, "RF Circuit Design," Second ed: McGraw Hill, 2009, pp. 104-106.

[40] P. H. Smith, "Transmission line calculator," *Electronics,* vol. 12, pp. 29-31, 1939.

[41] A. W. R. (AWR). (2015, Jan). *Microwave Office V.10*. Available: http://www.awrcorp.com, Accessed May 2016

[42] ANSYS. (2015, Nov). *High Frequency Structure Simulator (HFSS) V14.0*. Available: http://www.ansys.com, Accessed May 2016

[43] ANSYS. (2010, May). *Ansoft – Antenna/RF Training Guide*. Available: http://www.ansys.com, Accessed May 2016

[44] Keysight. (2015, Jan). *Keysight (Agilent) ADS, 2011* Available: http://www.keysight.com, Accessed May 2016

[45] LPKF. (2015, November). *LPKF Protomat C60 PCB Milling/Manufacturing Machine*. Available: http://www.lpkfusa.com, Accessed May 2016

[46] Beta Layout. (2015, November). *Printed Circuit Board Manufacturing*. Available: https://www.beta-layout.com, Accessed May 2016

[47] Rohde & Schwarz. (2015, November). *ZVRE 4 GHz, 2-Port Vector Network Analyzer*. Available: https://www.rohde-schwarz.com, Accessed May 2016

[48] Rohde & Schwarz. (2015, November). *ZV-Z32, 3.5 mm Manual Calibration Kit*. Available: https://www.rohde-schwarz.com/, Accessed May 2016

[49] ETS Lindgren. (2015, November). *Model SpaceSaver FAR 26 MHz - 40 GHz, Semi-Anechoic Shielded Chamber*. Available: http://www.ets-lindgren.com, Accessed May 2016

[50] Anritsu. (2015, November). *Model MS2038C, VNA Master (5 kHz to 20 GHz)* Available: https://www.anritsu.com, Accessed May 2016

[51] ETS Lindgren. (2015, November). *Model 2090 Multi-Device Positioning Controller*. Available: http://www.ets-lindgren.com, Accessed May 2016

[52] ETS Lindgren. (2015, November). *Model 2188, 1.2 m Turntable*. Available: http://www.ets-lindgren.com, Accessed May 2016

[53] National Instruments. (2015, November). *Labview 2010, (32-bit)*. Available: http://www.ni.com, Accessed May 2016

[54] Schwarzbeck. (2015, November). *Model BBHA 9120 D - Double Ridged Broadband Horn Antenna*. Available: http://www.schwarzbeck.de, Accessed May 2016

[55] Linx technologies. (2015, December). *Model ANT-418-YG5-N, Yagi Antenna*. Available: http://www.linxtechnologies.com, Accessed May 2016

[56] M. Ammann and M. John, "Some techniques to improve small groundplane printed monopole performance," in *IEEE Antennas and Propagation Society International Symposium*, 2007, pp. 2825-2828.

[57] S. Curto, M. John, and M. Ammann, "Groundplane dependent performance of printed antenna for MB-OFDM-UWB," presented at the IEEE Vehicular Technology Conference, Dublin, Ireland, 2007.

[58] B. Collins and S. Saario, "The use of baluns for measurements on antennas mounted on small groundplanes," in *Antenna Technology: Small Antennas and Novel Metamaterials, 2005. IWAT 2005. IEEE International Workshop on*, 2005, pp. 266-269.

[59] L. Loizou, J. Buckley, B. O'Flynn, J. Barton, C. O'Mathuna, and E. Popovici, "Design and measurement of a planar dual-band antenna for the Tyndall Multiradio wireless sensing platform," in *2013 IEEE Sensors Applications Symposium, SAS 2013 - Proceedings*, 2013, pp. 11-14.

[60] Fair-Rite Products Corp. (2015, Jan). *Model 74271633S, FERRITE CORE, SPLIT, 8.5 mm*. Available: http://katalog.we-online.de/pbs/datasheet/74271622S.pdf, Accessed May 2016

[61] P. Massey and K. Boyle, "Controlling the effects of feed cable in small antenna measurements," 2003.

[62] J. Buckley, B. O'Flynn, L. Loizou, P. Haigh, D. Boyle, P. Angove, J. Barton, C. O'Mathúna, E. Popovici, and S. O'Connell, "A novel and miniaturized 433/868MHz multi-band wireless sensor platform for body sensor network applications," in *Proceedings - BSN 2012: 9th International Workshop on Wearable and Implantable Body Sensor Networks*, 2012, pp. 63-66.

[63] C. Ó. Conaire, D. Connaghan, P. Kelly, N. E. O'Connor, M. Gaffney, and J. Buckley, "Combining inertial and visual sensing for human action recognition in tennis," in *ARTEMIS'10 - Proceedings of the 1st ACM Workshop on Analysis and Retrieval of Tracked Events and Motion in Imagery Streams, Co-located with ACM Multimedia 2010*, 2010, pp. 51-56.

[64] M. Crepaldi, P. Ros Motto, D. Demarchi, J. Buckley, B. O'Flynn, and D. Quaglia, "A physical-aware abstraction flow for efficient design-space exploration of a wireless body

area network application," in *Proceedings - 16th Euromicro Conference on Digital System Design, DSD 2013*, 2013, pp. 1005-1012.

[65] M. Gaffney, B. O'Flynn, A. Mathewson, J. Buckley, J. Barton, P. Angove, J. Vcelak, C. Ó Conaire, G. Healy, and K. Moran, "Wearable wireless inertial measurement for sports applications," *Proc. IMAPS-CPMT Poland 2009, Gliwice–Pszczyna, Poland, 22-24 Sept, 2009,* 2009.

[66] L. Loizou, J. Buckley, and B. O'Flynn, "Design and Analysis of a Dual-Band Inverted-F Antenna With Orthogonal Frequency-Controlled Radiation Planes," *Antennas and Propagation, IEEE Transactions on,* vol. 61, pp. 3946-3951, 2013.

[67] E. Popovici, D. Boyle, S. O'Connell, S. Faul, P. Angove, J. Buckley, B. O'Flynn, J. Barton, and C. O'Mathúna, "The s-Mote: A versatile heterogeneous multi-radio platform for wireless sensor networks applications," in *2011 20th European Conference on Circuit Theory and Design, ECCTD 2011*, 2011, pp. 421-424.

[68] C. Chee-Yee and S. P. Kumar, "Sensor networks: evolution, opportunities, and challenges," *Proceedings of the IEEE,* vol. 91, pp. 1247-1256, 2003.

[69] F. Sarrazin, S. Pflaum, and C. Delaveaud, "Radiation efficiency optimization of electrically small antennas: Application to 3D folded dipole," in *2016 International Workshop on Antenna Technology (iWAT)*, 2016, pp. 29-32.

[70] R. Verdone, D. Dardari, G. Mazzini, and A. Conti, *Wireless sensor and actuator networks: technologies, analysis and design*: Academic Press, 2010.

[71] M. Crepaldi, P. M. Ros, D. Demarchi, J. Buckley, B. O'Flynn, and D. Quaglia, "A Physical-Aware Abstraction Flow for Efficient Design-Space Exploration of a Wireless Body Area Network Application," in *Digital System Design (DSD), 2013 Euromicro Conference on*, 2013, pp. 1005-1012.

[72] A. Guinard, A. McGibney, and D. Pesch, "A wireless sensor network design tool to support building energy management," in *Proceedings of the First ACM Workshop on Embedded Sensing Systems for Energy-Efficiency in Buildings*, 2009, pp. 25-30.

[73] W.-S. Jang, W. M. Healy, and M. J. Skibniewski, "Wireless sensor networks as part of a web-based building environmental monitoring system," *Automation in Construction,* vol. 17, pp. 729-736, 2008.

[74] W. Wang, N. Wang, E. Jafer, M. Hayes, B. O'Flynn, and C. O'Mathuna, "Autonomous wireless sensor network based building energy and environment monitoring system design," in *Environmental Science and Information Application Technology (ESIAT), 2010 International Conference on*, 2010, pp. 367-372.

[75] W. Quinn, P. Angove, J. Buckley, J. Barrett, and G. Kelly, "Design and performance analysis of an embedded wireless sensor for monitoring concrete curing and structural health," *Journal of Civil Structural Health Monitoring,* vol. 1, pp. 47-59, 2011.

[76] S. Kingsley, "Advances in handset antenna design," *RF design,* pp. 16-22, 2005.

[77] M. Caldara, C. Colleoni, E. Guido, G. Rosace, V. Re, and A. Vitali, "A wearable sensor platform to monitor sweat pH and skin temperature," in *Body Sensor Networks (BSN), 2013 IEEE International Conference on*, 2013, pp. 1-6.

[78] Y.-D. Lee and W.-Y. Chung, "Wireless sensor network based wearable smart shirt for ubiquitous health and activity monitoring," *Sensors and Actuators B: Chemical,* vol. 140, pp. 390-395, 2009.

[79] S. Ullah, H. Higgins, B. Braem, B. Latre, C. Blondia, I. Moerman, S. Saleem, Z. Rahman, and K. S. Kwak, "A comprehensive survey of wireless body area networks," *Journal of medical systems,* vol. 36, pp. 1065-1094, 2012.

[80] A. Pantelopoulos and N. G. Bourbakis, "A Survey on Wearable Sensor-Based Systems for Health Monitoring and Prognosis," *Systems, Man, and Cybernetics, Part C: Applications and Reviews, IEEE Transactions on,* vol. 40, pp. 1-12, 2010.

[81] A. Lymberis and L. Gatzoulis, "Wearable Health Systems: from smart technologies to real applications," in *Engineering in Medicine and Biology Society, 2006. EMBS '06. 28th Annual International Conference of the IEEE*, 2006, pp. 6789-6792.

[82] M. C. Rocu, "Implementation for a WBAN-ECG monitoring system (preliminary results)," in *Optimization of Electrical and Electronic Equipment (OPTIM), 2014 International Conference on*, 2014, pp. 823-826.

[83] Moog Crossbow. (2015, November). *Mica 2 Mote*. Available: http://www.moog-crossbow.com, Accessed May 2016

[84] Moog Crossbow. (2015, November). *Mica Dot Mote*. Available: http://www.moog-crossbow.com, Accessed May 2016

[85] Libelium. (2015, Jan). *Wasp Mote Platform*. Available: http://www.libelium.com, Accessed May 2016

[86] Atmega. (2015, Jan). *AtMega128L, High-performance, 8-bit, RISC Microcontroller*. Available: http://www.atmel.com, Accessed May 2016

[87] P. Ali-Rantala, L. Sydanheimo, M. Keskilammi, and M. Kivikoski, "Indoor propagation comparison between 2.45 GHz and 433 MHz transmissions," in *Antennas and Propagation Society International Symposium, 2002. IEEE*, 2002, pp. 240-243 vol.1.

[88] M. Taj-Eldin, W. B. Kuhn, A. H. Fowles, B. Natarajan, G. Peterson, M. Alshetaiwi, O. Shuo, G. Sanchez, and E. Monfort-Nelson, "Study of Wireless Propagation for Body Area Networks Inside Space Suits," *Sensors Journal, IEEE,* vol. 14, pp. 3810-3818, 2014.

[89] M. D. Weiss, J. L. Smith, and J. Bach, "RF Coupling in a 433-MHz Biotelemetry System for an Artificial Hip," *Antennas and Wireless Propagation Letters, IEEE,* vol. 8, pp. 916-919, 2009.

[90] Linx Technologies Inc. (2015, November). *ANT-433-PW-QW-UFL, 1/4 Wave Whip, Straight*. Available: http://www.linxtechnologies.com, Accessed May 2016

[91] Linx Technologies. (2015, November). *Model ANT-433-SP 433 MHz Planar Antenna* Available: http://www.linxtechnologies.com, Accessed May 2016

[92] Linx technologies. (2015, December). *Model ANT-433-HESM, 433 Helical Antenna*. Available: https://www.linxtechnologies.com, Accessed May 2016

[93] Linx Technologies. (2015, November). *ANT-433-USP, Splatch 433 MHz Antenna*. Available: http://media.digikey.com, Accessed May 2016

[94] Linx Technologies. (2015, November). *Model ANT-433-PW-QW , 433 MHz 1/4 Wave Whip Antenna*. Available: http://www.linxtechnologies.com, Accessed May 2016

[95] A. Babar, L. Ukkonen, M. Soini, and L. Sydanheimo, "Miniaturized 433 MHz antenna for card size wireless systems," in *Antennas and Propagation Society International Symposium, 2009. APSURSI'09. IEEE*, 2009, pp. 1-4.

[96] S. Genovesi, A. Monorchio, and S. Saponara, "Double-loop antenna for wireless tyre pressure monitoring," *Electronics Letters,* vol. 44, pp. 1385-1387, 2008.

[97] X. Li-Jie, G. Yong-Xin, and W. Wen, "Dual-Band Implantable Antenna With Open-End Slots on Ground," *Antennas and Wireless Propagation Letters, IEEE,* vol. 11, pp. 1564-1567, 2012.

[98] MACOM. (2016, May). *MABA-007159-000000 E-Series RF 1:1 Transmission Line Transformer 4.5 - 3000 MHz*. Available: http://www.macom.com, Accessed May 2016

[99] C. Oliveira, M. Mackowiak, and L. M. Correia, "A comparison of phantom models for on-body communications," in *2012 IEEE 23rd International Symposium on Personal, Indoor and Mobile Radio Communications - (PIMRC)*, 2012, pp. 1666-1670.

[100] P. Dimbylow, "The development of realistic voxel phantoms for electromagnetic field dosimetry," in *Proc. Int. Workshop on Voxel Phantom Development*, 1996, pp. 1-7.

[101] F. Jia-Shiang, X. A. Zhu, J. D. Phillips, and A. Mortazawi, "A ferroelectric-based impedance tuner for adaptive matching applications," in *Microwave Symposium Digest, 2008 IEEE MTT-S International*, 2008, pp. 955-958.

[102] J. Lindstrand, I. Vasilev, and H. Sjöland, "A low band cellular terminal antenna impedance tuner in 130nm CMOS-SOI technology," in *European Solid-State Circuits Conference*, 2014, pp. 459-462.

[103] T. Ranta, R. Whatley, C. C. Cheng, and M. Facchini, "Next-generation CMOS-on-insulator multi-element network for broadband antenna tuning," in *European Microwave Week 2013, EuMW 2013 - Conference Proceedings; EuMC 2013: 43rd European Microwave Conference*, 2013, pp. 1567-1570.

[104] F. Sonnerat, R. Pilard, F. Gianesello, S. Jan, F. Le Pennec, C. Person, C. Durand, and D. Gloria, "30 dBm P1dB and 4 dB insertion losses optimized 4G antenna tuner fully integrated in a 130 nm CMOS SOI technology," in *IEEE Radio and Wireless Symposium, RWS*, 2013, pp. 73-75.

[105] F. Sonnerat, R. Pilard, F. Gianesello, S. Jan, F. L. Pennec, C. Person, C. Durand, and D. Gloria, "30 dBm P1db and 4 dB insertion losses optimized 4G antenna tuner fully integrated in a 130 nm CMOS SOI technology," in *2013 IEEE 13th Topical Meeting on Silicon Monolithic Integrated Circuits in RF Systems, SiRF 2013 - RWW 2013*, 2013, pp. 39-41.

[106] S. Caporal Del Barrio, A. Morris, and G. F. Pedersen, "Antenna miniaturization with MEMS tunable capacitors: Techniques and trade-offs," *International Journal of Antennas and Propagation,* vol. 2014, 2014.

[107] M. Chen, C. C. Chen, and J. L. Volakis, "Reconfigurable 800-1500MHz double stub tuner using MEMS capacitive switches," in *IEEE Antennas and Propagation Society, AP-S International Symposium (Digest)*, 2013, pp. 2157-2158.

[108] M. De Jongh, A. Van Bezooijen, K. R. Boyle, and T. Bakker, "Mobile phone performance improvements using an adaptively controlled antenna tuner," in *Microwave Symposium Digest (MTT), 2011 IEEE MTT-S International*, 2011, pp. 1-4.

[109] Y. Kwon and S. Lee, "RF MEMS - Enabling technology for millimeter-waves," *IEICE Transactions on Electronics,* vol. E89-C, pp. 898-905, 2006.

[110] J. Zhong, A. Kiourti, and J. L. Volakis, "Increasing the efficiency of electrically small antennas across a large bandwidth using matching networks," in *IEEE Antennas and Propagation Society, AP-S International Symposium (Digest)*, 2014, pp. 633-634.

[111] R. R. Mansour, "RF MEMS-CMOS Device Integration: An Overview of the Potential for RF Researchers," *Microwave Magazine, IEEE,* vol. 14, pp. 39-56, 2013.

[112] A. S. Morris, "Reconfigurable solutions for mobile device RF front-ends," in *Silicon Monolithic Integrated Circuits in RF Systems (SiRF), 2015 IEEE 15th Topical Meeting on*, 2015, pp. 63-66.

[113] B. Baxter, T. Ranta, M. Facchini, D. Jung, and D. Kelly, "The state-of-the-art in silicon-on-sapphire components for antenna tuning," in *IEEE MTT-S International Microwave Symposium Digest*, 2013.

[114] P. Semiconductor. (2015, Jan). *PE4251, RF Switch*. Available: http://www.psemi.com, Accessed May 2016

[115] C. H. Ko, K. M. J. Ho, R. Gaddi, and G. M. Rebeiz, "A 1.5–2.4 GHz tunable 4-pole filter using commercial high-reliability 5-bit RF MEMS capacitors," in *Microwave Symposium Digest (IMS), 2013 IEEE MTT-S International*, 2013, pp. 1-4.

[116] S. P. Natarajan, S. J. Cunningham, A. S. Morris Iii, and D. R. Dereus, "CMOS integrated digital RF MEMS capacitors," in *2011 IEEE 11th Topical Meeting on Silicon Monolithic Integrated Circuits in RF Systems, SiRF 2011 - Digest of Papers*, 2011, pp. 173-176.

[117] L. Sankey and Z. Popovic, "Adaptive tuning for handheld transmitters," in *Microwave Symposium Digest, 2009. MTT '09. IEEE MTT-S International*, 2009, pp. 225-228.

[118] C. Hoarau, N. Corrao, J.-D. Arnould, P. Ferrari, and P. Xavier, "Complete design and measurement methodology for a tunable RF impedance-matching network," *Microwave Theory and Techniques, IEEE Transactions on,* vol. 56, pp. 2620-2627, 2008.

[119] R. B. Whatley, Z. Zhou, and K. L. Melde, "Reconfigurable RF impedance tuner for match control in broadband wireless devices," *Antennas and Propagation, IEEE Transactions on,* vol. 54, pp. 470-478, 2006.

[120] K. R. Boyle, E. Spits, M. A. de Jongh, S. Sato, T. Bakker, and A. van Bezooijen, "A self-contained adaptive antenna tuner for mobile phones: Featuring a self-learning calibration procedure," in *Antennas and Propagation (EUCAP), 2012 6th European Conference on*, 2012, pp. 1804-1808.

[121] D. Nicolas, A. Giry, E. Ben Abdallah, S. Bories, G. Tant, T. Parra, C. Delaveaud, P. Vincent, and F. C. W. Po, "SOI CMOS tunable capacitors for RF antenna aperture tuning," in *2014 21st IEEE International Conference on Electronics, Circuits and Systems, ICECS 2014*, 2014, pp. 383-386.

[122] P. Shi, "Aperture-Tunable Antennas," *Tunable RF Components and Circuits: Applications in Mobile Handsets,* vol. 51, p. 191, 2015.

[123] H. Morishita, H. Furuuchi, and K. Fujimoto, "Performance of balance-fed antenna system for handsets in the vicinity of a human head or hand," *Microwaves, Antennas and Propagation, IEE Proceedings,* vol. 149, pp. 85-91, 2002.

[124] J.-Y. Jan and L.-C. Tseng, "Small planar monopole antenna with a shorted parasitic inverted-L wire for wireless communications in the 2.4-, 5.2-, and 5.8-GHz bands," *Antennas and Propagation, IEEE Transactions on,* vol. 52, pp. 1903-1905, 2004.

[125] M. Fallahpour, M. T. Ghasr, and R. Zoughi, "Miniaturized Reconfigurable Multiband Antenna For Multiradio Wireless Communication," *Antennas and Propagation, IEEE Transactions on,* vol. 62, pp. 6049-6059, 2014.

[126] Abracon. (2015, May). *APAMPSLJ-142, Multiband Antenna Module*. Available: http://www.abracon.com, Accessed May 2016

[127] R. S. Alrawashdeh, Y. Huang, M. Kod, and A. A. B. Sajak, "A Broadband Flexible Implantable Loop Antenna With Complementary Split Ring Resonators," *Antennas and Wireless Propagation Letters, IEEE,* vol. 14, pp. 1322-1325, 2015.

[128] H. Fu-Jhuan, L. Chien-Ming, C. Chia-Lin, C. Liang-Kai, Y. Tzong-Chee, and L. Ching-Hsing, "Rectenna Application of Miniaturized Implantable Antenna Design for Triple-Band Biotelemetry Communication," *Antennas and Propagation, IEEE Transactions on,* vol. 59, pp. 2646-2653, 2011.

[129] K. Jae Hee, C. Won Woo, and P. Wee Sang, "A Small Dual-Band Inverted-F Antenna With a Twisted Line," *Antennas and Wireless Propagation Letters, IEEE,* vol. 8, pp. 307-310, 2009.

[130] J. Buckley, K. G. McCarthy, B. O'Flynn, and C. O'Mathuna, "The detuning effects of a wrist-worn antenna and design of a custom antenna measurement system," in *Microwave Conference (EuMC), 2010 European*, 2010, pp. 1738-1741.

[131] J. Buckley, B. O'Flynn, P. Haigh, C. O'Mathuna, and K. G. McCarthy, "Antenna tuning for wearable wireless sensors," in *Sensors, 2011 IEEE*, 2011, pp. 1990-1993.

[132] M. Okoniewski and M. Stuchly, "A study of the handset antenna and human body interaction," *Microwave Theory and Techniques, IEEE Transactions on,* vol. 44, pp. 1855-1864, 1996.

[133] Speag. (2015, November). *SHO - Forearm Phantom V2* Available: http://www.speag.com, Accessed May 2016

[134] P. Liu, C. M. Rappaport, Y.-z. Wei, and S. Sridhar, "Simulated biological materials at microwave frequencies for the study of electromagnetic hyperthermia," in *Engineering in Medicine and Biology Society, 1992 14th Annual International Conference of the IEEE*, 1992, pp. 272-273.

[135] K. Ogawa, T. Matsuyoshi, H. Iwai, and N. Hatakenaka, "A high-precision real human phantom for EM evaluation of handheld terminals in a talk situation," in *Antennas and Propagation Society International Symposium, 2001. IEEE*, 2001, pp. 68-71.

[136] G. Hartsgrove, A. Kraszewski, and A. Surowiec, "Simulated biological materials for electromagnetic radiation absorption studies," *Bioelectromagnetics,* vol. 8, pp. 29-36, 1987.

[137] Isola FR4 Laminates. (2015, November). *Duraver Laminate, FR4*. Available: http://www.pcb-specification.com, Accessed May 2016

[138] M. Lazebnik, E. L. Madsen, G. R. Frank, and S. C. Hagness, "Tissue-mimicking phantom materials for narrowband and ultrawideband microwave applications," *Physics in medicine and biology,* vol. 50, p. 4245, 2005.

[139] Rogers Corporation. (2015, November). *RO4000® Series High Frequency Circuit Materials*. Available: https://www.rogerscorp.com/documents/726/acm/RO4000-Laminates---Data-sheet.pdf

[140] G. Qizheng and A. S. Morris, "A New Method for Matching Network Adaptive Control," *Microwave Theory and Techniques, IEEE Transactions on,* vol. 61, pp. 587-595, 2013.

[141] A. W. R. (AWR). (2015, Jan). *IMatch, 2010*. Available: http://www.awrcorp.com, Accessed May 2016

[142] Vishay electronic Components. (2015, November). *BFC280831809, CAP TRIMMER 6-80pF* Available: http://www.vishay.com/docs/28528/bfc2808-10mm.pdf

[143] American Technical Ceramics. (2015, November). *0402WL160JT, ATC WL Series, High Frequency Wire Wound Chip Inductors,* . Available: http://www.atceramics.com, Accessed May 2016

[144] Rohde & schwarz. (2015, November). *FSUP Signal Source Analyzer* Available: https://www.rohde-schwarz.com, Accessed May 2016

[145] MiniCircuits. (2015, Jan). *ZFBDC20-62HP Bi-Directional Coupler*. Available: http://www.minicircuits.com, Accessed May 2016

[146] MiniCircuits. (2015, Jan). *ZX47-55 Power Detector*. Available: https://www.minicircuits.com, Accessed May 2016

[147] Rohde & schwarz. (2015, November). *SML03 Signal Generator*. Available: https://www.rohde-schwarz.com, Accessed May 2016

[148] Maury. (2015, November). *Model 1878G Triple-Stub Tuner (200 to 500 MHz)* Available: https://www.maurymw.com, Accessed May 2016

[149] P. Semiconductor. (2015, Nov). *PE4210, SPDT RF Reflective Switch*. Available: http://www.psemi.com, Accessed May 2016

[150] J. de Mingo, A. Valdovinos, A. Crespo, D. Navarro, and P. Garcia, "An RF electronically controlled impedance tuning network design and its application to an antenna input impedance automatic matching system," *Microwave Theory and Techniques, IEEE Transactions on,* vol. 52, pp. 489-497, 2004.

[151] Beta Layout. (2015, November). *FR-4, 4 layer stackup specification*. Available: http://www.pcb-specification.com, Accessed May 2016

[152] American Technical Ceramics. (2015, November). *600 L Series Series, Ultra-Low ESR, High Q NPO, RF and Microwave Capacitors*. Available: http://www.atceramics.com, Accessed May 2016

[153] J. Buckley, D. Gaetano, K. G. McCarthy, L. Loizou, B. O'Flynn, and C. O'Mathuna, "Compact 433 MHz antenna for wireless smart system applications," *Electronics Letters,* vol. 50, pp. 572-574, 2014.

[154] Andus. (2015, November). *PROBIMER ® 77, 7179/7180, High Performance Photoimageable Solder Mask* Available: http://www.andus.de/_pdf/probimer-77.pdf

[155] L. Yue, Z. Zhijun, C. Wenhua, F. Zhenghe, and M. F. Iskander, "A Quadband Antenna With Reconfigurable Feedings," *Antennas and Wireless Propagation Letters, IEEE,* vol. 8, pp. 1069-1071, 2009.

[156] C. Zhizhang, A. D. Ganjara, and C. Xiaomin, "A dual-L antenna with a novel tuning technique for dual frequency applications," *Antennas and Propagation, IEEE Transactions on,* vol. 50, pp. 402-403, 2002.

[157] N. Gunavathi and D. S. Kumar, "A compact coplanar waveguide-fed slot antenna for UWB applications," in *2014 International Conference on Electronics and Communication Systems, ICECS 2014*, 2014.

[158] C. Storni, "Report in the reassembling health workshop: Exploring the role of the Internet of Things," *J. Particip. Med. Conf,* vol. 2, 2010.

[159] M. L. Scarpello, D. Kurup, H. Rogier, D. Vande Ginste, F. Axisa, J. Vanfleteren, W. Joseph, L. Martens, and G. Vermeeren, "Design of an implantable slot dipole conformal flexible antenna for biomedical applications," *Antennas and Propagation, IEEE Transactions on,* vol. 59, pp. 3556-3564, 2011.

[160] R. F. a. C. P. D.Andreuccetti. (1996). *An Internet resource for the calculation of the dielectric properties of body tissues in the frequency range 10 Hz to 100 GHz.* Available: http://niremf.ifac.cnr.it/tissprop/, Accessed May 2016

[161] ETS Lindgren. (2015, November). *AMS 8050 Antenna Measurement System*. Available: http://www.ets-lindgren.com, Accessed May 2016

[162] Emerson & Cuming Microwave Products. (2015, November). *ECCOSTOCK® PP-2, Flexible, Low Loss, Closed Cell Polyethylene Foam*. Available: http://www.lairdtech.com, Accessed May 2016

[163] Mathworks. (2015, Jan). *Matlab 2011*. Available: https://uk.mathworks.com, Accessed May 2016

[164] W. Yu-Shin, L. Ming-Chou, and C. Shyh-Jong, "Two PIFA-Related Miniaturized Dual-Band Antennas," *Antennas and Propagation, IEEE Transactions on,* vol. 55, pp. 805-811, 2007.

[165] R. B. Whatley, Z. Zhen, and K. L. Melde, "Reconfigurable RF impedance tuner for match control in broadband wireless devices," *Antennas and Propagation, IEEE Transactions on,* vol. 54, pp. 470-478, 2006.

[166] N. J. Smith, C. Chen, and J. L. Volakis, "An Improved Topology for Adaptive Agile Impedance Tuners," *Antennas and Wireless Propagation Letters, IEEE,* vol. 12, pp. 92-95, 2013.

[167] P. Semiconductor. (2015, Jan). *PE64102, Digital Tunable Capacitor*. Available: http://www.psemi.com, Accessed May 2016

[168] Coilcraft. (2015, Jan). *0807SQ-14NJLB, Air Core Inductor*. Available: http://www.coilcraft.com, Accessed May 2016

[169] MiniCircuits. (2015, Jan). *SYDC-20-62HP+ Coupler*. Available: http://www.minicircuits.com, Accessed May 2016

[170] Linear Technology. (2015, Jan). *LT5538, RF Power Detector*. Available: http://www.linear.com, Accessed May 2016

[171] K. L. Wong and C. Y. Tsai, "Low-Profile Dual-Wideband Inverted-T Open Slot Antenna for the LTE/WWAN Tablet Computer With a Metallic Frame," *IEEE Transactions on Antennas and Propagation,* vol. 63, pp. 2879-2886, 2015.

[172] J. L. Buckley, K. G. McCarthy, L. Loizou, B. O. Flynn, and C. O. Mathuna, "A Dual-ISM-Band Antenna of Small Size Using a Spiral Structure With Parasitic Element," *IEEE Antennas and Wireless Propagation Letters,* vol. 15, pp. 630-633, 2016.

[173] ANSYS. (2015, Nov). *Optimetrics*. Available: http://www.ansys.com, Accessed May 2016

[174] R. Fletcher, *Practical methods of optimization*: John Wiley & Sons, 2013.

[175] J. Pandey, L. Yu-Te, A. Lingley, R. Mirjalili, B. Parviz, and B. Otis, "A Fully Integrated RF-Powered Contact Lens With a Single Element Display," *Biomedical Circuits and Systems, IEEE Transactions on,* vol. 4, pp. 454-461, 2010.

[176] C. Kinetics. (2015, Jan). *32CKxxxY, SmarTune Antenna Tuner, PRODUCT BRIEF (2015)*. Available: http://www.cavendish-kinetics.com, Accessed May 2016

[177] E. L. Firrao, A.-J. Annema, and B. Nauta, "An automatic antenna tuning system using only RF signal amplitudes," *Circuits and Systems II: Express Briefs, IEEE Transactions on,* vol. 55, pp. 833-837, 2008.

[178] A. Van Bezooijen, M. De Jongh, F. Van Straten, R. Mahmoudi, and A. H. Van Roermund, "Adaptive impedance-matching techniques for controlling L networks," *Circuits and Systems I: Regular Papers, IEEE Transactions on,* vol. 57, pp. 495-505, 2010.